Alma Mater Studiorum - Università di Bologna

DOTTORATO DI RICERCA IN

CHIMICA

Ciclo 34

Settore Concorsuale: 03/A2 - MODELLI E METODOLOGIE PER LE SCIENZE CHIMICHE

Settore Scientifico Disciplinare: CHIM/02 - CHIMICA FISICA

ELECTROCHEMILUMINESCENCE: INSIGHTS INTO THE MECHANISMS AND NANOMATERIAL-BASED APPLICATIONS

Presentata da: Sara Rebeccani

Coordinatore Dottorato

Luca Prodi

Supervisore

Francesco Paolucci

Co-supervisore

Giovanni Valenti

Esame finale anno 2022

CONTENTS

ABSTRACT

Biomarkers are biological indicators of human health conditions. Their ultra-sensitive quantification is of paramount importance in clinical monitoring and early disease diagnosis. Biosensors are simple and easy-to-use analytical devices and, in their world, electrochemiluminescence (ECL) is one of the most promising analytical techniques that needs an ever-increasing sensitivity for improving its clinical effectiveness.

Scope of this project was the investigation of the ECL generation mechanisms for enhancing the ECL intensity also through the identification of suitable nanostructures. The combination of nanotechnologies, microscopy and ECL has proved to be a very successful strategy to improve the analytical efficiency of ECL in one of its most promising bioanalytical approaches, the bead-based immunoassay. Nanosystems, such as $[Ru(bpy)_3]^{2+}$-dye-doped nanoparticles (DDSNPs) and Bodipy Carbon Nanodots, have been used to improve the sensitivity of ECL techniques thanks to their advantageous and tuneable properties, reaching a signal increase of 750% in DDSNPs-bead-based immunoassay system.

In this thesis, an investigation of size and distance effects on the ECL mechanisms was carried out through the innovative combination of ECL microscopy and electrochemical mapping of radicals. It allowed the discovery of an unexpected and highly efficient mechanistic path for ECL generation at small distances from the electrode surface. It was exploited and enhanced through the addition of a branched amine DPIBA to the usual coreactant TPrA solution for enhancing the ECL efficiency until a maximum of 128%.

Finally, a beads-based immunoassay and an immunosensor specific for cardiac Troponin I were built exploiting previous results and carbon nanotubes features. They created a conductive layer around beads enhancing the signal by 70% and activating an ECL mechanism unobserved before in such systems.

In conclusion, the combination of ECL microscopy and nanotechnology and the deep understanding of the mechanisms responsible for the ECL emission led to a great enhancement in the signal.

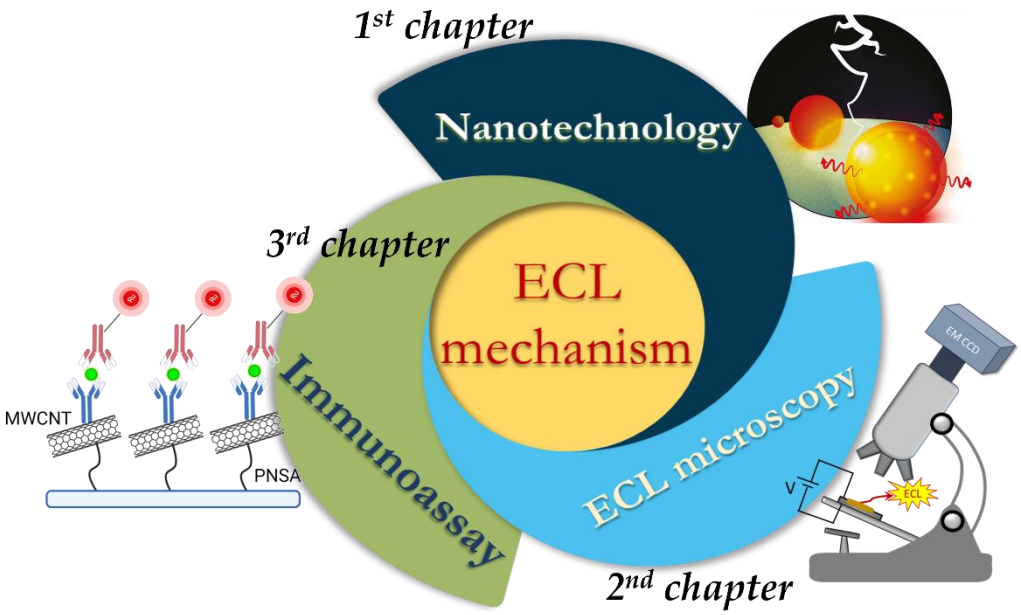
1st chapter
Nanotechnology
3rd chapter
ECL
mechanism
Immunoassay
ECL microscopy
2nd chapter
MWCNT
PNSA
EM CCD
V
ECL

INTRODUCTION

Effortless and accurate measurement of medical biomarkers levels is essential in prevention, diagnosis, treatment, and monitoring of diseases fighting against the diversity of dynamic range of different biomarkers in various body fluids and tissues among patients.[1] Bioanalysis includes all the biomarkers and biological entity measurements and immunoassays are a fundamental analytical technique that can detect a wide range of biomacromolecules, bacteria, viruses, and small molecules. In order to reach an even more efficient detection and monitoring of cancer and other diseases, multiplexing plays a key role for more reliable disease diagnostics thanks to the analysis of panels of biomarker proteins instead of single biomarkers.[2–6]

Immunoassays are based on the formation of an immuno-complex between an antigen and antibody, and includes system types as single analyte sensors, 96-well plate formats, arrays, microfluidic sensors, microfluidic arrays, etc. Antibodies, also known as immunoglobulins (Ig), are specialized Y-shaped soluble glycoproteins secreted by plasma cells with unique ability of binding and neutralizing specific target or antigens, representing a molecular defence of the immune systems against pathogens, such as viruses or bacteria. The affinity is due to the highly specific spatial complementarity between the paratope of the antibody and the epitope of the corresponding antigen and the antibodies are also present in different isotypes, differentiated by their heavy chain composition and their degree of polymerization.[7]

In immuno-complex construction different labels can be used for signal development defining the type of immunoassays. One of the main examples is the enzyme-linked immuno-sorbent assay (ELISA), where antibodies were immobilized on microplate, selectively capture analytes, and the colour changes due to enzymatic amplification reactions monitored. If chemical assay is combined with fluorescent, chemiluminescent, or radioactive labels, the analyte concentration can be quantitatively monitored and the immunoassay systems are called fluorescence immunoassay (FIA), radioimmunoassay (RIA), chemiluminescence immunoassay (CLIA). Other examples are electrophoretic immunoassay (EIA), colorimetric immunoassay, electrochemical immunoassay (ECIA), and electrochemiluminescence immunoassay (ECLIA), which is based on sandwich immunoassay and has high sensitivity, specificity, easy operation, and low background signal but the selective detection of trace biological analytes in real samples is highly challenging.[7,8] The molecular labels used onto the antibodies for quantification of biomarkers are gradually being replaced by functional composite nanomaterials, which have amazing optical and catalytic

properties, biological activities and/or enhanced chemical stability, allowing the improvement of the techniques.[8]

Biosensors are analytical devices that incorporate a biological sensing element and allow to perform complex bioanalytical measurements in simple and easy-to-use ways, combining the high sensitivity and specificity of biology with efficient physicochemical transducers (figure 1). Many are their application fields, ranging from medical diagnostics through food testing, drug discovery, process control and environmental monitoring, defence and security applications.[9] Biosensors are one of the most advanced analysis tools to convert biological response into electrical signals and are capable of on-spot transduction of molecular binding events into easily detectable signals.

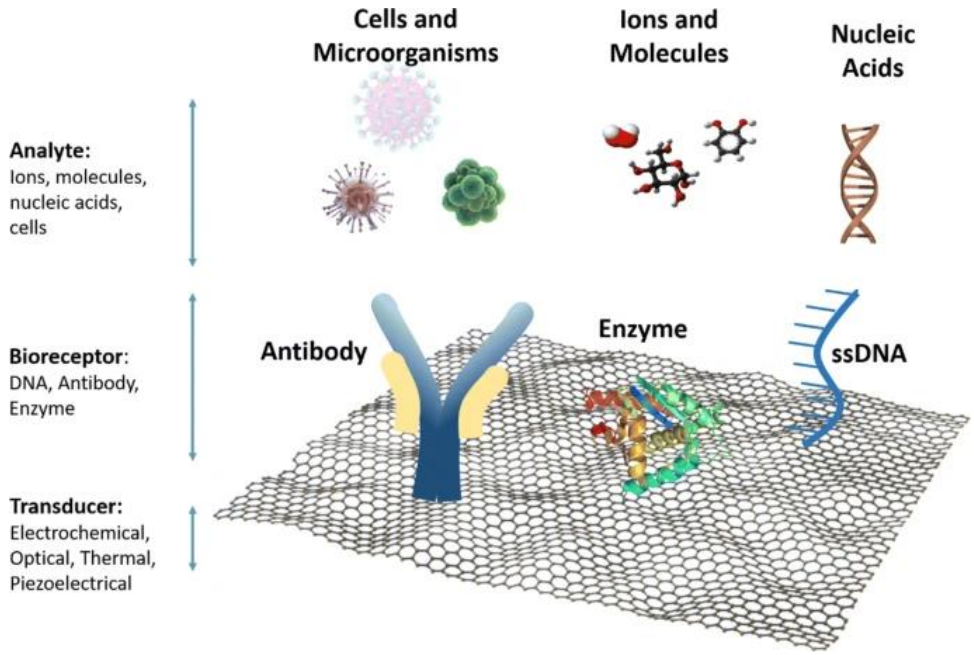

Figure 1. Examples of biosensors and components on a graphene platform. Reprinted with permission from [10].

They have many advantages compared with other traditional methods such as ELISA and PCR (polymerase chain reaction), such as low cost, short time, high sensitivity, good specificity, and good usability, making them extremely attractive for real-time detection and miniaturized applications such as wearable sensors.[11,12] Moreover, in recent years, the field of biosensors received a boost in their development thanks to progresses reached in nanotechnology. The nano-fabrication, the discovery, and optimization of nanomaterial, the progress in their assembly and on nanoscale surface chemistry improve the performance of nanoscale-based biosensors, achieving commercial success for a wide range of practical applications.[3,7,13]

Among all the technologies useful for the development of efficient biosensor to detect various target molecules, such as tumor biomarkers, microRNA, small molecule metabolites, ECL represents a good alternative thanks to the advantageous combination of electrochemistry and chemiluminescence, showing precise potential control, fast response time, no external light source, low cost, low noise, simple operation, high sensitivity, simple instrumentation, wide linear range, high flexibility controllability and so on.[11]

1. ELECTROCHEMILUMINESCENCE

Electrochemiluminescence (ECL) is luminescence generated by electrochemical reactions that involve a series of chemical reactions of reactive intermediates. They undergo high energy homogeneous electron-transfer reactions to generate excited states of the luminophore, which emits a photon relaxing to the ground state. ECL essentially implies the production of light by an excited luminophore species that is generated at the electrode surface, through the exergonic electron transfer (ET) reactions among the electrogenerated species.[14,15] ECL belongs to luminescence phenomenon like photoluminescence, chemiluminescence and electroluminescence but has many advantages compared with these techniques, such as the high signal-to-noise ratio, a broad dynamic range, rapid measurements with low volume and quite high spatio-temporal control and resolution, furtherly implemented by the combination with microscopy (see table 1). ECL microscopy will represent an important booster for the diffusion of this technique towards even more sensitive analytical applications and will be satisfying presented in the second chapter.[16–20] Photoluminescence or other optical methods rely on external light excitation; chemiluminescence is a result of chemical reactions between at least two reagents; and electroluminescence is a radiative recombination of holes and electrons in a material, directly converting electric energy to light. Compared with photoluminescence, one of the most studied and applied luminescence techniques in analytical fields, ECL does not need a light source, consequently increasing the spatio-temporal control and decreasing the background because light scattering and photobleaching phenomena aren't present. Although CL and ECL doesn't required an optical excitation, the application of an electrode potential in ECL allows a better control of reagents generation in the proximity of the electrode respect to CL, where reactions happen in the bulk and are simply determined by fluid flow.[21] Finally, EL is not related to electrochemical or chemical reactions, limiting too much its application. ECL combines the good control given by electrochemical stimulus and the high sensitivity, exponentially increasing its application as analytical method. [16,22,23]

The first observations of light emission during electrolysis were published in the 1920s,[24] but the success of ECL application began in 1970s with ECL derived from electrogenerated species of the $[Ru(bpy)_3]^{2+}$ complex followed by the discovery of ECL emission in aqueous media with tri-*n*-propylamine (TPrA), the most efficient coreactant used nowadays for (bio)analytical applications.[21,25–27]

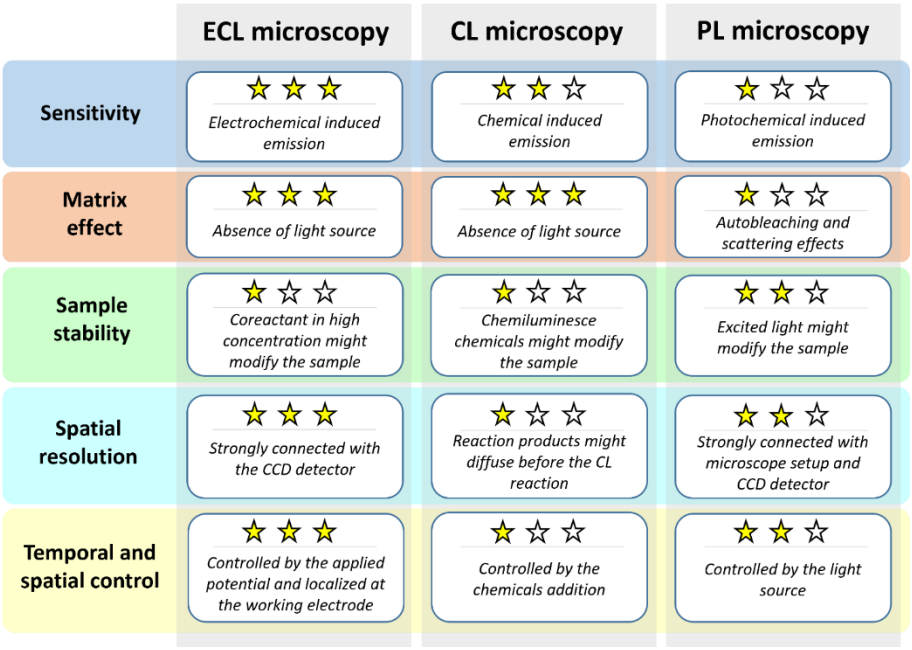

Table 1. Comparison table between abilities of electro-, chemi-, and photoluminescence microscopy (ECL, CL, and PL respectively) using a selection of features as references for analytical applications. Reprinted with permission from [16].

ECL processes have been established for several different molecules and nanosystems according to several mechanisms classified by nature of the final step producing the luminophore emissive states. The excitation reaction involves i) electron-transfer reactions of the luminophore, ii) bond-breaking reactions, or iii) hot electron-induced. In the path with the bond-breaking reactions or atom-transfer reaction, the luminophore can emit a photon just once and can't be regenerated. In the (iii) pathway hot electrons are electrons with energy higher than the thermal energy or the Fermi level of the solution. Although these other two pathways are possible, the most studied is (i) which involves an exergonic electron-transfer reaction of the luminophore for its emissive state production. Two sub-pathways can be evidenced and called annihilation and coreactant pathway.[24,28–30]

1.1 The Annihilation Pathway

In annihilation pathway, a homogeneous electron-transfer in solution takes place between two radicals $A^{\bullet-}$ and $B^{\bullet+}$, where A and B can be the same or different starting species, producing the

excited state of the luminophore. $A^{\bullet-}$ and $B^{\bullet+}$ are electrochemically generated at two separate electrodes close enough to one another or alternating pulsed potential at the same electrode.

$$A + e^- \rightarrow A^{\bullet-} \quad (1)$$

$$B - e^- \rightarrow B^{\bullet+} \quad (2)$$

$$A^{\bullet-} + B^{\bullet+} \rightarrow A^* + B \quad (3)$$

$$A^* \rightarrow A + h\nu \quad (4)$$

A successful annihilation ECL depends on chemical stability because reactions with solvents can decrease or quench the ECL signal, or lifetime of the species generated, which has to be long enough to react and produce excited states. The ECL annihilation is very simple and can be started by immersing electrode in a luminophore solution and applying alternated potentials, which can be chosen between a wide range of organic and inorganic compounds. The anodic and cathodic potential can be also applied by two electrodes or ultramicroelectrodes at nanometric distances in a tube (figure 2) or forming a dual electrode, generating anyway the ECL emission signal.[28,31,32] However, this pathway is mainly limited to the use of organic solvents because the potential window in water is not wide enough to generate the oxidized and reduced species.

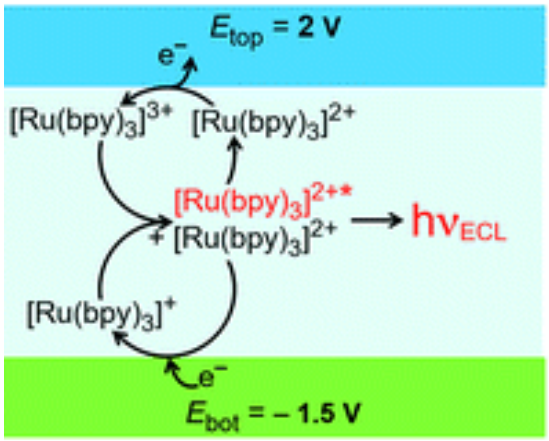

Figure 2. Schematic of the annihilation pathway leading to ECL emission exploiting $[Ru(bpy)_3]^{2+}$ as luminophore. Reprinted with permission from [32].

1.2 The Coreactant Pathway: heterogeneous and homogeneous mechanism

The coreactant pathway simply requires sacrificial reagents and the application of a single potential step or its sweeping in one direction. A coreactant is a chemical specie that undergoes electrochemical oxidation or reduction at the electrode surface producing very reactive intermediates that react with the luminophore to generate the excited state.[14,24] Typical coreactants are amines, such as TPrA and 2-(dibutylamino)ethanol (DBAE), oxalate ion, peroxydisulfate,

NADH, H_2O_2 or carbon nanomaterials and, they may generate ECL through the so-called 'oxidative-reduction' or 'reductive-oxidation' mechanisms.[33–37] Unlike the coreactant is a sacrificial molecule because irreversibly consumed, the luminophore can be regenerated and used for a new cycle and can be chosen between a large number of complexes and new innovative materials.[38,39]

The coreactant pathway is the most recently discovered and it can be applied in a wider range of fields than annihilation, such as the biological ones, unexplored by ECL technique until this important discovery. Thus the applications in aqueous environment became possible and paved the way to an increasing number of work about detection of proteins, DNA and micro RNA, cells, small molecules, metal ions, etc through creation of immunoassays and DNA bioassays for clinical diagnostics, biological and pharmaceutical analysis.[21,40–44]

The coreactant mechanism can be divided in homogeneous and heterogeneous mechanism and they mainly use the couple $[Ru(bpy)_3]^{2+}$ / TPrA. The "homogenous ECL" is the mainly applied and involves the direct oxidation of both the luminophores and the coreactant at the electrode surface followed by the deprotonation reaction of the oxidised coreactant that generates TPrA•, which reacts with $[Ru(bpy)_3]^{3+}$, forming the excited state $[Ru(bpy)_3]^{2+*}$. Then, it returns to the ground state after the release of a photon, thus emitting light (figure 3A). The equations below (1-6) represent the ECL homogeneous mechanism.[24]

$$TPrAH^+ \leftrightarrows TPrA + H^+ \quad (1)$$

$$TPrA - e^- \leftrightarrows TPrA^{\bullet+} \quad (2)$$

$$TPrA^{\bullet+} \leftrightarrows TPrA^{\bullet} + H^+ \quad (3)$$

$$\left[Ru(bpy)_3\right]^{2+} - e^- \leftrightarrows \left[Ru(bpy)_3\right]^{3+} \quad (4)$$

$$TPrA^{\bullet} + \left[Ru(bpy)_3\right]^{3+} \leftrightarrows P1 + \left[Ru(bpy)_3\right]^{2+*} \quad (5)$$

$$\left[Ru(bpy)_3\right]^{2+*} \rightarrow \left[Ru(bpy)_3\right]^{2+} + h\nu \quad (6)$$

However, in most of the analytical methods, the luminophore is constrained close to the electrode because it is attached to a sensing element (i.e. antibody, bead, DNA probe, ecc..) and thus not free to diffuse to the electrode.[45] In this case, ECL emission is therefore triggered exclusively by the radicals obtained by the anodic oxidation of TPrA, i.e. $TPrA^{\bullet+}$ and TPrA• that would react with the immobilised luminophore generating the excited state (figure 3B).[24,46] The oxidation and deprotonation steps of coreactant are the same of homogeneous mechanism (1-3), while the

reduction and oxidation of luminophore were performed directly by the products of coreactant oxidation (7-8) and not at the electrode surface.

$$TPrA^{\bullet} + [Ru(bpy)_3]^{2+} \leftrightarrows P1 + [Ru(bpy)_3]^{+} \quad (7)$$

$$TPrA^{\bullet+} + [Ru(bpy)_3]^{+} \leftrightarrows TPrA + [Ru(bpy)_3]^{2+*} \quad (8)$$

$$[Ru(bpy)_3]^{2+*} \rightarrow [Ru(bpy)_3]^{2+} + h\nu \quad (9)$$

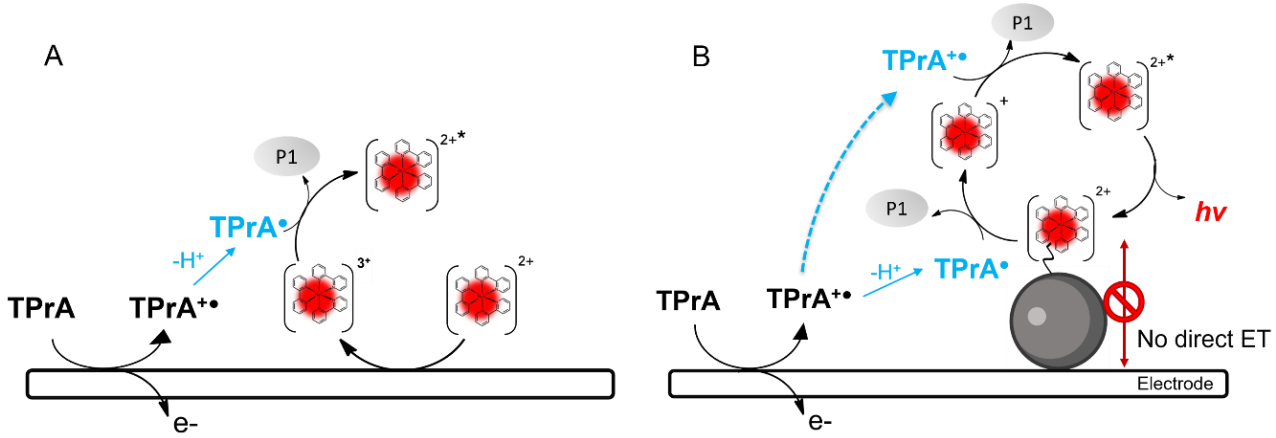

Figure 3. Schematic representation of electrochemiluminescent mechanism A) homogeneous where both coreactant and luminophore can be oxidized at the electrode surface and B) heterogeneous where only coreactant is oxidized at the electrode surface. Reprinted with permission from [47]. For further right and permission please contact American Chemical Society.

According to the heterogenous ECL mechanistic pathway, light is generated by the participation of both $TPrA^{\bullet+}$ and $TPrA^{\bullet}$, continuously flowing where luminophores are located and a spatial distribution of ECL efficiency may be expected. It will be higher, resulting also in a higher ECL intensity signal, where the radicals concentrations will be simultaneously the highest.[48–51]

1.3 ECL advantages and future improvements

In the last 20 years ECL has proved to be a versatile and powerful analytical technique in many different fields, from fundamental research to commercial clinical and biological applications.[46,52] In fact, ECL has remarkable advantages compared to other transduction methods and this partially explain its continuous development between 2000 and 2021, correlated with an even increased number of related articles. Between 2000 and 2012, the increase of ECL article published is slow, but the development of the materials field and the application potential of electrochemiluminescence technology in biological detection and analysis are continuous. Since 2012, the number of publications has shown an exponential growth trend and the annual publication volume has continued to reach more than 300 articles up to 803 articles by 2020. [11] In these years the development

of nanotechnology and materials disciplines together with new sensing ECL mechanisms adoptable in aqueous environments has accelerated the development of electrochemiluminescence field and ECL signal amplification strategies to representative sensing applications (figure 4). [53]

In the last 20 years, the continuous innovation and development of ECL technology gradually change from laboratory analysis to a technology addressed to commercialization and clinical application. In the industrial field, Roche Diagnostics[54] commercialized a clinical analyser based on ECL, Elecsys®, and optimized for more than 150 immunoassays. Also Meso Scale Discovery[55] commercialized analyser for multiplexing analysis and more recently Dropsense started the implementation of portable devices, combining ECL and screen-printed electrodes.[56]

Although electrochemiluminescence technology has achieved good and continuous innovation in the development of detection systems, in the design and synthesis of ECL properties of materials, and collaboration with other devices, there are challenges still present that have to be undertaken in the future. [41,57–59] The suggestions provided by analysing the current problems outlined four main points and fields that can be further improved:

1. ECL sensors performance, new ECL detection systems, sensing mechanisms, and simple, stable, and efficient ECL technology for quantitative or qualitative detection of important biomarkers in human samples, with the final goal of enhancing clinical application, such as diagnosis, monitoring and prognosing of the humans' physiological state or disease.
2. Low-cost and mass-produced materials with excellent ECL performance.
3. New combination of ECL with sensors and devices, improving also the just discovered collaborations with immunosensors, aptamer sensors and other sensors.
4. High-speed, high-throughput ECL sensors to reduce the workload and time period of technicians and improve detection efficiency and rapidity, providing timely diagnosis for patients.[11]

Many of these points are just under investigations and they are being faced up with many different strategies, from the combination of ECL with microscopy, bipolar electrode, enhanced electric fields or computational techniques, to the investigation of ECL generation mechanism.[16,20,24,60–62] Even more applications of ECL are possible thanks to its advantages and continuous improvements, finding in the biomarkers, viruses, toxins, cells and small molecules detection a huge applicability [43,63] and enhancing also the creation of sensors that could simultaneously detect different biomolecules.[4,5]

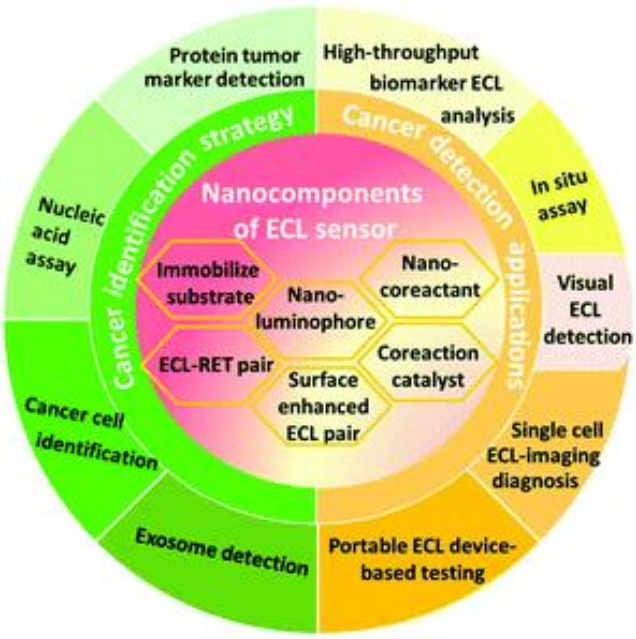

Figure 4. A summary of the ECL nanosensors with cancer identification strategies and diagnosis applications. Reprinted with the permission from [13].

1.4 The scope of the thesis

As outlined in the introduction, the ultra-sensitive quantification of biomarkers in complex matrices like blood and other biofluids is of paramount important in clinical monitoring and early disease diagnosis and ECL is even more promising in these fields.[57] In order to addressed some of the challenges for ECL sensors development explained in paragraph 1.3, my PhD project will be focalized on different ways to understand and improve the technique performances toward the development of a more sensitive biosensor.

In the first chapter, the combination between ECL and nanotechnology will represent the starting point for our strategic ECL enhancement, taking inspiration from the great contribution of nanoworld to this technique. New nano-luminophores will be investigated and increase the ECL emission acting on the synthetic procedure, exploiting the possibility of concentrate a huge number of luminophores, and investigating the emission mechanism. Specifically, nanocarbon dots modified with the organic compound BODIPY and $[Ru(bpy)_3]^{2+}$-doped silica nanoparticles will be synthesized through new efficient and promising synthesis that allow to control dyes features.[64,65]

In the second chapter, $[Ru(bpy)_3]^{2+}$-doped silica nanoparticles will be successfully applied in an ECL beads-based immunoassay system and its efficiency proved also through ECL microscopy (ECLM).[65] This beads-based immunoassay commercial system will be the protagonist of a deep investigation on the ECL generation mechanisms and on TPrA oxidation that bring to the discovery of a new ECL

mechanism active at small distances from the electrode. Exploiting this mechanism, a new family of coreactants/additives, among them branched amine DPIBA, has been proposed for ECL signal enhancement in commercial immunoassay system.[46]

Finally, in the third chapter, ECL, microscopy and nanomaterials will be combined for a further improvement and understanding of ECL mechanisms in a beads-based system. $[Ru(bpy)_3]^{2+}$-functionalized double walled carbon nanotubes will be the perfect tool for creating a conductive layer around magnetic beads attracted to the electrode. This sort of Faraday-cage created by CNTs will enhance the ECL signal through the oxidation of coreactant near the luminophore onto the CNTs, enhancing the ECL emitting layer, usually limited near the electrode for the short lifetime of the $TPrA^{\bullet+}$. Moreover, a new concomitant mechanism will be discovered and will contribute to the enhancement of the emission, in fact also the luminophore will be directly oxidized by the CNTs.[66] The successful CNTs will represent the fundamental substrate for the development of an ECL biosensor specific for cardiac Troponin I (cTnI), biomarker of Acute Myocardial Infarction (AMI).[67] It will consist in a sandwich immunoassay fixed onto a conductive transparent electrode (ITO), which will be substituted in the future, after its optimization, by micromagnetic beads and detect through ECLM.

In this work, we will demonstrate how the combination between ECL, microscopy, and nanotechnologies results very successful for sensitivity, temporal and spatial control improvements as just seen in previous works present in literature. Moreover, it paves the ways towards super-resolution technique and single molecule visualization, discovering mechanisms never proved before.

REFERENCES

1. Xiao, Y. *et al.* Mesoporous silica-mediated controllable electrochemiluminescence quenching for immunosensor with simplicity, sensitivity and tunable detection range. *Talanta* **231**, 122399 (2021).
2. Jones, A., Dhanapala, L., Kankanamage, R. N. T., Kumar, C. V. & Rusling, J. F. Multiplexed Immunosensors and Immunoarrays. *Anal. Chem.* **92**, 345–362 (2020).
3. Zheng, G., Patolsky, F., Cui, Y., Wang, W. U. & Lieber, C. M. Multiplexed electrical detection of cancer markers with nanowire sensor arrays. *Nat. Biotechnol.* **23**, 1294–1301 (2005).
4. Gao, W., Muzyka, K., Ma, X., Lou, B. & Xu, G. A single-electrode electrochemical system for multiplex electrochemiluminescence analysis based on a resistance induced potential difference. *Chem. Sci.* **9**, 3911–3916 (2018).
5. Lv, W. *et al.* Recent advances in electrochemiluminescence-based simultaneous detection of multiple targets. *TrAC Trends Anal. Chem.* **123**, 115767 (2020).
6. Cinquanta, L., Infantino, M. & Bizzaro, N. Detecting Autoantibodies by Multiparametric Assays: Impact on Prevention, Diagnosis, Monitoring, and Personalized Therapy in Autoimmune Diseases. *J. Appl. Lab. Med.* **7**, 137–150 (2022).
7. Zhang, S., Geryak, R., Geldmeier, J., Kim, S. & Tsukruk, V. V. Synthesis, Assembly, and Applications of Hybrid Nanostructures for Biosensing. *Chem. Rev.* **117**, 12942–13038 (2017).
8. Kannan, P., Chen, J., Su, F., Guo, Z. & Huang, Y. Faraday-Cage-Type Electrochemiluminescence Immunoassay: A Rise of Advanced Biosensing Strategy. *Anal. Chem.* **91**, 14792–14802 (2019).
9. Turner, A. P. F. Biosensors: sense and sensibility. *Chem. Soc. Rev.* **42**, 3184 (2013).
10. Peña-Bahamonde, J., Nguyen, H. N., Fanourakis, S. K. & Rodrigues, D. F. Recent advances in graphene-based biosensor technology with applications in life sciences. *J. Nanobiotechnology* **16**, 75 (2018).
11. Liu, X. *et al.* Frontier and hot topics in electrochemiluminescence sensing technology based on CiteSpace bibliometric analysis. *Biosens. Bioelectron.* **201**, 113932 (2022).
12. Zeng, X., Peng, R., Fan, Z. & Lin, Y. Self-powered and wearable biosensors for healthcare. *Mater. Today Energy* **23**, 100900 (2022).
13. Fu, Y. & Ma, Q. Recent developments in electrochemiluminescence nanosensors for cancer diagnosis applications. *Nanoscale* **12**, 13879–13898 (2020).
14. Bard, A. J. *Electrogenerated Chemiluminescence*. (CRC Press, 2004).
15. Park, S. M. & Bard, A. J. Electrogenerated Chemiluminescence. XXII. On the Generation of Exciplexes in the Radical Ion Reaction. *J. Am. Chem. Soc.* **97**, 2978–2985 (1975).
16. Zanut, A., Fiorani, A., Rebeccani, S., Kesarkar, S. & Valenti, G. Electrochemiluminescence as emerging microscopy techniques. *Anal. Bioanal. Chem.* **411**, 4375–4382 (2019).
17. Ding, H., Guo, W. & Su, B. Electrochemiluminescence Single-Cell Analysis: Intensity- and Imaging-Based Methods. *Chempluschem* **85**, 725–733 (2020).
18. Ding, H. *et al.* Spatially Selective Imaging of Cell–Matrix and Cell–Cell Junctions by Electrochemiluminescence. *Angew. Chemie Int. Ed.* **60**, 11769–11773 (2021).
19. Dong, J. *et al.* Direct imaging of single-molecule electrochemical reactions in solution. *Nature* **596**, 244–249 (2021).
20. Chen, M.-M., Xu, C.-H., Zhao, W., Chen, H.-Y. & Xu, J.-J. Super-Resolution Electrogenerated Chemiluminescence Microscopy for Single-Nanocatalyst Imaging. *J. Am. Chem. Soc.* **143**, 18511–18518 (2021).
21. Miao, W. Electrogenerated Chemiluminescence and Its Biorelated Applications. *Chem. Rev.* **108**, 2506–2553 (2008).

22. Bouffier, L. & Sojic, N. Chapter 1. Introduction and Overview of Electrogenerated Chemiluminescence. in *RSC Detection Science* 1–28 (2020). doi:10.1039/9781788015776-00001
23. Richter, M. M. Electrochemiluminescence (ECL). *Chem. Rev.* **104**, 3003–3036 (2004).
24. Miao, W., Choi, J. P. & Bard, A. J. Electrogenerated chemiluminescence 69: The Tris(2,2′-bipyridine)ruthenium(II), (Ru(bpy)32+)/tri-n-propylamine (TPrA) system revisited - A new route involving TPrA.+ cation radicals. *J. Am. Chem. Soc.* **124**, 14478–14485 (2002).
25. Tokel, N. E. & Bard, A. J. Electrogenerated chemiluminescence. IX. Electrochemistry and emission from systems containing tris(2,2′-bipyridine)ruthenium(II) dichloride. *J. Am. Chem. Soc.* **94**, 2862–2863 (1972).
26. Leland, J. K. & Powell, M. J. Electrogenerated Chemiluminescence: An Oxidative-Reduction Type ECL Reaction Sequence Using Tripropyl Amine. *J. Electrochem. Soc.* **137**, 3127–3131 (1990).
27. Zu, Y. & Bard, A. J. Electrogenerated Chemiluminescence. 66. The Role of Direct Coreactant Oxidation in the Ruthenium Tris(2,2′)bipyridyl/Tripropylamine System and the Effect of Halide Ions on the Emission Intensity. *Anal. Chem.* **72**, 3223–3232 (2000).
28. Wang, M. *et al.* Electrochemiluminescence Based on a Dual Carbon Ultramicroelectrode with Confined Steady-State Annihilation. *Anal. Chem.* **93**, 4528–4535 (2021).
29. Cui, C., Jin, R., Jiang, D., Zhang, J. & Zhu, J. J. Electrogenerated Chemiluminescence in Submicrometer Wells for Very High-Density Biosensing. *Anal. Chem.* **92**, 578–582 (2020).
30. Hesari, M. & Ding, Z. Review—Electrogenerated Chemiluminescence: Light Years Ahead. *J. Electrochem. Soc.* **163**, H3116–H3131 (2016).
31. Voci, S., Al-Kutubi, H., Rassaei, L., Mathwig, K. & Sojic, N. Electrochemiluminescence reaction pathways in nanofluidic devices. *Anal. Bioanal. Chem.* **412**, 4067–4075 (2020).
32. Al-Kutubi, H., Voci, S., Rassaei, L., Sojic, N. & Mathwig, K. Enhanced annihilation electrochemiluminescence by nanofluidic confinement. *Chem. Sci.* **9**, 8946–8950 (2018).
33. Irkham *et al.* Electrogenerated Chemiluminescence by in Situ Production of Coreactant Hydrogen Peroxide in Carbonate Aqueous Solution at a Boron-Doped Diamond Electrode. *J. Am. Chem. Soc.* **142**, 1518–1525 (2020).
34. Kerr, E., Doeven, E. H., Wilson, D. J. D., Hogan, C. F. & Francis, P. S. Considering the chemical energy requirements of the tri-n-propylamine co-reactant pathways for the judicious design of new electrogenerated chemiluminescence detection systems. *Analyst* **141**, 62–69 (2016).
35. Carrara, S., Arcudi, F., Prato, M. & De Cola, L. Amine-Rich Nitrogen-Doped Carbon Nanodots as a Platform for Self-Enhancing Electrochemiluminescence. *Angew. Chemie Int. Ed.* **56**, 4757–4761 (2017).
36. Cao, Z. & Su, B. Light enhanced electrochemistry and electrochemiluminescence of luminol at glassy carbon electrodes. *Electrochem. commun.* **98**, 47–52 (2019).
37. Kong, X., Wang, C., Pu, L., Gai, P. & Li, F. Self-Photocatalysis Boosted Electrochemiluminescence Signal Amplification via In Situ Generation of the Coreactant. *Anal. Chem.* **93**, 12441–12446 (2021).
38. Chen, L. *et al.* A conceptual framework for the development of iridium(<scp>iii</scp>) complex-based electrogenerated chemiluminescence labels. *Chem. Sci.* **10**, 8654–8667 (2019).
39. Cao, Z., Shu, Y., Qin, H., Su, B. & Peng, X. Quantum Dots with Highly Efficient, Stable, and Multicolor Electrochemiluminescence. *ACS Cent. Sci.* **6**, 1129–1137 (2020).
40. Valenti, G. *et al.* Single Cell Electrochemiluminescence Imaging: From the Proof-of-Concept to Disposable Device-Based Analysis. *J. Am. Chem. Soc.* **139**, 16830–16837 (2017).
41. Qi, H. & Zhang, C. Electrogenerated Chemiluminescence Biosensing. *Anal. Chem.* **92**, 524–

534 (2020).
42. Ma, C. *et al.* Hydrogen Evolution Reaction Monitored by Electrochemiluminescence Blinking at Single-Nanoparticle Level. *Nano Lett.* **20**, 5008–5016 (2020).
43. Zamolo, V. A. *et al.* Highly sensitive electrochemiluminescent nanobiosensor for the detection of palytoxin. *ACS Nano* **6**, 7989–7997 (2012).
44. Juzgado, A. *et al.* Highly sensitive electrochemiluminescence detection of a prostate cancer biomarker. *J. Mater. Chem. B* **5**, 6681–6687 (2017).
45. Zanut, A. *et al.* DNA-Based Nanoswitches: Insights into Electrochemiluminescence Signal Enhancement. *Anal. Chem.* **93**, 10397–10402 (2021).
46. Zanut, A. *et al.* Insights into the mechanism of coreactant electrochemiluminescence facilitating enhanced bioanalytical performance. *Nat. Commun.* **11**, 2668 (2020).
47. Rebeccani, S., Zanut, A., Santo, C. I., Valenti, G. & Paolucci, F. A Guide Inside Electrochemiluminescent Microscopy Mechanisms for Analytical Performance Improvement. *Anal. Chem.* **94**, 336–348 (2022). https://pubs.acs.org/doi/full/10.1021/acs.analchem.1c05065
48. Sentic, M. *et al.* Mapping electrogenerated chemiluminescence reactivity in space: mechanistic insight into model systems used in immunoassays. *Chem. Sci.* **5**, 2568–2572 (2014).
49. Chovin, A., Garrigue, P., Vinatier, P. & Sojic, N. Development of an Ordered Array of Optoelectrochemical Individually Readable Sensors with Submicrometer Dimensions: Application to Remote Electrochemiluminescence Imaging. *Anal. Chem.* **76**, 357–364 (2004).
50. Amatore, C. *et al.* Mapping Electrochemiluminescence as Generated at Double-Band Microelectrodes by Confocal Microscopy under Steady State. *ChemPhysChem* **7**, 1322–1327 (2006).
51. Szunerits, S., Tam, J. M., Thouin, L., Amatore, C. & Walt, D. R. Spatially Resolved Electrochemiluminescence on an Array of Electrode Tips. *Anal. Chem.* **75**, 4382–4388 (2003).
52. Sojic, N. *Analytical Electrogenerated Chemiluminescence*. (Royal Society of Chemistry, 2020). doi:10.1039/9781788015776
53. Liu, Y., Guo, W. & Su, B. Recent advances in electrochemiluminescence imaging analysis based on nanomaterials and micro-/nanostructures. *Chinese Chem. Lett.* **30**, 1593–1599 (2019).
54. Roche Diagnostic corporation. (2018). Available at: www.roche.com.
55. The Meso Scale Discovery. (2018). Available at: www.mesoscale.com/en/technical_resources/our_technology/multi-array.
56. Metrohm electrochemistry. Available at: https://www.metrohm.com/en/products/electrochemistry/portable-potentiostats/STATECL.
57. Ma, C., Cao, Y., Gou, X. & Zhu, J.-J. Recent Progress in Electrochemiluminescence Sensing and Imaging. *Anal. Chem.* **92**, 431–454 (2020).
58. Ma, X. *et al.* Rational Design of Electrochemiluminescent Devices. *Acc. Chem. Res.* **54**, 2936–2945 (2021).
59. Wang, Y. & Su, B. Deciphering the Mechanisms of Electrochemiluminescence by Spatially Resolved Measurements. *Anal. Sens.* **1**, 148–155 (2021).
60. Bouffier, L., Zigah, D., Sojic, N. & Kuhn, A. Bipolar (Bio)electroanalysis. *Annu. Rev. Anal. Chem.* **14**, 65–86 (2021).
61. Cui, C., Jin, R., Jiang, D., Zhang, J. & Zhu, J. Visualization of an Accelerated Electrochemical Reaction under an Enhanced Electric Field. *Research* **2021**, 1–9 (2021).
62. Imai, K. *et al.* Numerical Simulation of Doped Silica Nanoparticle Electrochemiluminescence. *J. Phys. Chem. C* **119**, 26111–26118 (2015).

63. Ma, Y., Colin, C., Descamps, J., Arbault, S. & Sojic, N. Shadow Electrochemiluminescence Microscopy of Single Mitochondria. *Angew. Chemie Int. Ed.* **60**, 18742–18749 (2021).
64. Arcudi, F. *et al.* Lighting up the Electrochemiluminescence of Carbon Dots through Pre- and Post-Synthetic Design. *Adv. Sci.* **8**, 2100125 (2021).
65. Zanut, A. *et al.* Dye-Doped Silica Nanoparticles for Enhanced ECL-Based Immunoassay Analytical Performance. *Angew. Chemie Int. Ed.* **59**, 21858–21863 (2020).
66. Rebeccani, S. *et al.* Electrochemiluminescent immunoassay enhancement driven by carbon nanotubes. *Chem. Commun.* **57**, 9672–9675 (2021).
67. Duque-Ossa, L. C., García-Ferrera, B. & Reyes-Retana, J. A. Troponin I as a Biomarker for Early Detection of Acute Myocardial Infarction. *Curr. Probl. Cardiol.* 101067 (2021). doi:10.1016/j.cpcardiol.2021.101067

Chapter I

ECL AND INNOVATIVE NANOSTRUCTURED LUMINOPHORES

In collaboration with

Prof. Maurizio Prato research group at the University of Trieste

Prof. Luca Prodi research group at the University of Bologna

1. INTRODUCTION

Nanotechnology is being applied in electronics, catalysis, optics, biology, and medicine. The mechanical, optoelectronic and physicochemical properties of nanomaterials become very attractive to scientists and can be exploited to improve current technologies or start new applications in fields like biosensing and clinical monitoring.[1]

Currently, there are many different detection techniques based on various analytical approaches useful for rapid, accurate, and selective detection. However, cost, mobility, reproducibility, and throughput often can represent a limitation if devices would be developed with higher selectivity and miniaturization for real-time and wearable applications. The development of nanoengineered biosensor components and materials is helpful in reaching higher sensitive and selective behaviour even of single molecules. Nanosized materials can solve some sensoristic issues because, firstly, nanoscale components are comparable in dimension to biological molecules and allow the design of highly compact sensor elements, direct molecule-to-molecule interactions and signal transduction. Then, nanomaterials can be synthesized to exhibit distinctive features, which are not present in traditional bulk materials, such as miniaturized size, insulating nature, elasticity, electrical conductivity, mechanical strength and high reactivity. In the last years, a lot of improvements were made in synthesis, assembly and integration of nanobiosensors and medical practices, and nanomaterials find applications in many fields like biomedical, environmental, agricultural and energy.[2] The main obstacle to the development of nanobiosensing is the incomplete and complex understanding of interfacial nanochemistry.[3]

They can be classified according to their geometry, morphology, agglomeration, uniformity and composition and they can be synthesised through various types of procedures. For example, they can be categorized as zero-dimensional (0D), one-dimensional (1D) and two-dimensional (2D) nanomaterials, depending on their confined size (figure 1.1). The 0D nanomaterials refer to the materials with all three dimensions in the nanoscale range (1–100 nm), such as quantum dots (QDs) and nanoparticles.[4,5] The 1D nanomaterials have two dimensions in the nanoscale range and include nanotubes, nanowires, and nanorods[6] while the main 2D nanomaterials are graphene and transition metal dichalcogenides (TMDs).[7]

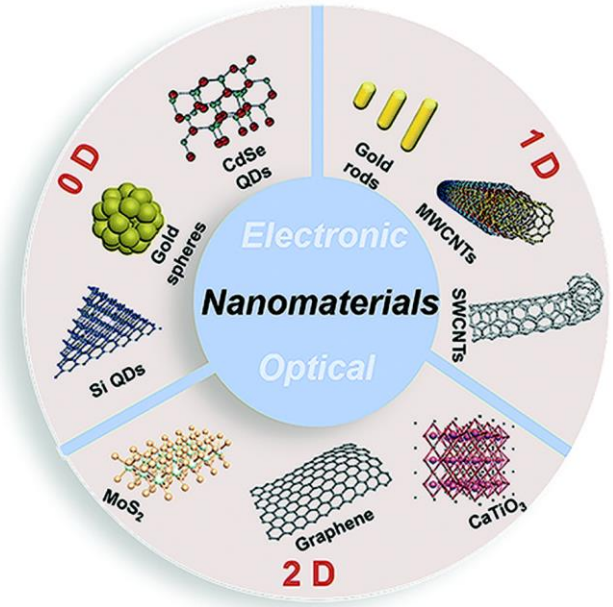

Figure 1.1. Examples of nanomaterials categorized according to their size. Reprinted with permission from Ref [7].

0D QDs are typically semiconductor nanoparticles with controllable photoluminescent properties due to the quantum confinement of their energy levels. They are highly fluorescent nanoparticles with a diameter between 2−10 nm and are typically core/shell materials composed of i) an inorganic semiconductor core, ii) a second semiconductor shell, and iii) a passivating layer of organic ligands in order to improve PL stability, control the size and prevent aggregation (figure 1.2a). They are characterized by a quantum confinement effect: when the QDs are excited the electron moves from the valence to the conduction band creating a hole in the valence band (electron-hole pair). The QDs' size is below the exciton Bohr radius and consequently the band structures change to discrete energy and the bandgaps of their electron−hole pairs becomes larger decreasing the size. This behaviour underlines the relationship between QD's bandgap, optical and electrical properties and its geometrical size. Changing the nanoscale size, shape and the material composition the emission can be modulated within the entire visible and near-IR spectrum (figure 1.2b).[3] For these reasons QDs display several advantages useful for multiplex sensing: symmetrical and narrow emission peaks and different emission bands in different QDs that can then be excited with a single UV wavelength, simultaneously imaging differently tagged components for multicolour detection. Although the great improvements in synthesis, PL emission modulation and stability to photobleaching, QDs have high toxicity due to their heavy metal components, which severely restrict their use in

bioanalysis and in vivo applications. However, researchers try to develop metal-free QDs or strategy to avoid the heavy metal release.[8–11]

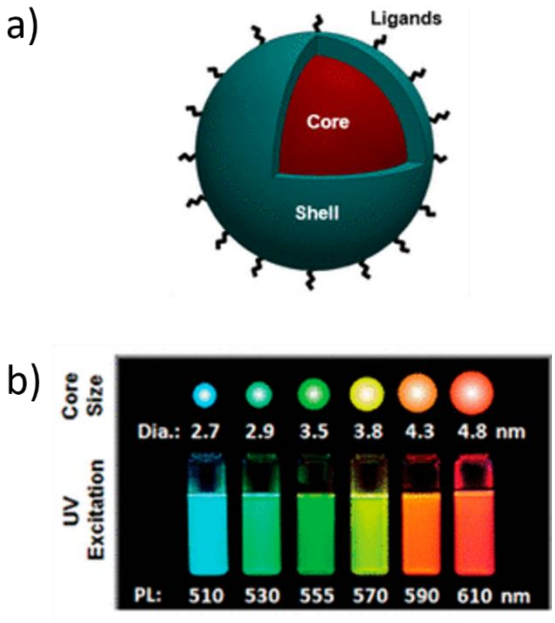

Figure 1.2. a) Schematic of a core/shell QD structure. Reprinted with permission from Ref [3].Copyright 2017 American Chemical Society. b) The emission wavelength correlated with the size of CdSe/ZnS QDs.[12] Reprinted with permission from Ref [12].Copyright 2011 American Chemical Society.

Another important type of nanomaterial is represented by carbon nanostructures that are recently widely used in different field and previously classified in 0D, 1D and 2D samples. Graphene (2D) has confined sp^2 hybridized orbitals that facilitate high electric conductivity and zero-gap linear electron momentum dispersion; carbon nanotubes (1D) present semi-1D confined sp^2 orbitals that allow their band gap tuning by diameter and chirality; graphene-based or carbon-based QDs or carbon dots (CDs, 0D) are attracting carbonaceous candidates that, despite the lower quantum yield, are nontoxic, stable, and low-cost respect to traditional QDs; finally there are also 3D carbon materials, nanodiamonds with carbon sp^3 orbitals and nitrogen defects that have mechanically, chemically robust, and nontoxic photoluminescence centers suitable for in vivo bioimaging.[3]

CDs are quasi-spherical nanoparticles with small sizes (<10 nm) composed of carbon, hydrogen, and oxygen atoms.[13,14] They emerged as photoluminescent and electrochemiluminescent (ECL) nanoparticles due to favorable photophysical and electrochemical properties not univocal for this type of material.[15–19] Compared to metal-based quantum dots, they are water-soluble, biocompatible, environmentally friendly and they have low toxicity and simple synthesis finding various

applications for biosensors creation, in gene transmission and as drug carriers and bioimaging probes.[11] They can be functionalized with various agents thanks to the presence of carboxylic acid moieties and of defects that give them flexibility.[20] An important role is played by synthetic methods that can tune material features, fluorescence and ECL performances. The synthetic procedures (figure 1.3) are classically divided in "top-down" approaches that include physical and chemical peel process where graphite materials are the carbon sources (graphene nanodots) and "bottom-up" methods which are performed with organic molecules. The "top-down" approach includes oxidation-passivation, electrochemical and acidization-hydrothermal methods as synthetic procedures, while "bottom-up" approach includes hydrothermal, ultrasonic, microwave and neutralization heat methods. The latter approach is more advantageous because it allows the modulation of the material features without the use of strong oxidants and acids.[11]

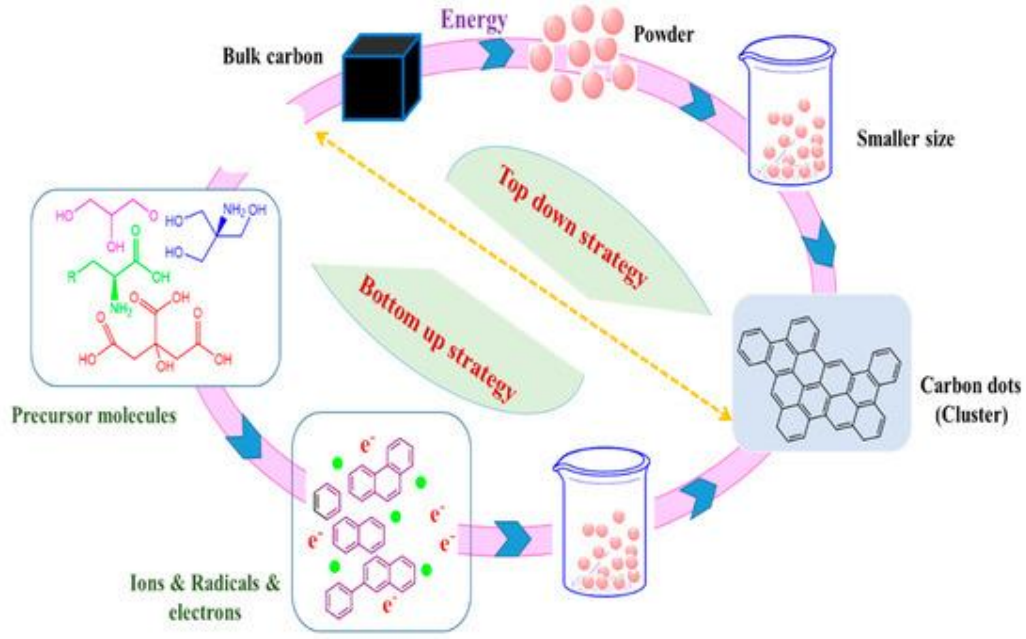

Figure 1.3. Generation of carbon dots by well-known top-down and bottom-up approaches.[21] Reprinted with permission from Ref [21].

Finally, nanoparticles of various organic, inorganic or metal materials can be useful because they are easily synthesized and functionalized. For example, silica nanoparticles doped with different dyes can represent a great improvement thanks to the presence of silica that i) allow to work in water solution because it is a hydrophilic material prone to bioconjugation; ii) increase the photostability; and iii) protect from the surrounding environment.[22]

1.1 ECL and nanomaterials

The features of some of the most promising and tuneable nanomaterials were showed as starting point for understanding their application in very different fields as luminescent probes, electrode materials, tumor therapy elements and so on. Recently, the quantification of diagnostic markers, or biomarkers, is one of the most stimulating and intriguing fields of research due to its enormous impact in the early diagnosis from basic research to clinical applications. However, the detection of very low amounts of these molecules with simple and accurate methods is still an open issue. In this context, ECL appears to be a leading transduction technique and the most used strategy to generate ECL in an aqueous environment is based on the so-called oxidative-reduction coreactant mechanism where tri-n-propylamine (TPrA) is used as sacrificial co-reactant and tris(2,2'-bipyridine)ruthenium-(II) ($[Ru(bpy)_3]^{2+}$) as luminophore,[23–25] allowing a tremendous number of applications.[26,27]

ECL is a promising analytical technique due to the several advantageous features, widely known and presented in the introduction. In the quest for ever-increasing sensitivity, several strategies can be adopted. For example, ECL is coupled to nanotechnologies when nanomaterials are used as alternative luminophores, substituting the inorganic or organic compounds, typically Ru(II) or Ir(III) complexes,[28–30] or embedding them. The use of nanoparticles allows to improve the ECL technique performance by acting at different levels in the signal generation:

a) increases the ECL efficiency of emission
b) increases the number of labels associated to a single biorecognition
c) optimizes the electron transfer kinetics
d) optimizes the electrode surface stability

Nanomaterials can also be used as alternative coreactants or as electrode materials, that are fundamental in ECL emission, and their modulation represents a resource for increasing the ECL signal intensity.[31,32] They represent a very important application of ECL-nanomaterials combination but they will not be the protagonist of this project.[33,34]

Dye-doped nanoparticles, quantum dots, polymer dots and carbon-based nanomaterials shown above are the most promising nanomaterials for ECL signal increase and their rational design and post-modification strategies underline the important relationship between nanostructure and ECL activity.

Nanocrystals, nanoclusters, and QDs, as anticipated, show excellent ECL properties and semiconductor features.[22,35] They have confinement effect of electron/hole structure and their

different photophysical performances can be modulated through different rational design because they have highly tunable energy levels, very sensitive to changes in surface and defect or vacancy densities.[10] They are promising candidate as ECL luminophore thanks to the good photo- and electrochemical stability, functional flexibility and excellent optical properties. ECL emission is typically red-shifted with respect to PL due to the different excitation mechanism and spatial location, ECL emission being associated to hole-electron recombination on QDs surface while PL is ascribed to excitation in the QDs core. The core/shell, core/shell/shell systems or metal doped QDs are the most promising as ECL luminophores and the ECL signal arising from surface states occurs at longer wavelength and lower potential and can be tuned by doping. These features and the solubility in aqueous solution, reached through different functionalization, are the reasons for the highly promising application of QDs in sensitive and low-potential ECL bio-assay.[22,35] The unique optical properties of QDs make them perfect for simultaneously monitoring multiple analytes, in vivo imaging, and clinical research.[8] This type of emitters recently results more efficient than polymer dots (PDs) that nevertheless have excellent properties like fluorescent brightness, fast emission, photostability, possibility of incapsulating a large amount of ECL active dyes. The main interesting application features of PDs are the ECL emission and stimuli-responsive proprieties.[36–38]

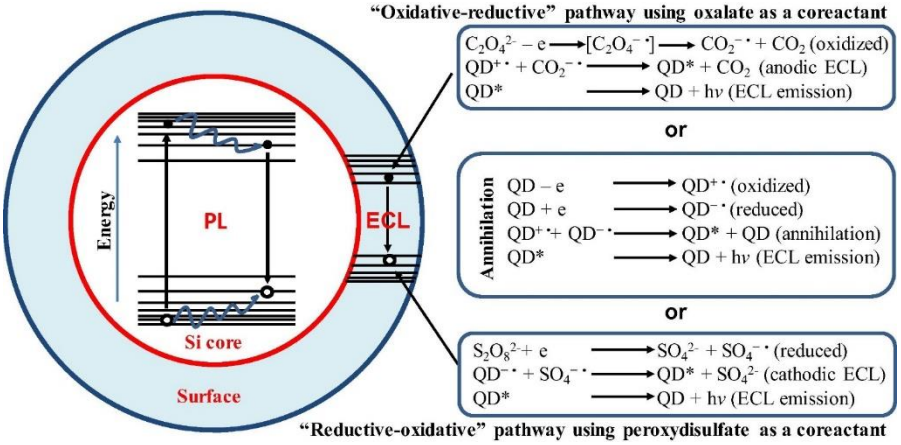

Figure 1.4. Schematics for PL and ECL emission of Si QDs (left), and ECL mechanism including annihilation and coreactant (oxidative-reductive and reductive-oxidative) pathways of ECL emission. Reprinted with permission from Ref [35].

However, QDs have intrinsic toxicity and can be efficiently substituted by carbon-based materials in biosensoristic ECL applications. In fact, the latter have high water solubility, low toxicity, high biocompatibility, facile functionalization, and high stability. The interesting electro-optical properties come from the quantum confinement effects of the core and edge effects of the surface and the PL and ECL properties can be easily modulated through synthetic procedure.[39–43] For

example, CDs show special excitation-dependent fluorescence emission properties, and the mechanism of light generation allows their analytical applications and it has quantum effect, surface state, and recombination of electron-hole pair as protagonists.[44,45] Quantum effect in particles with nanoscale dimensions show discrete energy level and a consequently size-dependent emission, as previously explained for QDs. Moreover, surface energy level and level gap are influenced by surface functional groups, thus tuning fluorescence efficiency and color.[46–48] CDs photophysical features were largely investigated while ECL properties have been less explored, although the useful correlation between electrochemical and photophysical processes. PL and ECL emissions from CDs are generated by different mechanisms and this aspect will be established in this chapter (figure 1.4):[9,49] PL is dominated by excitation and emission within the core, while ECL emission is due to the surface energy levels because the electron transfer occurs at the surface of CDs.[50] The so-called excitation-dependent emission is a common and characteristic feature of amorphous CDs and the optical heterogeneity can be explained through i) individual contributions from core and surface functional groups or ii) surface states with the PL activity originating from multiple individual surface exposed emitters or π–π conjugated fragments/molecular fluorophores in the carbon core.[51,52] Electron hole and rearrangement of radiation theory explains the luminescence behavior of CDs doped with heteroatoms, which created new surface state energy level influencing the radiation rearrangement, the fluorescence efficiency and the ECL improvements.[53,54] The nitrogen or sulfur doped CDs will be applied as alternative dyes, coreactants or as modifiers of electrode surface for increasing ECL efficiency.[33,55] Their great stability and huge specific surface area, their good electron mobility which facilitate charge transfer and boost the electrochemical activity are the mandatory features responsible in development of sensors and biosensors that exploit CDs.[20]

The modification of the carbon material can implement lacking features or key properties towards an optimal functionality, and the recognition specificity through the attachment of sensing molecules on the carbon material, the tuning of emission and charge transfer and the improvement of material processability. Together with carbon nanotubes, widely used in ECL application and that will be extensively discussed in the third chapter, another type of nanomaterial widely used is represented by carbon nitride nanosheets. They are non-toxic and stable metal-free semiconductors usually characterised by poor electrical conductivity which limits the electron transfer rate. However, the electrical conductivity can be enhanced through doping with metal nanoparticles.[56,57]

Nanomaterials represent a great boost in ECL development and limitation solution, showing nanoprobes with smaller size, larger specific surface area, higher surface activity and providing more subtle optical information and tunable properties.[58] However, the traditional ECL probes, $[Ru(bpy)_3]^{2+}$ or Ir(III) complexes, can acquired better performances by post-modifications or mainly through embedding in nanostructures. For example, DDSNPs are suitable for the enhancement of ECL signal intensity because, beyond the features presented before, they can concentrate a huge number of ECL active dyes in a single site as shown previously in the strategy (b). Moreover, NPs have dyes with higher quantum yield and photostability because silica is photo-physically inert and protect against oxygen and other quenching molecules. Different types of doping dye can be used, consequently tuning the emission properties.[35] For example Ru(II) complexes have high intense signals and synthetic versatility while Ir(III) complexes have wide emission between near-IR and deep blue, allowing the development of multichannel analytical technique.[30,59] The main issue related to the use of nanoparticles (NPs) is that coreactant radicals generated at the electrode surface have to diffuse and interact with luminophores inside the NPs within their diffusion length, underlining the complexity of DDSNPs not only due to their multichromophoric structures. To overcome this problem, researchers acted on either the synthetic procedure or the coreactant choice, after the investigation of ECL generation mechanism (figure 1.5).[60,61]

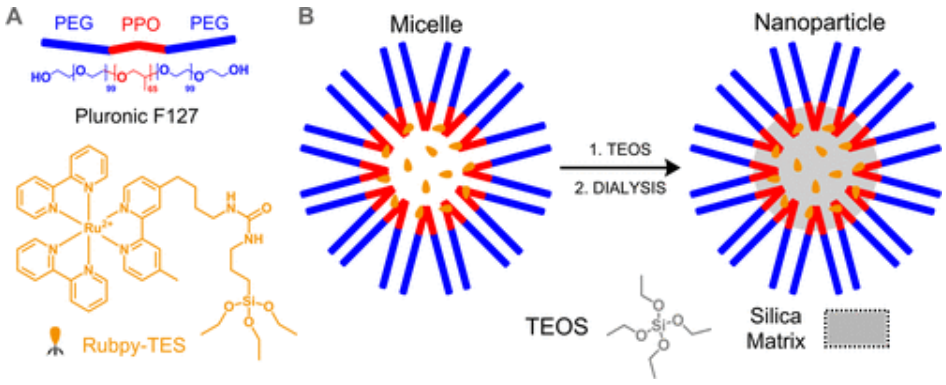

Figure 1.5. (A) Main synthetic reagents used for the synthesis of core–shell silica–PEG nanoparticles. (B) Schematic representation of the synthetic process. Reprinted with permission from Ref [60].Copyright 2016 American Chemical Society

In previous works, two concomitant mechanisms were outlined and related to the different properties of the nanoparticles, like the doping level, and the contribution of electron hopping between Ru(II) complexes inside the NPs was simulated.[62] For the formation of excited state of dye, the first ECL mechanism only involves radicals from coreactant oxidation while in the second also the Ru(II) complex oxidation at the electrode are involved (see mechanisms explained in the

introduction, paragraph 1.2). The ECL intensity of this system could be enhanced acting on different features like the doping level but also the surface charge because of DDSNPs-coreactant interaction.[22,60,61]

Only a small part of nanomaterials and biosensing strategies are shown before but the significant innovations in novel materials and highly creative detection strategies are growing more and more in every moment.

1.2 Outlook

The importance of nanomaterials in ECL sensitivity enhancement was widely studied during past years and thanks to the amazing results obtained, the correlation ECL-nanomaterials is continuously being studied during these recent years and herein briefly presented. Nanotechnologies represent a precious instrument for increasing the application of ECL technique in various analytical applications. They can be used as luminophores, coreactants and electrode materials but in this chapter, we will focus our attention on modulating the luminophores and their structures. Studying the ECL generation mechanism, the structure of the nanomaterials can be modulated for reaching the higher ECL efficiency because the emission is mainly related to their architecture and consequent interaction with the coreactant. Nitrogen CDs doped with boron-dipyrromethane compound was applied as more efficient ECL dye modulating their synthetic procedure and the structural properties (figure 1.6a). The modulation of synthetic procedure was useful also for $[Ru(bpy_3)]^{2+}$-doped silica nanoparticles, where a huge number of dyes can be concentrated without showing properties detrimental for ECL emission (figure 1.6b). Both nanomaterials give very promising results although they are very different according to the excited states involved in ECL emission.

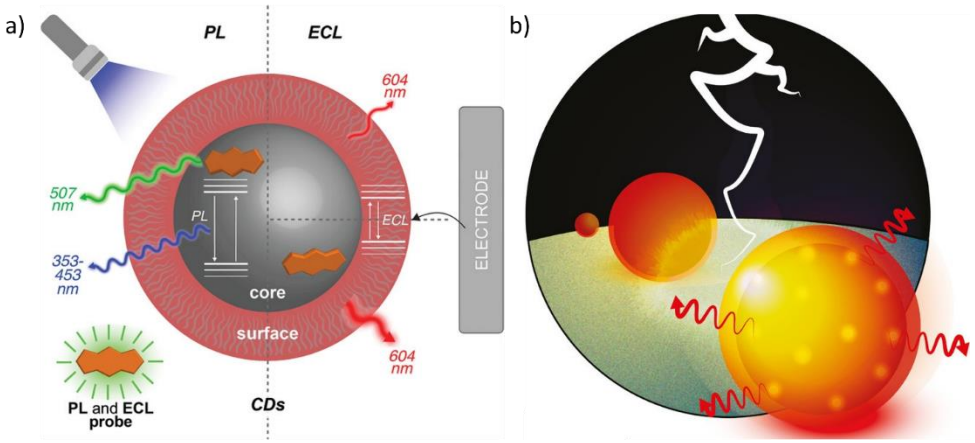

Figure 1.6. Nanomaterials studied in this chapter and their application as ECL novel and more efficient luminophores. a) Nitrogen Carbon Dots doped with Boron-dipyrromethane compound and structure influence on PL and ECL emission.[63] b) $[Ru(bpy_3)]^{2+}$-doped silica nanoparticles and their sketchy structure.[64]

2. ELECTROCHEMILUMINESCENCE OF CARBON DOTS DOPED WITH BODIPY[63]

CDs' promising features and unexplored ECL behavior motivated the investigation of the mechanism and the states responsible of emission, aiming to develop an efficient and non-toxic luminophore modifying the synthetic procedure and modulating the CDs structures. The variety of synthetic precursors and procedures that affect the CDs' PL and ECL properties hampered the understanding of their ECL properties and the development of general mechanistic models, which could ultimately drive the preparation of nanomaterials with better performance. The aim of our investigation was therefore the understanding of how their structure affects the ECL performance and how surface and core properties could be modulated to improve ECL response and make these promising nanoparticles more widely applicable. A path towards the creation of a huge library of nanoparticles for biosensing applications was opened.

2.1 New synthetic procedure

Nitrogen doped carbon dots (NCDs) were synthesized through the efficient microwave-assisted hydrothermal approach in collaboration with Prof Prato research group at the university of Trieste. They built a new approach that requires a pre-synthetic design and a post-synthetic modification. In the pre-synthetic design nitrogen doped carbon nanodots were synthesized using a precursor mixture composed by arginine (Arg) and ethylenediamine (EDA)[65]. NCDs are characterized by an amorphous carbogenic core and a surface rich in primary amino groups[66,67] and will be compared with NCDs doped with boron-dipyrromethene (BODIPY) dye as PL and ECL active probe, which were added in the precursor mixture. In the post-synthetic modifications, the primary amino group were modified in a second step with methyl or propyl groups, exploiting reductive alkylation reactions or Escheweiler-Clarke methylation or reductive propylation (figure 1.7).

BODIPYs have distinctive absorption/PL emission profiles, they are efficient ECL fluorophores, and their structural properties play a fundamental role in ECL emission but don't influence the morphology and structural properties.[68–71] A carboxylate function was introduced in a meso-phenyl substituent to facilitate the incorporation of the dye, forming amide bonds with the amines from the Arg and EDA under hydrothermal conditions. A homogeneous carbonization was reached through condensation, polymerization, and aromatization. The carboxylic group was introduced either at the *ortho* (BODIPY-*o*-COOH) or at the *para* (BODIPY-*p*-COOH) position of the phenyl ring of the

BODIPY in order to see if the PL quantum yield of the dye in the nanodots would be affected by the isomerism.[72,73]

B-NCDs were finally synthetised according to all the different precursors used and specifically we obtained *p*B-NCDs and *o*B-NCDs, with BODIPY-*p*-COOH and BODIPY-*o*-COOH as respective doping agent, that are methylated or propylated in a following moment (Figure 1.7). Managing synthetic parameters and optimising the molar ratio between precursors, water-soluble round shape nanoparticles of 2.17 ± 0.65 nm (TEM and AFM analysis) were synthesised. We performed the NCDs characterization through the more common techniques used for these types of material.[74] Although the CDs' dispersion is quite homogeneous without agglomerates, DLS was preferred for bigger nanoparticles size determination because it is less sensitive to so small CDs than TEM, which can also determine the sample's ultrastructure.[75,76] Moreover, AFM and FT-IR confirmed that the morphology and structural features of the NCDs synthetized are not influenced by the functionalization of the phenyl ring on the BODIPY; while XPS analysis show the presence of C, N, O, B, and F (respective atomic percentage 61.1, 22.4, 13.2, 1.2, and 2.1) and underline, observing the binding energy of F1s, the presence of an inorganic compound BF_2 that belong to BODIPY core and its consequent stability under synthetic procedure. The PL and ECL characterization and behaviour investigation are deeply conducted and required dedicated paragraphs.

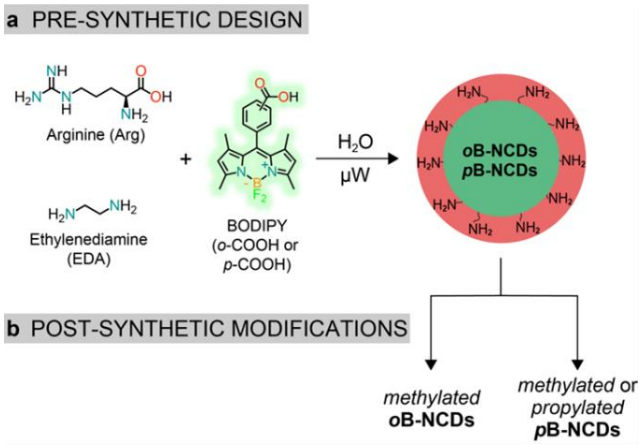

Figure 1.7. Precursors used for the a) synthesis of *o*B-NCDs and *p*B-NCDs and b) post-synthetic modification of the surface amino groups on the surface.

2.2 Photoluminescence of B-NCDs

PL spectra were performed on B-NCDs in water evidencing the incorporation of the dye in the nanoparticle. PL spectrum of *p*B-NCDs (figure 1.8a top) shows two emitting peaks upon excitation from 300 to 470 nm. The first peak was shifted from blue-green to the green region (353-453 nm)

increasing the excitation wavelength, a typical behaviour of NCDs (figure 1.8a middle).[14] Instead, the second peak centered at 507 nm is assigned to the BODIPY moiety (figure 1.8a bottom),[68,72] and its emission is highly photostable due to the fluorophore protection by the presence of carbonaceous matrix. Comparing PL spectra of *o*B-NCDs and *p*B-NCDs no great differences were observed: peak position of the BODIPY moiety is unchanged, while the emission in the blue region of *p*B-NCDs is slightly shifted (by ≈10 nm) than *o*B-NCDs (figure 1.8a top and 1.8b). However, changes in the photoluminescence quantum yield (PLQY) of *o*B-NCDs compared to *p*B-NCDs were observed: i) the PLQY of the blue emission is 6.0 ± 0.4% and 4.1 ± 0.1% for *p*B- and *o*B-NCDs, respectively; ii) the PLQY of the green emission is 26.7 ± 0.6% and 43.7 ± 1.2% for *p*B- and *o*B-NCD, respectively. The green PLQY has the same dependence on the substitution of the phenyl ring observed for the dyes BODIPY-*o*-COOH (82.3 ± 3.2%) and BODIPY-*p*-COOH (43.3 ± 1.2%) alone in water. However, the surface modification reactions affect the blue PLQY to a greater degree than the green PLQY[66] because primary, methylated and propylated amines probably introduce different surface states as surface functional groups and defects.[15,44] Specifically PLQY was calculated comparing the behaviour of the samples respect to standards and considering integrated fluorescence emission, absorption factor and media refractive index (see appendix for detailed calculation).[77] Possible aggregation or quenching effect were taken into account only if they affect the parameters just listed.

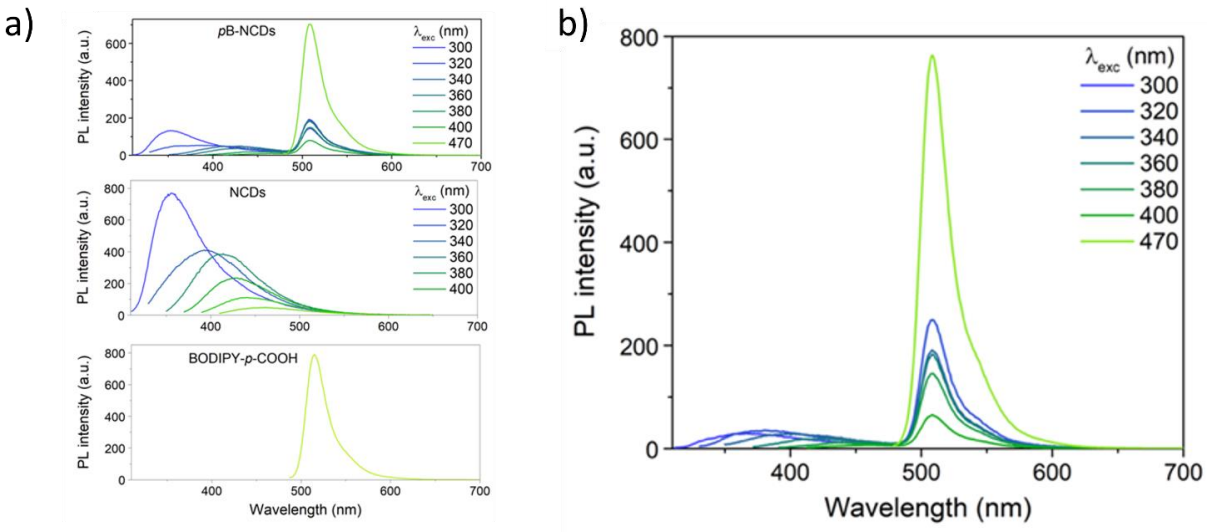

Figure 1.8. a) PL emission spectra at different excitation wavelengths of *p*B-NCDs in water (up), NCDs in water (middle) and BODIPY-*p*-COOH in DMSO (down). b) PL emission spectra of *o*B-NCDs at different excitation wavelengths, experiments performed in water at 298 K.

2.3 Electrochemistry of B-NCDs and ECL mechanism

The electrochemistry of B-NCDs was investigated and compared to BODIPY and NCDs by cyclic voltammetry in N,N-dimethylformamide (DMF) containing 0.1 M of Bu_4NPF_6 as supporting electrolyte. BODIPY dyes usually show reversible reductions and oxidations with peaks near -1.0 and +1.3 V, respectively. However, the BODIPY substituents may affect the electrochemical behaviour and BODIPY-*p*-COOH, one of the two dyes compound structures, shows in fact an irreversible oxidation peak at +1.14 V (peak potential vs SCE) and a reversible reduction at -1.09 V ($E_{1/2}$ vs SCE), shown in figure 1.9.[69,78]

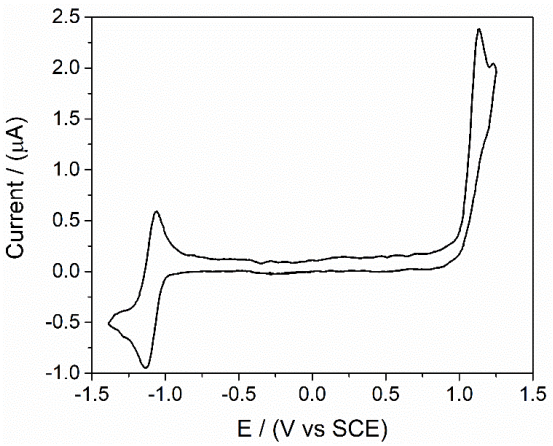

Figure 1.9. Cyclic Voltammetry of BODIPY-*p*-COOH (1.0 mM) in DMF/0.1 M Bu_4NPF_6, scanning the potential between +1.25 V and −1.4 V at scan rate 0.05 V s^{-1}.

In the case of NCDs the electrochemical behaviour can be modulated employing different precursors. In the present study, an irreversible peak was observed at +1.1 V due to the primary amines present on the NCDs surface (figure 1.10).

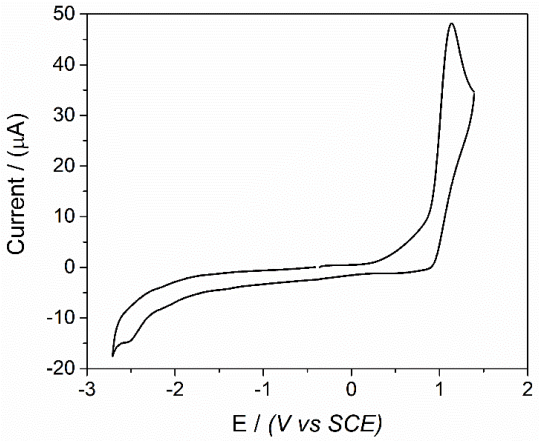

Figure 1.10. Cyclic Voltammetry of NCDs (1.0 mg mL^{-1}), in DMF/0.1 M Bu_4NPF_6, scanning the potential between +1.4 V and −2.7 V at scan rate 0.1 V s^{-1}.

Comparing the two cyclic voltametric curves, very useful information for interpretation of B-NCDs behaviour in ECL and PL can be extracted. In figure 1.11, *p*B-NCDs show a peak at +1.20 V that can be attributed to the oxidation of the amino groups on B-NCDs surface which overcomes the low current of BODIPY oxidation. However, dye organic compound availability was verified by the presence of an irreversible peak at -1.90 V attributed to BODIPY reduction. The differences in peak position and kinetics with respect to BODIPY reflect the novel nano-environment surrounding the dye. Despite the irreversibility, *p*B-NCDs oxidation is easily accessible and show solubility and photoluminescence in water. These are good reasons for applying this material as ECL dye in water solution, exploiting the coreactant strategy.

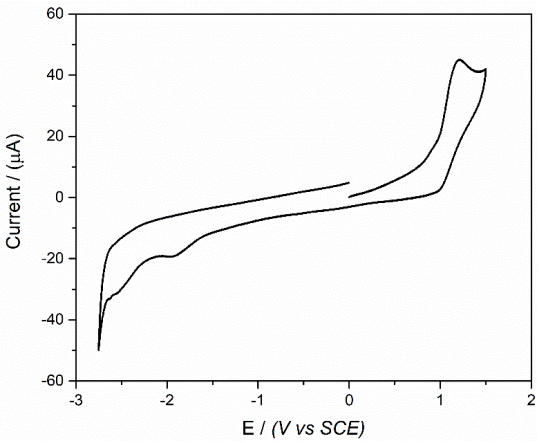

Figure 1.11. CV of *p*B-NCDs (1.0 mg mL^{-1}) in DMF/0.1 M Bu_4NPF_6, scanning the potential between +1.50 V and −2.75 V at scan rate 0.1 V s^{-1}.

ECL measurements were performed in phosphate buffer (PB) 0.2 M (pH=6.9) with tri-*n*-propylamine (TPrA) 180 mM as sacrificial coreactant in order to understand the ECL behaviour and mechanism of *p*B-NCDs. Current-potential curve shows the CV current dependence from TPrA oxidation (E_0= +0.88V vs SCE) while ECL-potential curve shows that the ECL intensity increases in correspondence of TPrA and *p*B-NCDs oxidation (figure 1.12a). This behaviour is the proof of an "oxidative-reduction" coreactant mechanism which involve the oxidation of both TPrA and *p*B-NCDs as shown in figure 1.12b.[23,79]

The ECL experiments were performed using a constant concentration of B-NCDs of 1 mg mL^{-1}, scanning the potential between 0 V and +1.6 V and Glassy Carbon GC as working electrode, thanks to its good ECL performance and low surface modification at high potential.[34] The role of coreactant was verified by experiments performed on different types of B-NCDs without TPrA, which did not provide any ECL signal (figure 1.13). In addition, the surface charge of CDs' might affect ECL final signal due to the interaction between the coreactant and the dye. However, this behaviour,

previously observed in our group, was found negligible for such small nanomaterial. Furthermore, nanomaterial and coreactant are both free in solution and the dye responsible of ECL emission isn't embedded in any charged matrix that repulses coreactant radicals.

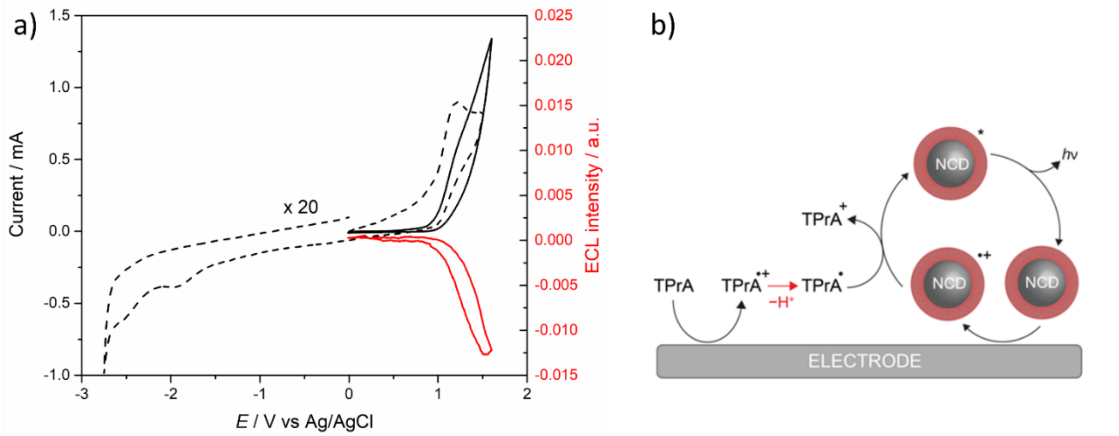

Figure 1.12. a) CV of *p*B-NCDs in DMF (dashed black line) and CV of *p*B-NCDs in PB 0.2 M and TPA 180 mM (solid black line) compared to CV-ECL emission of the same sample (red line). b) ECL emission "oxidative-reduction" coreactant mechanism hypothesis where both the coreactant TPrA and B-NCDs emitter oxidation occur on the electrode generating the B-NCDs excited states.

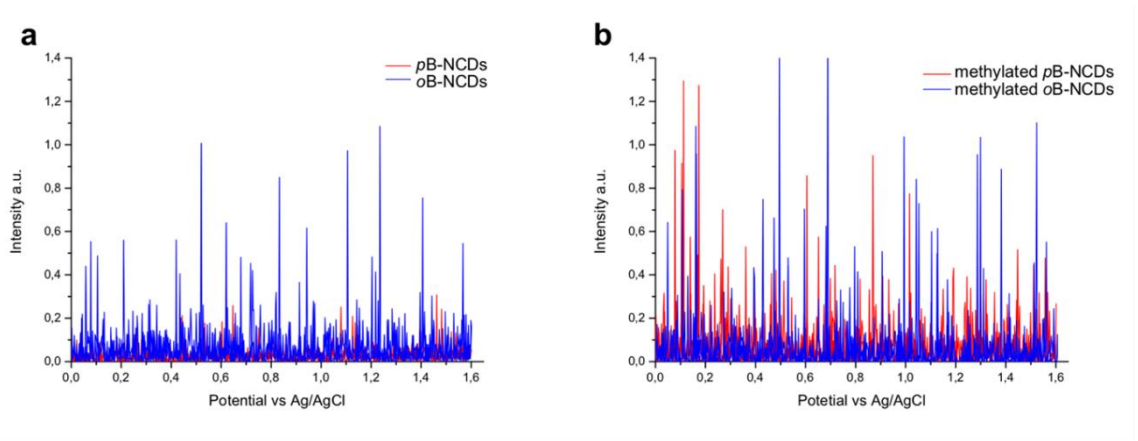

Figure 1.13. ECL intensities vs potential of (a) *p*B-NCDs (red line) and *o*B-NCDs (blue line) and (b) methylated *p*B-NCDs (red line) and methylated *o*B-NCDs (blue line). Experiments performed in PB 0.2 M, pH = 6.9. Potential applied from 0 V to 1.6 V, scan rate 0.1 V s^{-1}. Glassy Carbon electrode referred to Ag/AgCl. Pt spiral as counter electrode. PMT bias 750V.

2.4 Electrochemiluminescence of B-NCDs

Electrochemiluminescence of B-NCDs was compared to NCDs without BODIPY doping. The analysed B-NCDs differ for BODIPY structure (*p*B-NCDs and *o*B-NCDs shown in figure 1.7) and for the superficial amines, i) primary in case of no post-modification, ii) methylated or iii) propylated if post synthetic modifications were performed. ECL signals displayed the same decay rate for NCDs and B-NCDs with primary and methylated amine (figure 1.14). The comparisons were performed

on ECL emissions of the samples, which were obtained through chronoamperometric analysis performed in PB 0.2 M solution with TPrA 180 mM under a constant potential of 1.6 V. The observed decay behaviour of chronoaperometric analysis is due to different factors, such as electrode oxidation and side reactions connected with TPrA oxidation.[34,80,81]

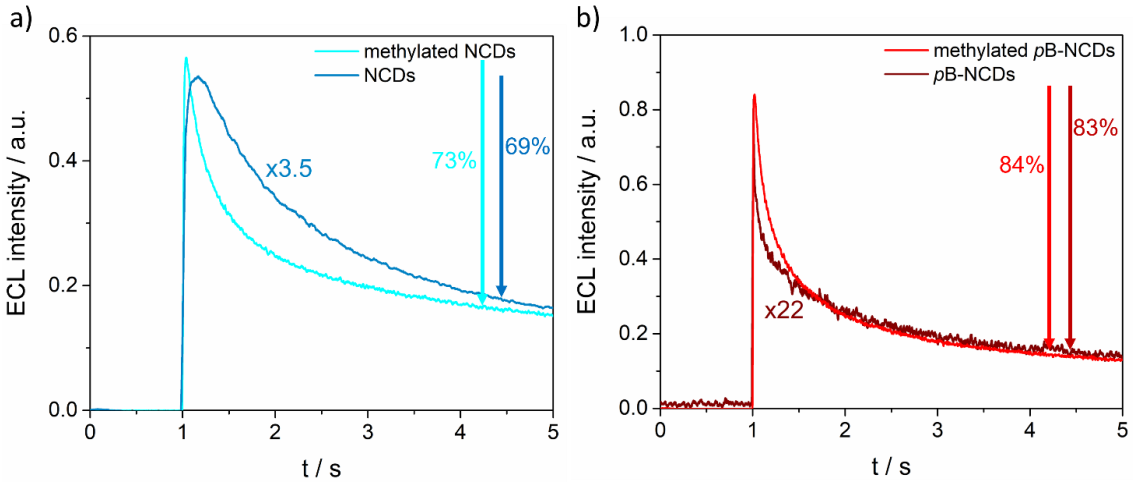

Figure 1.14. ECL vs time curves of a) methylated NCDs (blue line) and NCDs (dark blue line) and b) methylated *p*B-NCDs (red line) and *p*B-NCDs (wine line). Notice that a) the ECL intensity of NCDs is multiplied for a factor 3.5 for easy comparison with the ECL intensity of methylated NCDs and ECL intensities of methylated NCDs and NCDs show a drop of 73% and 69%, respectively; b) the ECL intensity of *p*B-NCDs is multiplied for a factor 22 for easy comparison with the ECL intensity of methylated *p*B-NCDs. ECL intensities of methylated *p*B-NCDs and *p*B-NCDs show a drop of 84% and 83%, respectively. Experiments performed with TPrA 180 mM as coreactant in PB 0.2 M as supporting electrolyte. Potential applied of 1.6 V. GC electrode potential referred to Ag/AgCl at room temperature. Platinum wire as counter electrode. PMT bias 750V.

However, ECL signal intensity is strongly influenced by the surface chemistry, as seen in previous works on colloidal quantum dots or silicon nanocrystals.[33,50] In order to identify the electrogenerated states and better understand the influence of the synthetic modifications on the nanoparticles performance, ECL spectra were measured and compared to PL spectra. Methylated *p*B-NCDs ECL spectra display a broad band at ≈ 604 nm, which is red-shifted by ≈ 100 nm with respect to PL peak ascribed to the BODIPY moiety and by ≈ 250 nm from the PL peak in the blue region ascribed to the NCDs structure of the spectrum (via excitation at 300 nm) (Figures 1.8a and 1.15). The same red-shift is observed for both methylated *o*B-NCDs and NCDs, which showed ECL peaks at 613 and 615 nm, respectively (Figures 1.8b and 1.17). The difference between ECL and PL spectra is due to the higher sensitivity of ECL to surface states: electrons and holes are separately injected into the dots and the relative kinetics are affected by the surface chemistry.[50]

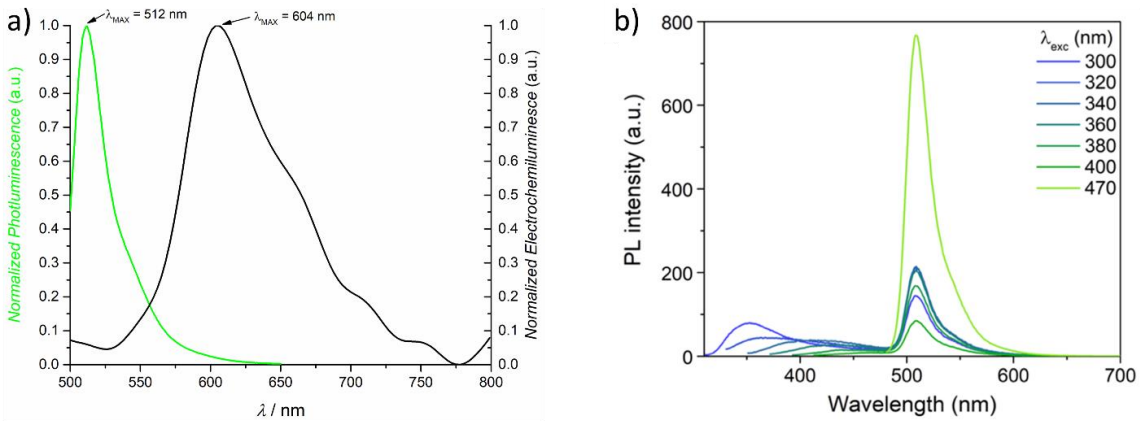

Figure 1.15. a) Maximum emission wavelength of normalized photoluminescence relative to methylated *p*B-NCDs (0.5 mg mL^{-1} in water, green line) compared to maximum wavelength of normalized electrochemiluminescence relative to the same sample methylated *p*B-NCDs (1.0 mg mL^{-1} with TPrA 180 mM in PBS 0.2 M, black line). b) PL emission spectra of *p*B-NCDs at different excitation wavelengths. Experiments performed in water at 298 K.

Beside the red-shift of bands, functionalization also affects the ECL intensity. B-NCDs with primary amines show an almost negligible signal compared to the intense signal obtained for both methylated or propylated NCDs and *o*B- or *p*B-NCDs, thereby confirming the importance of surface functional groups in the ECL emission. In fact, the influence of surface chemistry on ECL efficiency was investigated comparing *p*B-NCDs with different amino groups on the surface (figure 1.16). ECL intensity for propylated *p*B-NCDs is 1.7-fold higher than for the methylated ones, while *p*B-NCDs with primary amines do not present any ECL emission signal, as discussed above. In fact, primary amines electropolymerize on the electrode surface upon anodic oxidation, thereby decreasing the ECL signal due to electrode passivation.[82,83]

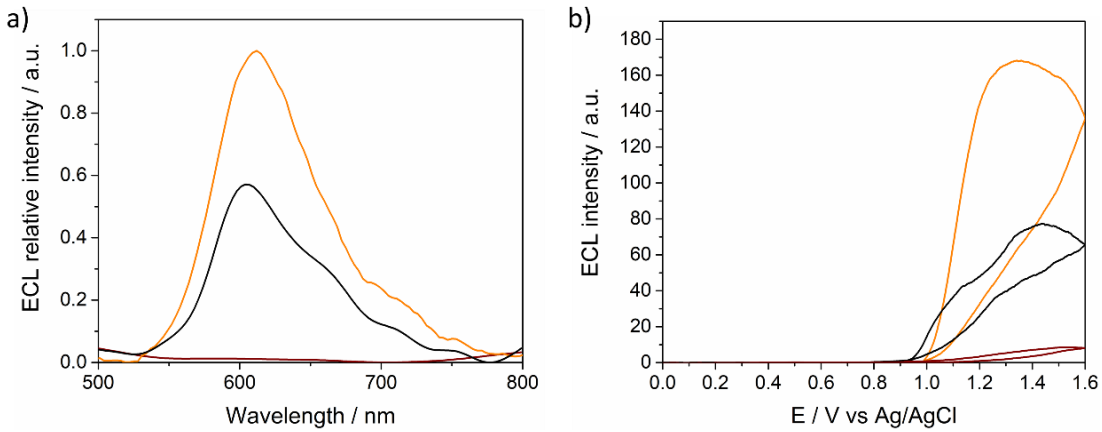

Figure 1.16. a) ECL emission spectra and b) ECL potential curves of 1.0 mg mL^{-1} of each sample: propylated *p*B-NCDs (orange line), methylated *p*B-NCDs (blue line) and *p*B-NCDs (wine line). Experiments performed with TPrA 180 mM as coreactant in PB 0.2 M as supporting electrolyte. GC electrode potential referred to Ag/AgCl at room temperature. Platinum wire as counter electrode. Cyclic voltametric analysis scanning from 0 V to 1.6 V, scan rate 0.1 V s^{-1}. PMT bias 750V.

By contrast, comparing the ECL intensity for *p*B-NCDs, *o*B-NCDs and NCDs, where the surface is rich with methylated amines (figure 1.17), smaller differences were observed. The ECL intensity for methylated *p*B-NCDs is 1.6-fold higher than for methylated NCDs, while the BODIPY in the methylated *o*B-NCDs partially quenches the ECL process and the ECL intensity is 3-fold lower than for methylated *p*B-NCDs.

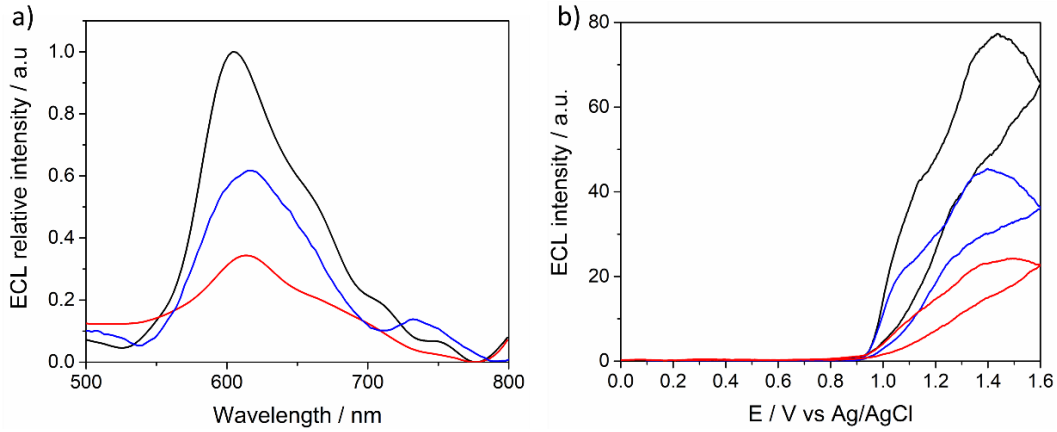

Figure 1.17. a) ECL emission spectra and b) ECL potential curves of 1.0 mg mL^{-1} of each sample: methylated *p*B-NCDs (black line), methylated NCDs (blue line) and methylated *o*B-NCDs (red line). Experiments performed with TPrA 180 mM as coreactant in PB 0.2 M as supporting electrolyte. GC electrode potential referred to Ag/AgCl at room temperature. Platinum wire as counter electrode. Cyclic voltammetric analysis scanning from 0 V to 1.6 V, scan rate 0.1 V s^{-1}. PMT bias 750V.

Based on these results, ECL emitting excited states would depend mainly on the surface properties but also the BODIPY moiety nano-environment shows a small effect on ECL efficiency. As to the different surface modifications, propylated *p*B-NCDs exerts a stronger stabilization effect on the amine-centered radical cations formed at the electrode surface than methylated *p*B-NCDs.[84] Moreover, a better energy alignment between the dye-doped core and the surface states with a consequent transfer of electronic density on the shell and stabilization of the excited state can be responsible of the more efficient ECL process. This behaviour reflects recent results on core/shell and core/shell/shell colloidal quantum dots, where band and lattice structure are important for ECL emission which occurs from the surface state and its efficiency is affected also by the core.[10] On the other hand, the organic shell was not altered considerably ruling out that surface modifications will affect the charge tunnelling through the shell.

In conclusion, novel dye doped CDs were synthesized combining pre- and post-synthetic modifications and varying synthetic procedures and precursors to modulate and improve PL and ECL properties. Electrochemistry and spectroscopy were used for understanding the nature of emitting states and outlined the structure of nanoparticles studied and contribution of shell and core

to the emission. Emitting states of PL and ECL are different because they are energetically different: ECL spectra of NCDs and B-NCDs red-shifted with respect to the PL. For PL analysis, blue emission is excitation-dependent and characteristic of NCDs, while the green one is due to the BODIPY dye. The PL and ECL efficiency of NCDs and B-NCDs showed that i) the surface-emitting states from the organic shell influence the efficiency of the blue excitation-dependent PL emission and the ECL efficiency and ii) the green PL emission is sensitive to states of the core, including the nano-environment of BODIPY, and not sensitive to the surface chemistry, but influence the ECL emission, despite of its primary dependence on surface states, suggesting that electron and hole wavefunctions can interact with the surface. B-NCDs structure was hypnotized having BODIPY moiety located in the core of the nanoparticle that can alter ECL emission intensity but not the maximum wavelength and affects mainly the PL properties of CDs (figure 1.18). Coupling pre- and post-synthetic approaches is crucial for improving the ECL performances. The pre-synthetic design does not enable fine control of core and surface emitting states, while post-synthetic modifications influence ECL intensity, which increases from primary amine, to methylated and to propylated tertiary amines. All the findings may be useful for development of other CDs or nanoparticles through new rational synthetic strategies in order to advance ECL performance and consequently ECL applications in aqueous environment.

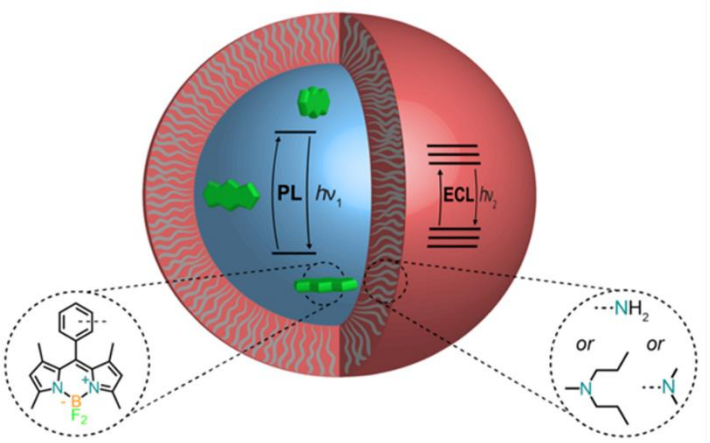

Figure 1.18. Scheme of the core/shell structure of B-NCDs. The core influences the PL emission, while the surface states influence the ECL emission with the core states contributing to the ECL efficiency.

3. ELECTROCHEMILUMINESCENCE OF DYE DOPED SILICA NANOPARTICLES[64]

The most used mechanism of ECL generation in aqueous environment allows a tremendous number of applications[26,27,85–88] and is based on the so-called oxidative-reduction coreactant mechanism where TPrA is used as sacrificial co-reactant and tris(2,2′-bipyridine)ruthenium (II) ($[Ru(bpy)_3]^{2+}$) as luminophore.[23–25] This strategy is applied also in commercialized ECL-based immunoassays developed by Roche Diagnostics (Elecsys®)[89] and Meso Scale Diagnostics.[90]

The combination between ECL and nanomaterials, such as nanoparticles, and their utilization as dyes or co-reactants was performed for increasing the sensitivity of this promising analytical technique. In particular, dye-doped silica nanoparticles (DDSNPs) show several advantages and are very interesting as ECL dyes for immunoassay because i) a large number of inner active dyes can be concentrated in a single nanoparticle, consequently enhancing the signal intensity,[60,62] they can ii) be easily synthetised, iii) have high colloidal stability in water, and iv) favour an easy bioconjugation.[91] However, there are some limitations on the use of DDSNPs that strongly depend on the synthetic method adopted.[35] Solubility and electrostatic interactions can be a problem in the NPs doping with organic and inorganic dyes. Nevertheless, a proper control of the synthetic procedures can solve this type of problem and also modulate the physical chemical properties of NPS as colloidal stability, good functionalization and derivatization, size, number of embedded dyes and porosity. All these properties are very important to improve the NPs performance and create useful nanomaterials where internal dyes can easily be reached by the coreactant reactive species for the ECL generation. In DDSNPs, the process leading to the formation of the ECL emitting excited state is very complex because it involves several electron-transfer processes. In particular, the oxidized species and products generated by the coreactant oxidation have to reach the dyes inside the NPs so as to generate the emitting state. For this reason, the control and modulation of all of the above parameters is mandatory to make the overall process efficient thus leading to a strong emission; according to our previous studies, the nanoparticle should ideally possesses a rather thin shell, be porous and display an overall negative ζ-potential.[92,93]

In view of these considerations, a different synthetic approach for DDSNPs was proposed in order to optimize DDSNPs features devoted to ECL mechanism investigations, ECL signal enhancement, and the consequently increase of ECL technique sensitivity for efficient applications in bioanalysis and medical diagnostics. The work was performed in collaboration with Prof Luca Prodi research

group at the university of Bologna and a new path towards more sensitive analytes detection, biosensors and point-of-care device is open.

3.1 Synthetic procedure and characterization

Until now the DDSNPs were obtained by a direct micelle-assisted method using Pluronic-F127 as surfactant. To further push the signal intensity, silica NPs were synthesized with a reverse microemulsion method, and the synthetic parameters can be easily controlled, obtaining a suspension of monodispersed NPs with adjustable size, surface properties and different surface functionalization.[60,92] In particular, using $[Ru(bpy)_3]^{2+}$-$Si(OEt)_3$ derivative as dye, two sets of $Ru(bpy)_3]^{2+}$-doped silica NPs was synthesized and named bio-Triton@RuNP and bio-Igepal@RuNP. They were labelled with a biorecognition unit through biotinylated polyethylenglycol triethoxy silane derivative (Biotin-PEG_{45}-$Si(OEt)_3$) and coated by an antifouling agent polyethylenglycol triethoxy silane derivative ($PEG_{6-9}Si(OEt)_3$). The names are connected to the two different types of nonionic surfactants, TritonX-100 and Igepal CO-520, used in the synthesis (figure 1.19).

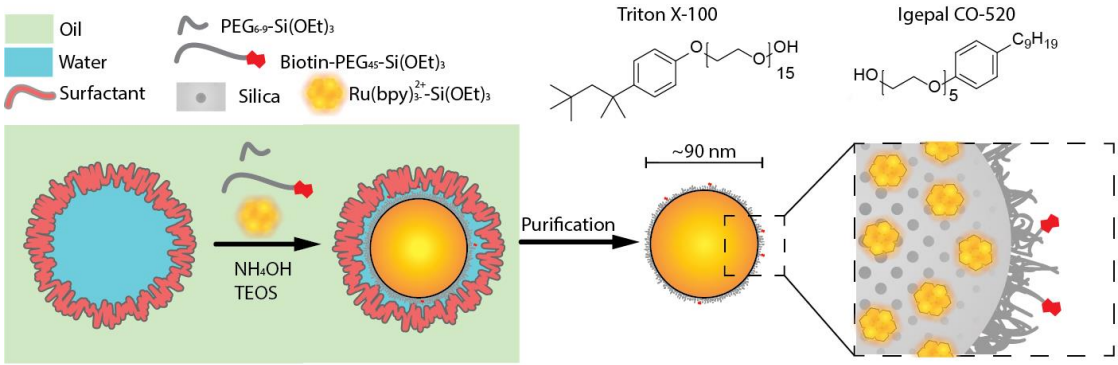

Figure 1.19. Schematic representation of the Reverse Micro Emulsion synthesis of $[Ru(bpy)_3]^{2+}$-doped silica nanoparticles. The synthesis starts with the preparation of the water in oil emulsion stabilized with non-ionic surfactants (Triton X-100 or Igepal CO-520), then upon the addition of $[Ru(bpy)_3]^{2+}$ triethoxy silane derivative ($Ru(bpy)_3^{2+}$-$Si(OEt)_3$), tetraethoxyorthosilicate (TEOS) and, ammonium hydroxide (NH_4OH) the dye-doped silica core is formed. The NPs are then coated with antifouling agent polyethylenglycol triethoxy silane derivative ($PEG_{6-9}Si(OEt)_3$) and with biotin tagged polythylenglycol triethoxysilane derivative(Biotin-PEG_{45}-$Si(OEt)_3$). The synthesis ends with the purification of the NPs from the surfactant and the oil phase.[94,95]

The characterization of RuNPs were performed before checking the ECL performances. TEM and DLS measurements show respectively the core (90 nm) and hydrodynamic (dH 150 nm) diameters of bio-Triton@RuNP and bio-Igepal@RuNP (figure 1.20). The diameters are almost independent of the surfactant used as well as the absorption and emission spectra, which show similar features for

both types of NPs and for $[Ru(bpy)_3]^{2+}$ in water solution (figure 1.21b). This behaviour suggests that electronic ground and excited states of luminophores are unperturbed by the silica matrix.

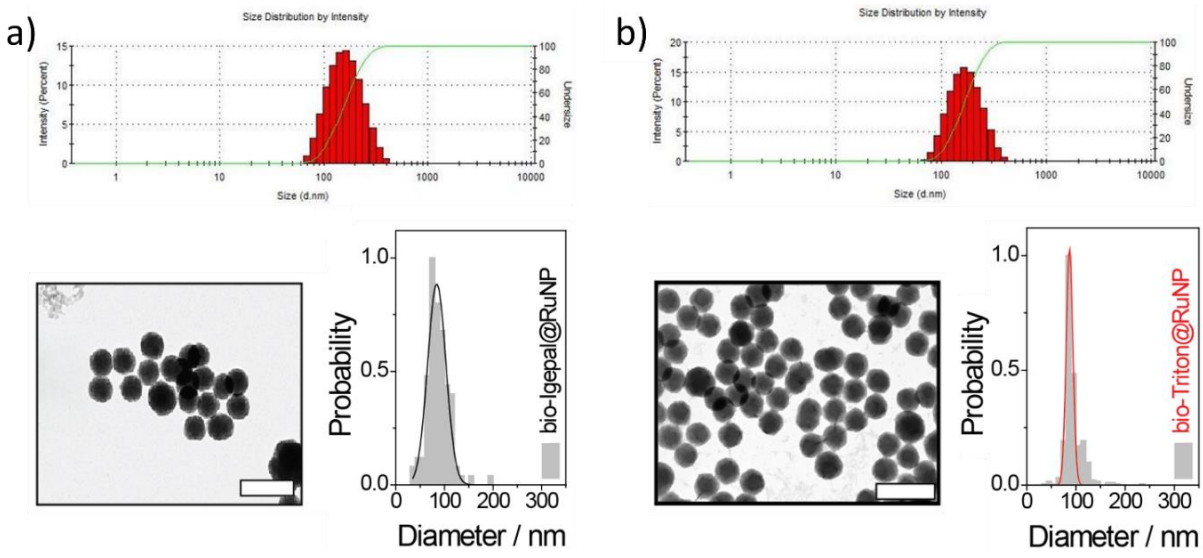

Figure 1.20. a) Hydrodynamic diameter distribution and undersize curve (up), TEM images (bottom left), and silica core diameters distributions computed by TEM (bottom right) of bio-Igepal@RuNP. b) Hydrodynamic diameter distribution and undersize curve (up), TEM images (bottom left), and silica core diameters distributions computed by TEM (bottom right) of bio-Triton@RuNP. Scale bar 200 nm.

However, the silica matrix has an influence on the diffusion of molecular oxygen with a consequent increase of phosphorescence quantum yield Φ and average lifetime τ (figure 1.21a). Bio-Triton@RuNPs (Φ_{PL}=0.080, τ=790 ns) show about a three-fold Φ_{PL} increase with respect to the free $[Ru\text{-}(bpy)_3]^{2+}$ dye (Φ_{PL} =0.028, τ =334 ns) in aerated water solutions, while a smaller increase was observed for bio-Igepal@RuNPs (Φ_{PL} =0.050, τ =618 ns).

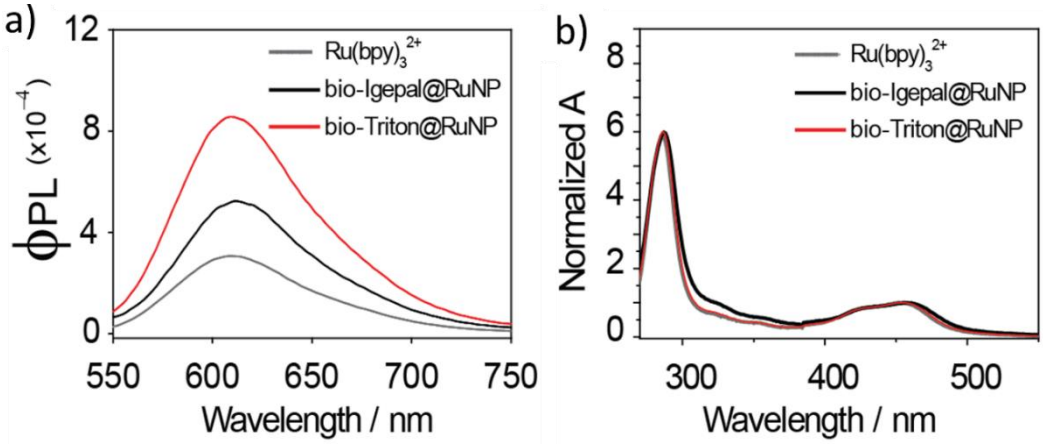

Figure 1.21. a) Phosphorescence quantum yield and b) normalized absorption of bio-Igepal@RuNP (black line), bio-Triton@RuNP (red line) and $[Ru(bpy)_3]^{2+}$ (grey line) in water as reference for comparison.

It was also possible to calculate the number of complexes inside each type of nanoparticle, assuming the same molar excitation coefficient of Ru complexes as in solution (at 452 nm ε=14600 cm^{-1} M^{-1}). Dividing this value by the concentration of the NPs is possible to estimate the average number of Ru complexes contained in each NP: 3200 and 4800 for bio-Igepal@RuNP and bio-Triton@RuNP, respectively, despite the same 2% doping level was used in the synthesis (table 1.1).

A very important analysis in view of its effect on the ECL efficiency, was the ζ- potential calculation. It is closed to 0 mV for bio-Triton@RuNP respect to bio-Igepal@RuNP that is slightly positive, although the number of complexes is higher for bio-Triton@RuNP (table 1.1).[60,61]

sample	% mol dye/ mol TEOS	N° dye/NP	d_H ± SD [nm]	d_H ± SD [nm]	PDI	ζ potential [mV]
bio-Triton@RuNP	2	4800	90 ± 10	145 ± 5	0.10	1.3+0.6
bio-Igepal@RuNP	2	3200	85 ± 20	150 ± 10	0.15	6.81 ± 1.5

Table 1.1. % mol of dyes vs mol of TEOS and number of dyes value of bio-Triton@RuNP and bio-Igepal@RuNP. Hydrodynamic diameter, core diameter, polidispersion index (PDI), ζ-potential measured at pH 6.7.

3.2 ECL performances of $[Ru(bpy)_3]^{2+}$-doped silica NPs

The ECL behaviour of bio-Igepal@RuNP and bio-Triton@RuNP was tested by CV performed in a 1 nM NPs solution using TPrA (180 mM) as sacrificial co-reactant while simultaneously acquiring the ECL signal by a photomultiplier tube PMT. The CV-ECL plot shown in Figure 1.22, reports the recorded ECL intensity against the potential scanned between 0 V and +1.6 V. ECL is generated here according to the "oxidative-reduction" co-reactant heterogeneous mechanism where TPrA is the coreactant is the only species oxidized at the electrode. The TPrA oxidation product have to reach the luminophores immobilised inside the NPs for the excited state formation (see the general scheme in the introduction paragraph 1.2).[23]

Bio-Triton@RuNPs show a much higher ECL intensity than bio-Igepal@RuNps. The higher number of Ru complexes inside the NPs synthesized with the Triton surfactant can explain this behaviour (figure 1.22a). However, other factors as the ζ-potential and the photoluminescence quantum yields should also be considered because, after normalizing the ECL intensity by the number of dyes/NP, bio-Triton@RuNP still displays a better performance (see table 1.2).

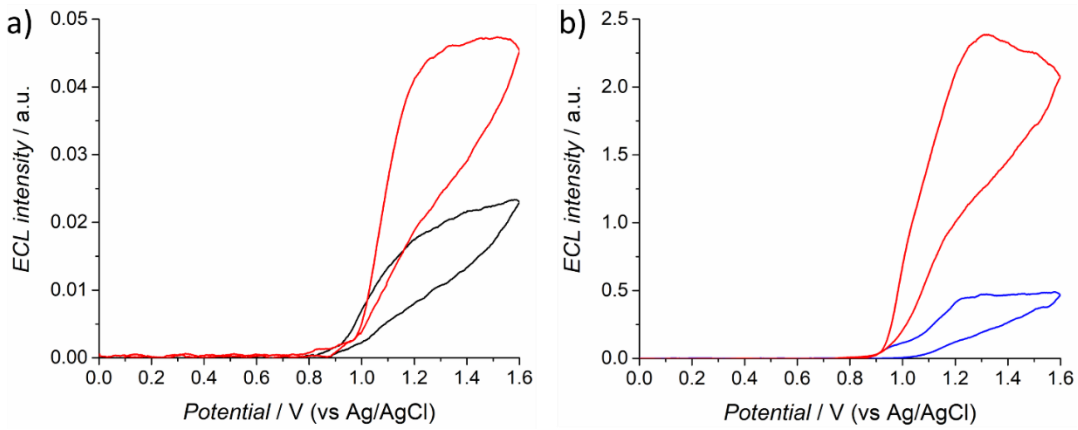

Figure 1.22. a) ECL intensity potential curves in the presence of TPrA 180mM in a 1nM solution of bio-Igepal@RuNp (black line) and of bio-Triton@RuNp (red line). b) ECL intensity potential curves in the presence of TPrA 180mM (red line) or DBAE 30mM (blue line) in a 10nM solution of bio-Triton@RuNp. Cyclic voltammetries with voltage scanned between 0 V and +1.6 V, scan rate 0.1 V s^{-1}. Glassy Carbon electrode referred to Ag/AgCl. Pt spiral as counter electrode. PMT bias 750V.

According to previous results,[61] the higher ζ-potential of bio-Igepal@RuNP is disadvantageous to the ECL emission, because of the electrostatic repulsion towards the approaching co-reactant radical cationic species. Solving this problem, not only relatively more hydrophilic co-reactants such as 2-(dibutylamino)ethanol as in our previous studies, but also TPrA may achieve high signal intensity (figure 1.22b).[60,61] In conclusion, through the new synthetic strategy it was possible to obtain NPs whose parameters (e.g., ζ-potentials, hydrophobicity, dye distribution and NP size) are suitable for an efficient ECL generation with TPrA.

sample	ECL intensity maximum	N° dye/NP	Relative ECL intensity	ECL intensity normalized for N° dye/NP	Relative ECL normalized intensity
bio-Triton@RuNP	0.047	4800	2	9.7E-06	1.4
bio-Igepal@RuNP	0.023	3200	1	7.1E-06	1

Table 1.2. Maximum ECL intensities obtained in cyclic voltammetry and performed on bio-Igepal@RuNp and on bio-Triton@RuNp (see figure 1.22a) and ECL intensity normalized for the number of dyes for NP.

In view of their promising performance, such DDSNPs were applied in a commercial ECL bead-based immunoassay showing results beyond any expectation, thus opening the way to the possibility of a real and very efficient application of NPs for more sensitive biosensor development for clinical analysis and early disease diagnosis.

4. CONCLUSIONS

In conclusion, both types of nanomaterials investigated in this chapter showed promising results for increasing the sensitivity of technique and the consequent application in different analytical and clinical fields.

B-NCDs were considered among the most promising and most efficient ECL luminophores if compared to the standard $[Ru(bpy)_3]^{2+}$ and to state-of-the-art ECL dyes shown in the two tables below (tables 1.3 and 1.4). ECL efficiency was calculated taking into account the ECL intensities reported in figure 1.23 and compared to the $[Ru(bpy)_3]^{2+}$/TPrA system taken as standard (see appendix for detailed calculations). Aggregation or quenching factors were eventually and automatically included in the different ECL emission obtained using different samples and they weren't considered as separate elements in the equation for calculating the ECL efficiency. A possible approach for enhancing the performance might be obtained by the inclusion of different dyes such as polyaromatic compounds (for example spirofluorene) that have an ECL efficiency higher than BODIPY. Those systems are currently under investigation in our laboratory. The stability of the material, the toxicity and the performances should be tested before being sure of the material success.

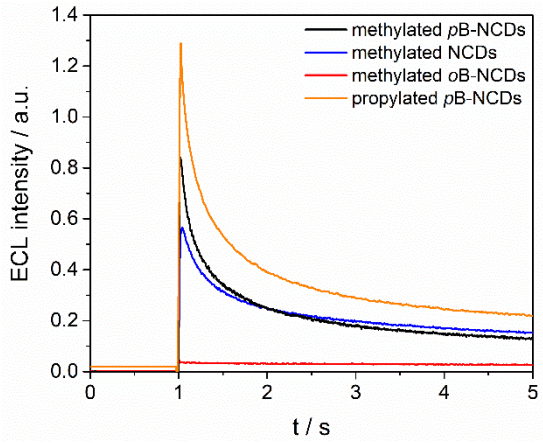

Figure 1.23. ECL vs time curves of methylated *p*B-NCDs (black line), methylated NCDs (blue line), methylated *o*B-NCDs (red line) and propylated *p*B-NCDs (orange line). Experiments performed with TPrA 180 mM as coreactant in PB 0.2 M as supporting electrolyte. Potential applied of 1.6 V. GC electrode potential referred to Ag/AgCl at room temperature. Platinum wire as counter electrode. PMT bias 750V.

DDSNPs reached a very efficient behaviour with high signal intensity also using TPrA as coreactant. This is a very successful results that will be very useful for application of $Ru(bpy)_3]^{2+}$-doped silica

NPs in commercial ECL-bead based immunoassay, obtaining very promising performances explained in the next chapter.

The combination between nanotechnologies and ECL for increasing the technique sensitivity acting on the luminophore was successful: both the strategy of increasing the ECL luminophore efficiency (B-NCDs) and concentrate a large number of luminophores $(Ru(bpy)_3]^{2+}$-doped silica NPs) are very promising for future applications in clinical monitoring and early disease diagnosis. In the next chapter we will describe a strategy for the ECL enhancing based on the choice of coreactants and also the combination of ECL with microscopy.

Table 1.3. Comparison between the relative ECL efficiency for oxidative-reduction mechanism (Φ_{ECL} see experimental methods for the details) performances of the NCDs with other recently reported, highly active ECL dye.

ECL emitters	Co-reactant	Solvent	Φ_{ECL} (%)[b]	Ref.
$Ru(bpy)_3^{2+}$	TPrA	PB[a]	100	-
$[(bpy)_2Ru]_2(bphb)^{2+}$	TPrA	PB[a]	5.8	(Richter et al., *Anal. Chem.* 1998)[96]
Copper metal cluster	TPrA	CH_2Cl_2	15	(Han et al., *J. Electroanal. Chem.*, 2017)[97]
$[((phen)_2Ru(dpp))_2RhCl_2]^{5+}$	TPrA	Tris buffer	1.4	(Wang et al., *Anal. Chem.* 2009)[98]
Spirofluorene Dye	TPrA	CH_2Cl_2	454	(Li et al., *Chem. Eur. J.*, 2016)[99]
Boron-dipyrromethene (BODIPY)	TPrA	CH_3CN	44	(P. Chauhan et al. *J. Electroanal. Chem.* 2016)[100]
Methylated *p*B-NCDs	TPrA	PB[a]	13	This work
Propylated *p*B-NCDs	TPrA	PB[a]	44	This work

a) PB is phosphate buffer; b) the ECL efficiency was calculated by comparison with $[Ru(bpy)_3]^{2+}$as reference (Φ_{ECL}= 100), see figure 4.2 in the appendix.

Table 1.4. Comparison between the ECL efficiency performances, obtained in annihilation (Φ_{ECL}), of the BODIPY dye with other recently reported.

ECL emitters	Φ_{ECL} (%)[b]	Ref.
$Ru(bpy)_3^{2+}$	5	(Rubinstein, L. et al., J. *Am. Chem. Soc.* 1981)[101]
Boron-dipyrromethene (BODIPY)	16	(P. Chauhan et al., *J. of Electroanal. Chem.*, 2016)[100]
BOPEG2	20	(A. B. Nepomnyashchii et al. *J. Phys. Chem. C*, 2013)[102]
BODIPY1	21	(A. B. Nepomnyashchii et al. *Acc. Chem. Res.*, 2012)[69]
BODIPY2	0.6	(A. B. Nepomnyashchii et al. *Acc. Chem. Res*, 2012)[69]
BODIPY3	0.8	(A. B. Nepomnyashchii et al. *Acc. Chem. Res*, 2012)[69]
BODIPY4	0.5	(A. B. Nepomnyashchii et al. *Acc. Chem. Res*, 2012)[69]
BODIPY5	15	(A. B. Nepomnyashchii et al. *Acc. Chem. Res*, 2012)[69]

a) the ECL efficiency in annihilation was calculated by comparison with $[Ru(bpy)_3]^{2+}$ as reference (Φ_{ECL} = 5%).

REFERENCES

1. Fiorani, A. *et al.* Advanced carbon nanomaterials for electrochemiluminescent biosensor applications. *Curr. Opin. Electrochem.* **16**, 66–74 (2019).
2. Singh, K. R., Solanki, P. R., Malhotra, B. D., Pandey, A. C. & Singh, R. P. Introduction to Nanomaterials. An overview toward broad-spectrum applications. in *Nanomaterials in Bionanotechnology: Fundamentals and Applications* 1–21 (2022).
3. Zhang, S., Geryak, R., Geldmeier, J., Kim, S. & Tsukruk, V. V. Synthesis, Assembly, and Applications of Hybrid Nanostructures for Biosensing. *Chem. Rev.* **117**, 12942–13038 (2017).
4. Hildebrandt, N. *et al.* Energy Transfer with Semiconductor Quantum Dot Bioconjugates: A Versatile Platform for Biosensing, Energy Harvesting, and Other Developing Applications. *Chem. Rev.* **117**, 536–711 (2017).
5. Yuan, T. *et al.* Carbon quantum dots: an emerging material for optoelectronic applications. *J. Mater. Chem. C* **7**, 6820–6835 (2019).
6. Garnett, E., Mai, L. & Yang, P. Introduction: 1D Nanomaterials/Nanowires. *Chem. Rev.* **119**, 8955–8957 (2019).
7. Yin, J. *et al.* Large scale assembly of nanomaterials: mechanisms and applications. *Nanoscale* **12**, 17571–17589 (2020).
8. Yao, J., Li, L., Li, P. & Yang, M. Quantum dots: from fluorescence to chemiluminescence, bioluminescence, electrochemiluminescence, and electrochemistry. *Nanoscale* **9**, 13364–13383 (2017).
9. Yang, E., Zhang, Y. & Shen, Y. Quantum dots for electrochemiluminescence bioanalysis - A review. *Anal. Chim. Acta* **1209**, 339140 (2022).
10. Cao, Z., Shu, Y., Qin, H., Su, B. & Peng, X. Quantum Dots with Highly Efficient, Stable, and Multicolor Electrochemiluminescence. *ACS Cent. Sci.* **6**, 1129–1137 (2020).
11. Tuerhong, M., XU, Y. & YIN, X.-B. Review on Carbon Dots and Their Applications. *Chinese J. Anal. Chem.* **45**, 139–150 (2017).
12. Algar, W. R., Susumu, K., Delehanty, J. B. & Medintz, I. L. Semiconductor Quantum Dots in Bioanalysis: Crossing the Valley of Death. *Anal. Chem.* **83**, 8826–8837 (2011).
13. Baker, S. N. & Baker, G. A. Luminescent Carbon Nanodots: Emergent Nanolights. *Angew. Chemie Int. Ed.* **49**, 6726–6744 (2010).
14. Arcudi, F., Đorđević, L. & Prato, M. Design, Synthesis, and Functionalization Strategies of Tailored Carbon Nanodots. *Acc. Chem. Res.* **52**, 2070–2079 (2019).
15. Tian, X. & Yin, X. Carbon Dots, Unconventional Preparation Strategies, and Applications Beyond Photoluminescence. *Small* **15**, 1901803 (2019).
16. Nekoueian, K. *et al.* Carbon-based quantum particles: an electroanalytical and biomedical perspective. *Chem. Soc. Rev.* **48**, 4281–4316 (2019).
17. Li, Z., Wang, L., Li, Y., Feng, Y. & Feng, W. Frontiers in carbon dots: design, properties and applications. *Mater. Chem. Front.* **3**, 2571–2601 (2019).
18. Kang, Z. & Lee, S.-T. Carbon dots: advances in nanocarbon applications. *Nanoscale* **11**, 19214–19224 (2019).
19. Dhenadhayalan, N., Lin, K. & Saleh, T. A. Recent Advances in Functionalized Carbon Dots toward the Design of Efficient Materials for Sensing and Catalysis Applications. *Small* **16**, 1905767 (2020).
20. Chen, Y., Cao, Y., Ma, C. & Zhu, J. J. Carbon-based dots for electrochemiluminescence sensing. *Mater. Chem. Front.* **4**, 369–385 (2020).
21. El-Shabasy, R. M. *et al.* Recent Developments in Carbon Quantum Dots: Properties, Fabrication Techniques, and Bio-Applications. *Processes* **9**, 388 (2021).

22. Kesarkar, S. *et al.* Dye-doped nanomaterials: Strategic design and role in electrochemiluminescence. *Curr. Opin. Electrochem.* **7**, 130–137 (2018).
23. Miao, W., Choi, J.-P. & Bard, A. J. Electrogenerated Chemiluminescence 69: The Tris(2,2'-bipyridine)ruthenium(II), (Ru(bpy) 3 2+)/Tri- n -propylamine (TPrA) System RevisitedA New Route Involving TPrA •+ Cation Radicals. *J. Am. Chem. Soc.* **124**, 14478–14485 (2002).
24. Leland, J. K. & Powell, M. J. Electrogenerated Chemiluminescence: An Oxidative-Reduction Type ECL Reaction Sequence Using Tripropyl Amine. *J. Electrochem. Soc.* **137**, 3127–3131 (1990).
25. Zu, Y. & Bard, A. J. Electrogenerated Chemiluminescence. 66. The Role of Direct Coreactant Oxidation in the Ruthenium Tris(2,2')bipyridyl/Tripropylamine System and the Effect of Halide Ions on the Emission Intensity. *Anal. Chem.* **72**, 3223–3232 (2000).
26. Miao, W. Electrogenerated Chemiluminescence and Its Biorelated Applications. *Chem. Rev.* **108**, 2506–2553 (2008).
27. Ma, C., Cao, Y., Gou, X. & Zhu, J.-J. Recent Progress in Electrochemiluminescence Sensing and Imaging. *Anal. Chem.* **92**, 431–454 (2020).
28. Kerr, E., Doeven, E. H., Wilson, D. J. D., Hogan, C. F. & Francis, P. S. Considering the chemical energy requirements of the tri-n-propylamine co-reactant pathways for the judicious design of new electrogenerated chemiluminescence detection systems. *Analyst* **141**, 62–69 (2016).
29. Theakstone, A. G., Doeven, E. H., Conlan, X. A., Dennany, L. & Francis, P. S. 'Cathodic' electrochemiluminescence of [Ru(bpy) 3] 2+ and tri- n -propylamine confirmed as emission at the counter electrode. *Chem. Commun.* **55**, 7081–7084 (2019).
30. Chen, L. *et al.* A conceptual framework for the development of iridium(<scp>iii</scp>) complex-based electrogenerated chemiluminescence labels. *Chem. Sci.* **10**, 8654–8667 (2019).
31. Bertoncello, P. & Ugo, P. Recent Advances in Electrochemiluminescence with Quantum Dots and Arrays of Nanoelectrodes. *ChemElectroChem* **4**, 1663–1676 (2017).
32. Chen, Y., Gou, X., Ma, C., Jiang, D. & Zhu, J.-J. A Synergistic Coreactant for Single-Cell Electrochemiluminescence Imaging: Guanine-Rich ssDNA-Loaded High-Index Faceted Gold Nanoflowers. *Anal. Chem.* **93**, 7682–7689 (2021).
33. Carrara, S., Arcudi, F., Prato, M. & De Cola, L. Amine-Rich Nitrogen-Doped Carbon Nanodots as a Platform for Self-Enhancing Electrochemiluminescence. *Angew. Chemie Int. Ed.* **56**, 4757–4761 (2017).
34. Valenti, G., Fiorani, A., Li, H., Sojic, N. & Paolucci, F. Essential Role of Electrode Materials in Electrochemiluminescence Applications. *ChemElectroChem* **3**, 1990–1997 (2016).
35. Valenti, G. *et al.* Electrogenerated chemiluminescence from metal complexes-based nanoparticles for highly sensitive sensors applications. *Coord. Chem. Rev.* **367**, 65–81 (2018).
36. Yu, J. *et al.* Nanoscale 3D Tracking with Conjugated Polymer Nanoparticles. *J. Am. Chem. Soc.* **131**, 18410–18414 (2009).
37. Li, H., Sentic, M., Ravaine, V. & Sojic, N. Antagonistic effects leading to turn-on electrochemiluminescence in thermoresponsive hydrogel films. *Phys. Chem. Chem. Phys.* **18**, 32697–32702 (2016).
38. Li, P. *et al.* A New Polymer Nanoprobe Based on Chemiluminescence Resonance Energy Transfer for Ultrasensitive Imaging of Intrinsic Superoxide Anion in Mice. *J. Am. Chem. Soc.* **138**, 2893–2896 (2016).
39. Li, L.-L. *et al.* A Facile Microwave Avenue to Electrochemiluminescent Two-Color Graphene Quantum Dots. *Adv. Funct. Mater.* **22**, 2971–2979 (2012).
40. Dong, Y., Dai, R., Dong, T., Chi, Y. & Chen, G. Photoluminescence, chemiluminescence and

anodic electrochemiluminescence of hydrazide-modified graphene quantum dots. *Nanoscale* **6**, 11240–11245 (2014).
41. Qin, Y. *et al.* Oxygen Containing Functional Groups Dominate the Electrochemiluminescence of Pristine Carbon Dots. *J. Phys. Chem. C* **121**, 27546–27554 (2017).
42. Wang, X. *et al.* Modulating the electronic structure of a semiconductor to optimize its electrochemiluminescence performance. *Nanoscale Adv.* **1**, 1965–1969 (2019).
43. Bao, L., Liu, C., Zhang, Z.-L. & Pang, D.-W. Photoluminescence-Tunable Carbon Nanodots: Surface-State Energy-Gap Tuning. *Adv. Mater.* **27**, 1663–1667 (2015).
44. Liu, M. L., Chen, B. Bin, Li, C. M. & Huang, C. Z. Carbon dots: synthesis, formation mechanism, fluorescence origin and sensing applications. *Green Chem.* **21**, 449–471 (2019).
45. Tepliakov, N. V. *et al.* sp 2 –sp 3 -Hybridized Atomic Domains Determine Optical Features of Carbon Dots. *ACS Nano* **13**, 10737–10744 (2019).
46. Ding, H., Yu, S.-B., Wei, J.-S. & Xiong, H.-M. Full-Color Light-Emitting Carbon Dots with a Surface-State-Controlled Luminescence Mechanism. *ACS Nano* **10**, 484–491 (2016).
47. Dekaliuk, M. O., Viagin, O., Malyukin, Y. V & Demchenko, A. P. Fluorescent carbon nanomaterials: "quantum dots" or nanoclusters? *Phys. Chem. Chem. Phys.* **16**, 16075–16084 (2014).
48. Nguyen, H. A., Srivastava, I., Pan, D. & Gruebele, M. Unraveling the Fluorescence Mechanism of Carbon Dots with Sub -Single-Particle Resolution. *ACS Nano* **14**, 6127–6137 (2020).
49. Zhu, S. *et al.* The photoluminescence mechanism in carbon dots (graphene quantum dots, carbon nanodots, and polymer dots): current state and future perspective. *Nano Res.* **8**, 355–381 (2015).
50. Ding, Z. *et al.* Electrochemistry and Electrogenerated Chemiluminescence from Silicon Nanocrystal Quantum Dots. *Science (80-.).* **296**, 1293–1297 (2002).
51. Song, Y. *et al.* Investigation from chemical structure to photoluminescent mechanism: a type of carbon dots from the pyrolysis of citric acid and an amine. *J. Mater. Chem. C* **3**, 5976–5984 (2015).
52. Luo, H. *et al.* Manipulating the Optical Properties of Carbon Dots by Fine-Tuning their Structural Features. *ChemSusChem* **12**, 4432–4441 (2019).
53. Zhang, R., Adsetts, J. R., Nie, Y., Sun, X. & Ding, Z. Electrochemiluminescence of nitrogen- and sulfur-doped graphene quantum dots. *Carbon N. Y.* **129**, 45–53 (2018).
54. Wang, M. *et al.* Effects of C-Related Dangling Bonds and Functional Groups on the Fluorescent and Electrochemiluminescent Properties of Carbon-Based Dots. *Chem. - A Eur. J.* **24**, 4250–4254 (2018).
55. Chen, Y. *et al.* Electrochemiluminescence of water-dispersed nitrogen and sulfur doped carbon dots synthesized from amino acids. *Analyst* **146**, 5287–5293 (2021).
56. Ye, J. *et al.* Dual-Wavelength Ratiometric Electrochemiluminescence Immunosensor for Cardiac Troponin I Detection. *Anal. Chem.* **91**, 1524–1531 (2019).
57. Sojic, N. *Analytical Electrogenerated Chemiluminescence*. (Royal Society of Chemistry, 2020). doi:10.1039/9781788015776
58. Zhang, S. & Liu, Y. Recent Progress of Novel Electrochemiluminescence Nanoprobes and Their Analytical Applications. *Front. Chem.* **8**, 1–7 (2021).
59. Kesarkar, S. *et al.* Iridium(III)-Doped Core-Shell Silica Nanoparticles: Near-IR Electrogenerated Chemiluminescence in Water. *ChemElectroChem* **4**, 1690–1696 (2017).
60. Valenti, G. *et al.* Variable Doping Induces Mechanism Swapping in Electrogenerated Chemiluminescence of Ru(bpy) 3 2+ Core–Shell Silica Nanoparticles. *J. Am. Chem. Soc.* **138**,

15935–15942 (2016).
61. Kesarkar, S. *et al.* Neutral Dye-Doped Silica Nanoparticles for Electrogenerated Chemiluminescence Signal Amplification. *J. Phys. Chem. C* **123**, 5686–5691 (2019).
62. Imai, K. *et al.* Numerical Simulation of Doped Silica Nanoparticle Electrochemiluminescence. *J. Phys. Chem. C* **119**, 26111–26118 (2015).
63. Arcudi, F. *et al.* Lighting up the Electrochemiluminescence of Carbon Dots through Pre- and Post-Synthetic Design. *Adv. Sci.* **8**, 2100125 (2021).
64. Zanut, A. *et al.* Dye-Doped Silica Nanoparticles for Enhanced ECL-Based Immunoassay Analytical Performance. *Angew. Chemie Int. Ed.* **59**, anie.202009544 (2020).
65. Arcudi, F., Đorđević, L. & Prato, M. Synthesis, Separation, and Characterization of Small and Highly Fluorescent Nitrogen-Doped Carbon NanoDots. *Angew. Chemie Int. Ed.* **55**, 2107–2112 (2016).
66. Đorđević, L., Arcudi, F. & Prato, M. Preparation, functionalization and characterization of engineered carbon nanodots. *Nat. Protoc.* **14**, 2931–2953 (2019).
67. Rizzo, C. *et al.* Nitrogen-Doped Carbon Nanodots-Ionogels: Preparation, Characterization, and Radical Scavenging Activity. *ACS Nano* **12**, 1296–1305 (2018).
68. Ulrich, G., Ziessel, R. & Harriman, A. The Chemistry of Fluorescent Bodipy Dyes: Versatility Unsurpassed. *Angew. Chemie Int. Ed.* **47**, 1184–1201 (2008).
69. Nepomnyashchii, A. B. & Bard, A. J. Electrochemistry and Electrogenerated Chemiluminescence of BODIPY Dyes. *Acc. Chem. Res.* **45**, 1844–1853 (2012).
70. Hesari, M., Lu, J., Wang, S. & Ding, Z. Efficient electrochemiluminescence of a boron-dipyrromethene (BODIPY) dye. *Chem. Commun.* **51**, 1081–1084 (2015).
71. Rosenthal, J., Nepomnyashchii, A. B., Kozhukh, J., Bard, A. J. & Lippard, S. J. Synthesis, Photophysics, Electrochemistry, and Electrogenerated Chemiluminescence of a Homologous Set of BODIPY-Appended Bipyridine Derivatives. *J. Phys. Chem. C* **115**, 17993–18001 (2011).
72. Loudet, A. & Burgess, K. BODIPY Dyes and Their Derivatives: Syntheses and Spectroscopic Properties. *Chem. Rev.* **107**, 4891–4932 (2007).
73. Nepomnyashchii, A. B., Cho, S., Rossky, P. J. & Bard, A. J. Dependence of Electrochemical and Electrogenerated Chemiluminescence Properties on the Structure of BODIPY Dyes. Unusually Large Separation between Sequential Electron Transfers. *J. Am. Chem. Soc.* **132**, 17550–17559 (2010).
74. Rosso, C., Filippini, G. & Prato, M. Carbon Dots as Nano-Organocatalysts for Synthetic Applications. *ACS Catal.* **10**, 8090–8105 (2020).
75. Zuo, P., Lu, X., Sun, Z., Guo, Y. & He, H. A review on syntheses, properties, characterization and bioanalytical applications of fluorescent carbon dots. *Microchim. Acta* **183**, 519–542 (2016).
76. Tomaszewska, E. *et al.* Detection Limits of DLS and UV-Vis Spectroscopy in Characterization of Polydisperse Nanoparticles Colloids. *J. Nanomater.* **2013**, 1–10 (2013).
77. Würth, C., Grabolle, M., Pauli, J., Spieles, M. & Resch-Genger, U. Relative and absolute determination of fluorescence quantum yields of transparent samples. *Nat. Protoc.* **8**, 1535–1550 (2013).
78. Krumova, K. & Cosa, G. Bodipy Dyes with Tunable Redox Potentials and Functional Groups for Further Tethering: Preparation, Electrochemical, and Spectroscopic Characterization. *J. Am. Chem. Soc.* **132**, 17560–17569 (2010).
79. Zhao, W., Chen, H.-Y. & Xu, J.-J. Electrogenerated chemiluminescence detection of single entities. *Chem. Sci.* **12**, 5720–5736 (2021).

80. Zu, Y. & Bard, A. J. Electrogenerated Chemiluminescence. 67. Dependence of Light Emission of the Tris(2,2′)bipyridylruthenium(II)/Tripropylamine System on Electrode Surface Hydrophobicity. *Anal. Chem.* **73**, 3960–3964 (2001).
81. Han, D., Goudeau, B., Jiang, D., Fang, D. & Sojic, N. Electrochemiluminescence Microscopy of Cells: Essential Role of Surface Regeneration. *Anal. Chem.* **93**, 1652–1657 (2021).
82. Adenier, A., Chehimi, M. M., Gallardo, I., Pinson, J. & Vilà, N. Electrochemical Oxidation of Aliphatic Amines and Their Attachment to Carbon and Metal Surfaces. *Langmuir* **20**, 8243–8253 (2004).
83. Bardini, L. *et al.* Electrochemical Polymerization of Allylamine Copolymers. *Langmuir* **29**, 3791–3796 (2013).
84. Yuan, Y., Han, S., Hu, L., Parveen, S. & Xu, G. Coreactants of tris(2,2-bipyridyl)ruthenium(II) Electrogenerated Chemiluminescence. *Electrochim. Acta* **82**, 484–492 (2012).
85. Zanut, A. *et al.* Insights into the mechanism of coreactant electrochemiluminescence facilitating enhanced bioanalytical performance. *Nat. Commun.* **11**, 2668 (2020).
86. Forster, R. J., Bertoncello, P. & Keyes, T. E. Electrogenerated Chemiluminescence. *Annu. Rev. Anal. Chem.* **2**, 359–385 (2009).
87. Irkham *et al.* Electrogenerated Chemiluminescence by in Situ Production of Coreactant Hydrogen Peroxide in Carbonate Aqueous Solution at a Boron-Doped Diamond Electrode. *J. Am. Chem. Soc.* **142**, 1518–1525 (2020).
88. Chinnadayyala, S. R., Park, J., Thi, H., Le, N. & Santhosh, M. Recent advances in micro fl uidic paper-based electrochemiluminescence analytical devices for point-of-care testing applications. *Biosens. Bioelectron.* **126**, 68–81 (2019).
89. Roche Diagnostic corporation. (2018). Available at: www.roche.com.
90. The Meso Scale Discovery. (2018). Available at: www.mesoscale.com/en/technical_resources/our_technology/multi-array.
91. Lora, B. & Jai-Pil, C. Electrogenerated Chemiluminescence of Semiconductor Nanoparticles and Their Applications in Biosensors. *ChemElectroChem* **4**, 1573–1586 (2017).
92. Montalti, M., Prodi, L., Rampazzo, E. & Zaccheroni, N. Dye-doped silica nanoparticles as luminescent organized systems for nanomedicine. *Chem. Soc. Rev.* **43**, 4243–4268 (2014).
93. Arap, R. Pasqualini, M. Montalti, L. Petrizza, L. Prodi, E. Rampazzo, N. Zaccheroni, S. Marchiò, W. Luminescent Silica Nanoparticles for cancer diagnosis. *Curr. Med. Chem.* **20**, 2195–2211 (2013).
94. Zanarini, S. *et al.* Synthesis and Electrochemiluminescence of a Ru(bpy) 3 -Labeled Coupling Adduct Produced on a Self-Assembled Monolayer. *J. Phys. Chem. C* **112**, 2949–2957 (2008).
95. Della Ciana, L., Hamachi, I. & Meyer, T. J. Synthesis of side-chain derivatives of 2,2′-bipyridine. *J. Org. Chem.* **54**, 1731–1735 (1989).
96. Richter, M. M., Bard, A. J., Kim, W. & Schmehl, R. H. Electrogenerated Chemiluminescence. 62. Enhanced ECL in Bimetallic Assemblies with Ligands That Bridge Isolated Chromophores. *Anal. Chem.* **70**, 310–318 (1998).
97. Han, A. *et al.* Electrochemistry and electrochemiluminescence of copper metal cluster. *J. Electroanal. Chem.* **795**, 116–122 (2017).
98. Wang, S. *et al.* Electrochemical and Electrogenerated Chemiluminescent Studies of a Trinuclear Complex, [((phen) 2 Ru(dpp)) 2 RhCl 2] 5+ , and Its Interactions with Calf Thymus DNA. *Anal. Chem.* **81**, 4068–4075 (2009).
99. Li, H., Daniel, J., Verlhac, J.-B., Blanchard-Desce, M. & Sojic, N. Bright Electrogenerated Chemiluminescence of a Bis-Donor Quadrupolar Spirofluorene Dye and Its Nanoparticles.

Chem. - A Eur. J. **22**, 12702–12714 (2016).
100. Chauhan, P., Chu, K., Yan, N. & Ding, Z. Comparison study of electrochemiluminescence of boron-dipyrromethene (BODIPY) dyes in aprotic and aqueous solutions. *J. Electroanal. Chem.* **781**, 181–189 (2016).
101. Rubinstein, I. & Bard, A. J. Organic acids. *Biotechnol. Bioeng.* **7**, 70–72 (1965).
102. Nepomnyashchii, A. B., Pistner, A. J., Bard, A. J. & Rosenthal, J. Synthesis, photophysics, electrochemistry and electrogenerated chemiluminescence of PEG-modified BODIPY dyes in organic and aqueous solutions. *J. Phys. Chem. C* **117**, 5599–5609 (2013).

CHAPTER II

INSIGHTS INTO ECL MICROSCOPY: MECHANISMS AND BEAD-BASED IMMUNOASSAY APPLICATION IMPROVEMENTS

In collaboration with

Prof. Luca Prodi research group at the University of Bologna

Prof. Stefania Rapino research group at the University of Bologna

Prof. Fabrizia Negri research group at the University of Bologna

Dr. Antonio Barbon of the University of Padua

Roche Diagnostics and Hitachi High-Technology

1. INTRODUCTION

In the last years, ECL was implemented as a powerful imaging technique exploiting its simplified optical setup.[1,2] It implemented the advantages of the technique with higher spatial and temporal resolution and the possibility to directly visualize electrochemical micro- and nano-objects and entities. Moreover, it brought important insights in the ECL mechanism generation, introducing advanced optical readout for imaging applications.

In 1987 Engstrom *et al*.[3,4] and then more intensely since 2003 Amatore and Sojic *et al*.,[5,6] pave the way to ECL imaging as an emerging electrochemical transduction technique, exploiting the electrochemical sensitivity and the spatial resolution of an optical readout. However, some problems related to the weak luminophore luminescence and consequent acquisition of highly resolved images were present. Recently, many technical problems were solved, for example related to numerical aperture of objective, allowing to reach a lot of improvements in ECL imaging and to exploit its advantages for application in many fields, such as bioanalysis.

An ECL microscopy (ECLM) setup is not yet commercial, but it is simple and includes a bright field microscope, an electrochemistry module (including an electrochemical cell and a potential generator) and a charge coupled device (CCD) or spectrometer acquiring the image or spectrum. For a high spatial resolution image, an objective with a high numerical aperture value and an electron multiplying CCD (EMCCD) are needed to increase the collection efficiency (see figures 2.1 and 2.2b and detailed information in the appendix).[7] To minimize the luminescence loss during the transmission, the distance between the sample and CCD should be as short as possible. Moreover, the mirrors or filters in the transmission pathway are recommended to be removed except for special applications.

ECLM possesses all the advantages of the electrochemical sensitivity together with the spatial resolution provided by its optical readout. It has been successfully used i) to quantify and map species, like cells, proteins, DNA, several biomarkers and nanoobjects, over the electrode surface, ii) to visualize electrochemical and/or biological events at the regions of interest, or iii) characterize single cells behaviour and electrochemical features of single particles (figure 2.1).[8–13] The electrochemical signals can be spatially and temporally resolved and well separated from surrounding information, allowing the development of advanced biosensors for multiplex bio-assay.[10,14]

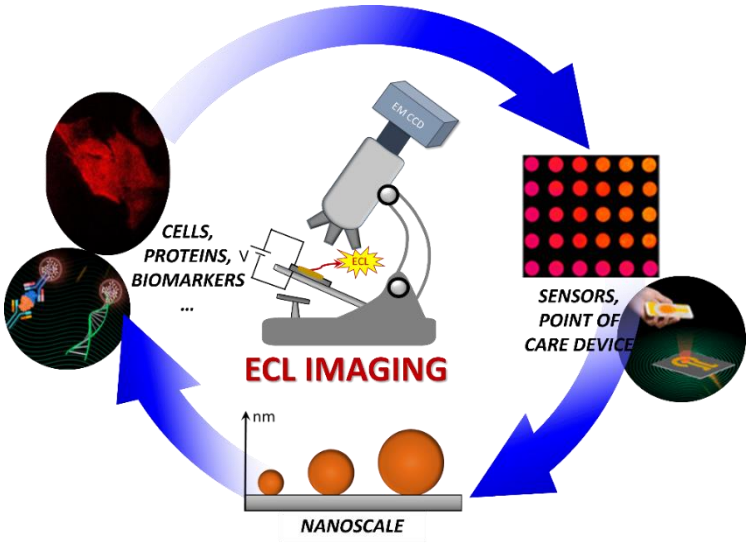

Figure 2.1. ECL imaging exemplified apparatus and different fields of applications. Adapted with the permission of [15]. Adapted with permission from [16]. Copyright 2020 American Chemical Society.

In the recent years, a significant number of works has been carried out to create electrode architectures and to design new ECL probes and find more efficient coreactants with the aim to improve strategies for detection of low concentrated analytes as well as the quality of ECL image, decreasing the signal-to-noise ratio.[15,17–19] The investigation of the ECL generation mechanism through ECLM played a pivotal role in this efficient calibration of electrode, luminophore and coreactant features.[20] Biocompatible methods and coreactants that enable to work in aqueous solution are fundamental for turning ECL microscopy into a more efficient analytical tool. The homogeneous and heterogeneous coreactant mechanisms are mainly involved in ECL imaging emission and, in the last years, the attention was focused on visualization of objects, cells and subcellular components at the electrode surface.[21]

1.1 ECL microscopy and insights into the mechanisms[20]

The ECL direct oxidative mechanism (homogeneous) is the first, most intuitive and easily applicable mechanism discovered in the field of aqueous ECL involving a coreactant.[22,23] As anticipated, the deep understanding of this apparently simple ECL generation mechanism allowed the discovery of new strategies and new materials[24,25] and some very innovative applications, mainly in the bioanalytical field[9,11] as well as in the wider field of sensors and the nano-world.[26] In particular, the combination with microscopy further enlightened ECL generation mechanism and gave a great boost to the use of ECL for more sensitive applications.[15] Although very interesting qualitative screening of drugs, based on colour and mechanism of emission, can be performed in organic

solvents,[27] the applications in aqueous solution are more interesting for environmental and medical applications, also in the commercial field.[28]

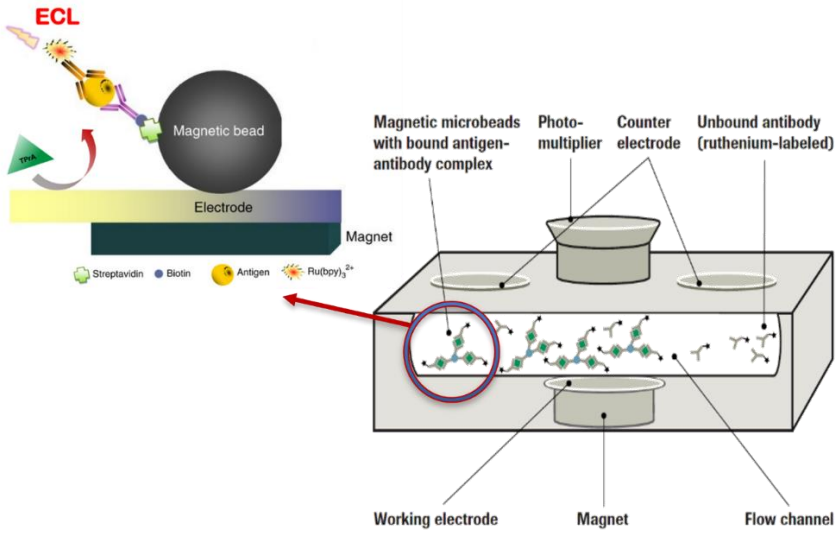

Figure 2.2. Schematic representation of Roche commercial device that exploits ECL for detection of proteins, biomarkers, enzimes, etc for disease diagnosis through Elecsys® assays. At the top of the image is present the usual system formed by magnetic beads where the formed immunoassay is labelled with dye responsible of ECL emission after potential application and reaction with oxidized species of TPrA coreactant (see paragraph 1.2 for more details).

ECL is essentially a surface confined technique with high spatial and temporal resolution where the roles of coreactant and diffusing luminophore are fundamental for mechanistic insights and where the ECL emitting layer is usually mostly confined within the first 3 μm from the electrode (figure 2.2 and 2.4c).[29] Lifetimes of coreactant radical cation and luminophore in their oxidized form are the main rate-limiting steps in the ECL signal generation. Analysing their behaviour in the reduced volume of a nanochannel device,[30] a diffusion distance of $Ru[(bpy)_3]^{2+*} < 1$ μm was observed due to the limited lifetime of the TPrA radical cation ($TPrA^{\bullet+}$) before deprotonation, which has a decay rate of 3500 s^{-1}.[31–33] The ECL emission layer thickness (TEL) and intensity are important parameters for ECL sensitivity modulation and they can be affected by several factors and experimental conditions as i) the electrode material,[17] ii) the coreactant,[34,35] iii) the applied voltage, and iv) the acquisition time.[36] A thin TEL allows the visualization of nanometric objects confined on the electrode with high throughput, while, when thicker, it may improve the ECL signal intensity thus entirely visualizing micrometric objects.

Confined geometries, like ultra-high-density gold microwell,[37] microtube,[38] and ensemble of microtube electrodes[39], enhance and restrict the ECL emission region that can be easily spatially resolved and largely used for the investigation of direct oxidative mechanistic route: i) at low

$[Ru(bpy)_3]^{2+}$ concentration direct oxidative coreactant mechanism is involved and ECL emission is limited by short TPrA radicals lifetime (thin TEL); ii) at high concentration and increasing the acquisition time, the "catalytic route" mechanism was involved and the diffusion profile of $[Ru(bpy)_3]^{3+}$ is the limiting factor (thicker TEL between 3.1 µm and 4.5 µm).[38] $Ru(bpy)_3^{3+}$ has higher lifetime and can catalyse the oxidation of TPrA farther from the electrode if the acquisition time of CCD camera is high enough to allow $Ru(bpy)_3^{3+}$ diffusion (figure 2.3b). By simply modulating the concentration of oxidized luminophore, the ECL emitting layer can be increased/decreased from few nanometres to several micrometres and is not limited to the first 3 µm,[29,38] allowing to spatially resolve objects at different distances from the electrode (figure 2.3a).

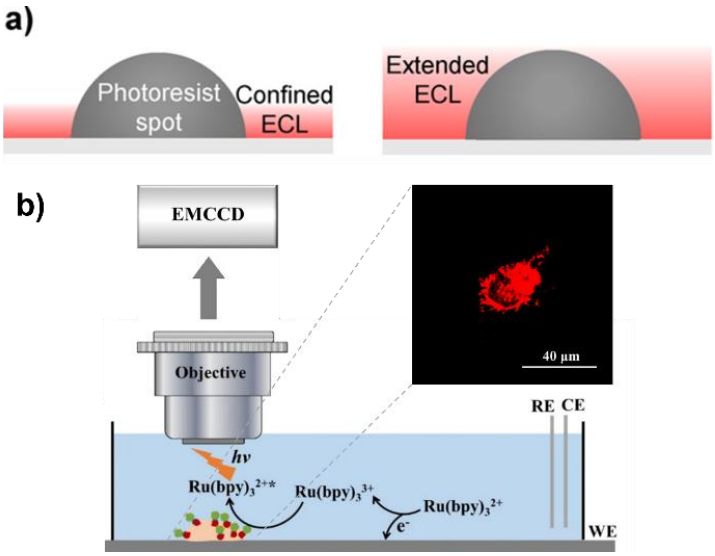

Figure 2.3. a) Modulation of the thickness of ECL layer for imaging an inert photoresist spot through variation of $[Ru(bpy)_3]^{2+}$ concentration. Reprinted with permission from [40]. b) The ECL imaging of the CEA on cell membranes was showed on top-right and was detect with a microscope coupled to an EMCCD camera. Cell visualization depends on the catalytic route of ECL reactions between freely diffusing $[Ru(bpy)_3]^{2+}$ and Hi-AuNF@G-ssDNA-Apt coreactants. Reprinted with permission from [41]. Copyright 2021 American Chemical Society

In fact, the ECLM sensitivity has been successfully exploited for distinguishing the normal cells from the apoptotic ones[42] and for the visualization of cells (figure 2.3b),[41] cell-matrix and cell-cell junctions,[40] intracellular structures, cellular processes and dynamic transport,[43] also thanks to great improvements achieved by the application of this specific homogeneous ECL mechanism called "catalytic route". The freely diffusing $[Ru(bpy)_3]^{2+}$ and, more precisely, the oxidized form $[Ru(bpy)_3]^{3+}$ catalyses the coreactant oxidation showing that ECL generation depends on $[Ru(bpy)_3]^{3+}$ lifetime and its reaction with the coreactant, while coreactant radical cation lifetime does not limit the TEL anymore.[29] Another strategy useful for cells visualization without modifications due to

surface functionalization and/or pre-treatment is the negative ECL or "shadow ECL". This labelling-free approach combined with ECL microscopy was exploited also for the visualization of small subcellular organelles and living mitochondria.[13] The negative ECL was successfully applied also in different fields paving the way to the research of different strategies for investigating the mechanism and exploiting new insights. For example, an additional electric field, produced at the interface between two materials with different dielectric constant, can be useful for the higher performance of the ECL system $[Ru(bpy)_3]^{2+}$/TPrA.[44] Another technique useful for contactless electrochemical and biological analysis with less or even without electric disturbance is the electrochemiluminescence waveguide (ECLW), where a single crystalline molecular wires of tris(1-phenylisoqsuinoline-C2, N)iridium (III) can act as waveguide and ECL emitter.[45] Moreover, the combination of ECL microscopy with super resolution radial fluctuations (SRRF) algorithm, push it to the limits of super-resolution.[14] The combination is possible because photons, in ECL, are generated in a stochastic way and the temporal variation in consecutive ECL frames allow the image reconstruction by SRRF. A high spatiotemporal resolution was reached showing great potential in the field of energy materials, and single-cell imaging and analysis.[14] Also the visualization of the positions of a single photon emitted by single luminophore was possible through a method where the reactivity of coreactant and the dye were highly controlled. The application was very successful and it gave a glimpse of a very bright future for ECL imaging.[10]

Observing all these researches we can deduce that ECLM can exploit the direct oxidative mechanism and the new insights discovered for the enhancement of ECL sensitivity, temporal and spatial resolution and it is important to i) modulate and study the TEL, ii) increase the lifetime of different ECL reagents, and iii) combine ECL with different strategies, materials and geometries. The latter point is very useful for biosensoristic applications because it allows ECLM to reach super-resolution and the efficient visualization of cells, subcellular organelles and cell processes avoiding their damage or death. In fact, many different applications can be possible, like biomarkers detection and the study of the behaviour of various chemical and biological systems, and point-of-care devices can be developed. Examples of applications are the detection of fingerprints and the exogenous substances on fingermarks,[46,47] nitroaromatic compounds precursors of explosives,[48] living cells through negative or direct ECL[49–51], the cell apoptosis process,[52] the study of reaction mechanism and electrocatalytic activity of new micro and nanosized materials,[53–56] and the investigation of boundaries and interfaces that play a key role in many chemical reactions.[57,58]

A useful variation of ECLM that generates ECL without the need of direct contact between the emitting sample and the electrode, prompting bioanalytical applications, is bipolar electrochemistry-ECL (BPE-ECL) microscopy, where an electric field is applied across an electrolyte solution and the control by the field strength and direction is a great advantage as its versatility. [59,60] An example of simple closed bipolar electrodes-based ECL (BPEs-ECL) imaging strategy for visual immunoassay of prostate specific antigen (PSA) in the serum samples and on the surface of individual cancer cell was developed using functional nanoprobes of heterogeneous $Ru(bpy)_3^{2+}$@SiO_2/Au nanoparticles. The synergic amplifying effect and the consequently introduced multiple-assisted ECL signal amplification allow the sensitivity increase of ECL microscopy, and the detection of tumor markers expressed on single-cell and not only in body fluids.[61]

BPE-ECLM helped in the detection and quantification of H_2O_2 or glucose within living cells,[62] in monitoring the evolution of the surface reactivity,[63] and in the creation of a bead-based immunoassay sensors, for example for detecting Salmonella typhimurium.[64]A massive array of carbon bipolar UME is suitable in combination with BPE for ECL microscopy imaging of fast and dynamic redox processes, improving the resolution at single electrode and imaging of variable redox concentrations.[65]

However, in most of the analytical methods the luminophore is constrained in proximity to the electrode because it is attached to a sensing element (i.e. antibody, bead, DNA probe, ecc..) and thus not free to diffuse to the electrode.[33] In these cases, heterogeneous mechanism is responsible for ECL generation and ECL emission is triggered exclusively by the radicals obtained by the anodic oxidation of TPrA. The heterogeneous mechanism was proposed by Bard et al.[23] at the beginning of 21st century and has consistently been investigated since its introduction. The need of labelling sensing elements makes heterogeneous mechanism the most applied in the biological field, opening the research of the most suitable luminophore.[66] Although the great diffusion and advantages such the huge spatio-temporal control, ECL heterogeneous mechanism has some limitations as the short $TPrA^{\bullet+}$ lifetime which is the main responsible of an emission layer confined really close to the electrode surface. In fact, ECL emission layer was higher in the first 500 nm and the total emission layer thickness was around 3 μm, where concentrations of $TPrA^{\bullet+}$ and TPrA radical ($TPrA^{\bullet}$) are the highest (figure 2.4b). These observations were investigated combining top or side view images of beads functionalized with $[Ru(bpy)_3]^{2+}$ and theoretical simulation (figure 2.2, 2.4a and c).[29] The

thickness of emission layer is limited by the short lifetime of $TPrA^{\bullet+}$ (200 μs) and ECL imaging efficiency and resolution strictly depend on it and coreactant diffusion.

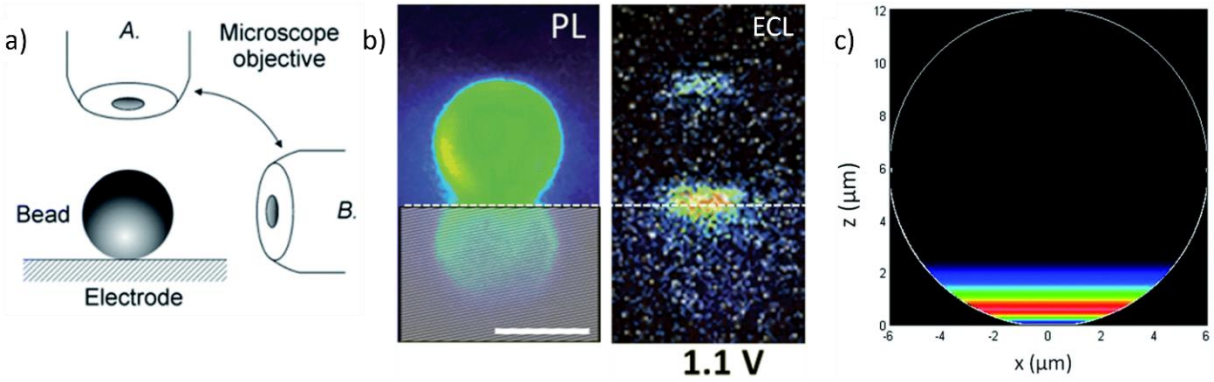

Figure 2.4. a) Schematic representation of top-view (A) and side-view (B) optical configurations possible to image the functionalized bead. b) Side-view images of a 12 μm PS bead labelled with $[Ru(bpy)_3]^{2+}$. The first image is obtained by PL and the following one by ECL applying a potential of 1.1 V vs. Ag/AgCl/ KCl in a PBS solution containing 100 mM TPrA (pH 7.4). The dashed line shows the position of the GC electrode surface (i.e., z=0) and the hatched zone represents the PL reflection on the electrode surface. Exposure time, 6 s. Scale bar: 10 μm. c) Side-view of the simulated distribution of the generated $[Ru(bpy)_3]^{2+*}$ excited state (i.e., ECL intensity) at the surface of a 12 μm bead. The ECL signals are simulated with a value of 2920 s^{-1} for the $TPrA^{\bullet+}$ deprotonation rate constant. Reprinted and adapted with permission from [29]

The role of coreactant diffusion was underlined in the visualisation of tumour cells thicker than 3 μm, where only the ECL emission from cell border can be detected thanks to the use of luminophores functionalised with antibodies specifically recognising antigens overexpressed onto the cell membrane.[67] The central part of the cell is too far from the electrode to be reached by the short-lived coreactant radicals but this limitation can be overcome adopting a permeabilization protocol for cells thus allowing the coreactant to pass through the cell and be oxidized at the electrode to create the luminophore excited state throughout all cell.[68] Those investigations opened the way to the combination between ECL and microscopy for the surface-confined mapping and quantification of different analytes using the heterogeneous mechanism.

Many different strategies can be exploited for improving this promising analytical technique: coreactant radical cations lifetime can be extended/reduced acting on the reaction medium, for example using phosphate buffer solutions with different strengths that can modulate the TPrA deprotonation rate;[69] electrical properties of carbon nanomaterials can be exploited for modulating the ECL emission layer thickness;[19,70] electrochemical treatments on electrode surface can lower the ECL signal decay, increasing the oxidation rate of the coreactant. [17,71,72]

The heterogeneous and homogeneous mechanisms, together with the catalytic one and ECL combined with BPE, were presented as the responsible of ECL generation. Some limitations are present, but they can be overcome using many different strategies, briefly resumed in this paragraph and in table 2.1. Thanks to these improvements, an ever increasing number of different applications are possible. In the biological field heterogeneous mechanism is suitable for real immunoassay direct detection while the homogeneous can be used for revealing unlabelled objects through a negative mode thus lowering the risk of damage. The final goal of the mechanistic study and strategies of improvement is the increase of ECL sensitivity and spatio-temporal resolution (figure 2.5).[20]

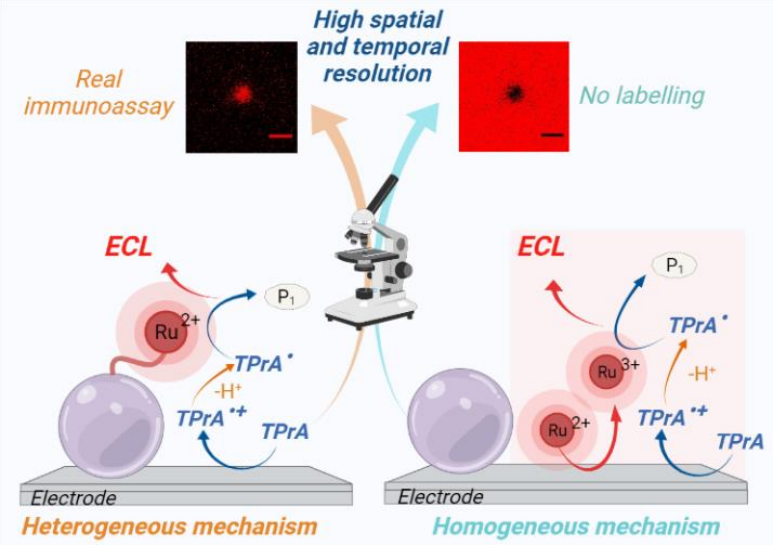

Figure 2.5. Brief summary of the two mechanisms involved in the ECL emission from micro- and nano-metric objects and studied for increasing sensitivity and spatio-temporal resolution of the technique. Reprinted with permission from [20]. For further right and permission please contact American Chemical Society.

Type of mechanism	Main limiting factors	Advantages	Strategies for ECL higher sensitivity
Homogeneous	τ of C radical cation and D ox form	• Absence of labelling	• Confined geometries • Two materials with different dielectric constant in contact • Images elaboration with SRRF algorithm
Catalytic	τ of D ox form	• Absence of labelling • Higher TEL	• Increase D concentration and acquisition time • Different type of C
BPE-ECL	τ of C radical cation and D ox form	• Absence of contact between sample and electrode	• Combination with magnetic fields • Nanostructures
Heterogeneous	τ of C radical cation	• Higher spatial and temporal resolution • Simulation of real immunoassay application	• Different D for optimization of C diffusion towards D • Two different mechanisms at short and long distance • Increase of TEL (chemical lens, conductive materials) • Electrode cathodic treatment

Table 2.1. Summary of all the mechanisms illustrated with relative limiting factors, advantages and strategies for ECLM signal enhancement. C is for coreactant; D is for dye/luminophore. Reprinted with permission from [20]. For further right and permission please contact American Chemical Society.

1.2 Beads-based immunoassay for biomarkers detection

Diagnostic markers, or biomarkers, are biomolecules (e.g., enzymes, proteins, peptides, and hormones) that can be detected, identified and accurately quantify in human body fluids and can precisely predict relevant clinical outcomes or diseases, representing an important help for clinical diagnostic and therapeutic monitoring.[73–76] In particular, research into non-invasive, sophisticated, and sensitive methods and strategies plays a fundamental role in early diseases diagnosis and treatment.[77] The detection of ultralow concentrations of biomarkers in the human body and in complex matrices, such as blood, urine, and tissues is challenging but ECL and ECLM showed really promising performance in this direction.[1,2,78,79]

The ECL immunoassay is one of the principal methods for sensitive and accurate detection of diagnostic markers or biomarkers and it is at the basis of commercial devices like Elecsys® widely used in biological and clinical fields (figure 2.2).[15,31] For the application of clinical tests, combination of ECLM strategies and commercial immunoassays should offer promising applications in high throughput and ultrasensitive analysis.

Today, there are instruments commercially available that combine immunoassay and ECL for quantification of biomarkers or analytes, like drugs, hormones, vitamins, tumor markers, or antibodies, that bind to specific biomolecules as antibodies or specifiers. Immuno-complexes are

formed after incubation of an aliquot of sample with two antibodies or specifiers carrying either an ECL label (usually $[Ru(bpy)_3]^{2+}$) or a biotin label and after the separation of unbound sample and reagent components they are linked to streptavidin coated magnetic microparticles (beads). The magnetic beads are attracted towards the electrode surface by a magnet and ECL label of immuno-complexes emit light after a potential application in a coreactant solution (usually TPrA). The intensity of the emitted light allow to quantify the concentration of $[Ru(bpy)_3]^{2+}$ and consequently of biomarkers (figure 2.6).[80] This beads-based immunoassay system is commercialized as Elecsys® and governed by the ECL heterogeneous mechanism. In fact, $[Ru(bpy)_3]^{2+}$ is attached to the beads and can't be oxidized by the electrode because too far from it. Many others luminophores were tried together with optimized linkers and site-specific conjugation methods.

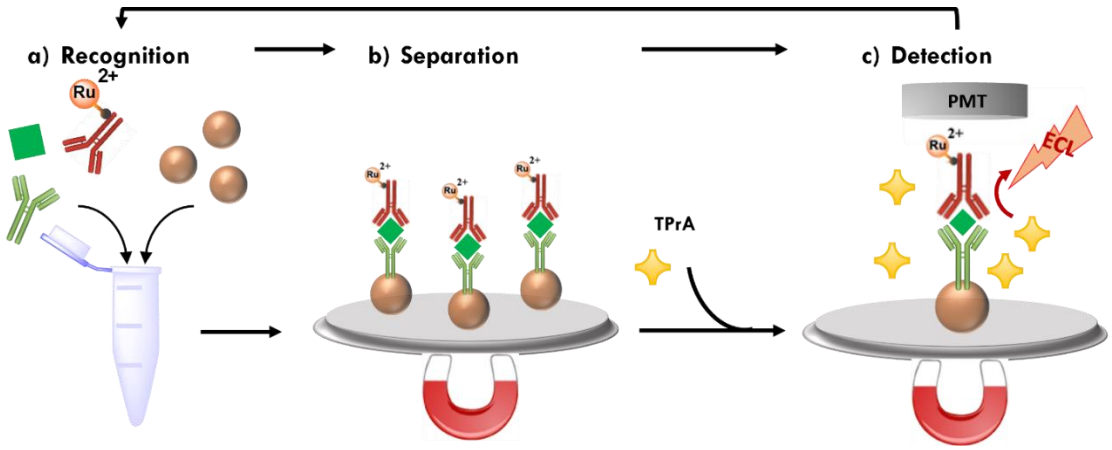

Figure 2.6. Schematic representation of the commercial ECL immunoassay (sandwich assay). a) Recognition: a specific antigen (green square) is mixed together with an antigen-specific biotinylated monoclonal antibody (in green) and an antigen-specific monoclonal antibody labelled with $[Ru(bpy)_3]^{2+}$ (Ru^{2+} in red) to form a sandwich complex which bind to streptavidin-coated microparticles (brown spheres); b) separation: microparticles are magnetically captured onto the surface of the electrode with a magnet and non-specific substances are removed; c) detection: a voltage is applied to the electrode immersed in a coreactant solution (TPrA), inducing ECL emission, which is measured by a photomultiplier tube (PMT). TPrA: tri-*n*-propylamine. Reprinted with permission from [81].

Roche Diagnostics in cooperation with Hitachi High-Technologies produced many different and improved analyzer since 1996: Elecsys® analyzer 2010, **cobas e** 411, MODULAR ANALYTICS E170, **cobas e** 601, e 602, and e 801 (figure 2.7). For automation of Elecsys® immunoassays, the analyzers are equipped with a sampling area, a reagent area, a mixer to homogenize the magnetic beads, sample and reagent pipetters, an incubator, AssayCups (single-use reaction vessels) and AssayTips (single-use tips for the sample pipetter) in a consumable area, mechanism to transfer these consumables and a liquid flow path to transport the incubate to a temperature controlled detection

unit, where the ECL measurement takes place in the electrochemical flow cell. The electrochemical cell has three electrodes: Pt for working and counter electrode and Ag/AgCl as reference electrode. From MODULAR ANALYTICS E170 a PreWash was added for washing magnetic beads carrying immuno-complexes before being put in electrochemical cell and can be used optionally for specific assays. Also, the quantity of samples and reagents depends on assay types. The reagents used are i) ProCell, which contains TPrA for ECL detection, ii) CleanCell, which is the cleaning solution used for electrochemical cell after detection and iii) PreClean buffer used for PreWash process. After a well-established process the ECL light can be amplified and detected by a photomultiplier tube (PMT) in constant measuring conditions.

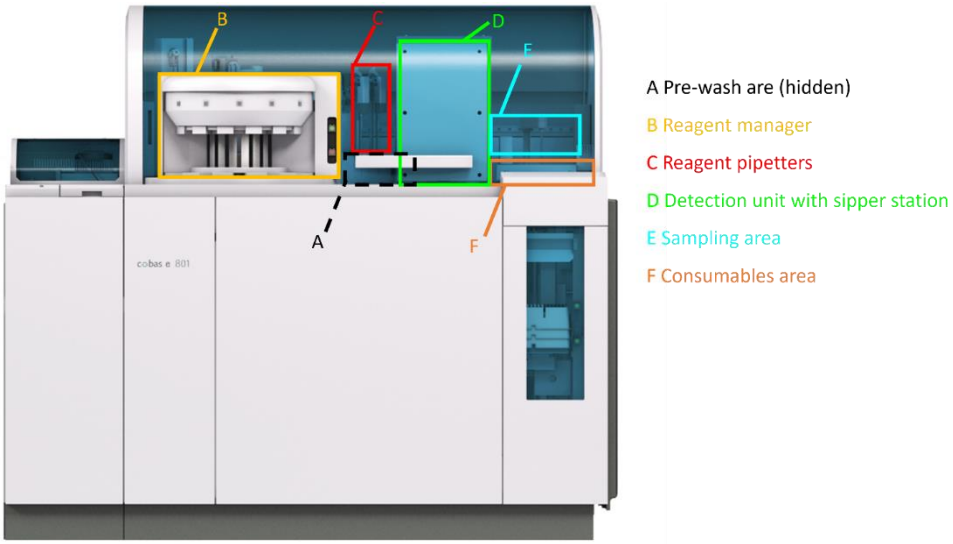

Figure 2.7. **cobas e** 801 analytical unit and overview of the main components.

Elecsys® immunoassay are conspicuous and are adapted to different analytes, because for example small molecules and big antibody need different assay principles for detection. The most used is the sandwich assay, also previously described, where are present an analyte, an analyte specific biotinylated antibody and an analyte specific ruthenylated antibody (figure 2.6). However, there are many other types of detection assays, and they can be also combined between each other's: i) Double Antigen Sandwich Assays for antibody detection (DAGS); ii) Competitive Assay for very small molecules or hormones; iii) Back-titration Binding Assay for small molecules like proteins and often needs a pre-treatment; iv) μ-Capture Assay specific for IgM antibodies relevant for diagnosis of infections. Roche Diagnostic cobas e immunoassay analyzers have a broad assay menu with more than 100 different assays and applications, going from small molecule, hormones, small and large proteins to different types of antibodies, covering a very wide area of medical indication.[28,80]

1.3 Outlook

In this chapter, ECL microscopy will be combined with the beads-based immunoassay system, simulating the commercial Elecsys®. The principal aim is the achievement of higher ECL signals using two different strategies based on the heterogeneous mechanism and its investigation. The ECL mechanism and the final signal efficiency are affected by (i) the kinetics of the heterogeneous electron transfer reactions of the coreactant, (ii) the stability of coreactant radicals, and (iii) the distribution of ECL luminophores. In the first strategy, dye-doped silica nanoparticles (DDSNPs) analysed in the first chapter will be used to successfully enhance signal of built sensors, tuning the distribution of the dyes. Nanoparticles were widely and successfully studied as ECL emitters but the application in ECL microscopy was less investigated.[18,82,83] In fact, the main issue is that coreactant radicals generated at the electrode surface have to diffuse and interact with luminophores inside the NPs within their lifetime length. For these reasons, the modulation of the synthetic procedure or the coreactant choice are mandatory.[84,85] All the advantages of the $[Ru(bpy)_3]^{2+}$-doped silica nanoparticles presented in the first chapter and synthesised with a new method, will be exploited for the construction of a bead-based immunoassay system more sensitive respect to the analytical approach adopted in commercial ECL-based immunoassay system. The single $[Ru(bpy)_3]^{2+}$ used as beads label will be substituted with $[Ru(bpy)_3]^{2+}$-doped silica nanoparticles, showing an ECL signal intensity 660-fold higher[86] and paving the way to image a single biomolecule, and a cellular membrane protein.[12]

Instead, the second strategy will tune the oxidation of coreactant, consequently optimizing the heterogeneous mechanism responsible of emission in commercial ECL-based immunoassay system and increasing the sensitivity of the technique. Herein, after mapping ECL generation close to the electrode surface (≤1 μm), a new unobserved path at short distance will be discovered and the introduction of additive will successfully optimize coreactant oxidation, reaching a higher ECL signal also in a series of Elecsys® assays in the Roche Diagnostics Cobas e 801 immunoassay analyzer.[28,81]

2. DYE-DOPED SILICA NANOPARTICLES FOR ENHANCED ECL-BASED IMMUNOASSAY ANALYTICAL PERFORMANCE[86]

In the first chapter two sets of monodispersed $Ru(bpy)_3^{2+}$-doped silica NPs were presented, bio-Triton@RuNP and bio-Igepal@RuNP, and were synthesised with an innovative method that allow a good control of the parameters,[87,88] such as size, solubility, ζ-potential, for reaching the best features and ECL performance for silica NPs. Some limitations had to be overcome in order to obtain a good ECL signal: i) oxidized species of the coreactant are radicals with a limited lifetime and have to diffuse to reach the ECL probes inside the silica matrix for generating the excited state; ii) NP volume have to be optimized for concentrating the right amount of ECL-active species;[82] iii) the NPs shell has to be suitable for making them colloidally stable in water and for allowing the fast diffusion of coreactant radicals.[85]

As just presented, the modulation of the synthetic procedure allowed to overcome the limitations and obtain dye-doped silica nanoparticles (DDSNPs) with very promising performances that can be applied in a commercial ECL bead-based immunoassay. It was observed that bio-Triton@RuNPs have much higher ECL intensity than bio-Igepal@RuNps and they have the correct NPs parameters (e.g. ζ-potentials, hydrophobicity, dye distribution and NP size) for an efficient ECL generation using TPrA. The electrochemical and ECL behaviours of the system bio-Triton@RuNPs/TPrA underline the successful oxidation of the species, a conspicuous charge and current generation in the order of mA, due to the high concentration of TPrA and consequently of radicals that will react with the luminophore generating the emission observed (figure 2.8). Instead, the PL spectra can't be obtained and compared to ECL behaviour because the signal of nanoparticles is too low.

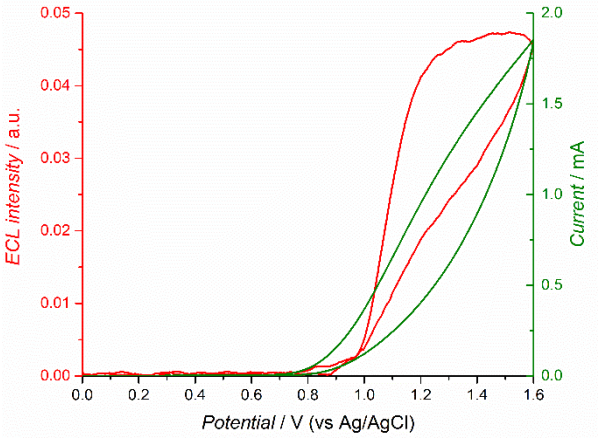

Figure 2.8. ECL intensity potential curves (red line) and current potential curve (green line) in the presence of TPrA 180mM in a 1nM solution of bio-Triton@RuNp. Cyclic voltammetries with voltage scanned between 0 V and +1.6 V, scan rate 0.1 V s^{-1}. Glassy Carbon electrode referred to Ag/AgCl. Pt spiral as counter electrode. PMT bias 750V.

These results inspired the test of bio-Triton@RuNPs in ECL imaging, which was unsuccessful with other core-shell NPs, mainly due to the detrimental effects of non-optimized NPs structure and positive surface charge (ζ-potential), which repulses the positive $TPrA^{\bullet+}$. In figure 2.9, single 2.8 μm magnetic bead is functionalized with bio-Triton@RuNps (beads@Triton) and the heterogeneous mechanism involved for ECL emission generation is shown. Their ECL imaging results will be compared to 2.8 μm beads functionalized with a biotinylated antibody labelled with $[Ru(bpy)_3]^{2+}$ complex (Ru@beads), mimicking the analytical approach of commercial ECL bead-based immunoassay system.

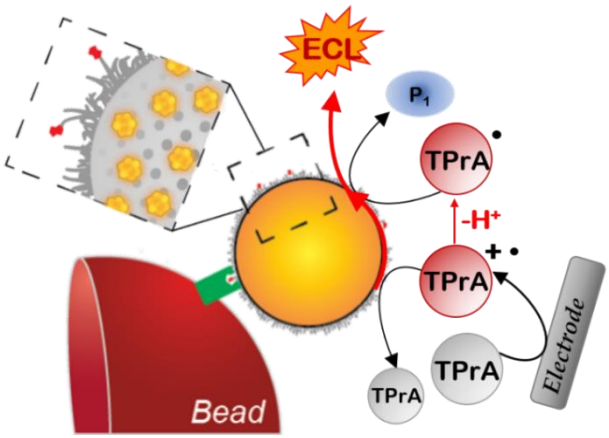

Figure 2.9. The heterogeneous mechanism for the "oxidative-reduction" co-reactant ECL generation obtained using 2.8 μm beads labelled with bio-Triton@RuNp (yellow sphere) through a streptavidin (green tool)-biotin (red tool) bond. Tri-*n*-propylamine (TPrA) is oxidized at the electrode, generating the radical cation ($TPrA^{+\bullet}$), which deprotonates, forming the radical ($TPrA^{\bullet}$). $TPrA^{+\bullet}$ and $TPrA^{\bullet}$ react with the ECL luminophore $[Ru(bpy)_3]^{2+}$ (yellow square), inside the bio-Triton@RuNp located on magnetic beads (red semi-sphere).

2.1 ECL images and ICP-MS analysis

ECL images (figure 2.10) were acquired after the application of 1.4 V for 4 s in a solution of PB 0.2 M with 180 mM of TPrA, used as coreactant. The measurements were repeated for several times, acquiring the ECL intensity of almost 3-6 beads per image and finally making the average of the values obtained from images elaboration. The important parameters under investigations are the integrated intensities and the profiles of the emissions both calculated on the single beads.

A very interesting and promising result was obtained: the ECL intensity integrated of beads@Triton resulted 8.5-fold higher respect to Ru@beads (figure 2.11A). The massive signal enhancement was confirmed by multiple beads ECL intensity integrated and respective ECL emission profiles (figure 2.11B) of both beads@Triton (grey line) and Ru@beads, (black line). The profiles map the ECL emission of the single bead respect to the space, showing the maximum intensity and the distribution along the beads. In fact, a line was designed across the bead image acquired and the intensity profile line obtained (inset of figure 2.11B). To quantitively compared the two cases, the luminophore quantification is mandatory because the quantity of $[Ru(bpy)_3]^{2+}$ complexes was different on the two different types of labelled beads.

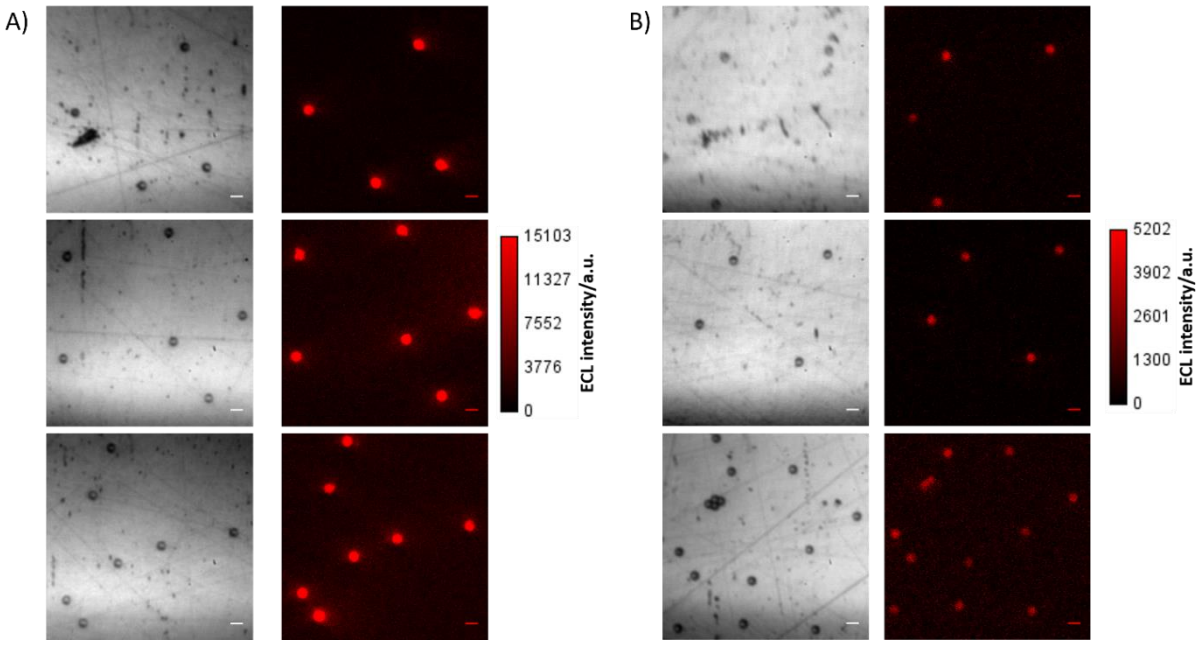

Figures 2.10. A) Optical (left column) and respective ECL images (right column) of 2.8 μm single bead labelled with bio-Triton@RuNp (beads@Triton). B) Optical (left column) and respective ECL images (right column) of 2.8 μm single bead labelled with biotinylated $Ru(bpy)_3^{2+}$ complex (Ru@beads). They were obtained by applying a constant potential of 1.4 V (vs. Ag/AgCl) for 4 s in 180 mM TPrA and 0.2 M phosphate buffer (PB). Pt wire as counter electrode. EMCCD camera coupled with a potentiostat. Integration time: 8 s; magnification: X100; Scale bar, 5 μm.

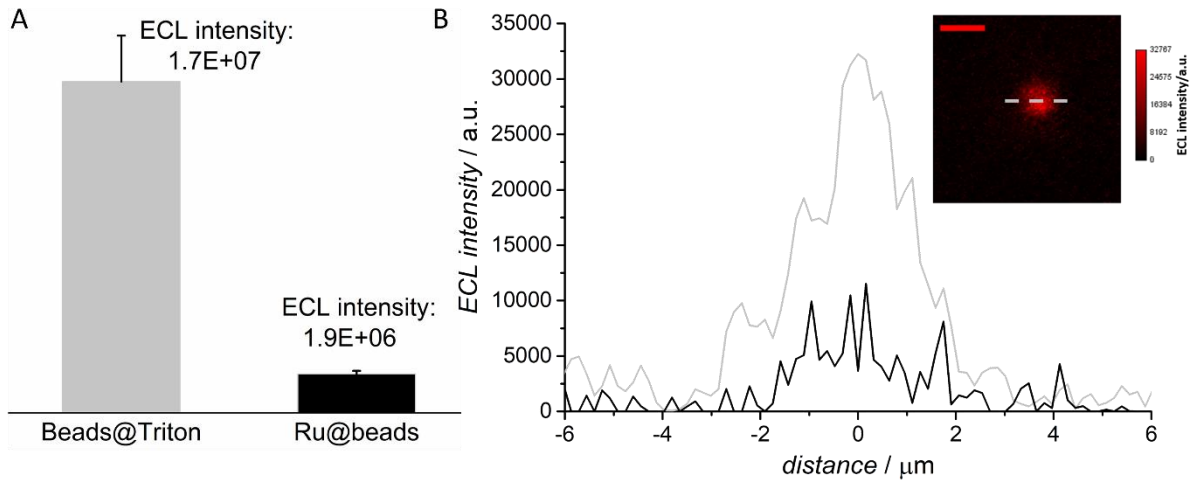

Figure 2.11. A) Comparison between integrated intensity values calculated for Ru@Beads (black) and Beads@Triton (grey), error bar shows the standard deviation (n=9). B) Comparison of the beads profile lines (black line, Ru@beads; grey line, Beads@Triton). Integrated intensity and profile lines are obtained from elaboration of the images in figure 2.10. Inset image show the method for acquiring the ECL profiles: a dashed grey line is designed across a beads@Triton and the intensity acquired. Scale bar 5 μm.

ICP-MS analysis was used for the quantification of Ruthenium (Ru) immobilised onto the surface of the microbeads, that need a treatment before the analysis in order to obtain a reliable result (procedure explain in the appendix). The dye concentration [Ru] was about 660 times higher in the case of beads@Triton respect to Ru@beads and was directly obtained by the inductively coupled plasma mass spectrometry (ICP-MS) analysis (table 2.2). Instead, the number of Ru per μm^2 was calculated taking into account the total area of beads and the area related to the single beads.

sample	Total area	Area of 0.5mL beads	[Ru] / ppb	[Ru] / M	N° Ru	Ru/μm^2
Ru@beads	7.1E+09	4.4E+09	0.723	7.2E-09	2.2E+13	4.9E+3
beads@Triton	7.1E+09	4.4E+09	479	4.7E-06	1.4E+16	3.2E+6

Table 2.2. ICP-MS parameters relative to the dye quantification obtained from the analyses of 500 μL Ru@beads and beads@Triton having an established area of 4.42E+09 μm^2. The concentration of Ruthenium [Ru] is directly obtained from ICP-MS analysis. N° Ru is the number of ruthenium ion obtained by the product of Ru concentration, the volume (500 μL) and the Avogadro constant. Ru/ μm^2 is the number of ruthenium divided by the beads area in 500 μL.

Observing the value of these parameters, the higher quantity of luminophores present on single beads@Triton is evident respect to Ru@beads, reflecting the experimental conditions. In fact, the Ru concentration obtained is in line with an expected similar occupancy of the active sites onto the microbead surface by either the biotinylated antibody labelled with Ru or bio-Triton@RuNps, which contain respectively 6[89] and 4800 $[Ru(bpy)_3]^{2+}$complexes. Comparing this values and results, we can

conclude that only a small portion of the Ru complexes, around 1.3%, participate to the 750% increase of ECL emission with respect to the commercially available approach.

2.2 ECL signal stability

As anticipated in DDSNPs presentation, the silica matrix plays an important role in the NPs performances. For example, investigating the stability of both functionalized beads, a lower ECL signal decay for beads@Triton was observed with respect to Ru@beads (figure 2.12). This behaviour is due to the nano-environment of silica matrix that protects against undesired electrochemical reactions, increasing their potential performance and the magnetic beads ECL stability. The embedding of luminophores inside silica matrix represents an alternative strategy for increasing the dye stability, decreasing the ECL decay usually observed and caused by the presence of reactive and undesired products of electrochemical reaction and modification of electrode surface after the application of anodic potentials, which reduced the kinetic and efficiency of coreactant oxidation. In fact, the other strategy presented by Sojic et al. concerns the application of an electrochemical treatment for regenerating the electrode surface.[71,72]

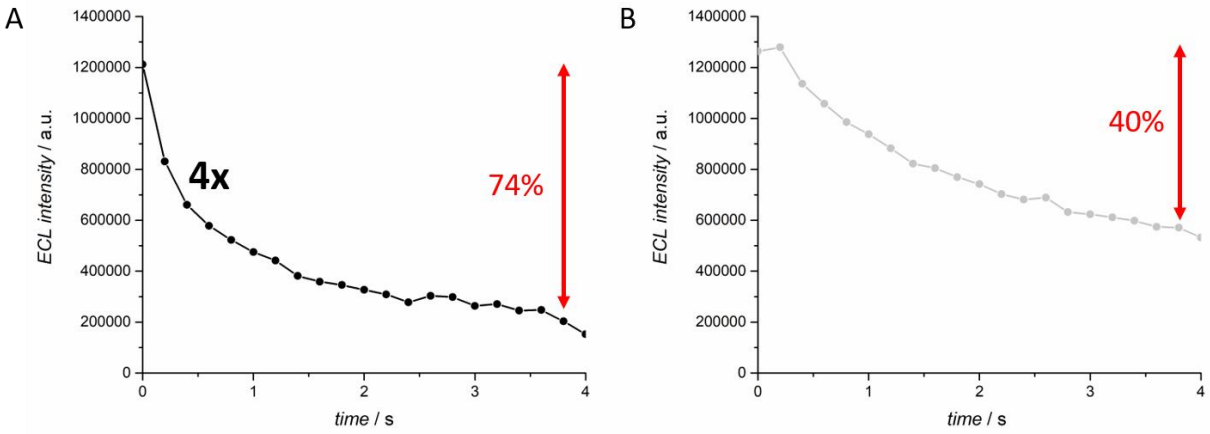

Figure 2.12. ECL intensity stability of 2.8 µm single bead labelled with (A) biotinylated $Ru(bpy)_3^{2+}$ complex (Ru@beads) and (B) with bio-Triton@RuNp (beads@Triton). ECL images were acquired each 200 ms (integration time) and ECL intensity integrated is plotted against time. Notice that ECL intensity of Ru@beads is multiplied for a factor 4 for easier comparison with ECL intensity of beads@Triton. ECL intensities have a drop of 74% and 40% for Ru@beads and beads@Triton, respectively. They were obtained by applying a constant potential of 1.4 V (vs. Ag/AgCl) for 4 s in 180 mM TPrA and 0.2 M phosphate buffer (PB). Pt wire as counter electrode.

Instead, concerning the luminescence behaviour of the dye, the inclusion of the Ru complex inside the silica matrix, responsible of the increase of luminescence lifetime and quantum yield, is only in a minimal part the cause of the observed signal increase. In fact, through the confocal analysis bio-

Ru dyes in Ru@beads show a lifetime nearly as long as $[Ru(bpy)_3]^{2+}$ in Triton NPs (FLIM images in figure 2.13 and table 2.3), but it is noticeably longer than the $[Ru(bpy)_3]^{2+}$ complex lifetime in water.

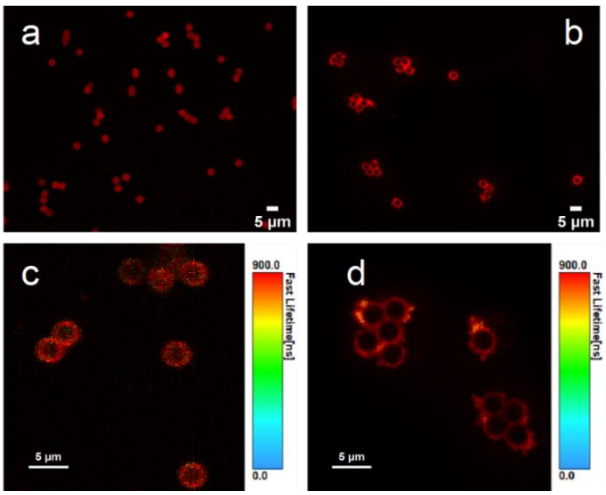

Figure 2.13. Confocal images of Ru@beads (a) and beads@RuNPs (b), λ_{exc} = 401 nm, emission filter 595/50 nm. Time-gated FLIM images (t > 100 ns) of Ru@beads (c) and beads@RuNPs (d), λ_{exc} =405 nm, emission filter longpass 560 nm. The average photon arrival time («fast» lifetime) is represented by the colorscale.

The results observed for ECL and ECLM performances related to $Ru(bpy)_3^{2+}$-doped silica nanoparticles are very promising and confirm the fundamental role of the synthetic procedure in improving the signal emission. In fact, this new batch of silica NPs reached better performances, from ECL emission point of view, respect to the ones previously studied and synthesised.[18,84,85,90] In particular, oppositely to what observed with another kind of NPs,[18,85] the high dye doping degree (ca 4800 complexes every NP) did not bring to a positive surface charge thus allowing a high ECL emission (table 2.3). Moreover, they can be applied for the first time in combination with ECL microscopy in a system with TPrA, mimicking the commercial ECL bead-based immunoassay system and observing unexpected and promising results that can be furtherly implemented and used for the development of biosensors devoted to detection of ultralow concentrations of analytes for clinical monitoring and early disease diagnosis.[12]

sample	ECL intensity	Ru active site^{-1}	Lifetime (FLIM)
Ru@beads	1946131	6	830 ns
beads@Triton	16588240	4800	870 ns

Table 2.3. ECL intensity at a single bead level of Ru@beads and beads@Triton together with the quantitative parameters of dye present. The lifetime of Ru is obtained by the FLIM analysis of confocal microscopy.

3. INSIGHTS INTO THE MECHANISM OF COREACTANT ELECTROCHEMILUMINESCENCE FACILITATING ENHANCED BIOANALYTICAL PERFORMANCE[81]

In the second part of this chapter, the combination of ECL and microscopy and the use of labelled microbeads continue. However, in this case the investigation will be more focused on mapping the ECL generation close to the electrode surface and thus studying mechanisms responsible of ECL emission. After this, a strategy related to coreactants will be identified to improve the efficiency of ECL emission generation mechanism.

The final scope of these investigations is the improvement in ECL as analytical technique for the development of biosensors even more sensitive and suitable for disease diagnosis and for reaching better performances and lower limits of detection in the commercial devices just present in the world, like Elecsys® (see paragraph 1.2).

3.1 Surface generation–bead emission experiments

First of all, the effect on ECL generation of luminophore spatial distribution respect to the electrode surface was investigated exploiting beads with different sizes. Streptavidin-coated polystyrene magnetic microbeads with different diameters (2.8, 1, 0.5, and 0.3 μm) were functionalized with a biotinylated antibody labelled with $[Ru(bpy)_3]^{2+}$ luminophore (Ru@beads; see appendix for the functionalization procedure). The ECL/optical imaging of surface generation–bead emission was obtained using a PTFE homemade electrochemical cell comprising Pt working (0.16 cm^2), Pt counter, and Ag/AgCl (3M KCl) reference electrodes. ECL emission of these functionalized beads was collected by a direct microscope equipped with an electron multiplying charge-coupled device (EMCCD) camera and compared in order to correlate ECL emission as a function of distance to the electrode (figure 2.14). ECL images were recorded while applying a constant potential of 1.4 V (vs. Ag/AgCl 3M KCl) for 4 s (0.5 s for TOF calculations) with an integration time of 8 s. However, the direct comparison of objects with different sizes was possible thanks to the introduction of a new and very useful parameter, the turnover frequency (TOF), and the combination of different analytical techniques allow the ECL efficiency quantification. Turnover frequency (TOF),[91] as a function of bead size, was defined as the number of photons generated by 1 mol of luminophore per time unit and calculated using the following equation:

$$\mathrm{TOF} = \frac{(\mathrm{ECL}_{Ru@Bead} - \mathrm{ECL}_{Bead})}{n°\ of\ [\mathrm{Ru}(bpy)_3^{2+}] \times \mathrm{time}}$$

where $ECL_{Ru@Bead}$ is the integrated ECL signal of a single bead, ECL_{Bead} is the background in absence of $[Ru(bpy)_3]^{2+}$ luminophores, and $[Ru(bpy)_3]^{2+}$ is the amount of Ru luminophores, which were quantified after sample mineralization via inductively coupled plasma mass spectrometry (ICP-MS) (see the procedure in the appendix), that provide the Ru concentration in ppb (see the table 2.4).

Beads / µm	Total beads area	Area of 500 µL beads	[Ru] / ppb	[Ru] / M	N° Ru	Ru / µm²
0.3	7.09E+09	4.42E+09	1.183	1.17E-08	3.52E+13	7969
0.5	7.09E+09	4.42E+09	1.262	1.25E-08	3.76E+13	8501
1	7.09E+09	4.42E+09	1.210	1.20E-08	3.60E+13	8151
2.8	7.09E+09	4.42E+09	0.652	6.45E-09	1.94E+13	4392

Table 2.4. Ru density (Ru/µm²), Ru concentration ([Ru]/M) and Ru amount (n° Ru) calculated from Ru ppb concentration normalized for the total surface area of each bead type (0.3 µm, 0.5 µm, 1 µm, 2.8 µm).

The TOF relative to ECL performance of small beads resulted much higher with respect to large beads (figure 2.14b), confirming i) the exponential increase in ECL emission close to the electrode surface and ii) the far superior efficiency of 0.3 µm beads compared with that of 2.8 µm beads (8 times higher signal). The spatial distribution of dyes was optimized obtaining a higher signal if they are localized near the electrode surface. A complementary investigation aimed at understanding this behaviour and the underlying generation mechanism was conducted starting from the kinetics elaboration of tip generation-surface emission. This experimental approach was already used by Bard and coworkers in 2002 for the innovative investigation of ECL distribution close to the electrode surface using a hemispherical microelectrode controlled by a micromanipulator.[23] ECL emission can occur only when both $TPrA^{\bullet}$ and $TPrA^{\bullet+}$ are present and it can be modulated changing the distance of tip from surface, because $TPrA^{\bullet+}$ shows short lifetime and influence the thickness of emission layer.

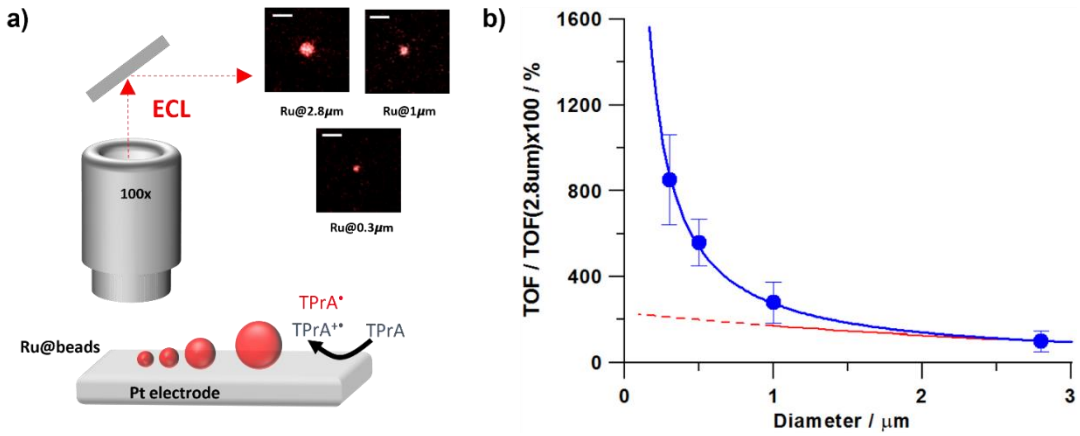

Figure 2.14. a) Schematic representation of the surface generation–bead emission experiment where Ru@beads are magnetic beads labelled with $[Ru(bpy)_3]^{2+}$, blocked on platinum electrode (Pt) by a magnet and shows the ECL images acquired for beads with different sizes. Ru@2.8 μm, Ru@1 μm and Ru@0.3 μm are ECL images of magnetic beads labelled with $[Ru(bpy)_3]^{2+}$ with a diameter of 2.8, 1, and 0.3 μm, respectively. Magnification X100, scale bar 5 μm; potential applied, 1.4 V (vs. Ag/AgCl, 3M KCl); acquisition time, 0.5 s. b) Turnover frequency (TOF) as a function of bead size (blue curve and dots) and ECL intensity of the ref. [23](red curve). The TOF is the number of photons emitted in 1 s by a single Ru luminophore. TOF@2.8 μm is the turnover frequency for 2.8 μm beads (Ru@2.8 μm).

3.2 Tip generation–surface emission experiments

We followed and reproduced Bard's approach, in collaboration with Prof. Stefania Rapino from the University of Bologna, using a system composed by a transparent indium tin oxide (ITO) electrode functionalized with a $[Ru(bpy)_3]^{2+}$ monolayer as the emitting surface (Ru@ITO) and two different hemispherical Pt microelectrodes, with a diameter of either 1.5 or 0.5 mm (optical images in figure 2.17 a), for TPrA oxidization all positioned above an inverted microscope equipped with an EMCCD camera (figure 2.15). All measurements were performed in a PTFE homemade electrochemical cell comprising a Pt hemispherical microelectrode, Pt as counter electrode and Ag/AgCl (3M KCl) as reference electrode in contact with a solution of 0.2 M PB (pH 6.9) with 180mM of TPrA. The images and relative intensities were recorded by moving at velocity of 0.1 μm s^{-1} the electrode with a micropotitioner from a distance of 0.1 μm to 2.8 μm after the recognition of distance 0 through the observation of a spike in the current when the tip is in contact with the Ru@ITO.

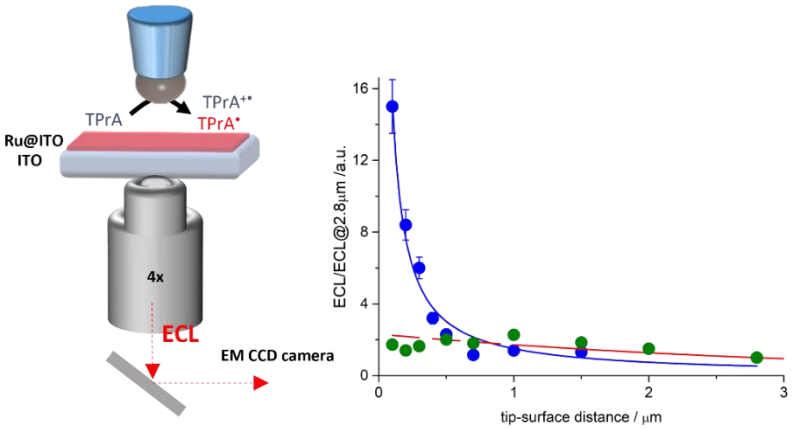

Figure 2.15. Schematic representation of the tip generation–surface emission experiment where Ru@ITO is transparent indium tin oxide (ITO) electrode functionalized with a $[Ru(bpy)_3]^{2+}$ monolayer as the emitting surface. ECL intensity obtained by the experiment was reported as a function of the tip–surface distance for a small electrode (blue curve and dots) and a large electrode (green dots) and ECL intensity of the ref. [23] (red curve). ECL@2.8 μm is the ECL intensity for 2.8 μm distance between tip and surface. The potentials applied via cyclic voltammetry at a scan rate of 100 mV s^{-1} ranged from 0 to 1.4 V (vs. Ag/AgCl 3M KCl). TPrA is tri-*n*-propylamine. Error bar shows the standard deviation (n =10).

ECL signals and currents were recorded scanning a potential from 0 V to 1.4 V (vs. Ag/AgCl 3M KCl) through CV at a scan rate of 100 mVs^{-1}. Observing the cyclic voltammetries (figure 2.16 a and c), the current was enhanced beyond 0.6 V by the oxidation of TPrA coreactant. The TPrA oxidation current was instead not affected by the microelectrode–surface distance because the very large electrode minimized the hindering effects on current generation.

For ECL imaging, the system was triggered to allow the acquisition of images in real-time during the application of potential. Images were obtained in a CCD mode sequence with an integration time of 200ms at 4X magnification (figures 2.16 b and d).[92]

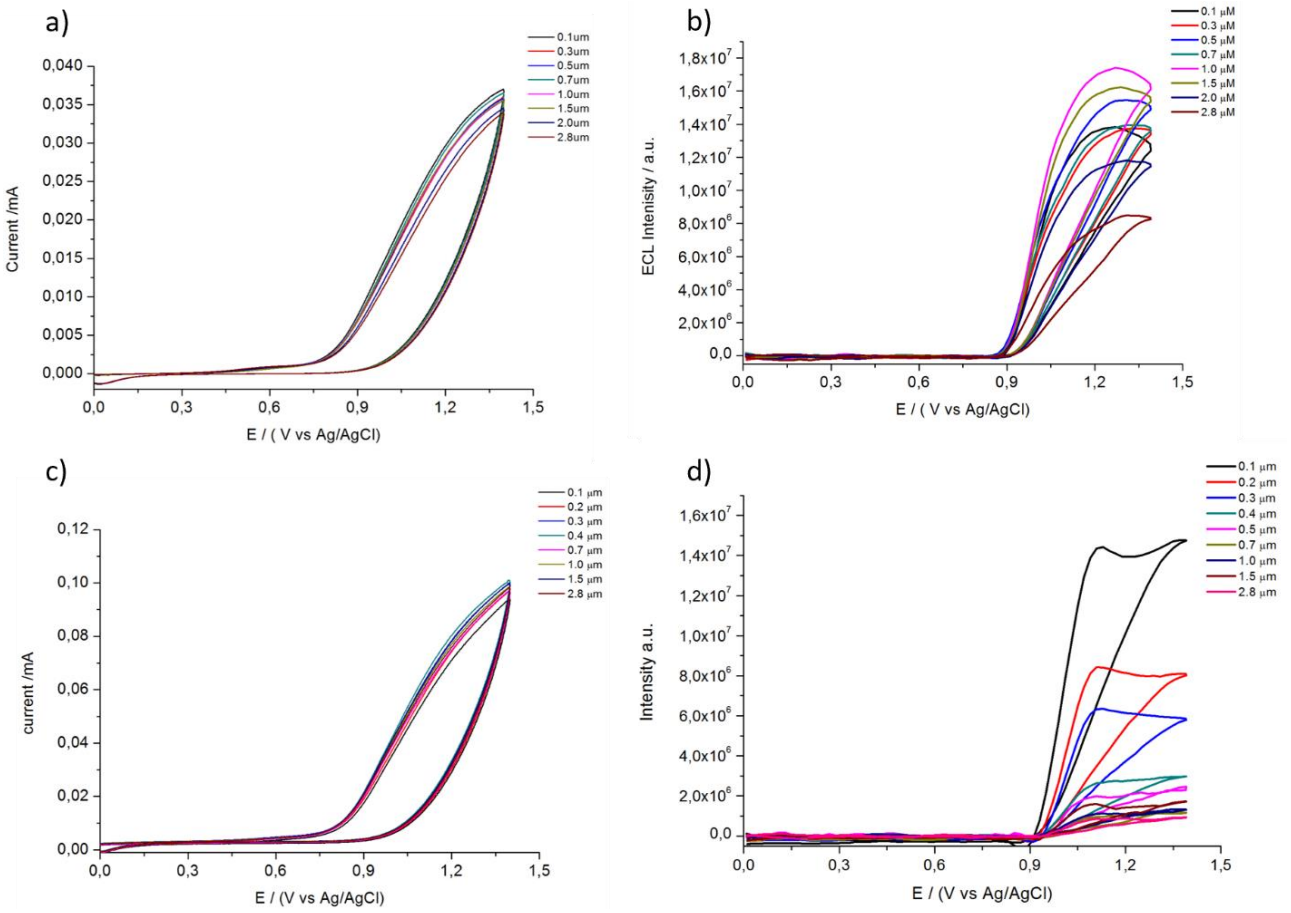

Figure 2.16. Cyclic voltammograms (CV) currents (a and c) and corresponding ECL signals (b and d) at different distances (0.1 – 2.8 µm) from the ITO modified surface applying a potential range of 0-1.4 V, scan rate 100 mV s^{-1}. All measurements were obtained in PB 0.2 M with TPrA 180 mM (pH 6.9), potential vs Ag/AgCl (3 M KCl). First row (a and b) hemispherical large electrode characterization. Second row (c and d) hemispherical small electrode characterization. ECL intensity is obtained by ECL images acquired during CV in a CCD mode sequence; integration time: 200ms, magnification X4.

An emitting disc under the microelectrode tip was the protagonist of ECL images (figures 2.17 b and c) and its intensity and dimension increase with the applied potential. The correlation between its intensity and tip–surface distances is similar to the one obtained by Bard and coworkers in 2002 (figure 2.15 red line).[23] This is true at large distances (≥1 µm) but if the 1.5-mm microelectrode tip was approached very close to Ru@ITO (<1 µm), an emitting disk with not homogeneous ECL emission and lower intensity from the inner part was observed (first row of figures 2.17 b and c). Such a behaviour was associated with the strong hindrance of TPrA diffusion to the central part of Ru@ITO under the microelectrode tip. This hindrance effect was diminished by using a smaller microelectrode (0.5 mm), showing a relative increase of ECL intensity and emission homogeneity at very short tip-surface distance, which reflect the behaviour of ECL intensity related to beads with small diameters (second row of figures 2.17 b and c).[93]

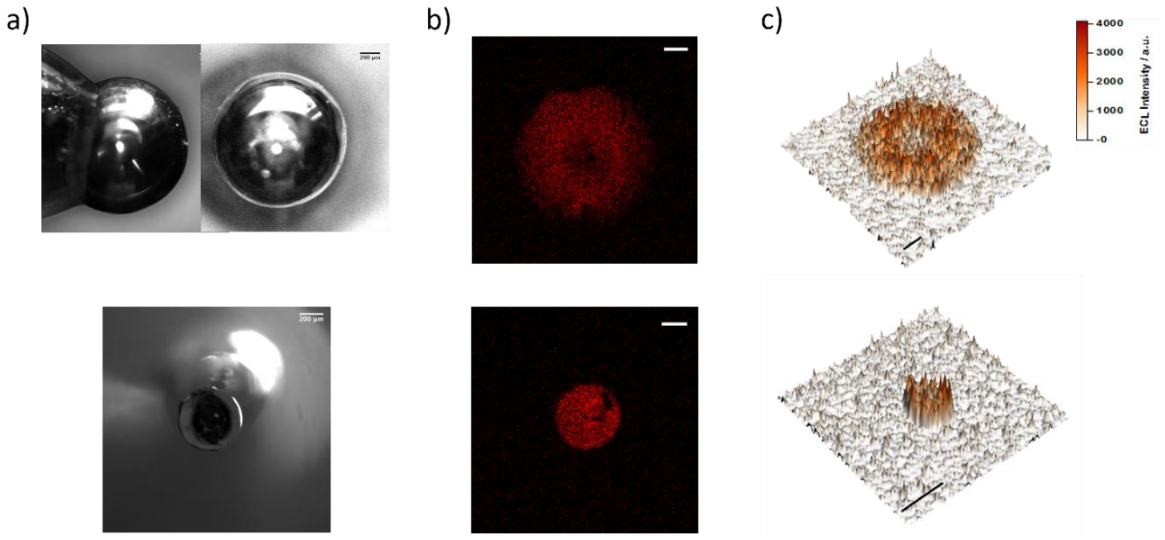

Figure 2.17. First row characterization of hemispherical large Pt microelectrodes with a diameter of 1.5 mm. Second row characterization of hemispherical small Pt microelectrodes with a diameter of 0.5mm. a) Optical images of lateral and front view of the large electrode and only front view of the small one. Scale bar 200 μm. b) ECL emission generated at 0.1 μm distance from the Ru@ITO surface at 1.4 V, magnification X4, scale bar 200 μm, exposure time 200ms. c) ECL intensity image profile acquired at 1.4 V. Magnification X4, scale bar, 500 μm, exposure time 200ms.

The ECL intensity behaviour with smaller tip at high distances (≥ 1 μm) reflects the behaviour observed with bigger tip and in previous observation (figure 2.15),[23] but a new trend was outlined for short distances (< 1 μm), prompting us in deeper investigations. Before presenting more detailed hypothesis, a control experiment was performed on contribution of the Pt electrode to the overall ECL intensity. The hemispherical electrode showed a non-negligible but constant luminescence contribution at different distances for both tip dimensions (figure 2.18).

The different trends at small and long tip-surface distances reflect the behaviour of beads with different diameters and highlight the presence of a very efficient ECL generation mechanism operating very close to the electrode surface (figure 2.19). Using the ECL intensity–distance dataset, we estimated the lifetime of radical species by converting each tip–surface distance to the corresponding (travel) time. The equation $t = \frac{d^2}{36D}$ was used for the conversion, where d is the distance (in cm) between the tip and the Ru@ITO surface, and D is the diffusion coefficient for TPrA (7.4×10^{-6} cm^2 s^{-1}).[23] Thanks to this conversion, the travelling time was analysed as a function of ECL intensity and the different trends correlate to lifetimes of species: i) at d > 1 μm (black fitting line in figure 2.19), the analysis confirmed a half-life of ~700 μs, related to the $TPrA^{\bullet+}$, as just observed;[23,94] ii) at d < 1 μm (red fitting line in figure 2.19) a faster decay transient and a consequently much shorter half-life (~ 5 μs) was observed.

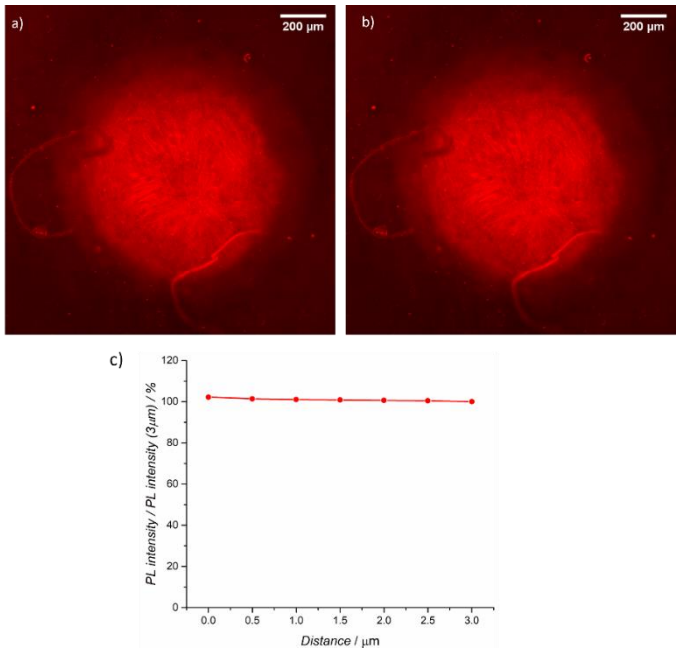

Figure 2.18. Reflection investigation of the electrode tip. Images of fluorescence intensity acquired for a PDMS/rhodamine-functionalized glass slide under the large Pt hemispherical electrode (diameter = 1.5 mm) positioned at distance of a) 1 µm and b) 3 µm from the glass. c) Integrated intensity normalized for intensity at 3 µm as a function of the tip–glass distance. The electrode was put in contact with the substrate and then moved up of 0.5 µm each step acquiring the fluorescence and integrating the intensity of the overall area. Magnification X4; filter, Texas Red®; scale bar, 200 µm.

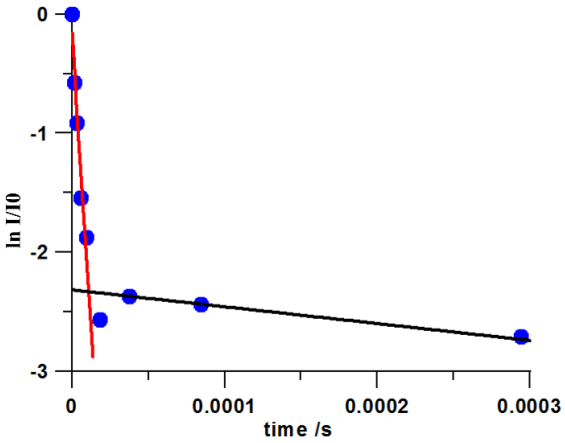

Figure 2.19. Travel time calculation. Time resolved spatial map of ECL intensity calculated using equation $t = \frac{d^2}{36D}$. The black line corresponds to $t_{1/2} \sim 700\ \mu s$ while the red line coincides with a shorter path and $t_{1/2} \sim 5\ \mu s$. Data (blue dots) were obtained with tip generation-substrate emission experiment using hemispherical small electrode (figures 2.16 and 2.17 second row).

3.3 Hypothesis outlines

ECL heterogeneous mechanism (see the scheme in the main introduction in paragraph 1.2 and figure 2.5) is the main responsible of ECL generation in biosensing and commercial immunoassay applications, where radical and radical cation of coreactant obtained after oxidation are only

responsible of the generation of ECL luminophore excited states, which cannot be oxidized by the electrode.

The ECL emission was assumed to be higher at small distances from the electrode in virtue of the higher concentrations of radical and radical cation, the latter in particular for its limited lifetime.[23,29] In order to further investigate this behaviour, we exploited the advantages of ECL imaging for deciphering the ECL mechanism generation. As reported before, using beads with different diameters, the exponential increase observed at shorter distances than 1 μm was unexpectedly much higher than what expected according to Bard and coworkers,[23] with an 8-fold increase in ECL signal of 0.3-μm beads with respect to 2.8-μm beads (see the blue curve in figure 2.20b and 2.14b). The direct oxidation of $[Ru(bpy)_3]^{2+}$ was definitely excluded by performing the same ECL analysis using an anodic potential lower than the luminophore oxidation (<1.2 V defined by CV of $[Ru(bpy)_3]^{2+}$ shown in figure 2.20a) and observing the same TOF values of experiments performed at 1.4 V (see the comparison of the red signal and blue curve in figure 2.20b).

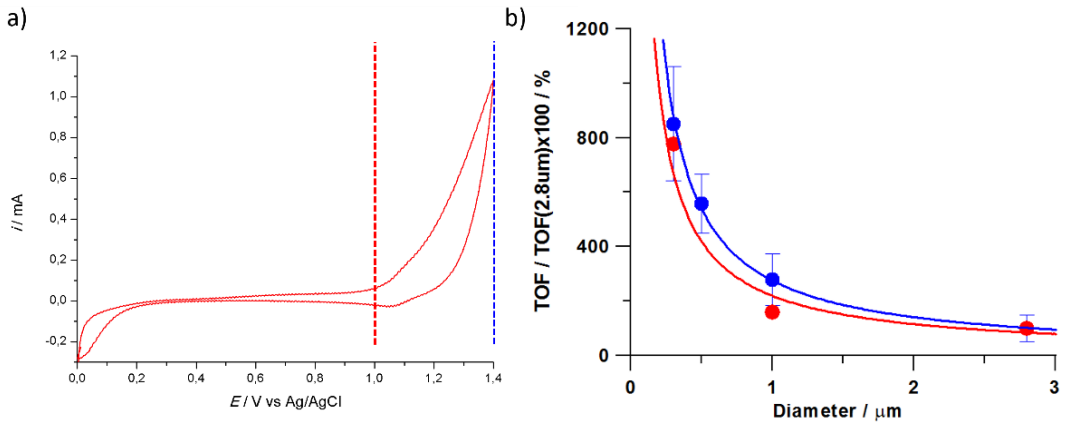

Figure 2.20. Effect of the potential on the surface generation beads emission. a) Cyclic voltammetry of the 0.5 mM $[Ru(bpy)_3]^{2+}$/PB solution showing the potential used for the surface generation–bead emission experiment. b) Surface generation–bead emission experiment performed at 1 V (red line) and at 1.4 V (blue line), respectively, before and after the potential for the $[Ru(bpy)_3]^{2+}$ oxidation. Error bar shows the standard deviation (n=10).

The tip generation-surface emission method was used for trying to map the stability of $TPrA^{\bullet+}$, explaining the trend obtained by emission of beads with different diameters. The half-life of $TPrA^{\bullet+}$ was 700 μs, while at short distances (< 1 μm), we observed a different transient which involved other reactive species with a shorter lifetime. The measured half-life of 5 μs suggests the presence of an additional mechanism related to electrogenerated species formed by TPrA oxidation. The combination of this analysis with spin-trapping experiments[95] on prolonged electrolysis products and mass fragmentation patterns of TPrA, allowed to proof the generation of an additional product

in parallel to the $TPrA^{\bullet+}$ and $TPrA^{\bullet}$. In fact, the amine oxidation process cleaves a C–N bond (figure 2.21, blue path) generating a N-centred dipropylamine radical that could convert into a C-centred radical, and are responsible of an active pathway at small distances with an efficiency ~10 times higher than the mechanism at large distances.[96–99]

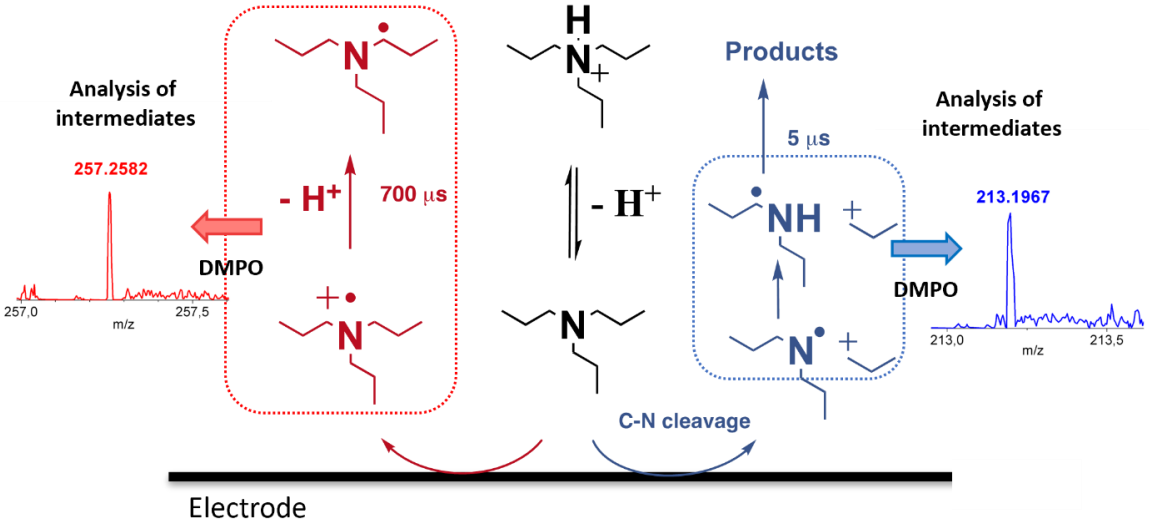

Figure 2.21. Schematic representation of the proposed parallel pathways. Tri-*n*-propylamine (TPrA) was oxidazied at the electrode generating $TPrA^{\bullet+}$ and $TPrA^{\bullet}$ (red pathway) and dipropylamine radical ($DPrA^{\bullet}$) (blue pathway). The scheme reaction is supported by spin-trapping experiments with DMPO, which stabilized the radicals and allowed identification by mass spectrometry analysis (MS) and electron paramagnetic resonance (EPR). The inset shows the MS analysis for the possible adducts DMPO-TPrA (red) and DMPO-DPrA (blue).

3.4 Spin-trapping and analysis of radical intermediates

Spin-trapping experiments were conducted in collaboration with Dr. Antonio Barbon of the university of Padua, and unequivocally identified the radicals generated following the oxidation of TPrA after the solution electrolysis. The spin traps 5,5-dimethyl-pyrroline N-oxide (DMPO ≥98%, 0.05M before the electrolysis) was added to a solution of TPrA 180 mM, formic acid pH 6.8 in order to stabilize the electrogenerated radicals and transform short-living radicals into long-living systems with paramagnetic character, suitable to be characterized by Electron Paramagnetic Resonance (EPR). The electrolysis was performed at 1.4 V (vs Ag/AgCl) for 1 h under Ar-saturated atmosphere to reduce oxygen content, radicals were trapped by DMPO and then EPR and Mass spectrometry analysis (MS) using fast flow injection (FFI) in a water/acetonitrile were performed.

Oxidation of TPrA can lead to radical products,[100,101] and the nitroxide group can be lately reduced to give the analogous nitroxylamine (DMPOH) adduct (figure 2.22).

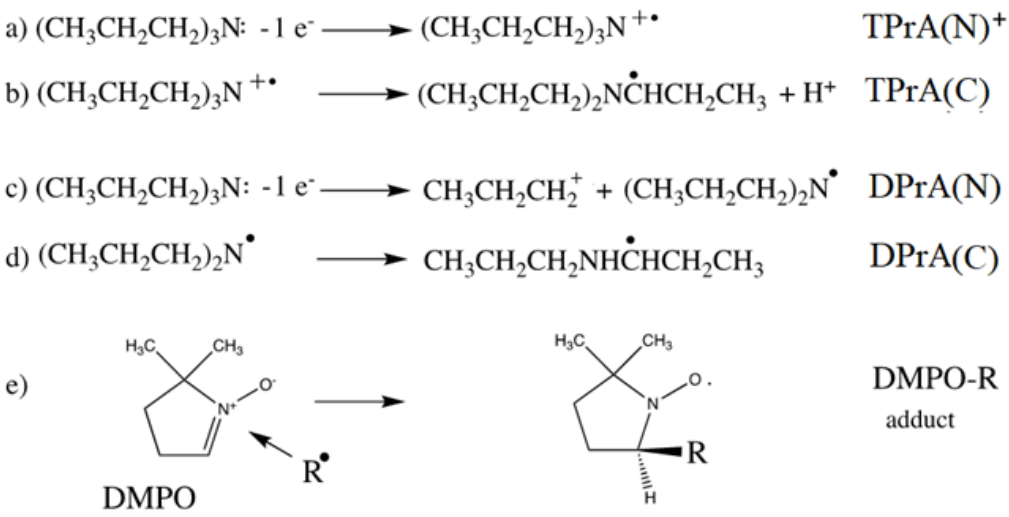

Figure 2.22. Reactions involved in the spin trapping experiments. a-d) Schematic reaction pathway for the oxidation of TPrA and the generation of TPrA and DPrA radicals. e) Spin trap 5,5-dimethyl-pyrroline N-oxide (DMPO) and formation of the spin-adducts by reaction of radicals R• with DMPO.

The experimental EPR spectrum (figure 2.23, black line) confirms the formation of a spin adduct with an amine (asterisks) with typical values for the hyperfine coupling constants (hfcc) for nitroxyde N a_N=15.5-16 G and for the characteristic β-proton $a_{N\text{-}\beta}$ =18-23 G (table 2.5 and spin-trap database[102,103]), but a difficult attribution to a trapping of either a N-centred (Add-N) or a C-centred (Add-C) adduct. Besides that, the spectrum shows the DMPO adduct with OH, and a normal nitroxide (RNO•), often present, and possibly formed from the decomposition of DMPO adducts.[104]

Adduct	a_N (G)	$a_{H\text{-}\beta}$ (G)	$a_{N\text{-}\beta}$ (G)	$a_{H\text{-}\gamma}$ (G)
DMPO-OH	14.95	14.67	/	/
Add-C	15.8	20.9	/	2.0
Add-N	17.4	19.4	2.0	/
RNO•	16.30	/	/	/

Table 2.5. Fitting parameters of spectrum in figure 2.23. The tentative attribution of the C-centred radical or the N-centred radical spin adducts is conducted on the base of the figure 2.21 and 2.22). The Greek labelling indicates the position with respect to the nitroxide N.

The results of the mass spectra evidence the formation of species DMPO-DPrA(C): the nitrogen radical cation undergoes a transposition to form a C-centred radical before to be trapped by DMPO. For the primary radical of TPrA, instead, we observe a peak relative to ions DMPO-TPrA(N)⁺ and/or DMPO-TPrA(C)-H⁺, with an extra proton because often nitroxides in acid solution can undergo disproportion to hydroxylamine and oxammonium cation.[105] From the mass spectra, it is not possible to distinguish between the formation of adduct DMPOH-TPrA(C) and DMPOH-TPrA(N)⁺ because the masses of the relative charged ions are the same.

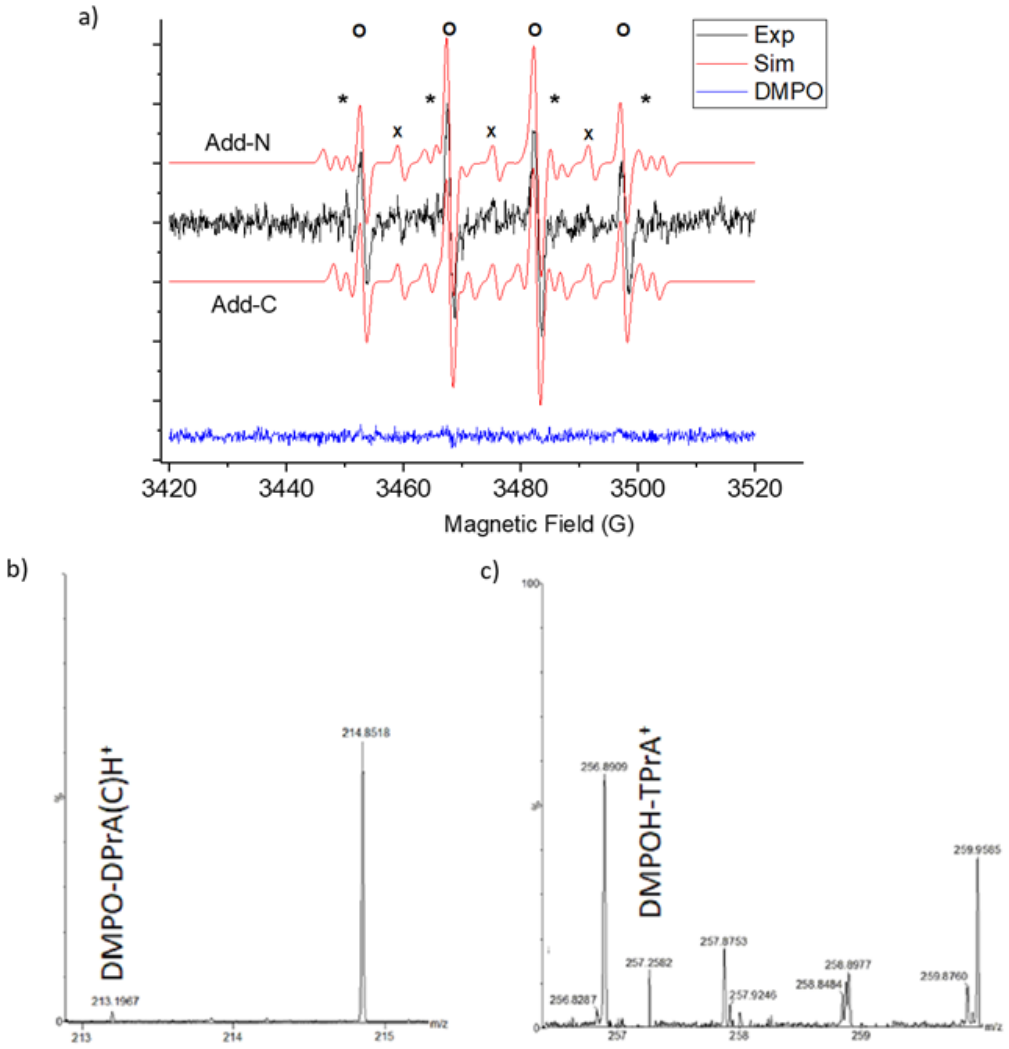

Figure 2.23. Spin Trapping experiments and analysis of radical intermediates. Analysis of the adducts formed during 1h electrolysis at 1.4V vs Ag/AgCl 1 mL solution in Ar saturated solution of DMPO (0.05 M)/TPrA (0.18 M) in formiate buffer at pH=6.8. a) EPR experimental spectrum (black line) and simulated (red lines) as sum of three adducts (accordingly with Supplementary table 2): DMPO-OH **(O)** +RNO• **(x)** + either an adduct compatible with an amine radical N-centred (Add-N) or a C-centred (Add-C) **(*)**. For reference, the spectrum of the solution of just the distilled DMPO exposed to air for 1 h is shown at the bottom (blue line). b) and c) Mass spectra of a solution showing the formation of spin adducts DMPO-DPrA(C)H^+ (m/z=213.1961) and DMPOH-TPrA $(+H)^+$ (m/z=257.2587); this label indicates the charged forms of DMPOH-TPrA$(N)^+$ and DMPOH-TPrA(C)-H^+, with an extra proton.

Mass spectra show the formation of DMPO-DPrA(C), and of the precursor DMPO-DPrA(N), as reported in figure 2.23b and on the inset blue pathway of figure 2.21 (DMPO-DPrA(C)H^+, m/z=213.1961). It was also observed the formation of a C-centred or a N-centred radical adduct of TPrA with DMPO, the charged forms with an extra proton DMPOH-TPrA$(N)^+$ and DMPOH-TPrA(C)H^+. The reduced form where the nitroxide turned into hydroxylamine was identified and showed in figure 2.23c and on inset red pathway of figure 2.21 (DMPOH-TPrA $(+H)^+$ with

m/z=257.2587). These last species have a larger signal that might be related to a larger concentration in the solution (table 2.6).

Adduct	m/z
DMPOH-TPrA(N)$^+$	257.2587
DMPOH-TPrA(C)H$^+$	257.2587
DMPO-DPrA(N)H$^+$	214.2040
DMPO-DPrA(C)H$^+$	213.1961

Table 2.6. Adducts obtained from the mass spectrometry analysis reported in figures 2.23b and 2.23c. For the structure schematization see figure 2.22 and 2.21.

3.5 Computational analysis

Quantum mechanical calculations were performed in order to estimate and compare the stability of the amine respect to the cleavage of the C–N bond close to the electrode (figure 2.24). The calculations were performed by Prof Fabrizia Negri research group of the university of Bologna using both the restricted and unrestricted density functional theory (DFT) methods, with the M062X functional[106] and the 6-31+G* basis set and the Gaussian16 suite of programs.[107] The calculations were performed in vacuo or including the effect of water as a solvent using the integral equation formalism model.[108] The potential energy curve (PES) of the C–N bond dissociation was computed under the effect of a strong external electric field[109] oriented along the C–N bond (pointing toward the N atom, red arrow in figure 2.24) and a strength of 0.025 a.u., which is typical during inner sphere electron transfer (of the order of 108 Vcm^{-1}).[110] The presence of electric field is important for inducing mechanistic changes in the reaction,[111] reproducing more realistically the experimental procedures and conditions. The elongation of the C–N bond acquires a typical reaction profile with a limited energy barrier to be overcome (around 1 eV for TPrA) and the mechanism shows a prevailing ionic character, suggesting the formation of carbocation. They were performed on TPrA (black curve in figure 2.24) and a new branched amine N-dipropyl isobutyl amine (DPIBA, grey curve in figure 2.24), and PES curve of DPIBA presents an easier C-N bond cleavage respect to the one of TPrA, consequently forming a more stable carbocation.

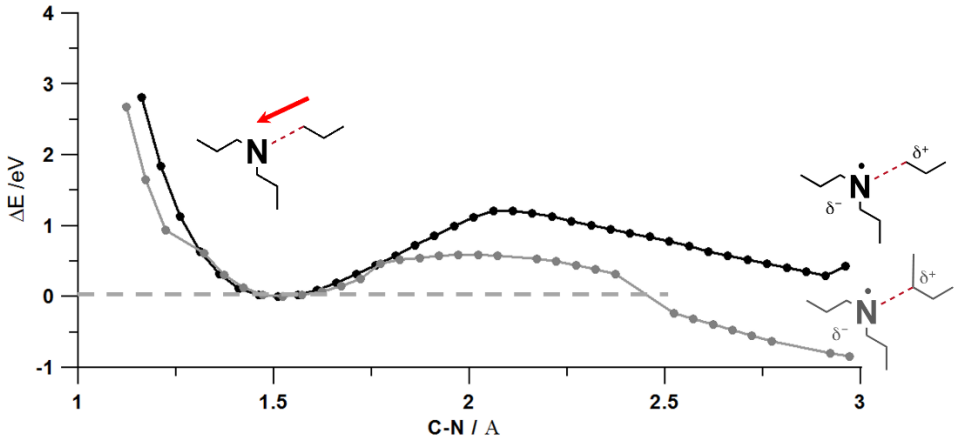

Figure 2.24. Potential energy curve along C–N (dashed red bond in the depicted molecular structures) stretching of TPrA (black curve and dots) and DPIBA (grey curve and dots) computed with UM062X/6-31G* in H_2O (described with IEFPCM method at each point of the curve; the energy of the equilibrium structure has been subtracted). The calculations are run in the presence of an external electric field (~108 V cm^{-1}) whose orientation is represented by the red arrow. Under the effect of the external electric field the curves acquire a typical reaction profile. The mechanism shows a prevailing ionic character with the formation of a carbocation propyl fragment (represented by the δ+ charge on the molecular structures).

3.6 ECL intensity enhancement proposal

ECL experiments allow the identification of two regions of reactivity: i) at long distances the just discovered heterogeneous mechanism[23] and radical and radical cation generated were responsible of ECL emission; ii) at small distance a new active pathway was observed and has an efficiency ~10 times higher than the one at long distance (figure 2.19). Intermediates analysis and quantum mechanical calculations confirmed what observed in these experiments giving the proofs for the identifications of the new intermediates.

A new and innovative strategy for the increase of technique sensitivity was designed exploiting all these findings. The idea was to increase the efficiency of the pathway at small distances, adding to TPrA solution a species with a more stable carbocation thus increasing the efficiency of C–N cleavage. The particular branched amine DPIBA[112] was proposed as additive, relying the decision on computational calculations that evidenced its larger C–N dissociative kinetic constant with respect to the one of TPrA (figure 2.24). In fact, the computed potential energy curve of DPIBA C–N dissociation in the presence of a strong interfacial electric field (figure 2.24, grey line) shows a higher stability of the reaction products than that of TPrA (figure 2.24, black line), with an even lower energy barrier to be overcome. This dissociation mechanism is much more efficient for DPIBA than for TPrA and the combination of these two amines was used for ECL signal enhancement acting simultaneously on both the reactive pathways: i) TPrA maintains efficient ECL emission at large

distances while ii) DPIBA increases the efficiency at small distances, favouring the formation of radical intermediates (figure 2.21). The success of this strategy and the role of DPIBA were tested by measuring ECL emission at the single-bead level in a surface generation–bead emission configuration (see appendix and paragraph 3.1 for the complete experimental setup). ECL images of 2.8-μm Ru@beads were acquired using 180mM TPrA in PB solution with or without different DPIBA concentrations (30 and 50 mM) as additive and their profiles were compared showing a clear difference in ECL intensity (figure 2.25). Specifically, analyzing the % signal gain, where 0.2 M PB with 180 mM TPrA is used as reference, we observed an increase in the ECL emission when 30 and 50 mM of additive were used. % Signal Gain was calculated using the following equation:

$$\%\ Signal\ Gain = \frac{\text{ECL intensity at X mM DPIBA}}{\text{ECL intensity with 0 mM DPIBA}} \text{ x } 100$$

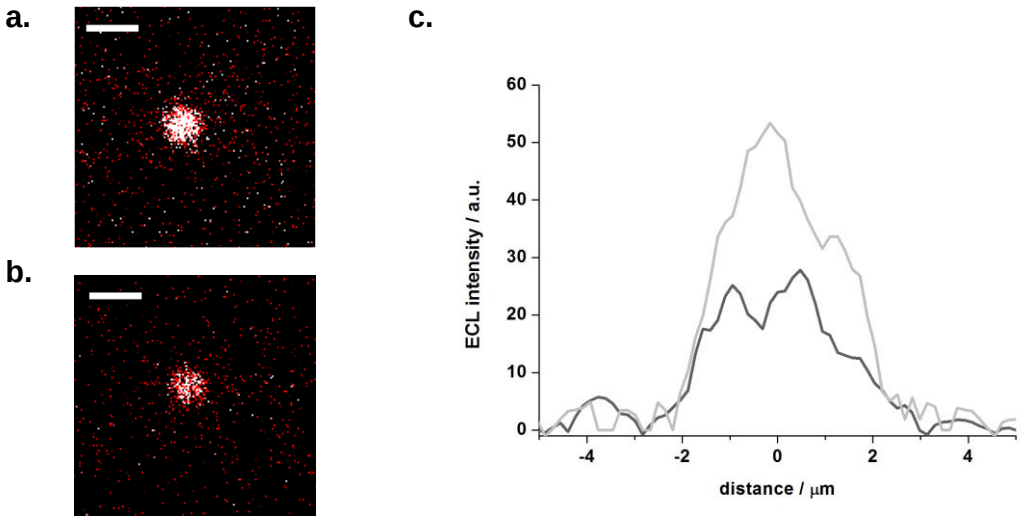

Figure 2.25. Bead-based assay using N-dipropyl isobutyl amine (DPIBA) as additive. ECL imaging of a 2.8 μm single bead was obtained by applying a constant potential of 1.4 V (vs. Ag/AgCl) for 4 s in 180 mM TPrA and PB 0.2 M a) with 50 mM DPIBA and b) without DPIBA. Integration time, 4 s; magnification, X100; scale bar, 5 μm. c) Comparison of the bead profile lines (black, without DPIBA; and grey, with 50 mM DPIBA).

DPIBA added to reaction solution at concentration of 30 mM increased the signal by 66% with respect to TPrA solution without additive, positively affecting ECL efficiency (figure 2.26). The increase of ECL efficiency is even more evident if 0.3 μm Ru@beads was used with 30 mM DPIBA as an additive in the surface generation–bead emission. An increase of 128% was observed compared to the analysis performed with TPrA alone, furtherly confirmed the DPIBA high reactivity at small distances and the efficient synergistic work between the two parallel mechanisms for technique sensitivity improvement (figure 2.26).

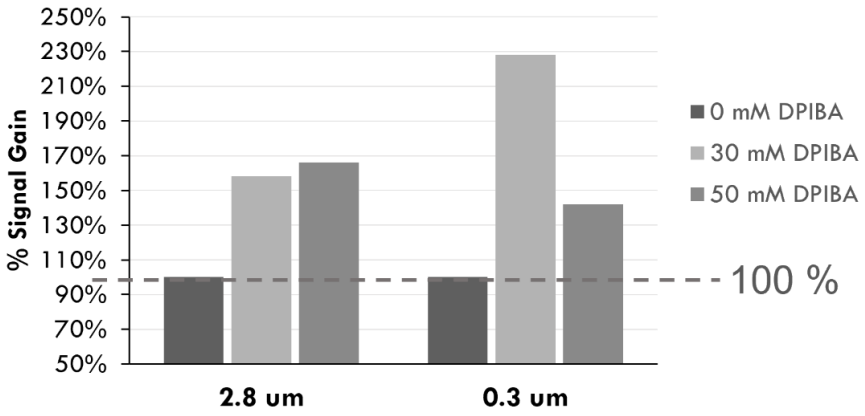

Figure 2.26. ECL Signal gain % calculated from ECL intensities of 2.8 μm and 0.3 μm beads in TPrA 180 mM solution in PB 0.2 M (pH 6.9), with 0 mM, 30 mM and 50 mM of DPIBA as additive. Potential was applied for 4 s at 1.4 V, the scan rate was 100 mV s^{-1} and the magnification X100, integration time 8s.

Two types of control experiments were performed to be sure of the new mechanistic pathway presented and of the new branched amines role as additive. In the first experiment, an equivalent total TPrA concentration substituted DPIBA as additive in the usual solution (180mM TPrA) and did not show significant enhancement with respect to the standard 180mM TPrA (figure 2.27). The design of the additive is fundamental for obtaining a molecule with a high C-N dissociation kinetic constant, necessary for stabilizing the carbocation and consequently the pathway active at small distances.

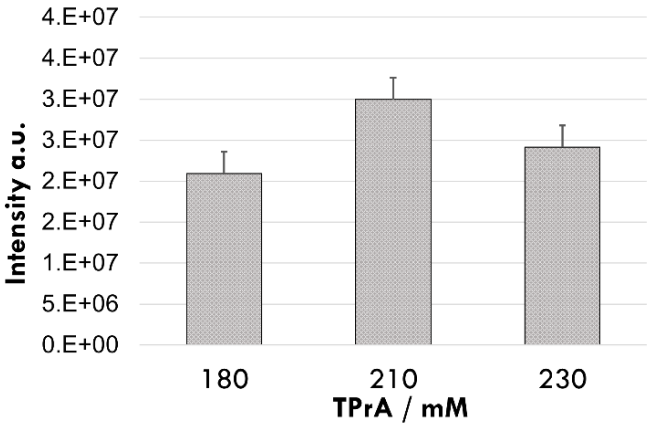

Figure 2.27. ECL intensities from single bead experiments of 2.8 μm beads in solution of PB 0.2 M (pH 6.9) with 180 mM, 210 mM and 230 mM of TPrA. Potential was applied for 4 s at 1.4 V. Magnification X100, integration time 8s. Error bar shows the standard deviation (n=10).

Instead, in the second type of experiments, DPIBA alone was used as coreactant (50, 100 and 180 mM) in the PB 0.2 M solution, resulting in a lower ECL signal than TPrA (figure 2.28). These final experiments underlined the importance of mechanism at long distance where TPrA oxidation

generates radical and radical cation more stable and efficient far from the electrode and respect to the ones of DPIBA.

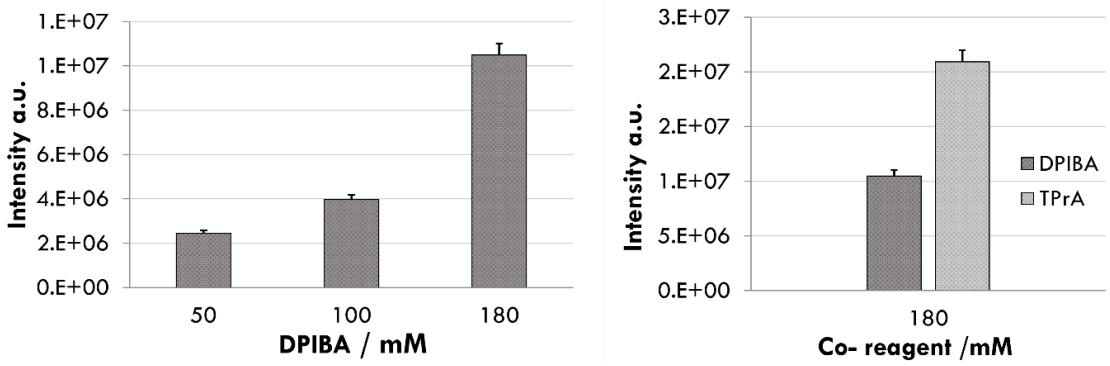

Figure 2.28. Surface generation–bead emission experiment performed with a) 2.8 μm beads in 50, 100, and 180 mM DPIBA in PB 0.2 M (pH 6.9) and b) 2.8 μm beads in 180 mM DPIBA in PB 0.2 M (pH 6.9) and 180 mM TPrA in PB 0.2 M (pH 6.9). Potential was applied for 4 s at 1.4 V. Magnification, X100, integration time 8s. Error bar shows the standard deviation (n=10).

3.7 Application of the new promising strategy in commercial immunoassay

The signal-enhancing effect of DPIBA observed in the surface generation–bead emission experiments was evaluated also on a Roche Diagnostics Cobas e 801 immunoassay analyzer using a series of Elecsys® assays. All the determinations were performed on a cobas® 8000 / cobas e 801 analyzer (figure 2.7) using the implemented assay protocols. The commercial ECL bead-based immunoassays Elecsys® combines automated immunoassays using magnetic microbeads and ECL detection in the $[Ru(bpy)_3]^{2+}$/TPrA system as presented in paragraph 1.2 and figures 2.2 and 2.6.[80] As mentioned above, ECL signals were generated under standard operating conditions on a Cobas e 801 analyzer using a biomarker containing the calibrator as sample. The only difference in reagents used was the replacement of TPrA coreactant solution ProCell II with PB 0.2 M, 180 mM TPrA and 0.1% polidocanol, which were supplemented with 0 mM (reference), 30 mM, and 50 mM of DPIBA, maintaining a constant conductivity (25 mS cm^{-1}) and pH (6.9). The ECL signals generated were normalized against the reference signals obtained with the reference buffer lacking DPIBA (signal gain [%]). All the commercially available Elecsys® assays tested here for the detection of specific biomarkers, TSH, troponin T, ferritin, and IgM antibodies against Toxoplasma gondii and hepatitis A, showed an increase in ECL signal when DPIBA was used as additive (figure 2.29). The first three assays are sandwich assay while the IgM are μ-capture assay type.[80] These experiments furtherly proved the efficiency of the new strategy in ECL signal increase and the use of DPIBA as an

additional coreactant is an example of how biomarker detection can benefit from this new proposed mechanism.

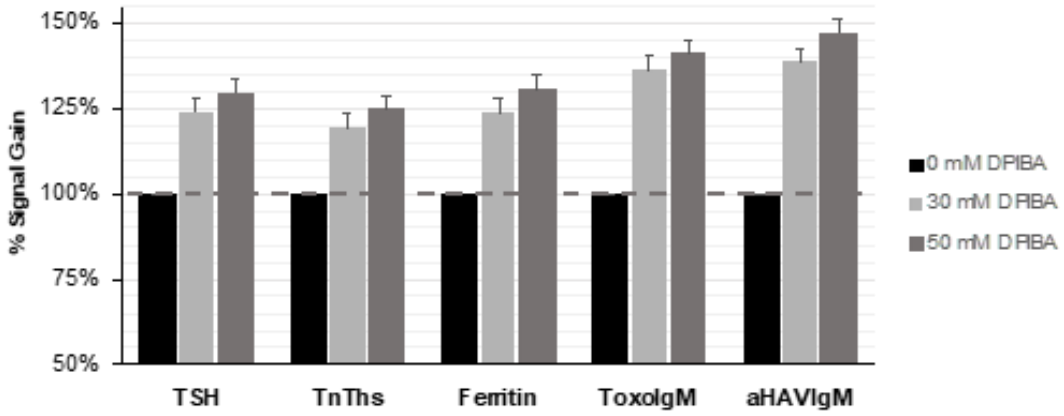

Figure 2.29. ECL signal gain observed in the presence of 30 and 50mM DPIBA (light and dark grey column, respectively) in 180mM TPrA, PB 0.2M, and 0.1% polidocanol solution compared with a reference buffer without DPIBA (black column). Measurement performed on a Roche Diagnostics Cobas e 801 immunoassay analyzer using the Elecsys® assays thyroid stimulating hormone (TSH), cardiac troponin T (TnThs), Ferritin, Toxoplasma gondii IgM (Toxo IgM), and hepatitis A IgM (A-HAV IgM) and a biomarker containing calibrator as sample. Error bar shows the standard deviation (n = 10).

All the results obtained in this second part among ECL imaging and combination with immunoassay provided insights into the emission mechanism useful for the discover of new and promising strategies towards the development of ultrasensitive biomarker analysis. This investigation allows to reach a concrete increase of ECL signal also in the case of commercially available Elecsys® assays performed with Cobas e 801 analyzer. The discovery of a new active pathway at small distances from the electrode allowed to increase the ECL emission up to 128% exploiting the mechanistic studies that have TPrA oxidation as protagonist. The two ways useful for increasing are i) the optimization of luminophore distribution by decreasing the bead size and ii) the addition of a branched amine to increase the efficiency of the coreactant mechanism. In the future, the combination of these two ways would bring to an unprecedented enhancement in the sensitivity and efficiency of ECL technique.

4. CONCLUSIONS

The protagonists of this chapter were the ECL immunoassays combined to ECL microscopy and the investigations on heterogeneous mechanism related to their emission generation. Many strategies were followed in the past for solving mechanistic and consequently reaching an increase in ECL sensitivity but, here, we focused on dye distribution and on the tuning of coreactant TPrA oxidation, the most important step in the heterogeneous mechanism, obtaining unexpected and astonishing results.

Firstly, an improved number of complexes active in the generation of ECL signals were concentrated in a single nanoparticle improving the NPs features toward higher signal intensity and the possibility to apply DDSNPs in a bead-based immunoassay system, respect to the past researches.[84,85] The coreactant diffusion towards emitting dyes were optimized and it will be further improved in order to reach all the dyes into the nanoparticles, increasing even more ECL signal intensity. Moreover, the silica matrix was able to increase the stability of the ECL signal from almost 70% to 40%, increasing even more the potential performances of these NPs. This improved stability and the signal increase of 750% open a new promising path towards more sensitive analyte detection, even in biosensing and in point-of-care devices.

The distribution of dyes, in the second part, was improved exploiting the surface-confined nature of ECL imaging technique. The $[Ru(bpy)_3]^{2+}$ was concentrated on micromagnetic beads with different diameters. An exponential increase in ECL signal was observed decreasing the distances from the electrode. Two different trends were observed at small and long distances, promoting a mechanistic investigation with the goal of tuning the TPrA oxidation and the consequent improvement in the sensitivity of the technique. A new path at short distances (< 1 μm) from the electrode surface was discovered and the introduction of additive successfully optimized coreactant oxidation, obtaining a 128% higher ECL signal. The combination of two complementary approaches (surface generation-bead and tip generation–surface emission) allowed to investigate the spatial distribution of ECL emission efficiency: at short distances the short-lived $TPrA^{\bullet+}$ is intercepted by luminophores more efficiently but also there are new species with a much shorter lifetime than $TPrA^{\bullet+}$ (200 μs) and responsible for a huge increase of ECL efficiency at distances < 1 μm. A parallel mechanism of TPrA oxidation was hypothised and proved: a N-centred dipropylamine radical is generated by C-N bond cleavage simultaneously with the usual formation of $TPrA^{\bullet}$ and $TPrA^{\bullet+}$ (figure 2.21). In order to

increase the efficiency of the mechanism at short distances a new branched amine coreactant (i.e. N-dipropyl isobutyl amine, DPIBA) with more stable carbocation was added to TPrA solution, reaching finally higher ECL performance also in commercial Elecsys® assays performed in the Roche Diagnostics Cobas e 801 immunoassay analyzer.

These findings more deeply underline how mechanistic investigations allow to single out different strategies for increasing signal intensity and temporal and spatial resolution towards a super-resolved technique. Several ECL based immunoassays are run worldwide every day and recent developments gave an important boost to the technique for application in single-molecule detection and imaging.

REFERENCES

1. Miao, W. Electrogenerated Chemiluminescence and Its Biorelated Applications. *Chem. Rev.* **108**, 2506–2553 (2008).
2. Richter, M. M. Electrochemiluminescence (ECL). *Chem. Rev.* **104**, 3003–3036 (2004).
3. Engstrom, R. C., Pharr, C. M. & Koppang, M. D. Visualization of the edge effect with electrogenerated chemiluminescence. *J. Electroanal. Chem. Interfacial Electrochem.* **221**, 251–255 (1987).
4. Engstrom, R. C., Johnson, K. W. & DesJarlais, S. Characterization of electrode heterogeneity with electrogenerated chemiluminescence. *Anal. Chem.* **59**, 670–673 (1987).
5. Szunerits, S., Tam, J. M., Thouin, L., Amatore, C. & Walt, D. R. Spatially Resolved Electrochemiluminescence on an Array of Electrode Tips. *Anal. Chem.* **75**, 4382–4388 (2003).
6. Chovin, A., Garrigue, P., Vinatier, P. & Sojic, N. Development of an Ordered Array of Optoelectrochemical Individually Readable Sensors with Submicrometer Dimensions: Application to Remote Electrochemiluminescence Imaging. *Anal. Chem.* **76**, 357–364 (2004).
7. Zhang, J. & Jiang, D. Chapter16. Electrochemiluminescence imaging. in *Analytical Electrogenerated Chemiluminescence: From Fundamentals to Bioassays* (ed. Sojic, N.) 471–491 (Royal Society of Chemistry, 2020).
8. Ding, H., Guo, W. & Su, B. Electrochemiluminescence Single-Cell Analysis: Intensity- and Imaging-Based Methods. *Chempluschem* **85**, 725–733 (2020).
9. Qi, H. & Zhang, C. Electrogenerated chemiluminescence biosensing. *Anal. Chem.* **92**, 524–534 (2020).
10. Dong, J. *et al.* Direct imaging of single-molecule electrochemical reactions in solution. *Nature* **596**, 244–249 (2021).
11. Husain, R. A., Barman, S. R., Chatterjee, S., Khan, I. & Lin, Z.-H. Enhanced biosensing strategies using electrogenerated chemiluminescence: recent progress and future prospects. *J. Mater. Chem. B* **8**, 3192–3212 (2020).
12. Liu, Y. *et al.* Single Biomolecule Imaging by Electrochemiluminescence. *J. Am. Chem. Soc.* **19**, jacs.1c06673 (2021).
13. Ma, Y., Colin, C., Descamps, J., Arbault, S. & Sojic, N. Shadow Electrochemiluminescence Microscopy of Single Mitochondria. *Angew. Chemie Int. Ed.* **60**, 18742–18749 (2021).
14. Chen, M.-M., Xu, C.-H., Zhao, W., Chen, H.-Y. & Xu, J.-J. Super-Resolution Electrogenerated Chemiluminescence Microscopy for Single-Nanocatalyst Imaging. *J. Am. Chem. Soc.* **143**, 18511–18518 (2021).
15. Zanut, A., Fiorani, A., Rebeccani, S., Kesarkar, S. & Valenti, G. Electrochemiluminescence as emerging microscopy techniques. *Anal. Bioanal. Chem.* **411**, 4375–4382 (2019).
16. Qi, H. & Zhang, C. Electrogenerated Chemiluminescence Biosensing. *Anal. Chem.* **92**, 524–534 (2020).
17. Valenti, G., Fiorani, A., Li, H., Sojic, N. & Paolucci, F. Essential Role of Electrode Materials in Electrochemiluminescence Applications. *ChemElectroChem* **3**, 1990–1997 (2016).
18. Valenti, G. *et al.* Electrogenerated chemiluminescence from metal complexes-based nanoparticles for highly sensitive sensors applications. *Coord. Chem. Rev.* **367**, 65–81 (2018).
19. Fiorani, A. *et al.* Advanced carbon nanomaterials for electrochemiluminescent biosensor applications. *Curr. Opin. Electrochem.* **16**, 66–74 (2019).
20. Rebeccani, S., Zanut, A., Santo, C. I., Valenti, G. & Paolucci, F. A Guide Inside Electrochemiluminescent Microscopy Mechanisms for Analytical Performance Improvement. *Anal. Chem.* **94**, 336–348 (2022). https://pubs.acs.org/doi/full/10.1021/acs.analchem.1c05065

21. Wang, Y. & Su, B. Deciphering the Mechanisms of Electrochemiluminescence by Spatially Resolved Measurements. *Anal. Sens.* **1**, 148–155 (2021).
22. Zu, Y. & Bard, A. J. Electrogenerated Chemiluminescence. 66. The Role of Direct Coreactant Oxidation in the Ruthenium Tris(2,2′)bipyridyl/Tripropylamine System and the Effect of Halide Ions on the Emission Intensity. *Anal. Chem.* **72**, 3223–3232 (2000).
23. Miao, W., Choi, J.-P. & Bard, A. J. Electrogenerated Chemiluminescence 69: The Tris(2,2′-bipyridine)ruthenium(II), (Ru(bpy) 3 2+)/Tri- n -propylamine (TPrA) System RevisitedA New Route Involving TPrA •+ Cation Radicals. *J. Am. Chem. Soc.* **124**, 14478–14485 (2002).
24. Song, X. *et al.* Peptide-Based Electrochemiluminescence Biosensors Using Silver Nanoclusters as Signal Probes and Pd-Cu 2 O Hybrid Nanoconcaves as Coreactant Promoters for Immunoassays. *Anal. Chem.* **93**, 13045–13053 (2021).
25. Cao, Z., Shu, Y., Qin, H., Su, B. & Peng, X. Quantum Dots with Highly Efficient, Stable, and Multicolor Electrochemiluminescence. *ACS Cent. Sci.* **6**, 1129–1137 (2020).
26. Ma, C., Cao, Y., Gou, X. & Zhu, J.-J. Recent Progress in Electrochemiluminescence Sensing and Imaging. *Anal. Chem.* **92**, 431–454 (2020).
27. Adamson, N. S. *et al.* Emission from the working and counter electrodes under co-reactant electrochemiluminescence conditions. *Chem. Sci.* **12**, 9770–9777 (2021).
28. Roche Diagnostic corporation. (2018). Available at: www.roche.com.
29. Sentic, M. *et al.* Mapping electrogenerated chemiluminescence reactivity in space: mechanistic insight into model systems used in immunoassays. *Chem. Sci.* **5**, 2568–2572 (2014).
30. Voci, S., Al-Kutubi, H., Rassaei, L., Mathwig, K. & Sojic, N. Electrochemiluminescence reaction pathways in nanofluidic devices. *Anal. Bioanal. Chem.* **412**, 4067–4075 (2020).
31. Sojic, N. *Analytical Electrogenerated Chemiluminescence: From Fundamentals to Bioassays. Detection Science.* (Royal Society of Chemistry (RSC) Publishing, 2020).
32. Kong, X., Wang, C., Pu, L., Gai, P. & Li, F. Self-Photocatalysis Boosted Electrochemiluminescence Signal Amplification via In Situ Generation of the Coreactant. *Anal. Chem.* **93**, 12441–12446 (2021).
33. Zanut, A. *et al.* DNA-Based Nanoswitches: Insights into Electrochemiluminescence Signal Enhancement. *Anal. Chem.* **93**, 10397–10402 (2021).
34. Carrara, S., Arcudi, F., Prato, M. & De Cola, L. Amine-Rich Nitrogen-Doped Carbon Nanodots as a Platform for Self-Enhancing Electrochemiluminescence. *Angew. Chemie Int. Ed.* **56**, 4757–4761 (2017).
35. Kerr, E., Doeven, E. H., Wilson, D. J. D., Hogan, C. F. & Francis, P. S. Considering the chemical energy requirements of the tri-n-propylamine co-reactant pathways for the judicious design of new electrogenerated chemiluminescence detection systems. *Analyst* **141**, 62–69 (2016).
36. Zhang, J., Arbault, S., Sojic, N. & Jiang, D. Electrochemiluminescence Imaging for Bioanalysis. *Annu. Rev. Anal. Chem.* **12**, 275–295 (2019).
37. Ding, J., Zhou, P., Guo, W. & Su, B. Confined Electrochemiluminescence Generation at Ultra-High-Density Gold Microwell Electrodes. *Front. Chem.* **8**, 1–8 (2021).
38. Guo, W., Zhou, P., Sun, L., Ding, H. & Su, B. Microtube Electrodes for Imaging the Electrochemiluminescence Layer and Deciphering the Reaction Mechanism. *Angew. Chemie Int. Ed.* **60**, 2089–2093 (2021).
39. Ding, H., Guo, W., Ding, L. & Su, B. Confined Electrochemiluminescence at Microtube Electrode Ensembles for Local Sensing of Single Cells †. *Chinese J. Chem.* **39**, 2911–2916 (2021).

40. Ding, H. *et al.* Spatially Selective Imaging of Cell–Matrix and Cell–Cell Junctions by Electrochemiluminescence. *Angew. Chemie Int. Ed.* **60**, 11769–11773 (2021).
41. Chen, Y., Gou, X., Ma, C., Jiang, D. & Zhu, J.-J. A Synergistic Coreactant for Single-Cell Electrochemiluminescence Imaging: Guanine-Rich ssDNA-Loaded High-Index Faceted Gold Nanoflowers. *Anal. Chem.* **93**, 7682–7689 (2021).
42. Ma, C. *et al.* Catalytic route electrochemiluminescence microscopy of cell membranes with nitrogen-doped carbon dots as nano-coreactants. *Chem. Commun.* **57**, 2168–2171 (2021).
43. Ma, C. *et al.* Bio-Coreactant-Enhanced Electrochemiluminescence Microscopy of Intracellular Structure and Transport. *Angew. Chemie Int. Ed.* **60**, 4907–4914 (2021).
44. Cui, C., Jin, R., Jiang, D., Zhang, J. & Zhu, J. Visualization of an Accelerated Electrochemical Reaction under an Enhanced Electric Field. *Research* **2021**, 1–9 (2021).
45. Guo, W., Ding, H., Zhou, P., Wang, Y. & Su, B. Electrochemiluminescence Waveguide in Single Crystalline Molecular Wires. *Angew. Chemie Int. Ed.* **59**, 6745–6749 (2020).
46. Li, S. *et al.* Fingerprints mapping and biochemical sensing on smartphone by electrochemiluminescence. *Sensors Actuators B Chem.* **285**, 34–41 (2019).
47. Hu, S., Cao, Z., Zhou, L., Ma, R. & Su, B. Electrochemiluminescence imaging of latent fingerprints by electropolymerized luminol. *J. Electroanal. Chem.* **870**, 114238 (2020).
48. Li, S. *et al.* Electrochemiluminescence on smartphone with silica nanopores membrane modified electrodes for nitroaromatic explosives detection. *Biosens. Bioelectron.* **129**, 284–291 (2019).
49. Gao, H., Han, W., Qi, H., Gao, Q. & Zhang, C. Electrochemiluminescence Imaging for the Morphological and Quantitative Analysis of Living Cells under External Stimulation. *Anal. Chem.* **92**, 8278–8284 (2020).
50. Liu, G., Ma, C., Jin, B. K., Chen, Z. & Zhu, J. J. Direct Electrochemiluminescence Imaging of a Single Cell on a Chitosan Film Modified Electrode. *Anal. Chem.* **90**, 4801–4806 (2018).
51. Liu, G. *et al.* Electrochemiluminescence Investigation of Glucose Transporter 4 Expression at Skeletal Muscle Cells Surface Based on a Graphene Hydrogel Electrode. *Anal. Chem.* **91**, 3021–3026 (2019).
52. Zhang, H. *et al.* Electrochemiluminescence-Microscopy for microRNA Imaging in Single Cancer Cell Combined with Chemotherapy-Photothermal Therapy. *Anal. Chem.* **91**, 12581–12586 (2019).
53. Chen, Y. *et al.* In Situ Imaging Facet-Induced Spatial Heterogeneity of Electrocatalytic Reaction Activity at the Subparticle Level via Electrochemiluminescence Microscopy. *Anal. Chem.* **91**, 6829–6835 (2019).
54. Ma, C. *et al.* Hydrogen Evolution Reaction Monitored by Electrochemiluminescence Blinking at Single-Nanoparticle Level. *Nano Lett.* **20**, 5008–5016 (2020).
55. Chen, M.-M. *et al.* Spatiotemporal imaging of electrocatalytic activity on single 2D gold nanoplates via electrogenerated chemiluminescence microscopy. *Chem. Sci.* **10**, 4141–4147 (2019).
56. Zhu, H., Jiang, D. & Zhu, J.-J. High-resolution imaging of catalytic activity of a single graphene sheet using electrochemiluminescence microscopy. *Chem. Sci.* **12**, 4794–4799 (2021).
57. Glasscott, M. W., Dick, J. E. & Dick, J. E. Visualizing Phase Boundaries with Electrogenerated Chemiluminescence. *J. Phys. Chem. Lett.* **11**, 4803–4808 (2020).
58. Glasscott, M. W., Voci, S., Kauffmann, P. J., Chapoval, A. I. & Dick, J. E. Mapping Solvent Entrapment in Multiphase Systems by Electrogenerated Chemiluminescence. *Langmuir* **37**, 2907–2912 (2021).

59. Bouffier, L., Manojlovic, D., Kuhn, A. & Sojic, N. Advances in bipolar electrochemiluminescence for the detection of biorelevant molecular targets. *Curr. Opin. Electrochem.* **16**, 28–34 (2019).
60. Bouffier, L., Zigah, D., Sojic, N. & Kuhn, A. Bipolar (Bio)electroanalysis. *Annu. Rev. Anal. Chem.* **14**, 65–86 (2021).
61. Cao, J.-T. *et al.* Immuno-Electrochemiluminescent Imaging of a Single Cell Based on Functional Nanoprobes of Heterogeneous Ru(bpy) 3 2+ @SiO 2 /Au Nanoparticles. *Anal. Chem.* **90**, 10334–10339 (2018).
62. Wang, Y., Jin, R., Sojic, N., Jiang, D. & Chen, H. Intracellular Wireless Analysis of Single Cells by Bipolar Electrochemiluminescence Confined in a Nanopipette. *Angew. Chemie Int. Ed.* **59**, 10416–10420 (2020).
63. Ismail, A. *et al.* Bipolar Electrochemiluminescence Imaging: A Way to Investigate the Passivation of Silicon Surfaces. *ChemPhysChem* **22**, 1094–1100 (2021).
64. Luo, Y. *et al.* A multicolor electrochemiluminescence device based on closed bipolar electrode for rapid visual screening of Salmonella typhimurium. *Sensors Actuators B Chem.* **349**, 130761 (2021).
65. Anderson, T. J., Defnet, P. A. & Zhang, B. Electrochemiluminescence (ECL)-Based Electrochemical Imaging Using a Massive Array of Bipolar Ultramicroelectrodes. *Anal. Chem.* **92**, 6748–6755 (2020).
66. Chen, L. *et al.* A conceptual framework for the development of iridium(<scp>iii</scp>) complex-based electrogenerated chemiluminescence labels. *Chem. Sci.* **10**, 8654–8667 (2019).
67. Valenti, G. *et al.* Single Cell Electrochemiluminescence Imaging: From the Proof-of-Concept to Disposable Device-Based Analysis. *J. Am. Chem. Soc.* **139**, 16830–16837 (2017).
68. Voci, S. *et al.* Surface-Confined Electrochemiluminescence Microscopy of Cell Membranes. *J. Am. Chem. Soc.* **140**, 14753–14760 (2018).
69. Fiorani, A. *et al.* Spatially resolved electrochemiluminescence through a chemical lens. *Chem. Sci.* **11**, 10496–10500 (2020).
70. Adhikari, J., Rizwan, M., Keasberry, N. A. & Ahmed, M. U. Current progresses and trends in carbon nanomaterials-based electrochemical and electrochemiluminescence biosensors. *J. Chinese Chem. Soc.* **67**, 937–960 (2020).
71. Dutta, P. *et al.* Reactivity mapping of luminescence in space: Insights into heterogeneous electrochemiluminescence bioassays. *Biosens. Bioelectron.* **165**, 112372 (2020).
72. Han, D., Goudeau, B., Jiang, D., Fang, D. & Sojic, N. Electrochemiluminescence Microscopy of Cells: Essential Role of Surface Regeneration. *Anal. Chem.* **93**, 1652–1657 (2021).
73. Zheng, G., Patolsky, F., Cui, Y., Wang, W. U. & Lieber, C. M. Multiplexed electrical detection of cancer markers with nanowire sensor arrays. *Nat. Biotechnol.* **23**, 1294–1301 (2005).
74. Poudineh, M., Sargent, E. H., Pantel, K. & Kelley, S. O. Profiling circulating tumour cells and other biomarkers of invasive cancers. *Nat. Biomed. Eng.* **2**, 72–84 (2018).
75. Rusling, J. F., Kumar, C. V, Gutkind, J. S. & Patel, V. Measurement of biomarker proteins for point-of-care early detection and monitoring of cancer. *Analyst* **135**, 2496 (2010).
76. Whitesides, G. M. The 'right' size in nanobiotechnology. *Nat. Biotechnol.* **21**, 1161–1165 (2003).
77. Walcarius, A., Minteer, S. D., Wang, J., Lin, Y. & Merkoçi, A. Nanomaterials for bio-functionalized electrodes: recent trends. *J. Mater. Chem. B* **1**, 4878 (2013).
78. Turner, A. P. F. Biosensors: sense and sensibility. *Chem. Soc. Rev.* **42**, 3184 (2013).
79. Hesari, M. & Ding, Z. Review—Electrogenerated Chemiluminescence: Light Years Ahead. *J. Electrochem. Soc.* **163**, H3116–H3131 (2016).

80. Faatz, E. *et al.* Chapter 15. Automated Immunoassays for the Detection of Biomarkers in Body Fluids. in *Analytical Electrogenerated Chemiluminescence: From Fundamentals to Bioassays* 443–470 (Royal Society of Chemistry (RSC) Publishing, 2019). doi:10.1039/9781788015776-00443
81. Zanut, A. *et al.* Insights into the mechanism of coreactant electrochemiluminescence facilitating enhanced bioanalytical performance. *Nat. Commun.* **11**, 2668 (2020).
82. Imai, K. *et al.* Numerical Simulation of Doped Silica Nanoparticle Electrochemiluminescence. *J. Phys. Chem. C* **119**, 26111–26118 (2015).
83. Kesarkar, S. *et al.* Dye-doped nanomaterials: Strategic design and role in electrochemiluminescence. *Curr. Opin. Electrochem.* **7**, 130–137 (2018).
84. Valenti, G. *et al.* Variable Doping Induces Mechanism Swapping in Electrogenerated Chemiluminescence of Ru(bpy) 3 2+ Core–Shell Silica Nanoparticles. *J. Am. Chem. Soc.* **138**, 15935–15942 (2016).
85. Kesarkar, S. *et al.* Neutral Dye-Doped Silica Nanoparticles for Electrogenerated Chemiluminescence Signal Amplification. *J. Phys. Chem. C* **123**, 5686–5691 (2019).
86. Zanut, A. *et al.* Dye-Doped Silica Nanoparticles for Enhanced ECL-Based Immunoassay Analytical Performance. *Angew. Chemie Int. Ed.* **59**, 21858–21863 (2020).
87. Qi, L. Synthesis of Inorganic Nanostructures in Reverse Micelles. *Encycl. Surf. Colloid Sci.* **2**, 183–6207 (2006).
88. Chang, C.-L. & Fogler, H. S. Controlled Formation of Silica Particles from Tetraethyl Orthosilicate in Nonionic Water-in-Oil Microemulsions. *Langmuir* **13**, 3295–3307 (1997).
89. *Biotinilated antibody labelled Ru(bpy)32+ where used for increase the number of dye for active site with an averege of 6 dye for microbeads active site.*
90. Kesarkar, S. *et al.* Iridium(III)-Doped Core-Shell Silica Nanoparticles: Near-IR Electrogenerated Chemiluminescence in Water. *ChemElectroChem* **4**, 1690–1696 (2017).
91. Kozuch, S. & Martin, J. M. L. "Turning Over" Definitions in Catalytic Cycles. *ACS Catal.* **2**, 2787–2794 (2012).
92. Zu, Y., Ding, Z., Zhou, J., Lee, Y. & Bard, A. J. Scanning Optical Microscopy with an Electrogenerated Chemiluminescent Light Source at a Nanometer Tip. *Anal. Chem.* **73**, 2153–2156 (2001).
93. Amemiya, S., Bard, A. J., Fan, F. F., Mirkin, M. V & Unwin, P. R. Scanning Electrochemical Microscopy. *Annu. Rev. Anal. Chem.* **1**, 95–131 (2008).
94. Wightman, R. M., Forry, S. P., Maus, R., Badocco, D. & Pastore, P. Rate-Determining Step in the Electrogenerated Chemiluminescence from Tertiary Amines with Tris(2,2'-bipyridyl)ruthenium(II). *J. Phys. Chem. B* **108**, 19119–19125 (2004).
95. Giorio, C. *et al.* Online Quantification of Criegee Intermediates of α-Pinene Ozonolysis by Stabilization with Spin Traps and Proton-Transfer Reaction Mass Spectrometry Detection. *J. Am. Chem. Soc.* **139**, 3999–4008 (2017).
96. Costentin, C., Robert, M. & Savéant, J.-M. Concerted proton–electron transfers in the oxidation of phenols. *Phys. Chem. Chem. Phys.* **12**, 11179 (2010).
97. Smith, P. J. & Mann, C. K. Anodic methoxylation of tertiary amines. *J. Org. Chem.* **33**, 316–317 (1968).
98. Costentin, C., Robert, M. & Savéant, J.-M. Electron transfer and bond breaking: Recent advances. *Chem. Phys.* **324**, 40–56 (2006).
99. Portis, L. C., Bhat, V. V. & Mann, C. K. Electrochemical dealkylation of aliphatic tertiary and secondary amines. *J. Org. Chem.* **35**, 2175–2178 (1970).
100. Adenier, A., Chehimi, M. M., Gallardo, I., Pinson, J. & Vilà, N. Electrochemical Oxidation of

Aliphatic Amines and Their Attachment to Carbon and Metal Surfaces. *Langmuir* **20**, 8243–8253 (2004).
101. Das, S. & von Sonntag, C. The Oxidation of Trimethylamine by OH Radicals in Aqueous Solution, as Studied by Pulse Radiolysis, ESR, and Product Analysis. The Reactions of the Alkylamine Radical Cation, the Aminoalkyl Radical, and the Protonated Aminoalkyl Radical. *Zeitschrift für Naturforsch. B* **41**, 505–513 (1986).
102. Migita, C. T. & Migita, K. Spin Trapping of the Nitrogen-centered Radicals. Characterization of the DMPO/DEPMPO Spin Adducts. *Chem. Lett.* **32**, 466–467 (2003).
103. https://tools.niehs.nih.gov/stdb/index.cfm/spintrap/.
104. Zerbi, G. *et al.* Graphite particles induce ROS formation in cell free systems and human cells. *Nanoscale* **9**, 13640–13650 (2017).
105. Sen, V. D. & Golubev, V. A. Kinetics and mechanism for acid-catalyzed disproportionation of 2,2,6,6-tetramethylpiperidine-1-oxyl. *J. Phys. Org. Chem.* **22**, 138–143 (2009).
106. Zhao, Y. & Truhlar, D. G. The M06 suite of density functionals for main group thermochemistry, thermochemical kinetics, noncovalent interactions, excited states, and transition elements: two new functionals and systematic testing of four M06-class functionals and 12 other function. *Theor. Chem. Acc.* **120**, 215–241 (2008).
107. Frisch, M. J.; Trucks, G. W.; Schlegel, H. B.; Scuseria, G. E.; Robb, M. A.; Cheeseman, J. R.; Scalmani, G.; Barone, V.; Petersson, G. A.; Nakatsuji, H.; Li, X.; Caricato, M.; Marenich, A. V.; Bloino, J.; Janesko, B. G.; Gomperts, R.; Mennucci, B.; Hratch, D. J. Gaussian 16, Revision B.01. *Gaussian, Inc., Wallingford CT* 2016 (2016).
108. Tomasi, J., Mennucci, B. & Cammi, R. Quantum Mechanical Continuum Solvation Models. *Chem. Rev.* **105**, 2999–3094 (2005).
109. Schirmer, B. & Grimme, S. Electric field induced activation of H2—Can DFT do the job? *Chem. Commun.* **46**, 7942 (2010).
110. Bockris John, R. A. *Modern Electorchemistry Volume 2*. (1970).
111. Stuyver, T., Danovich, D., Joy, J. & Shaik, S. External electric field effects on chemical structure and reactivity. *WIREs Comput. Mol. Sci.* **10**, 1–22 (2020).
112. Josel, H.-P., Andres, H., Windfuhr, M., Larbolette, O. & Quint, S. Branched-chain amines in electrochemiluminescence detection. (2017).

CHAPTER III

CARBON NANOTUBES BIOSENSORS

In collaboration with

Prof Maurizio Prato research groups at

research center CIC biomaGUNE in San Sebastian

and at the University of Trieste

1. INTRODUCTION

Carbon nanomaterials (CNMs) are a class of nanomaterials based on carbon allotropes. Many different types of carbon structure exist and are classified for the number of dimensions in the nanoscale size, thanks to the ability of carbon to form sp^2 and sp^3 bonds with others carbon atoms (figure 3.1). The peculiar properties, as electrical conductivity, optical and magnetic properties, mechanical strength, and multifunctional nature allow the applications of this kind of material in many different fields ranging from electronics, optoelectronics, and photovoltaics to sensing, bioimaging, and therapeutics.[1] Nanocarbon-based theragnostic (i.e., therapeutics and diagnostics) is one of the most intensively studied applications that includes tissue engineering, drug delivery/gene carriers, photothermal nanoagents for cancer therapy, and fluorescent nanolabels for cell and tissue imaging.[2–4] Among them, carbon nanotubes (CNTs) and graphene (and its derivatives) have received the greatest interest in particular for sensing applications.[5,6]

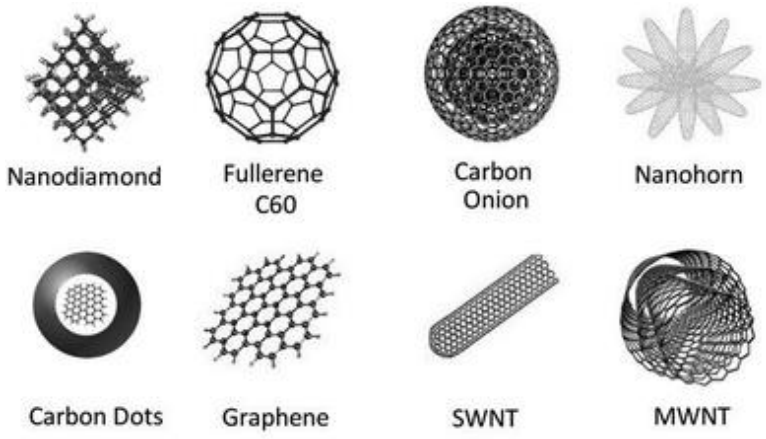

Figure 3.1. Different types of carbon nanomaterials (CNMs). Reprinted with permission from [6].

1.1 Graphene

In 2004 Geim and Novoselov discovered graphene, a single layer of graphite composed by a honeycomb lattice of sp^2 hybridized carbon atoms with gapless linear electron dispersion and extreme mechanical robustness. It can present two types of achiral edges usually both present, zig-zag or armchair, defined by the relative orientation of hexagons and with different properties and reactivity. Graphene can be present as monolayer, as several two-dimensional layers stacked together (graphene nanosheets) or in the form of graphene oxide (GO), and reduced graphene oxide (rGO).

Graphene has a high carrier mobility due to the sp^2 hybridization of carbon electrons to form conjugated π bond and an electrocatalytic activity that makes it an excellent nanoelectrode material for electrochemical biosensors.[7] It also has low thermal noise and layer dependent band tunability which make it a channel material for FET-based biosensors.[8,9] Many others applications were possible thanks to its amazing features like high thermal conductivity, superior mechanical strength, optical properties and excellent electronic conductivity, due to delocalized electrons, quality of the graphene lattice and number of layers.[10]

Several methods were developed to produce graphene taking into account a synthetic limitation: graphene 2D crystallites cannot be chemically grown because, increasing the lateral size, the crystallites lose stability and grow in the third dimension.[11] The synthetic methods can be divided into bottom-up and top-down approaches. The bottom-up approach consists in the direct formation of graphene from smaller carbon sources while top-down in separating the stacked sheets of graphite. For top-down strategies the most used are: i) micromechanical cleavage or "scotch tape";[11] ii) mechanochemical treatment through ball-milling,[12] used to exfoliate graphite with the help of an intercalating agent; iii) liquid-phase exfoliation by exploiting ultrasounds.[13] Despite the widespread use in large scale production of some of them, few layers with low quality and many defects can be obtained. The bottom-up strategy resulted more efficacious in the production of high-quality graphene sheet and include growth on silicon carbide substrate and chemical vapour deposition (CVD) on transition metals.[14,15] Moreover, graphene can be exfoliated by partially oxidizing graphite into graphene oxide (GO) layers with strong oxidants and concentrated acids, in order to weaken the interlayer bonding. The Hummers method[16] is the most used and allow to obtained materials with a great amount of oxygenated moieties, epoxy and hydroxyl on the basal plane and carboxylic and carbonyl on the edges,[17,18] improving hydrophilicity and easiness in functionalization, which is useful for a more stable material.[19] Then, the GO nanomaterials can be reduced by chemical or thermal methods to form reduced GO (rGO), recovering aromaticity but with defects still present. Their functionalization allows a better dispersion and non-aggregation of rGO nanosheets, representing a good alternative to graphene for biosensors.[20] GO or r-GO have many different functional groups on the surface that make them easier to be functionalized and consequently more biocompatible with respect to graphene, whose surface can be modified with a wide range of molecule and biomolecule, but its functionalization is limited by the stability of the aromatic π system. Moreover, rGO has higher electrical conductivity than graphene and it has quantum

confinement for optically excited electron−hole pairs that makes it optically active. Both features are due to percolation pathways between the sp^2 hybridized, small regions isolated. By tuning the sp^3/sp^2 ratio in GO, their band gap and optical properties can be modulated for bioelectronic applications.[21,22]

1.2 Carbon nanotubes (CNT)

Carbon nanotubes (CNT), which were discovered in 1991 by Iijima,[23] are defined as a graphene sheet rolled up in a well-known cylindrical shape (figure 3.2). They are composed by carbon, in a sp^2 hybridization, creating a hexagonal network and they can be classified through the number of layers (also called walls) they are made of: i) Single-walled carbon nanotubes (SWCNTs), that are comprised of a single cylinder with inner diameter ranging from 0.4 to 2 nm and the length up to several micrometers; ii) Multi-walled carbon nanotubes (MWCNTs), that are made of two or more concentric cylindrical sheets, and have diameters ranging between 2 and 100 nm. An interesting type of CNTs within this group are double-walled carbon nanotubes (DWCNTs), which are composed of two cylindrical sheets.[10]

CNTs can be also classified according to the different ways in which the graphene sheet is rolled up, revealing the importance of adopting two indices, *n* and *m*, for structure description, that are related to translational vector (T) and chiral vector (C_h), and the chiral angle θ between C_h and the zigzag direction of the graphene sheet (figure 3.2). T is parallel to the CNT axis, and C_h is orthogonal to T and connects two equivalent carbon atoms. The nanotubes are usually described using the chiral vector $C_h = n\mathbf{a}_1 + m\mathbf{a}_2$, which connects two crystallographically equivalent sites on a graphene sheet, where $\mathbf{a}_1$ and $\mathbf{a}_2$ are unit vectors of the hexagonal honeycomb lattice and *n* and *m* are integers. Each nanotube topology is usually characterized by these two integers, vectors, angle classifying them in i) zig-zag ($m = 0$, $n > 0$, $\theta = 0°$), ii) armchair ($n = m$, $\theta = 30°$), and iii) chiral ($0 < |m| < n$, $0 < \theta < 30°$) .[24]

They have high surface to volume ratio and an exceptional charge transport efficiency, the ability to tune their bandgaps over a broad wavelength range, semiconducting and metallic properties depending on the chiral vector, and high optical transparency values with low resistivity. Electronic properties of CNTs will depend on the angle in which graphene sheet is rolled up, defined by the indices (*n*, *m*).

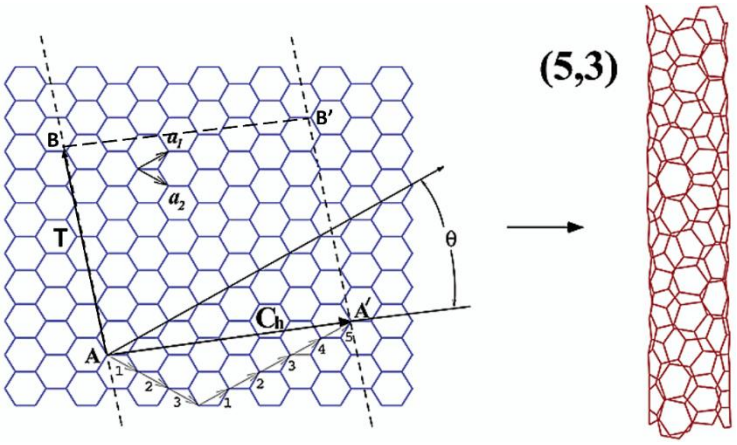

Figure 3.2. In the unrolled honeycomb lattice of a nanotube (left image) when we connect sites A and A', and sites B and B', a portion of a graphene sheet can be rolled seamlessly to form a SWCNT. The vectors AA' and AB define the chiral vector C_h and the translational vector T of the nanotube, respectively. The rectangle AA'B'B defines the unit cell for the nanotube. In this example, a (5,3) nanotube is illustrated on the right. Adapted with permission from [25]. Copyright 2002 American Chemical Society.

Hence, metallic CNTs, as armchair CNTs, have $m = n$; semi-metallic have $m - n = 3N$ (N = integer), and semi-conductor, as zig-zag CNTs, have $m - n \neq 3N$ (figure 3.3).[26] The structural and electronic properties, such as the carbon rings orientation and the diameter of the tube, are fully related. Instead, excellent mechanical strength is due to the strong carbon-carbon bond. SWCNTs have higher mechanical strength and flexibility than MWCNTs, reaching the performance of diamond and overcome the steel of five times.[27] Moreover, the electronic properties can be influenced by the introduction into the nanotubes structure of some defects, that are classified into i) topological (introduction of ring sizes other than hexagons), ii) rehybridization (ability of carbon atom to hybridize between sp^2 and sp^3), iii) incomplete bonding defects (vacancies, dislocations, ...), and iv) doping with other elements than carbon.[25]

CNTs can be mixed with engineering materials showing improved performance in terms of superior strength, flexibility, resistance, and isotropy. Finally, the optical properties are determined by relationship between thickness of film and wavelength of light. When the last one is higher than film thickness, light is transmitted with a minimum of absorbance and CNTs layer results transparent if the thickness is lower than 50 nm.[28]

The understanding of structure–property relationship was fundamental in the synthetic procedure improvement for controlling the structures of CNTs in the most accurate way. The chirality control was one of the most difficult to reach while the structure modulation is easier. Different chirality

depends on the direction where the graphene sheet is rolled in and are important because they dictate CNTs band structures and consequently their optoelectronic properties.

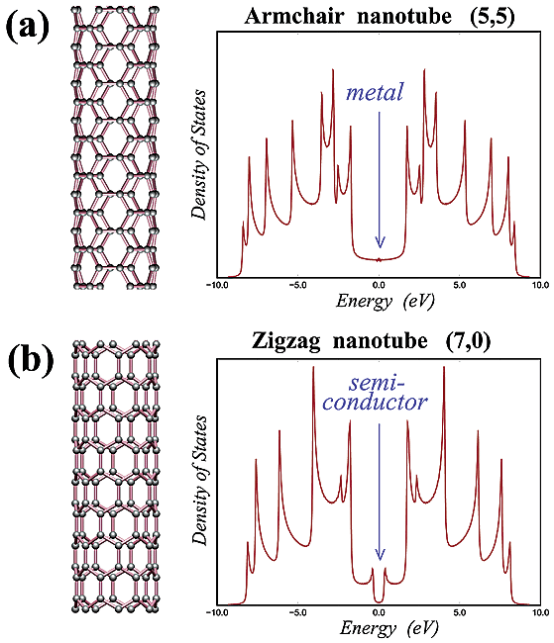

Figure 3.3. Electronic properties of two different carbon nanotubes. (a) The armchair nanotube exhibits a metallic behaviour (finite value of charge carriers in the DOS at the Fermi energy, located at zero). (b) The zigzag nanotube is a small gap semiconductor (no charge carriers in the DOS at the Fermi energy). Sharp spikes in the DOS are van Hove singularities (a,b). Reprinted with permission from [25]. Copyright 2002 American Chemical Society.

1.2.1 CNTs synthetic strategies

Many different types of synthesis were discovered since 1991 and they were constantly improved. The main ones are arc-discharge evaporation, laser ablation and chemical vapour deposition and all of them required a purification step.[29] Arc-discharge evaporation was used for the first time when CNTs were discovered.[23] It consists on the production of an arc in a small gap (> 1 mm) between two high-purity graphite electrodes exploiting a low voltage (30-35 V), high current (50-150 A) and power supply. This method is performed at very low pressures in controlled atmosphere and high temperatures (until almost 4000 °C) in the inner space between electrodes that make carbon sublimate from the anode, creating a plasma. When carbon condensates at the cathode, it acquires the shape of CNTs if metals were present in the anode that was consumed. Using this approach, large amounts of contaminated CNTs can be obtained and they require purification.

MWCNTs and SWCNTs can be also obtained by laser ablation.[30] In this method, metal-graphite composite is irradiated at high temperatures (almost 1200 °C) with laser under inert atmosphere and graphite vaporizes producing a soot which contains CNTs. The soot produced by laser vaporization

is swept by Ar gas from the high-temperature zone and deposited onto a water-cooled copper collector. With this method, the obtained CNTs have higher purity than arc-discharge CNTs, but the amount of material produced is lower.

Finally, chemical vapor deposition (CVD) is the class of process that seem to offer the best chance to obtain a controllable methodology for CNTs production of high quality and quantity. It involves the deposition of a solid material on a substrate from a gaseous source and specifically the formation of carbon filaments occurs from the catalytic decomposition of carbon-containing gas over metal surfaces. For CNTs production, a catalytic metallic nanoparticle (NP) is heated (500 – 1000 °C) in a tube furnace with a hydrocarbon gas flow. The CNT grows as consequence of the dissociation of hydrocarbon molecules catalysed by transition metal and saturation of carbon atoms in metal NP, after the cooling of the system at room temperature.[29] With this method, characteristics of CNTs can be tuned by varying operating conditions as temperature, pressure, concentration and kind of hydrocarbon, reaction time and characteristics of the catalytic metal NP. For example, by using different NP sizes, CNTs with different diameters can be obtained, and by varying the reaction time, length of nanotube can be modulated. CVD method allows the production of several structural forms of carbon, such as filaments and powder of amorphous carbon, graphite layers, SWCNTs and MWCNTs, and the selective CNT growth in a variety of forms, such as powder and aligned forest of CNTs is possible.

The modulation of parameters and the improvements in synthetic procedure allow to synthesize CNTs align in both vertical and horizontal directions as well as CNTs network which are highly required in integrated circuits, energy, and environmental applications, but also the researchers are making the synthesis of chirality pure CNTs even more accessible.[31]

The functionalization of CNTs represents a good strategy for properties modulation like the increase of solubility through introduction of functional groups with high oxygen ratio, and allows to improve the application of this material in more fields, like biosensor, where the immobilization of a receptor onto a transducer is mandatory.[32] The different functionalization approaches can be classified in three different groups: i) non-covalent adsorption, ii) endohedral filling of empty cavity inside, iii) and covalent attachment onto the tube walls through chemical reaction.[33]

Non-covalent functionalization of CNTs is based on non-covalent interactions such as Van der Waals forces or π-π stacking, that do not affect the electronic network of the tube. For example, they can be modified with surfactants but they are in dynamic equilibrium with molecules in bulk solution,

which makes them easy to remove, while the use of polymers wrapped on CNTs can overcome this disadvantage.[34] These π-π interactions have also allowed the non-covalent binding of biomolecules to CNTs, as proteins (streptavidin, cytochrome c or antibodies..), enzymes, oligonucleotides or DNA.[35]

In endohedral filling, the empty inner cavity of CNTs has been exploited to the functionalization with different substances, starting from liquid lead until metals, metal oxide, water, dielectric and organic molecules, or other carbon forms.[36]

Covalent functionalization is based on the covalent linking of functional groups to the outer wall of CNTs and it presents a high stability and different electronic properties. For example, fluorination allows to create starting points for new modifications as alkylation of the tubes and Diels-Alder cycloadditions.[37] Otherwise, CNTs can be functionalized with carboxylic groups by oxidation with acids, which can be further modified by amidation and esterification (figure 3.4).[38] Thanks to the extended π conjugation on CNTs walls, they undergo different cycloadditions and also allow the conjugation of polymers. One of the most used covalent attachments on CNTs is the arylation, a radical addition, by electrochemical reduction of aryldiazonium salts. Covalent attachment allows also a double functionalization of the CNTs and many different methods are discovered during these years, trying to solve the involvement of harsh conditions that brings several defects.[39–42]

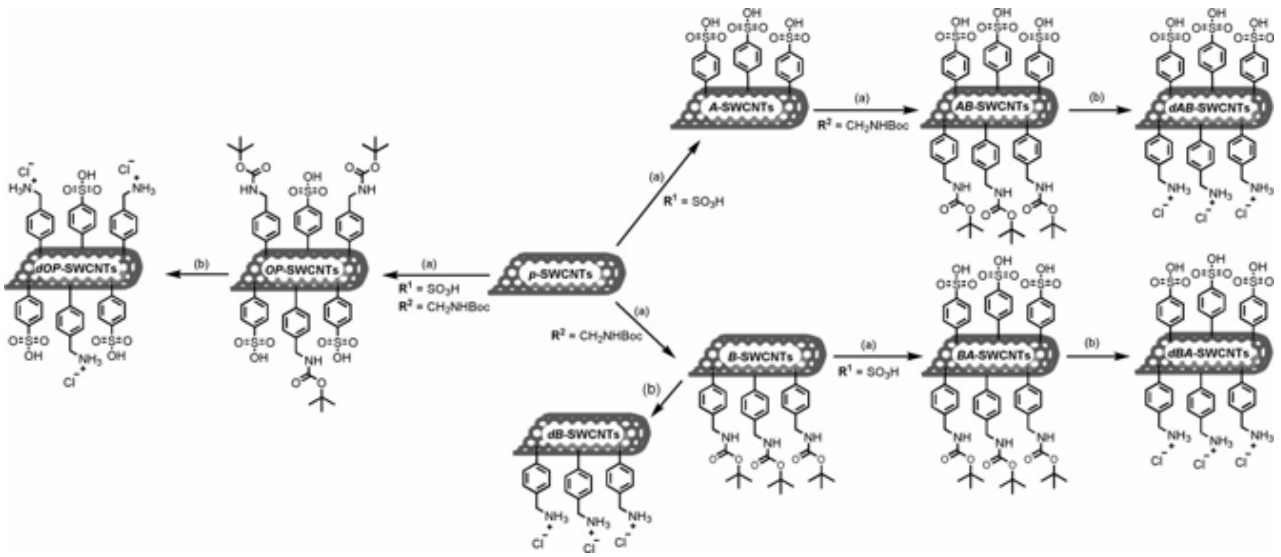

Figure 3.4. Example of CNT covalent functionalization sequence. Conditions: a) sulfanilic acid and/or 4-[(N-Boc)aminomethyl]aniline, isopentyl nitrite, DMF, 1 h, 808C; b) HCl (4m), RT, overnight. Reprinted with permission from [40].

1.2.2 CNTs and graphene characterization

Characterization techniques are very important for studying the structures, the features and the possible modifications and applications of the CNTs and graphene produced.

Raman spectroscopy is a very powerful technique for the characterization of sp^2 carbon materials, and it is based on the study of inelastic scattering of monochromatic light irradiating a sample, providing structural information on defects, stacking of layers or crystalline size.[43] Both graphene and CNTs present some characteristic Raman-features:

- graphite band (G band) around 1580 cm^{-1}
- G' band (or 2D band) between 2500 – 2900 cm^{-1}
- disorder band (D band) around 1530 cm^{-1}

and the relative intensity of D to G allow the determination of the number of defects in the sample. CNTs also present a characteristic Raman feature, due to their cylindrical shape, the radial breathing mode (RBM) between 100 – 300 cm^{-1}.

Another important characterization is thermogravimetric analysis (TGA) which records the weight of a sample as a function of an increasing temperature, usually until 1000 °C for carbon nanomaterials, and gives information on thermal stability and/or presence of other substances and bound organic moieties.

The elemental composition can be also defined and more precisely quantify by X-ray photoelectron spectroscopy (XPS), where the sample after irradiation with X-rays, emits photoelectrons from sample surface, whose intensity and the binding energy are measured by a photodetector. Moreover, the presence of primary amine on CNTs and graphene can be detected by a colorimetric analysis, the Kaiser test.[42] Finally, microscopy techniques, like transmission electron microscopy (TEM), scanning electron microscope (SEM) or atomic-force microscopy (AFM), give morphological information on graphene and CNTs, as diameter, length and CNTs number of walls or graphene number of layers.[40]

1.2.3 CNTs applications

The improvements in CNTs features control and synthesis enable the effective application of this knowledge to electronics, photonics, optoelectronics, wearable electronics, the Internet of Things (IoT), and artificial intelligence.[31,44]

In electrochemical systems CNTs found applications in lithium-ion battery and lead acid batteries, improving the potentiality of the anode and the electrical interface conductance through the increase of surface area, the cyclic activity of the battery and lowering the shedding of the material from the

electrodes or the destruction of electrodes. Moreover, CNTs can be used for digital circuits developments and can exploit their advantages and benefits compared to conventional materials to be inserted into many components of integrated circuit (ICs), like smartphone and tablet. CNT-based standard and flexible devices were continuously and feverishly being developed requiring less energy than conventional nanoscale manufacturing[45] and semiconductor CNTs are used as channel in field-effect transistors (FET).[44]

The use of high-density pure SWCNTs represents an important improvement together with the application of CNTs in memory and processing devices integrated in one chip, in floating transistors for the fabrication of artificial synapses for neuromorphic computing, and in tissue engineering research based on the neurogenesis. The goal of tissue engineering is the development of stimulus-responsive biomaterials, the scaffolds, that mimic the extracellular matrix of the native tissue being biocompatible, immunologically inert, conductive, and infection-resistant. Carbon nanotubes (CNTs) are one of the most promising materials to interface with electrically active tissues, because boost the electrical activity of neurons and increase the number and lengths of their neurites.[46]
Instead, photoluminescence and electroluminescence of semiconducting SWCNTs, due also to their chirality modulation, can be exploited for nanoscale photonic and optoelectronic devices including efficient light-emitting diodes, electrically driven bright thermal light emitters, and room-temperature photodetectors. Also electron gun sources for electron microscopes, electron lithography and microelectromechanical devices like AFM tips can be produced with CNTs showing their huge variety of applications due to even improvable features and adaptability.[44]

Finally, sensors are one of the most important applications of CNTs thanks to their high sensitivity, excellent physical and electronic properties, and solution processability.[10,47] They were used for detection of pressure, bending, thermal effects, strain, chemicals present in gas or liquid,[48,49] and biological particles in biological mediums like DNA, hormones, and antibodies.[44,50] Various types of electronic device architectures exist for the CNT-based sensors, including transistors, capacitors, and chemiresistors.[51] This last class was used for DNA detection[52–54] while other types of sensor based on electrical conductivity or on fluorescence as transducer element are devoted to detection of gas and organic molecules.[6,55–59] CNT-polymer composites can be used for pressure sensors for healthcare and tactile applications. The pressing motion and friction could be recognized through the difference in electrical resistance[60]and the MWCNT-gelatin hydrogel has ideal electronic skin performance.[61,62] In addition, CNTs composite were used for humidity sensing, fabrication of electrochemical sensors

and breath sensors on flexible substrates,[63] thermotherapy pad with a thermochromic indicator for controlling overheating,[64] and triboelectric nanogenerators for highly efficient high-power energy harvesters.[65] Instead, CNTs filaments have been adopted in inertial sensors to detect human motions, such as walking, jumping, and squatting, and they are self-powered by mechanical energy collected from coiled CNT.[31,66]

Thanks to their optical and fluorescent properties; CNTs can be used as a fluorescent-contrast agent for deep tissue fluorescence imaging,[67] for the tumor recognition and sensing,[68,69] for being transparent conductor in flexible organic light-emitting diodes (OLEDs) and applications in solar cells and photodetector.[31,70,71] CNTs can be modified with a biological sensing element, such as nucleic acids and peptides, or antibodies and enzymes, groups capable of recognising biomolecules or monitoring bioprocesses.[72] CNTs-based biosensors were successful and spread for detection of analytes such as toxins, drugs, genotoxic analytes, glucose and Hg^{+}, Ag^{+} and Pb^{+} ions in solution.[6]

Electrochemiluminescent sensors that use CNTs as electrode materials or working electrode modifications or emitting elements[73] are widely diffused and exploit high electron conductivity and large specific surface area, combined with fast kinetics for amine oxidation of this promising material.[32] In specific sensors, the chemical modification is also useful for anchoring the nanomaterial as a transducing component on the electrode and built an ultrasensitive ECL immunosensor array.[74] CNTs are highly suitable for carrying a recognition unit (e.g. the antibody), the luminophore or a catalyst to amplify the light signal, and the wiring allows the electric contact even at long distance from the electrode surface.[75] In fact, they were applied for detection of cancer biomarkers, such as prostate-specific membrane antigen[76] and carcinoembryonic antigen (CEA), or palytoxins,[75] small organic molecules such as organophosphorus pesticides or diclofenac, Escherichia coli bacteria,[77] and the emission ECL signal can be further improved adding catalytic materials to CNTs as NPs.[32] Moreover, the transparent CNTs electrodes opened a new path towards a more sensitive and higher spatially resolved ECL imaging detection of biological stuff as cells.[78,79] Even concerning the electrochemiluminescent (ECL) imaging detection, recently a novel 3D-printed automated miniature immunoarray was fabricated and validated to detect multiple proteins with ultralow detection limits, thanks to SWCNTs−antibody conjugates in the microwells and employing labelled antibody-decorated RUBPY-silica nanoparticles to generate ECL (figure 3.5). [74,80]

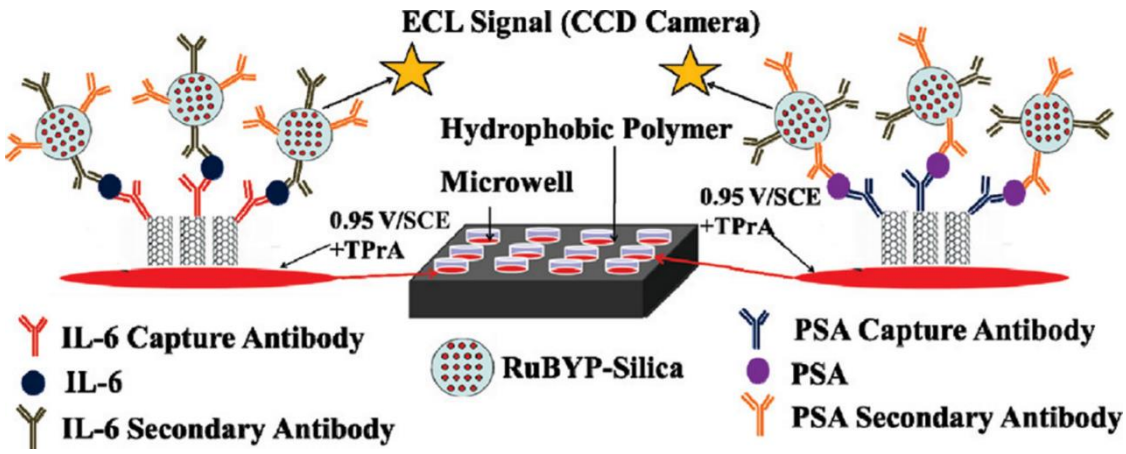

Figure 3.5. Representation of ECL Immunoarray. Discrete wells are shown in red on a 1 in. × 1 in. pyrolytic graphite chip (black). SWCNT forests are surrounded by hydrophobic polymer (white) to make microwells on the chip. Wells are filled with sample solutions and SWCNT forests decorated with primary antibodies in the bottom of the well, capture the analyte proteins. RuBPY-silica nanoparticles with cognate secondary antibodies are added and bind to the captured protein analytes. Appropriate washing with blocking buffers minimizes nonspecific binding. The chip is placed in an open top electrochemical cell, 0.95 V vs. SCE is applied, and ECL is detected by a CCD camera. Reprinted with permission from [74]. Copyright 2002 American Chemical Society

All the applications reported are only a really brief summary of the wide world of CNTs-based device, but it has the goal to give an idea of the importance of CNTs discovery and features/structures modulation.

1.3 Nanocarbon materials and Faraday-cage ECL approach[81]

Currently, sandwich-type immunoassay is the most used mode for electrochemiluminescence immunoassay ECLIA that allow to reach a high level of sensitivity and specificity. However, respect to the other types of sandwich-based technique (ELISA, RIA; CLIA…), in ECLIA is important the distance between electrochemiluminophores on the detection antibody and the electrode surface where they are anchored, and directly influences the generation of signals.

In electrode kinetics, OHP is the plane where solvated ions can approach the electrode. The electrons on the electrode (figure 3.6 A) and the electrochemiluminophores near the OHP were activated with the same energy when appropriate potential is applied. The electron transfer for activation of dyes is usually considered as tunnelling of the electron between them and states in the electrode. However, the electrochemiluminophores used as label of detection antibody are at a fixed distance x from the electrode, and only the ones inside the OHP can participate to electrochemical reactions generating the ECL while the luminophores too far away can't be excited. This behaviour is observed in the ECLIA system because the sandwich immunoassays are immobilized on the electrode and not

all the luminophore are inside the OHP. The Faraday-cage approach want to create a system where all the luminophore of all the immobilized immunocomplexes can participate to electrochemical reactions, consequently increasing the ECL signal intensity. It was defined "in-electrode" system (figure 3.6 D) because all the dyes present on detection antibody are inside the OHP thanks to the addition of conductive materials that extend the distance where electron transfer occurred through a conductive cage formation around immunocomplexes. Guo et al. used multi-functionalized graphene oxide (GO) materials to create a faraday-cage system, exploiting material unique properties, such as large surface area and good electric conductivity. These materials were connected to both the capture antibody and the detection antibody specific for neurotensin and favour electron transfer reactions and high loading. The capture unit was created by immobilizing capture antibody Ab1 on GO coated by Fe_3O_4 nanoparticles (nanoFe_3O_4@GO) and the detector unit by simultaneously immobilizing detector antibody Ab2 and electrochemiluminophore ABEI on the GO sheet. Both of them had three functional entities: i) in capture unit, Ab1 is the capture antibody, nanoFe3O4@GO allows one-step preparation, and the size of nanoFe3O4@GO ensured the construction of ''in-electrode'' nanoscale immune complex system; ii) in detector unit, ABEI is the electrochemiluminophore, Ab2 is the detection antibody; GO load a great amount of ABEI molecules and allow their participation to ECL reaction, improving the sensitivity.[81]

The ECL emission procedure is the same of a normal ECLIA but the presence of GO in the detector unit extends the OHP of the electrode. All the dye-labels can be excited because they are immobilized directly on the surface of the electrode or on the GO, becoming part of the electrode. In facts, the electrons can flow freely between the detection unit and the electrode (''in-electrode''). This system was called Faraday cage and all the electrochemiluminophores could be called "effective" and take part in the electrode reaction of ECL emission (Figure 3.6). In this way, a higher number of detection antibody can be labelled with dyes and all the dyes can participate to electrochemical reactions.

The FCT-ECLIA (Faraday cage type-ECLIA) technique attracted attention for the electrochemiluminescence analysis of several targets thanks to its high sensitivity, non-destructiveness and simplicity. Thus, the sensitive detection of a huge variety of elements like biomarkers, bacteria, pathogen, microRNA was facilitated by a shortened electron transfer distance between the electrode and dyes, also thanks to the powerful potentialities of multi-functionalize graphene oxide usually combined with catalytic materials.[82–84] It represents a really promising sensing technique with further possible optimizations.

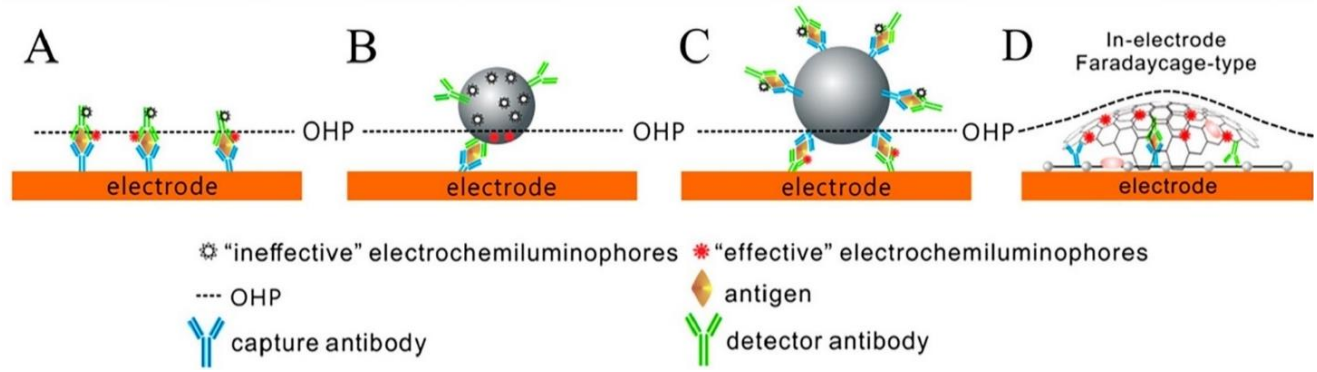

Figure 3.6. Schematic representation of (A-C) the conventional "on-electrode" sandwich-type ECLIA and (D) "in-electrode" Faraday-cage-type ECLIA. Reprinted with permission from [81].

1.4 Outlook

All the knowledge acquired in the previous chapters on the ECL heterogenous mechanism and from the combination with nanomaterial will be exploited in this chapter for creating a bead-based immunoassay system with enhanced ECL performance, thanks to the adoption of GO or CNTs as conductive material with great advantageous features for ECL generation and consequent detection of biomarkers. Firstly, a Faraday cage approach will be exploited for modulating the ECL emission layer, a limiting factor in ECL generation mechanism.[81,83–85] Herein, reduced graphene oxide and double-walled carbon nanotubes (f-CNTs) labelled with $[Ru(bpy)_3]^{2+}$ complex will be used for the functionalization of micromagnetic beads and the consequent formation of a conductive network, due to the intrinsic conductivity of CNTs.[86] The conductive layer activates an additional mechanism for ECL generation which is usually not active in heterogeneous beads system: the luminophore can be oxidized together with the coreactant making the homogeneous ECL path viable. Dyes are in close contact with a conductive material and their distance from the underlying electrode loses importance. The concomitant presence of the new mechanism and the heterogenous one enhanced ECL emission layer and ECL intensity with respect to the conventional micromagnetic beads labelled with $[Ru(bpy)_3]^{2+}$ complex without functionalized CNTs. All these findings open new and very promising routes towards an increase in the sensitivity of ECL immunoassays based on ECLM. Following this purpose, an immunoassay biosensor that exploits CNTs features will be started to create, in particular for the detection of cardiac Troponin, biomarker of Acute Myocardial Infarction, reaching the limit of detection of 0.74 ng mL^{-1}, which is under the critical point but still above the limit reached in literature.

2. ELECTROCHEMILUMINESCENT IMMUNOASSAY ENHANCEMENT DRIVEN BY CARBON NANOTUBES[86]

Inspired by the Faraday cage method explained in paragraph 1.3[81] we would create a conductive layer around the beads exploiting the amazing features of carbon-based nanomaterials that were successfully applied in the implementation of the ECL signal [87–90] thanks to the advantages previously presented and in particular to the fast kinetics for amine oxidation.[22,32,83,91–94] Despite the brilliant sensitivity, ECL has some limitations due to the diffusion of the electrogenerated coreactant radicals that remain near the electrode surface, due to their short lifetime, defining a confined ECL active layer.[95–97] Many strategies were adopted in the past for enhancing and controlling this ECL emitting layer and consequently the technique sensitivity.[82,83,98–105] Faraday cage strategy inspired a really promising method based on the construction of a conductive layer electronically wired to the electrode surface for extending the surface responsible of electron transfer and consequently enhancing the thickness of ECL emission layer. In fact, the idea was to oxidize the coreactant not only onto the "real" electrode surface but also onto the "extended" one, i.e. onto the carbon nanomaterials positioned at certain distances from the electrode but connected to it.

The idea was realized by covering magnetic beads with functionalized graphene oxide fGO (figure 3.7) and double walled carbon nanotubes (f-CNT) and the ECL signal was monitored and investigated through ECL microscopy, mimicking a commercial ECL beads-based immunoassay system. This system will be finally improved by the successful combination of nanomaterials, ECL, microscopy and mechanism investigation, obtaining more sensitive, specific, stable and highly performing system to be applied for detection of biomarkers, essential in the management of the actual pandemic scenario and the prevention of future epidemics.[106–108]

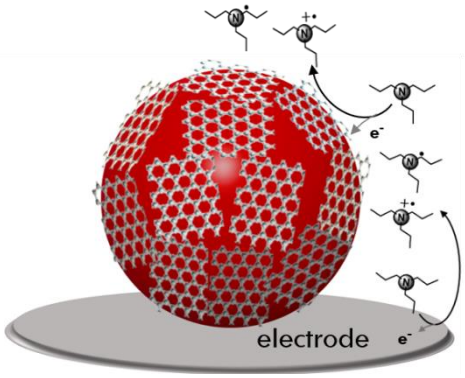

Figure 3.7. Magnetic bead (red sphere) covered by GO sheets and representation of the oxidation of TPrA coreactant on the electrode and on the conductive layer created by GO sheets.

2.1 Beads functionalization with fGO-Ru and ECL measurements

Graphene oxide (GO) were functionalized in collaboration with Prof Prato research group at the research center CICbiomaGUNE in San Sebastian obtaining a material (fGO-Ru) suitable for the functionalization of magnetic beads. Pristine GO sheet was functionalized with amino moieties, protected with two orthogonal protective groups which can be selectively removed, necessary to introduce the active moieties needed for the ECL, i) the $[Ru(bpy)_3]^{2+}$ complex as luminophore and ii) the biotin for linking fGO-Ru sheets to the beads. The functionalization was performed in a one-pot synthetic step using a Boc-monoprotected diamine and a TFA-monoprotected diamine.[19] Then, Boc protective group was removed and Ru moiety introduced and after, the other group, TFA, was removed and the free terminal amine bound to biotin (synthetic procedure in figure 3.8 and in the appendix).

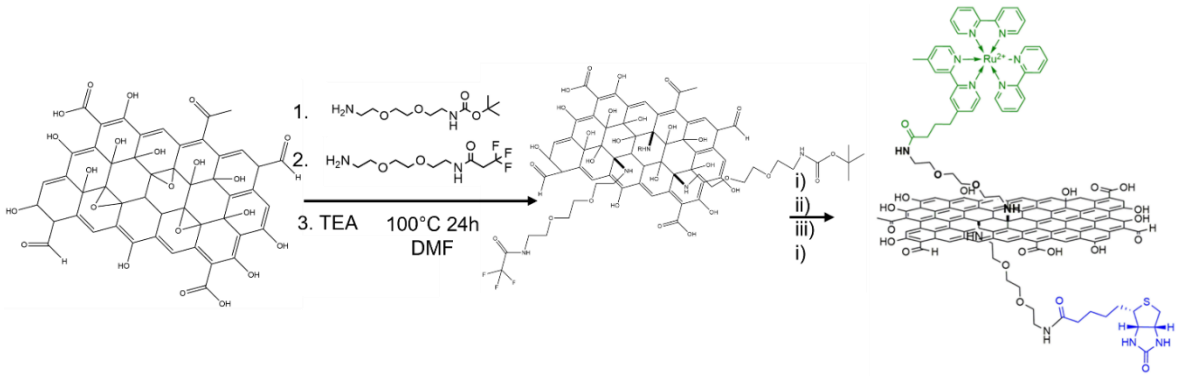

Figure 3.8. Schematic representation for the synthesis of fGO-Ru labelled with $[Ru(bpy)_3]^{2+}$ and biotin; 1) Boc-monoprotected diamine, 2) TFA-monoprotected diamine, 3) Triethylamine, 100 °C for 24 h in DMF; i) HCl concentrated, 1,4-dioxane, r.t. overnight (Boc deprotection); ii) $Ru(bpy)_3C_3H_6COOH$, EDC, NHS in DMF overnight; iii) NH_3, MeOH, overnight under stirring; iv) biotin, EDC, NHS in MES buffer (pH 6).

The fGO was used for labelling the 2.8 µm magnetic beads exploiting the strong bonding biotin-streptavidin (see more information in the appendix) and creating a conductive layer labelled with $[Ru(bpy)_3]^{2+}$ that cover the microparticles (beads@fGO-Ru, figure 3.7). The ECL signal was acquired through a microscope combined to an EMCCD camera in the presence of 180 mM of TPrA and after beads immobilization onto a Pt electrode. The ECL intensity acquired was inhomogeneous (some beads didn't emit any light) and really lower with respect to beads functionalized with the biotinylated antibodies labelled with $[Ru(bpy)_3]^{2+}$ (beads@Ru) that mimics the usual beads-based immunoassay system (figure 3.9).

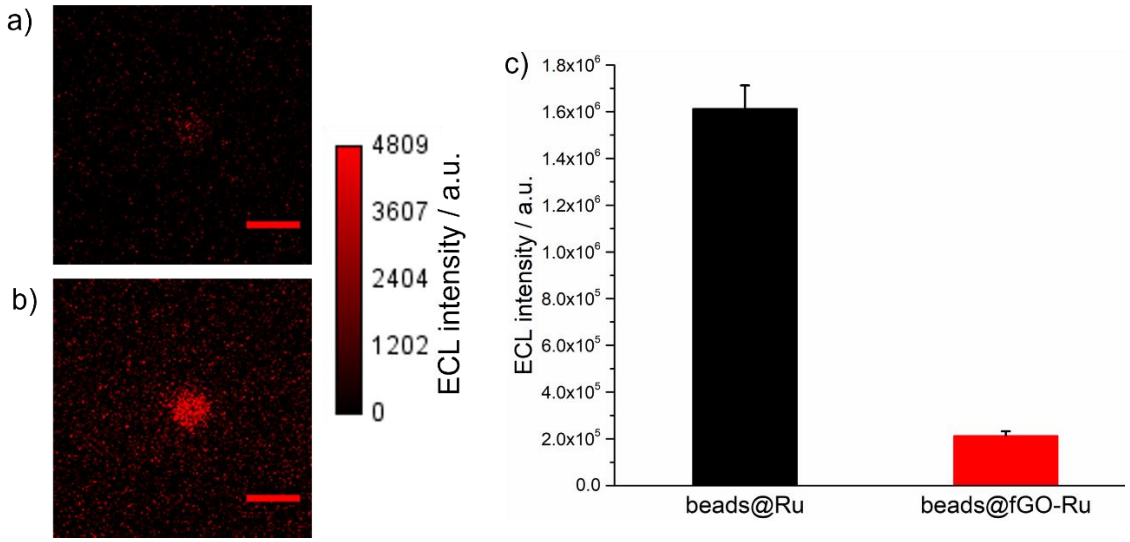

Figure 3.9. ECL images of beads labelled with a) GO double functionalized with biotin and $[Ru(bpy)_3]^{2+}$ complex (beads@fGO-Ru) and b) with the biotinylated antibodies labelled with $[Ru(bpy)_3]^{2+}$. c) Comparison between ECL intensity values of 2.8 µm beads@Ru (black) and 2.8 µm beads@fGO (red). Error bars show the standard deviation ($n \geq 6$). They were obtained by applying a constant potential of 1.4 V (vs. Ag/AgCl) for 4 s in 180 mM TPrA and PB 0.2 M (pH 6.9). Pt wire as counter electrode. EMCCD camera coupled with a potentiostat. Magnification X100, scale bar 5µm, integration time 8 s.

The fGO-Ru sheets were analysed by ICP-MS for quantifying the Ru content, which was really low (0.30 µg mL^{-1}) and explains the low ECL intensity observed. Moreover, the lateral size of a single fGO sheet was around 2-3 µm observed by TEM analysis (figure 3.10) and only one or two sheets can be put around a 2.8 µm bead. The combination of fGO high dimension and low amount of $[Ru(bpy)_3]^{2+}$ can explain the results observed and the inhomogeneous emission, imputable to the absence or a too low functionalization of some beads. Although the sensitivity was not improved, the strategy was promising and was applied again but with a different CNM: the functionalized CNTs.

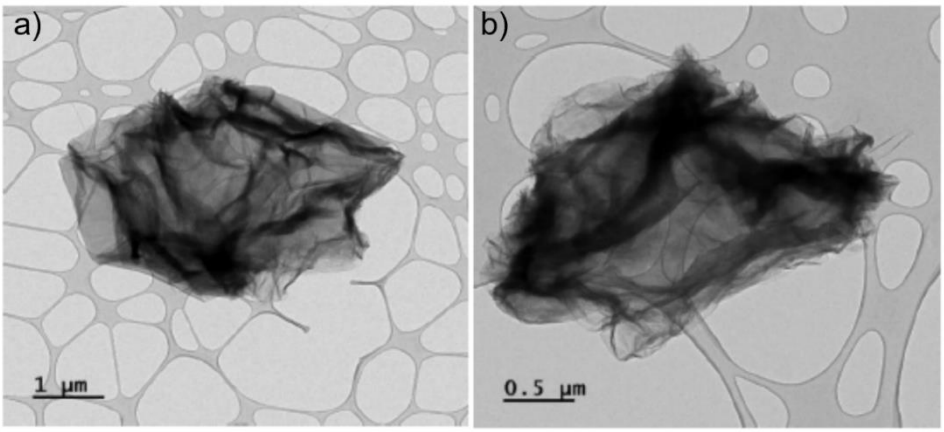

Figure 3.10. TEM images of GO double functionalized. a) Magnification 3000x and scale bar 1 µm; b) magnification 6000x and scale bar 0.5 µm.

2.2 Synthesis and characterization of $[Ru(bpy)_3]^{2+}$ functionalized CNTs

Functionalized carbon nanotubes (CNT-Ru) were synthesized in collaboration with Prof Prato research group at the research center CICbiomaGUNE in San Sebastian by combining 1,3-dipolar cycloaddition reaction and amidation of carboxylic groups (figure 3.11). They were prepared functionalizing oxidized double walled carbon nanotubes DWCNTs with i) the $[Ru(bpy)_3]^{2+}$ complex as a luminophore, and ii) an amine functional group to link biotin. The approach followed for the synthesis provided tubes with a controllable labelling capability, high surface area, and electronic properties useful for promoting the fast electrochemical oxidation of amines (detailed synthetic procedure in the appendix).

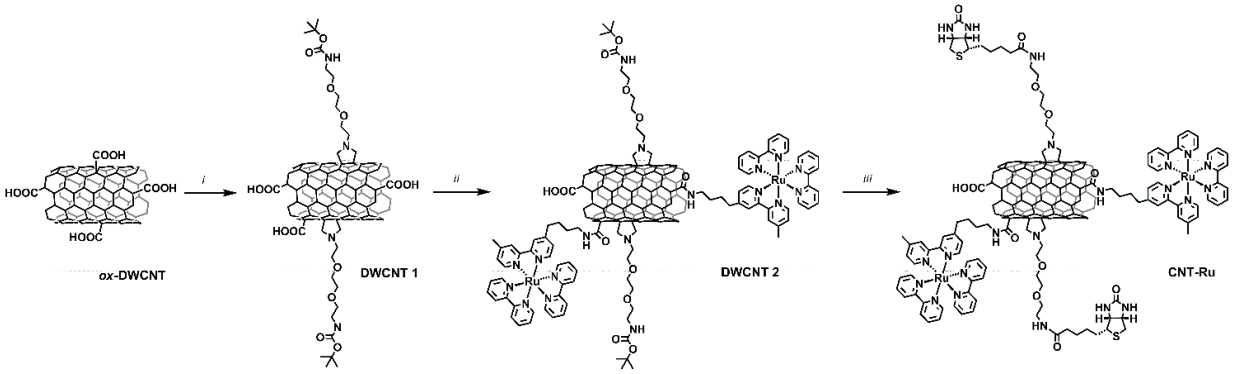

Figure 3.11. Schematic representation for the synthesis of f-CNTs labelled with $[Ru(bpy)_3]^{2+}$ and biotin (named CNT-Ru); i: paraformaldehyde, BocNH-PEG2-$NHCH_2CO_2H$, DMF, 115 °C, rt; iia: DIEA, EDC, DMF, rt, 1 h; iib: NHS, DMF, rt, 15 h; iic: $Ru(bpy)_3^{2+}$ amine derivative, 45 °C, 24 h; iiia: HCl:1,4-dioxane (1/2), rt; 15 h; iiib: EDC, NHS, biotin, MES, rt, 72 h

These CNTs-Ru obtained were characterized through different techniques. Fluorescent spectra (figure 3.12) confirmed the functionalization of CNTs and ICP-MS spectrometry showed a Ru concentration of 1.57 µg mg^{-1}.

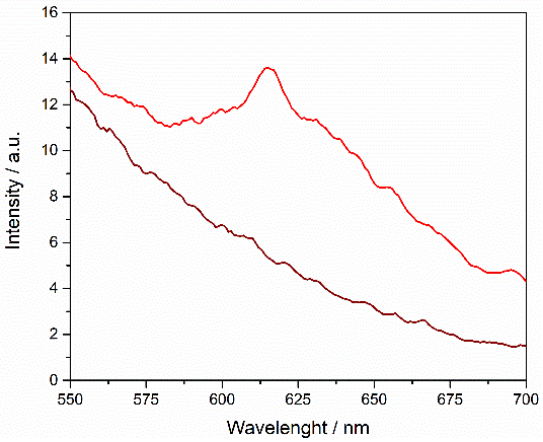

Figure 3.12. Emission spectra of a DMF solution of ox DWCNTs (dark red line) and CNTs labelled with $[Ru(bpy)_3]^{2+}$ complex (named DWCNT 2' light red line).

Instead, the structure was analysed by TEM imaging, TGA, and Raman spectroscopy (figures 3.13 and 3.14).

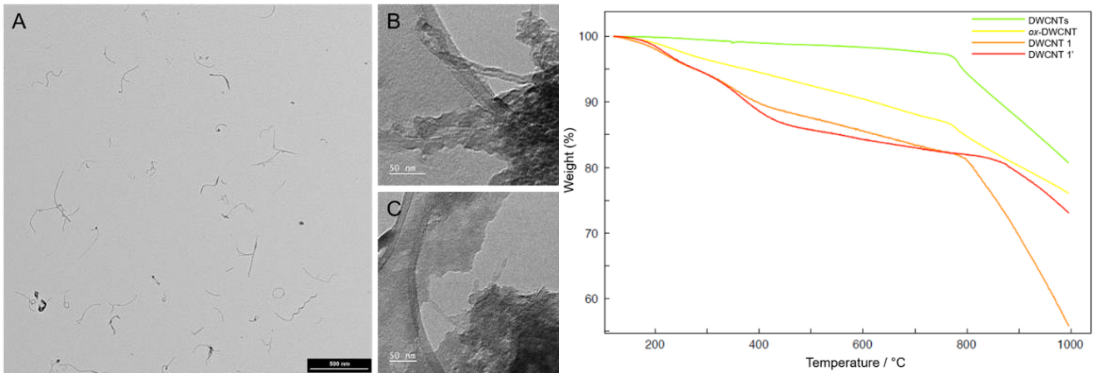

Figure 3.13. Left images) TEM images of DWCNT 1 (A) and DWCNT 2' (B, C) dispersed in DMF. Scale bar 500 nm (A) and 50 nm (B, C). Right image) Comparison between TGAs performed under N_2 of pristine DWCNTs (green line), ox-DWCNT (yellow line), DWCNT 1 (orange line) and DWCNT 1' (red line) show the introduction of different organic moieties that decompose between 200 and 400 degrees. The weight loss corresponds to 1.7 mmol/g for ox-DWCNT, 186 μmol/g for DWCNT 1 and 480 μmol/g for DWCNT 1'.

Due to the high fluorescence and broad signal of Ru complex at 1600 cm^{-1} (figure 3.14), the Raman signals of carbon nanotubes are hindered. Therefore, the characterization of CNT-Ru by Raman spectroscopy is not possible.

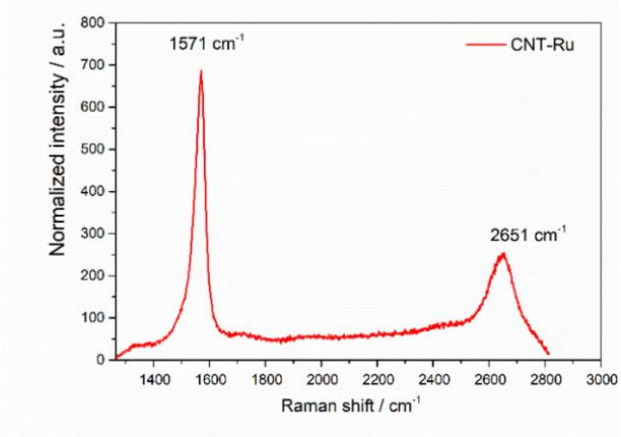

Figure 3.14. Raman spectroscopy analysis of CNT-Ru. Raman spectra were recorded using a 532 nm green laser (100% laser power) and 1 second of exposition time.

2.3 Beads functionalization with CNT-Ru

CNT-Ru was used for 2.8 µm and 4 µm micromagnetic beads functionalization through the biotin-streptavidin strong bond (beads@CNT-Ru). Then, they will be compared to the commercialized immunosystem, which involved micromagnetic beads functionalized with the biotinylated antibodies labelled with $[Ru(bpy)_3]^{2+}$ (beads@Ru) and TPrA as coreactant (both functionalization presented in the appendix).[103,109] Before performing the ECL analysis, characterizations by Raman and SEM were performed and beads@CNT-Ru show a smoother surface than bare 2.8 µm bead surface, which evidence a surface modification (figures 3.15 and 3.16).

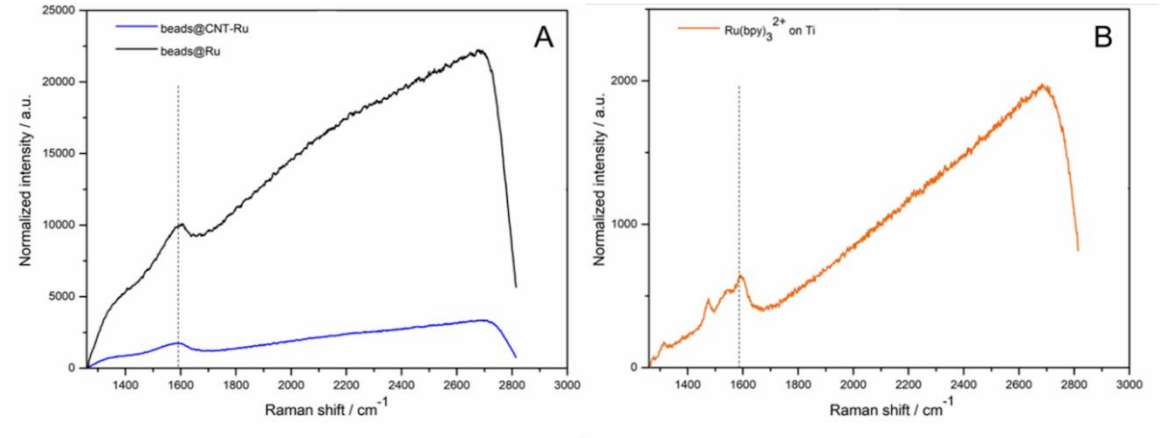

Figure 3.15. Raman spectra of (A) beads functionalized with a biotinylated antibody labelled with $Ru(bpy)_3^{2+}$ complex (2.8 µm beads@Ru, black line) and CNT-Ru 2.8 µm (beads@CNT-Ru, blue line); (B) Raman spectra of $Ru(bpy)_3^{2+}$ dropcasted on titanium surface. Raman spectra were recorded using a 532 nm green laser (100% laser power) and 1 second of exposition time.

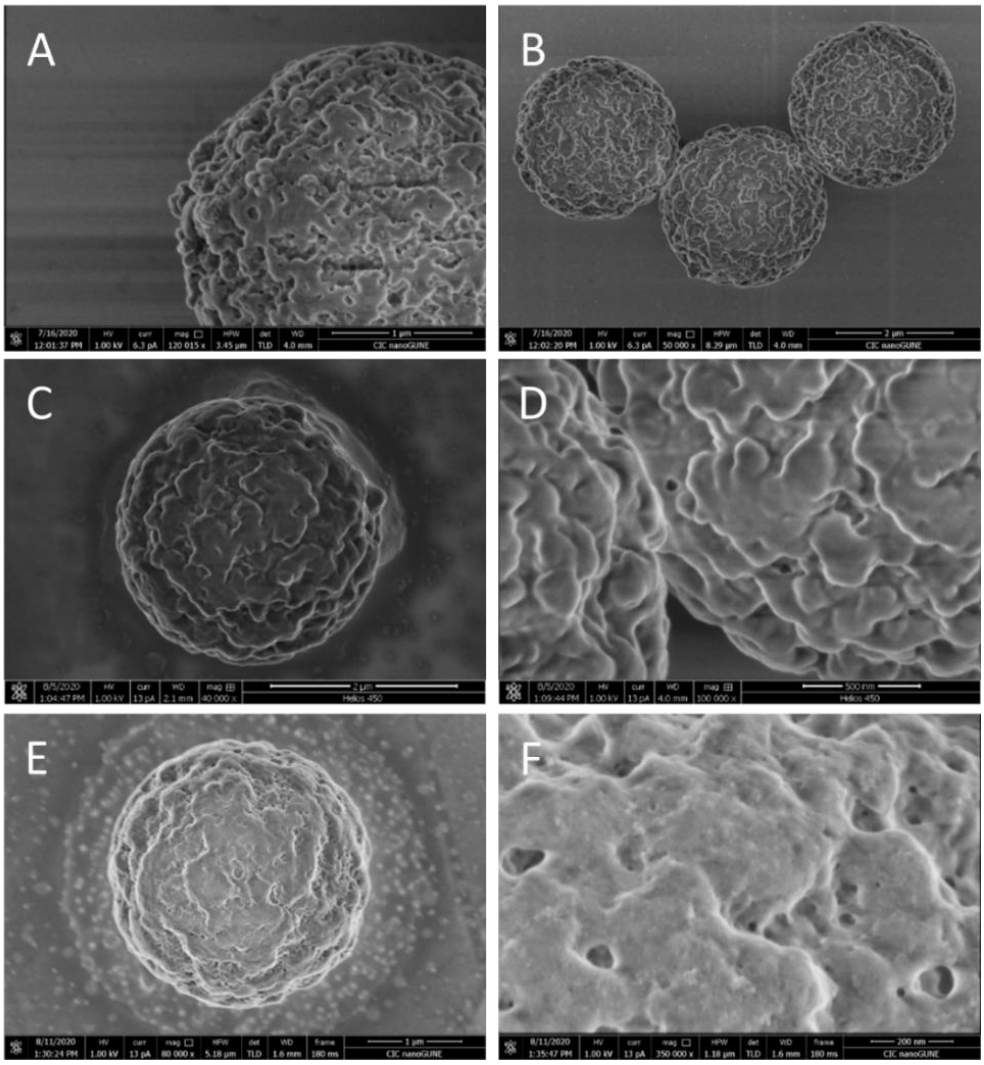

Figure 3.16. SEM images of bare 2.8 μm beads (A, B), 2.8 μm beads@Ru (C, D) and 2.8 μm beads@CNT-Ru (E, F).

Finally, laser scanning confocal microscopy was performed on functionalized beads in order to quantify the amount of Ru complexes present on a single bead (figure 3.17). The fluorescence values are different for beads@Ru and for beads@CNT-Ru and allow to compare their ECL performance in a more precise way.

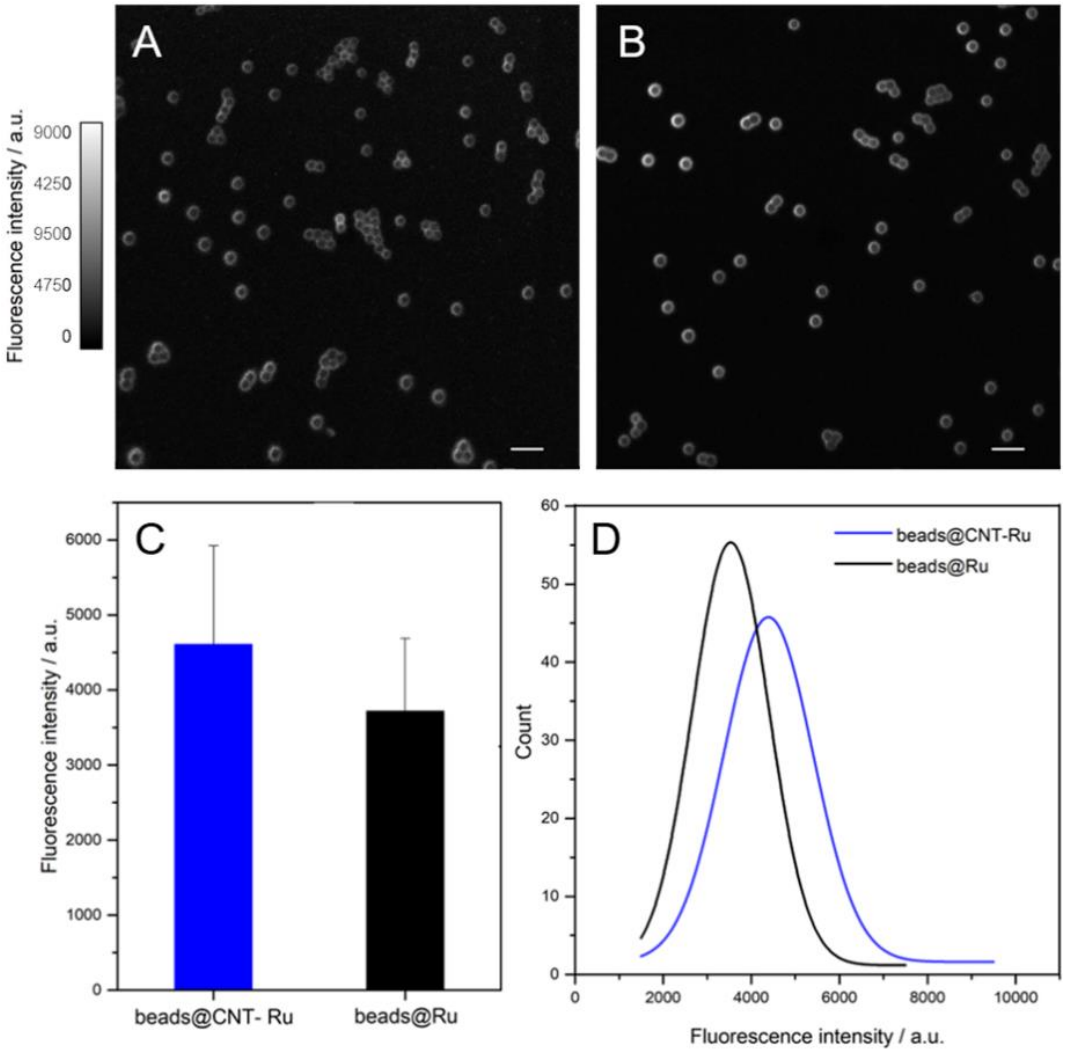

Figure 3.17. Laser scanning confocal microscopy images of (A) 2.8 μm beads@Ru and (B) 2.8 μm beads@CNT-Ru. Laser 405 nm, filter 575 nm LP, pinhole 136 μm, section 1 μm. Scale bar 10 μm. (C) Histograms of mean fluorescence intensity expressed as mean grey value of 2.8 μm beads@CNT-Ru (blue) and 2.8 μm beads@Ru (black). Error bars show the standard deviation (n=126). (D) Fluorescence intensity gaussian distribution of beads@CNT-Ru and beads@Ru.

2.4 ECL behaviour of beads@Ru and beads@CNT-Ru

ECL emission of beads with a diameter of 2.8 μm was acquired in the presence of 180 mM of TPrA after their immobilization onto a Pt electrode as in all the beads-based systems seen until now, where the only ECL generation mechanism observed was the so-called "oxidative reduction" coreactant heterogeneous mechanism.

Single beads@CNT-Ru (figure 3.18A) shows an increase of ~4 times in the ECL intensity integrated respect to beads@Ru (figure 3.18B), increment confirmed by beads emission profiles (figure 3.18C). The ECL emission signals reported were reproducible and are the average of the intensities of more than 10 beads, where almost 3-4 beads are analysed for each image taken. Moreover, the integrated signals were normalized considering the

different luminophore loadings between the two types of beads and obtaining the turnover frequency (TOF), which is the number of photons emitted in 1 s by a single luminophore (inset of figure 3.18C). It was obtained by dividing the integrated ECL emission from the single bead by the number of luminophores present on the bead surface and by the integration time (see also appendix and chapter II for TOF explanation and Figure 3.18C). TOF for beads@CNT-Ru increased by 70% compared to that of beads@Ru; thus, confirming the strategical role played by CNTs in promoting enhanced ECL signals.

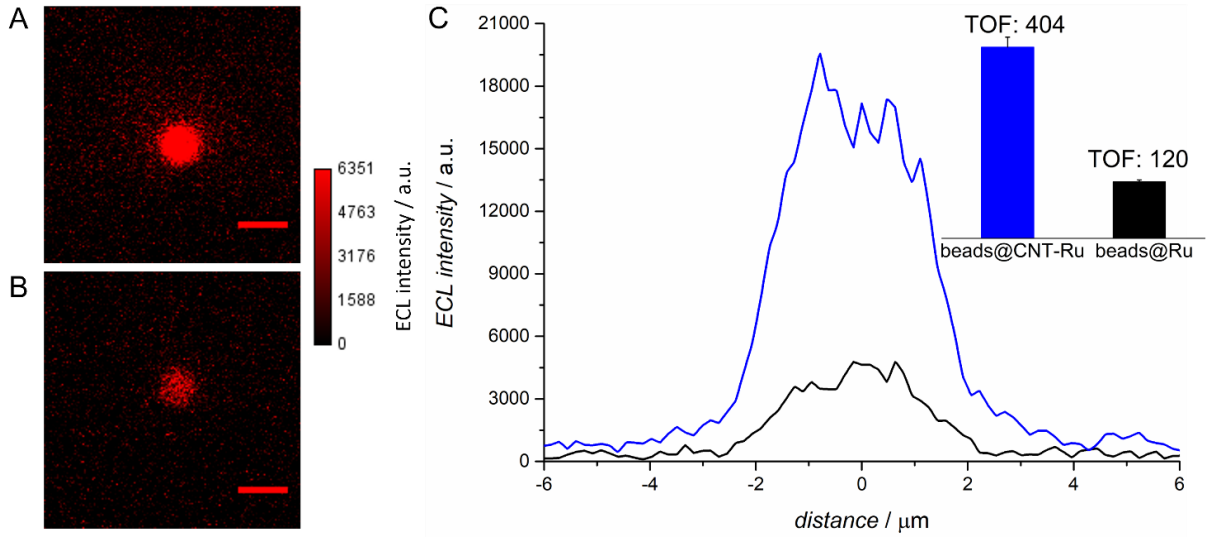

Figure 3.18. (A) ECL imaging of 2.8 µm single-bead labelled with CNTs labelled with $[Ru(bpy)_3]^{2+}$ (beads@CNT-Ru) and (B) with biotinylated antibody functionalized with $[Ru(bpy)_3]^{2+}$ (beads@Ru). The images were obtained by applying a constant potential of 1.4 V (vs. Ag/AgCl) for 4 s in 180 mM TPrA and PB 0.2 M. Pt wire was used as counter electrode. EMCCD camera was coupled with a potentiostat. Integration time, 8 s; magnification, X100; scale bar, 5 µm. (C) Comparison of the beads profile lines (black line, beads@Ru; blue line, beads@CNT-Ru). Inset of the comparison between TOF values calculated for beads@Ru (black) and beads@CNT-Ru (blue). Error bars show the standard error (n ≥ 10). EMCCD camera was coupled with a potentiostat. Integration time, 200 ms.

A possible explanation for the observed effect is associated with the previously observed ability of CNTs and carbonic nanomaterials to promote the efficient anodic oxidation of amines.[32,75,78,110–112] In fact, as shown in Figure 3.20A and according to heterogeneous mechanism explained in the introduction and in the previous chapters the ECL signal depends entirely on the direct oxidation of TPrA and in particular, the limited $TPrA^{\bullet+}$ lifetime is among the major intrinsic limiting factors for the signal intensity, causing an emission restricted to the luminophores within few micrometers (~3 µm).[85,103,113] Additionally, the ECL distribution around the beads is not homogeneous, due to the decaying radicals distribution.[103] The CNT-Ru moieties are randomly distributed onto the bead surface, likely

creating a conductive electrocatalytic network, which is electronically wired to the electrode surface and where TPrA oxidation may occur. TPrA radicals' concentration increased over the whole bead surface compared with beads@Ru, where coreactant oxidation only occurs at the electrode surface. The more homogeneous and higher emission created by the conductive network of CNTs around the beads was observed also for beads with bigger diameter (4 μm), which were functionalized with either CNT-Ru or Ru labels as 2.8 μm beads (figures 3.19 A and B and insets of 3.19C). The more homogeneous behaviour is evident in figure 3.19C, where the ECL intensity is normalized in beads profiles plot.

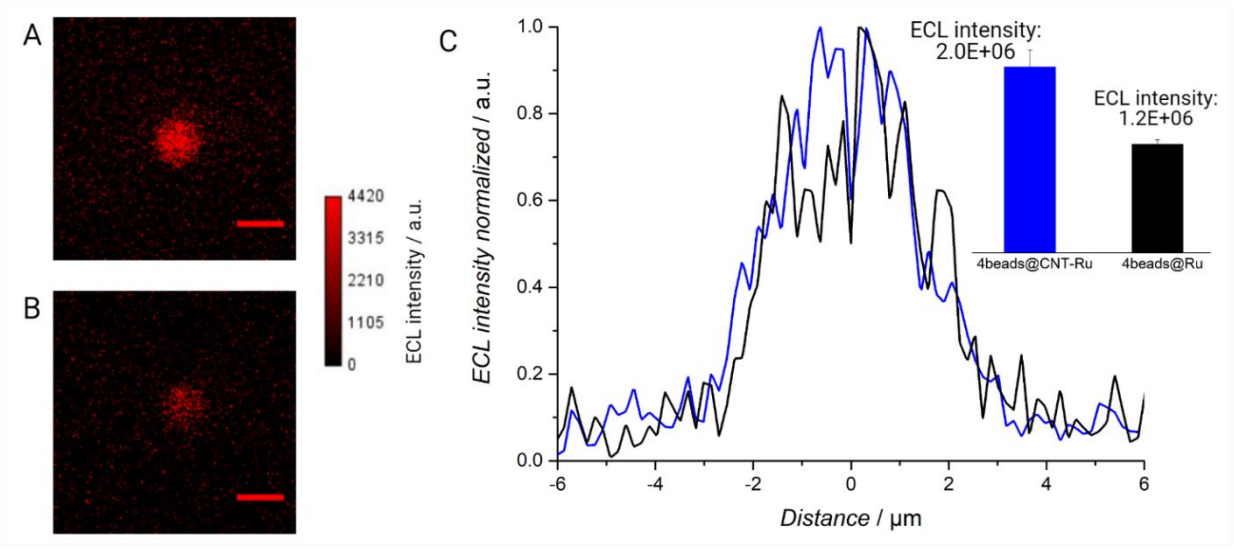

Figure 3.19. (A) Electrochemiluminescence (ECL) imaging of 4 μm beads@CNT-Ru and (B) 4 μm beads@Ru. The ECL images were obtained by applying a constant potential of 1.4 V (vs. Ag/AgCl) for 4 s in 180 mM TPrA and 0.2 M PB. Pt wire as counter electrode. EMCCD camera coupled with a potentiostat. Integration time, 8 s; magnification, X100; Scale bar, 5 μm. (C) Comparison of the beads profile lines normalized (black line, 4beads@Ru; blue line, 4beads@CNT-Ru). Inset of the comparison between ECL intensity integrated values (50x50 pixel square) of 4beads@Ru (black) and 4beads@CNT-Ru (blue). Error bars show the standard deviation (n=12).

2.5 ECL enhancement

Carbon nanotubes create a conductive layer around the beads, extending the ECL active layer and enhancing the ECL signal not only thanks to the coreactant oxidation at higher distances from the electrode but also through the direct oxidation of the luminophore on this new conductive layer (figure 3.20 B). This latter mechanism is not active in conventional bead system, in which the direct oxidation of the luminophores is neglected (figure 3.20 A).[103,113,114] The additional ECL generation mechanism, the homogeneous one, even responsible of the signal intensity enhancement, was highlighted by acquiring the ECL signal from the

individual beads (either beads@Ru or beads@CNT-Ru) during a cyclic potential scan from 0 V to 1.4 V (acquisition time 200 ms).

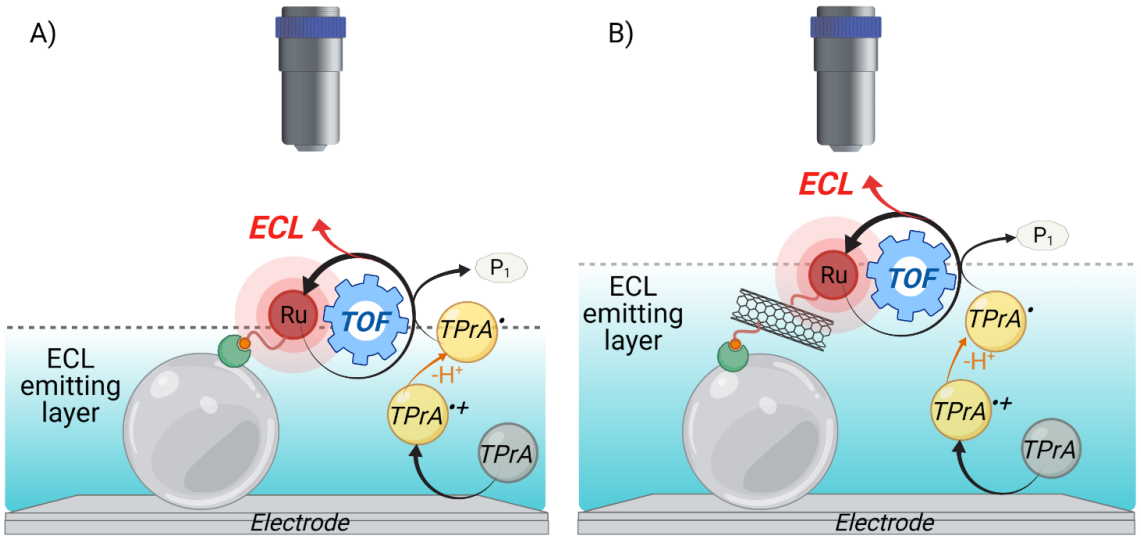

Figure 3.20. "Oxidative-reduction" coreactant mechanisms for the electrochemiluminescent emission of micromagnetic beads (light grey sphere) systems (biotin, red circle, and streptavidin, green shape), involving TPrA as coreactant and $[Ru(bpy)_3]^{2+}$ as luminophore. A) Only TPrA is oxidized on the electrode. B) $[Ru(bpy)_3]^{2+}$ is also oxidized on the double-walled carbon nanotubes (f-CNTs). Created with BioRender.com

The analysis was elaborated showing two deconvolution curves at ~ 0.9-1.1 V (oxidation potential of TPrA) and at ~1.2-1.4 V (oxidation potential of $[Ru(bpy)_3]^{2+}$). This last one gives a higher contribution to the curve related to beads@CNT-Ru respect to the curves related to beads@Ru (figure 3.21).

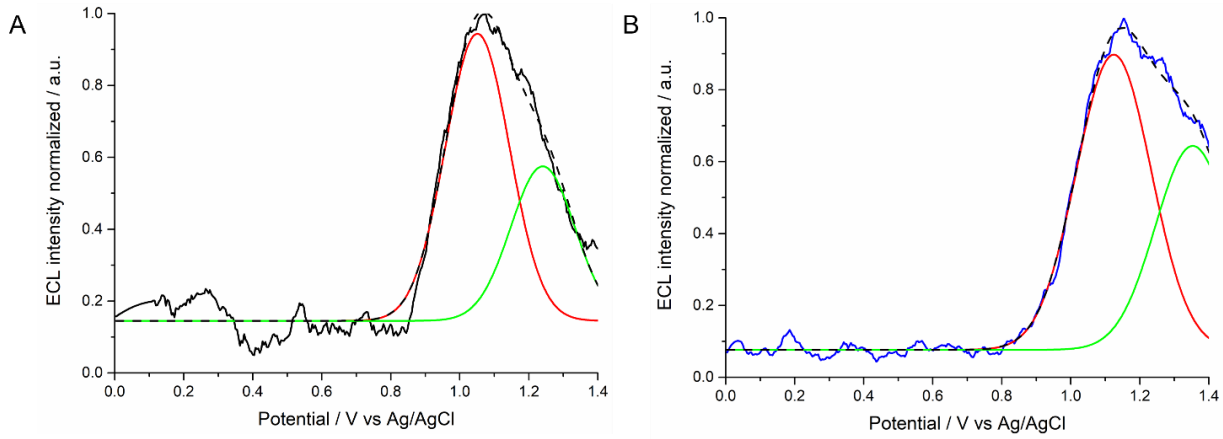

Figure 3.21. Cyclic voltammetry performed on 2.8 µm A) beads@Ru (black) and B) beads@CNT-Ru (blue), scanning the potential between 0 V and 1.4 V and ECL emission signal acquired each 200 ms. Deconvolution of the cyclic voltammetry peak at 1 V (red line) and 1.2 V (green line), in which the TPrA and $[Ru(bpy)_3]^{2+}$ were oxidized, respectively. The sum of these two peaks deconvolution was represented by dotted black line. EMCCD camera was coupled with a potentiostat. Integration time, 200 ms.

This behaviour may be associated with the anodic oxidation of the $[Ru(bpy)_3]^{2+}$ moieties also supported by the comparison between the electrochemical behaviour of beads@CNT-Ru and beads@Ru in absence of coreactant (figure 3.22). The oxidation process occurs onto the CNTs surface because of the flexibility of the linker connecting the luminophore to the CNT moiety, allowing an alternative mechanism for ECL generation. Such a mechanism involves the parallel oxidation of both TPrA and $[Ru(bpy)_3]^{2+}$, usually characteristic of homogeneous systems but never observed before this discovery in heterogeneous ones.[113]

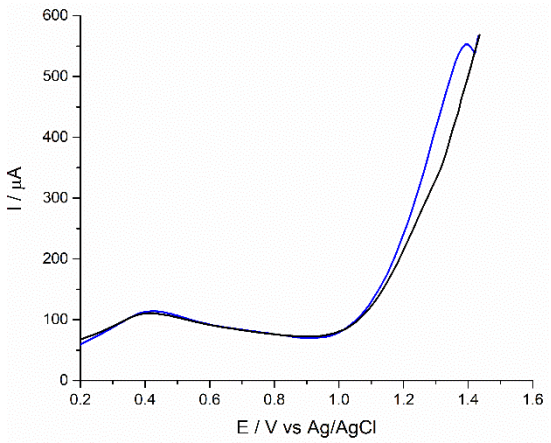

Figure 3.22. Square wave voltammetries performed on 30µL of beads@CNT-Ru (blue line) or beads@Ru (black line), scanning the potential from 0.2 V to 1.45 V (vs. Ag/AgCl) in 0.2 M PB, scan rate 0.1 V s^{-1}. Pt plate was used as working electrode. Pt wire was used as counter electrode.

Another important proof of such behaviour is the ECL analysis at a single-beads level performed with dibutylaminoethanol (DBAE) as coreactant instead of TPrA (figure 3.23). DBAE exhibited an analogous mechanism to TPrA but its radical cation has a very short lifetime,[85] and the emission from beads@Ru was not observed. In contrast, beads@CNT-Ru showed stronger signal than beads@Ru because the presence of the CNT electrocatalytic network, allows the oxidation of the luminophore and of coreactant at a very short distance from the luminophore. The presence of the luminophores onto the beads and the application of a sufficiently high oxidation potential for overcoming the ohmic drop due to the high concentration of coreactant are mandatory for ECL generation.[103] This was confirmed by the absence of ECL emission from 2.8 µm beads functionalized with CNT not labelled with $[Ru(bpy)_3]^{2+}$, underlying the absence of an ECL signal from CNTs alone (figure 3.24).

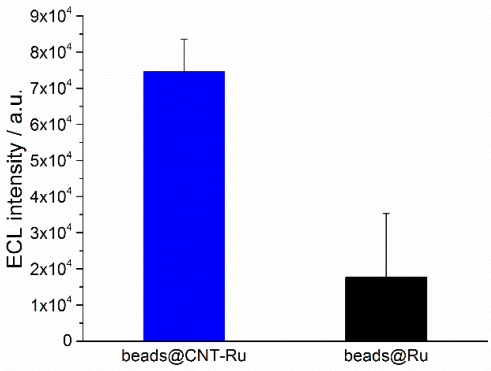

Figure 3.23. Comparison between ECL intensity values of 2.8 μm beads@Ru (black) and 2.8 μm beads@CNT-Ru (blue). Error bars show the standard deviation (n=5). They were obtained by applying a constant potential of 1.4 V (vs. Ag/AgCl) for 4 s in 180 mM DBAE and 0.2 M PB. Pt wire as counter electrode. EMCCD camera coupled with a potentiostat. Integration time, 8 s.

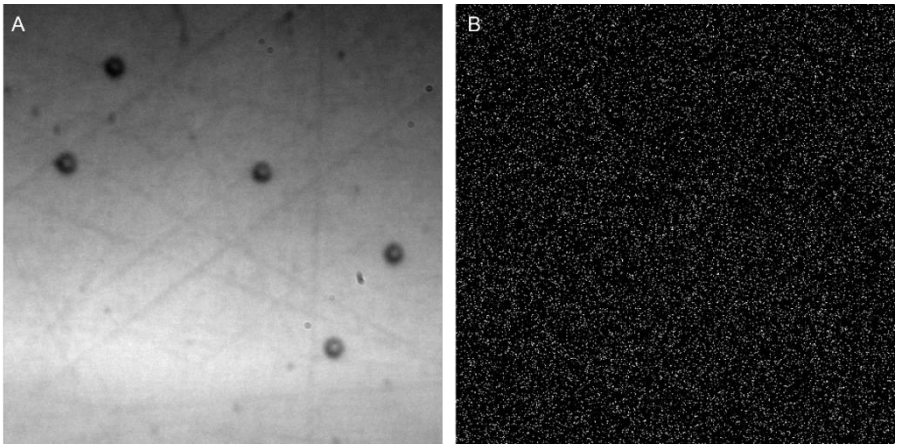

Figure 3.24. (A) Optical and (B) ECL images of beads functionalized with CNT not labelled with $[Ru(bpy)_3]^{2+}$. They were obtained by applying a constant potential of 1.4 V (vs. Ag/AgCl) for 4 s in 180 mM TPrA and 0.2 M PB. Pt wire as counter electrode. EMCCD camera coupled with a potentiostat. Integration time, 8 s.

In conclusion, a new and very promising route is opened for increasing the sensitivity of ECL immunoassays based on the ECL imaging technique. A model that includes functionalized CNTs that increase and homogenize the ECL-emitting layer was optimized for a real and sensitive creation of a biosensor for specific biomarkers detection and consequently early disease detection. To mimic the real beads-based commercial immunoassays and enhance the ECL performance, CNTs were used as an interlayer between the luminophores and the magnetic microbead increasing the ECL signal, thanks to the combined effect of the higher efficiency of the remote heterogeneous ECL mechanism, usually involved in such systems, and the concurrence of an additional ECL-generating mechanism, generally limited to homogeneous systems.

3. AN IMMUNOASSAY SYSTEM SPECIFIC FOR CARDIAC TROPONIN

The development of a more sensitive bead-based immunoassay exploiting carbon nanotubes was followed by the development of a system specific for cardiac Troponin (cTn) built with MWCNTs. Troponin contains three sub-units: T, I and C, that interact with tropomyosin creating the troponin-tropomyosin complex located on the actin filament which form together with thick filaments the contractile apparatus, the sarcomere, of cardiomyocytes (figure 3.25).

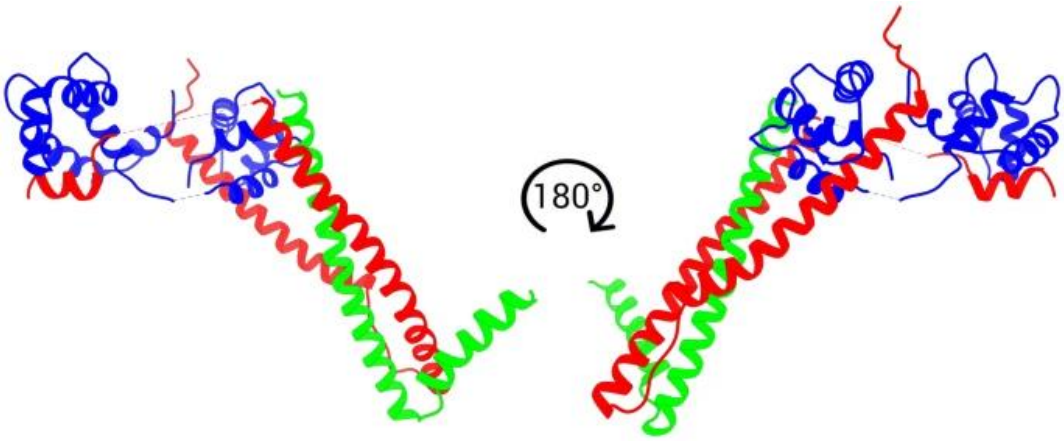

Figure 3.25. Front and back view of the 46 kDa core domain of human cardiac Troponin in the Ca^{2+}-activated form. TnC is depicted in blue, TnT in green and TnI in red. PDB accession code 1J1D. Reprinted with permission from [115].

Cardiomyocytes are formed by myofibrils, composed of long proteins (actin, myosin and titin) and troponin open myosin binding sites only in presence of muscle contraction, signalled through the Ca^{2+} ion.[116] Each troponin subunit has a different role in the regulation of muscle contraction: i) Troponin C (cTnC) attaches to calcium and provokes structural changes in the complex; ii) Troponin I (cTnI) inhibits actin/myosin interactions; iii) Troponin T (cTnT) binds the whole complex to tropomyosin.[115] The subunit I and T are released into the bloodstream after heart muscle cells death and thus are suitable for the detection of myocardial damage (detecting cardiomyocyte necrosis and tissue ischemia). However, cTnI has a higher specificity and sensitivity than the other two since its cardiac isoform has a larger dissimilarity to the cTnI from other tissues.[117] This feature made it the preferred biomarker for Acute Myocardial Infarction (AMI), which is mainly caused by irregular work and rest habits. The onset of AMI is not symptomatic, provoking a high mortality rate of cardiovascular and cerebrovascular diseases in the world. There are different biomarkers for AMI detection[118,119] but cTnI is one of the most specific and sensitive, acquired as "gold

standard biomarker".[120] A wide variety of platforms for detection of biomarkers have been established, such as fluorescence immunoassay, enzyme-linked immunosorbent assay, electrochemistry, surface plasmon resonance, colorimetric, chemiluminescence, electrochemical impedance spectroscopy (EIS) immunoassay, and so on.[121,122] However, some of these methods require expensive instruments, complex operation procedures and tedious detection time, while several examples of ECL system were developed reaching good results in terms of dynamic range, detection limit (LOD), sensitivity and speed, meeting the requirements of reliable and accurate diagnosis.[118,123–125] The significant range of cTnI in the human blood is around 0.001–0.1 ng mL^{-1}. The levels of cTnI around 0.1 ng mL^{-1} indicate an increased risk for acute heart failure and 1 ng mL^{-1} is the critical value.[124,126,127] The cut-off levels can have little variations respect to different parameters as the sex of the patient.[126] The cut-off was recommended by International Federation of Clinical Chemistry and Laboratory Medicine (IFCC) to be considered as the lowest troponin (I and T) concentration close to the 99^{th} percentile of the reference population with 10% imprecision in the measurements.[128] More recently, values <2 pg mL^{-1} allow to identify 99% of patients with AMI.[129] However, the more diffuse cut-off values identified for cTnI in serum useful for AMI establishment are in the range of 10-30 pg mL^{-1}, with diagnostic techniques that can reach LOD values around few fg mL^{-1}.[122,124–126,130] These values are useful for the early detection of AMI before reaching a clear positive test, which has levels of cTnI around 5-50 ng mL^{-1}. The concentration of cTnI goes up to 50 ng mL^{-1} within 3–6 h from AMI, and finally to a level around 550 ng mL^{-1} that remains elevated for almost 10 days with a peak after 1-2 days.[121] This information underlines the need of a cTnI biomarker detection method with quick response, good selectivity, high sensitivity, and simple operation in order to timely tracking cTnI level for on time and appropriate treatments.[120,131,132] For these reasons, rapid and accurate point-of care diagnosis and development of quicker and portable detectors are attracting even more attention for early or non-hospital diagnosis of AMI.[119,132]

Following all the past biosensor examples for cTnI detection[133,134] and trying to answer to the detection demand of this important biomarker we started to develop a system combining the brilliant features of ECL and carbon nanotubes towards more ambitious project of ECL-beads based immunoassay system, involving the high spatio-temporal resolved ECL imaging technique.

3.1 Sandwich immunoassay formation

Our project deals with the creation of a sandwich immunoassay upon the Indium Tin Oxide (ITO) electrode, transparent material good to be functionalized and to be analysed through spectroscopy.[75] After ITO cleaning, we performed the electrografting of N-succinimidyl acrilates (NSA) on the electrode surface, polymerizing the electrode with PNSA. It was performed in a three-electrode electrochemical cell with Pt spiral as counter electrode and Ag spiral as quasi-reference electrode using a solution of dimethylformamide (DMF) anhydrous with NSA 0.1 M and tetrabutylammonium hexafluorophosphate (TBAH) 0.05 M.[135] A cyclic voltammetry was performed after 15 minutes of degassing with Ar, in order to remove all the oxygen/water content for obtaining the optimal polymerization (as shown in figure 3.26) and not burning ITO surface at so cathodic potential applied, because ITO potential window becomes smaller in presence of water and oxygen.[136–138] The potential was scanned from 0 V to -2.1 V for 20 times at scan rate of 0.1 Vs^{-1}.

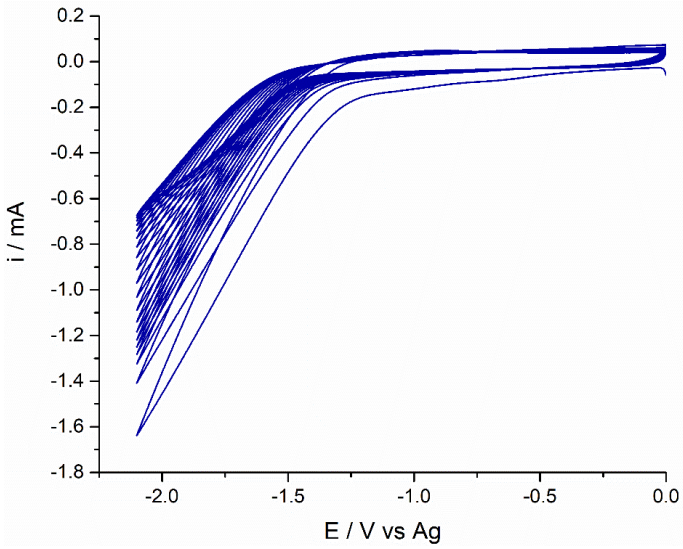

Figure 3.26. CV polymerization of ITO electrode surface with PNSA. 20 CV cycles performed scanning the potential between 0 and -2.1 V in DMF, TBAH 0.05 M and NSA 0.1 M, scan rate 100 mV s^{-1}, after degassing with Ar for 15 min. ITO as working electrode, Pt spiral as counter electrode, Ag spiral as quasi-reference electrode.

After electropolymerization, ITO electrode was washed with EtOH, dried with Ar, and introduced in the second three-electrode electrochemical cell for sandwich assay building, confining an area of the electrode through an o-ring with 8 mm of diameter.

Only an area of 50 mm^2 will be functionalized by the sandwich immunoassay through several steps and at the end ready to be measured with ECL technique (figure 3.27). It was composed

by i) MWCNTs functionalized with primary antibodies and covalently bind to the electrode, ii) cardiac Troponin I at different concentrations, and iii) secondary antibodies labelled with $[Ru(bpy)_3]^{2+}$ complex. The antibodies are specific for cardiac Troponin subunit I (cTnI).

The research group of Prof. Prato at the university of Trieste synthesised the MWCNTs double functionalized with terminal amine and capture antibody (Primary mAb1 is 19c7ccby from HyTest) and successfully functionalized the detection antibody (secondary mAb2 is 560cc from HyTest) with a $[Ru(bpy)_3]^{2+}$ complex, passing through a long process of dialysis purification.

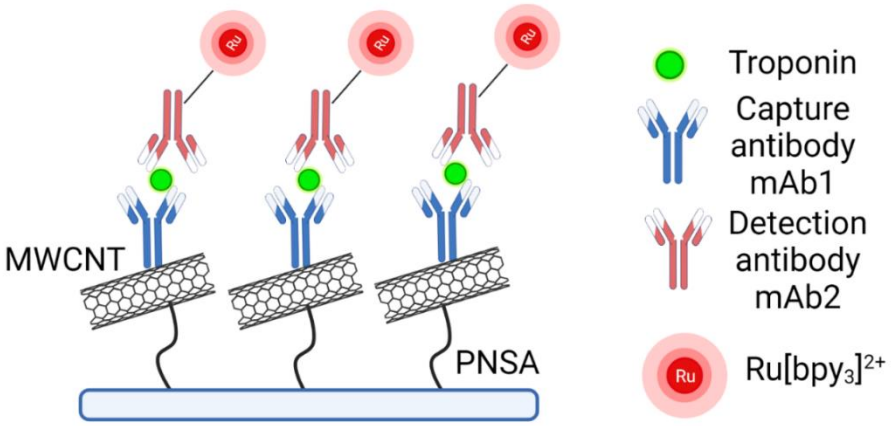

Figure 3.27. Schematic representation of sandwich-immunoassay built onto a transparent ITO electrode (light blue rectangle).

The MWCNTs-mAb1 were functionalized by combining the 1,3-dipolar cycloaddition reaction with the amidation reaction occurring at the oxidized CNT tips and defects (figure 3.28a) and the successful functionalization was tested by TGA analysis (figure 3.28b). The antibodies were covalently linked to the ammonium-derivatized pyrrolidine rings present on the walls of CNTs, while the amine terminal linker inserted at the open ends of the tubes allowed CNTs anchoring to the electrode surface, previously polymerized and rich in carboxylic groups.

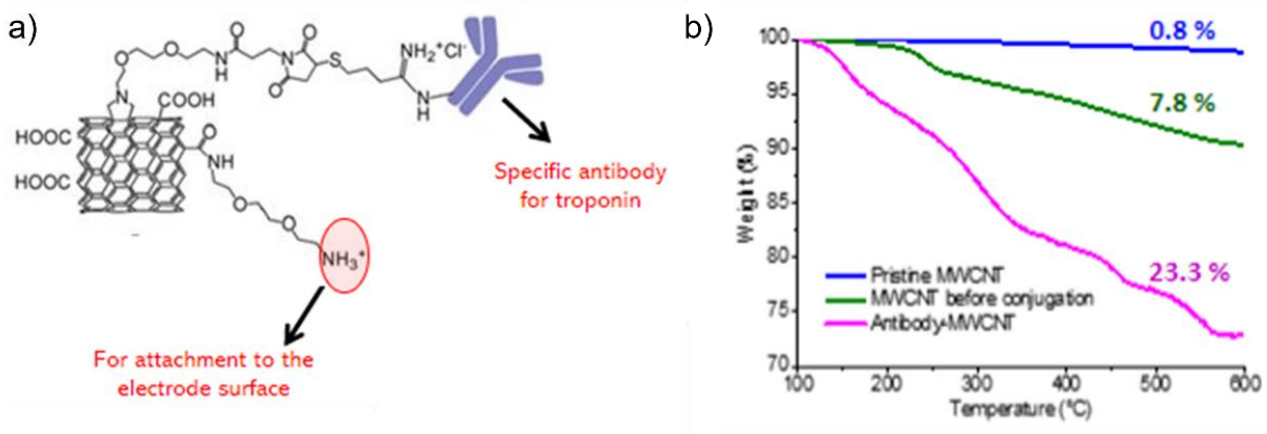

Figure 3.28. a) MWCNTs double functionalized with a terminal amine to bind to ITO electrode surface and primary antibody specific for cTnI. b) TGA analysis of the MWCNTs-mAb1 successful synthesis.

3.2 ECL measurements of cardiac Troponin different concentrations

ECL measurements were performed in the second three-electrode electrochemical cell (ITO as WE, Pt wire as CE, Ag/AgCl as RE) using a solution of 200 mM of TPrA in PB 0.2 M (pH 6.9) and acquiring the ECL signal intensity through a photomultiplier tube (PMT). The potential necessary for ECL generation was applied through several consecutive chroamperometric cycles planned like shown in figure 3.29b: 0V for 1s; 2V for 1s; 0V for 1s; 2V for 1s. They were performed to stabilize the signal, which continuously decrease for the non-specific signal (figure 3.29a).

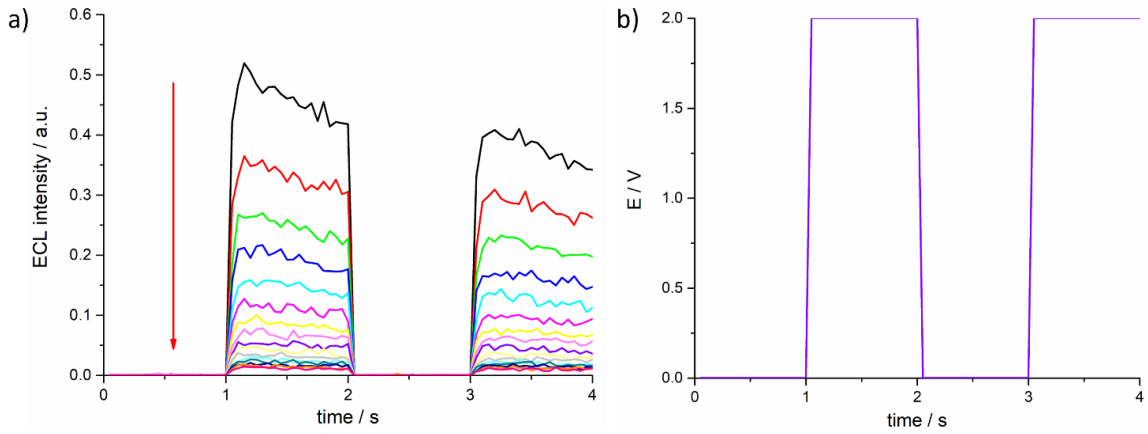

Figure 3.29. a) Consecutive chronoamperometric steps from the first step (black one) to the following ones in the direction of the red arrow. Measurements performed with 0.05 µg mL^{-1} of cTnI. b) Trend of potential applied in each chronoamperometric step: 0V for 1s; 2V for 1s; 0V for 1s; 2V for 1s. Chronoamperometries performed in a PB 0.2 M solution with 200 mM TPrA in an electrochemical cell with ITO functionalized as WE, Pt wire as CE and Ag/AgCl as RE.

Different concentrations of cardiac troponin from 0.5 μg mL^{-1} to 10 μg mL^{-1} were tested showing a quite good linearity but showing a quite variability in the results, probably because the dispersion of CNTs presented aggregates, was inhomogeneous and we can't precisely control their distribution onto the electrode surface. Our suspects were confirmed by a Raman mapping of the ITO surface modified with CNTs and relative immunoassay. It showed a spotted distribution of MWCNTs' agglomerates on electrode surface (figure 3.30). Despite the inhomogeneity, maybe due also to a non-efficient electrode functionalization, some CNTs were attached to the surface.

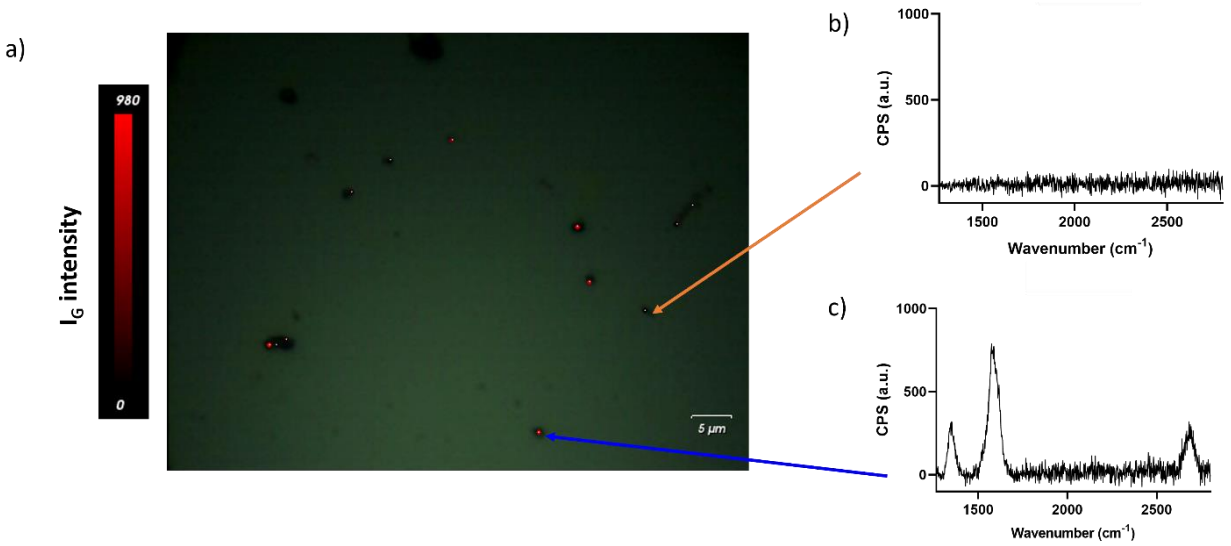

Figure 3.30. Raman spectroscopy analysis performed on ITO functionalized. a) Optical image of an area of ITO functionalized. b) Raman spectra of the points without MWCNTs. c) Raman spectra of points with MWCNTs, with characteristic CNTs band G at 1580 cm^{-1} and band G'at 2685 cm^{-1}. Raman analyses were performed using laser at 532nm, 50% intensity, 100X objective, 2 seconds exposition, 4 accumulation.

The experiments on the ECL built system were compared to a common ELISA performed on a plastic substrate (figure 3.31). CNTs presence didn't represent an obstacle to signal acquisition but the absence of the capture/primary antibody caused the attachments of the cTnI directly on the substrate showing a luminescent signal (grey column). This non-specific adsorption can be a further reason of the variability of our measurements.[139]

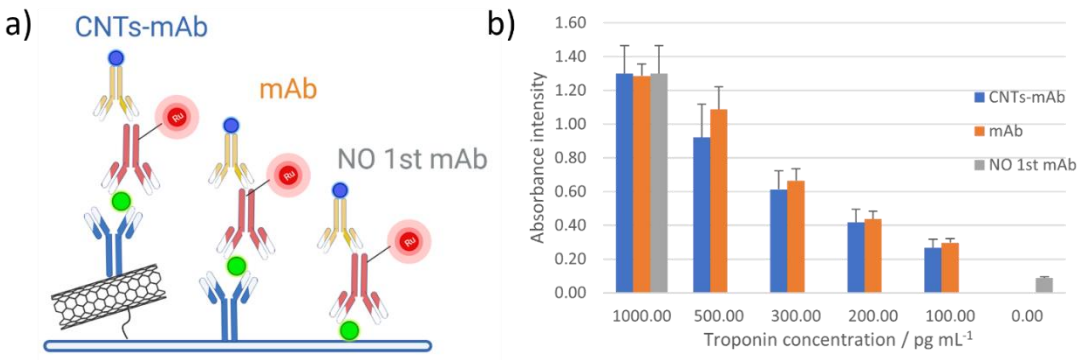

Figure 3.31. ELISA experiment control a) scheme and b) absorbance intensity measured with different cTnI concentration using the first scheme with capture antibody mAb on CNTs (blue column), the second with mAb without CNTs (orange column) and without mAb (grey column). Antibodies: capture of cTnI (blue), detection of cTnI (red), third antibody@HRP (yellow). Spheres: green is troponin and blue is HRP substrate.

Finally, the main problem to be solved is the too high signal of the blank sample, which was performed following the same procedure of the other immunoassays but without addition of cardiac Troponin antigen (black signal in figure 3.32). The results shown in figure 3.32 are the more representative between all the performed measurements. The lowering of the blank signal will allow to further decrease the just good limit of detection (LOD of 0.74 ng mL^{-1}) calculated by analysing the linear slope of the line in figure 3.33, where ECL intensities of figure 3.32 were plotted against the logarithm of the biomarker concentration.

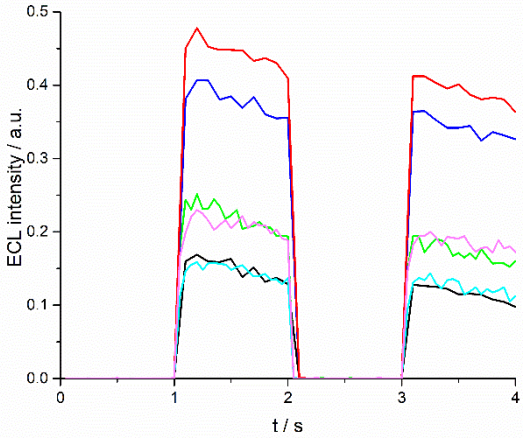

Figure 3.32. Chronoamperometries reporting ECL intensity vs time signals of sandwich immunoassay with different concentration of cTnI: 10 ng mL^{-1} (red line), 5 ng mL^{-1} (blue line), 2 ng mL^{-1}(pink line), 1 ng mL^{-1}(green line), 0.5 ng mL^{-1}(light blue line), blank (black line). Chronoamperometries performed in a PB 0.2 M solution with 200 mM TPrA in an electrochemical cell with ITO functionalized as WE, Pt wire as CE and Ag/AgCl as RE.

This project is in the initial phase and it will need several improvements in the sandwich building for optimizing the sensitivity but we obtained good and promising preliminary

results, reaching a LOD value below the critical concentration for determining AMI (1 ng mL^{-1}), but not yet competitive with the used cut-off values. The advantages of our biosensors concern the use of a non-invasive and very sensitive ECL technique, which can allow rapid measurements with low-cost materials, easy to handle and produce. It would open the path towards an ultrasensitive and rapid detection of the cTnI in order to decrease the mortality due to infarction.

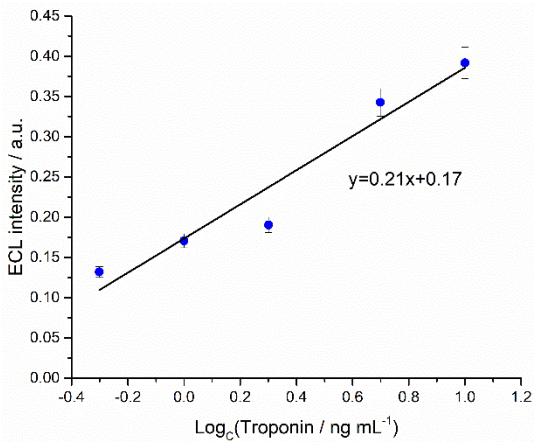

Figure 3.33. Calibration plot of ECL intensity signals at 3.5 s of chronoamperometries reported in figure 3.32 against the logarithm of cTnI concentration.

4. CONCLUSIONS

This final chapter further improved the ECL sensitivity exploiting all the knowledges acquired along the previous chapters. The innovation introduced for a more sensitive ECL beads-based immunoassay system dealt with the creation of conductive layer around the beads, electronically wired to the electrode surface. Functionalized GO and CNTs and their amazing conductive features and large surface area were exploited for realizing the layer and copying the Faraday cage type-ECLIA strategy.

The role of this carbon nano-based layer was the enhancement of the ECL emission layer acting both on the oxidation rate of TPrA, spatial distribution of its radical and radical cation and the activation of homogeneous mechanism never observed before in a beads-based system.

The second and last challenge, not yet completed, was the development of a sandwich immunoassay ECL sensor specific for cTnI, biomarker of AMI. Despite the promising results, some problems have to be solved performing modifications in the CNTs dispersion and in CNTs attachment procedure to the electrode surface. Moreover, new and more specific antibodies could be used for decreasing the just promising LOD obtained, which is under the critical point for AMI detection but is not enough competitive with the literature and for determination of critical cTnI concentrations in healthy patients, useful for prevention.

After the optimization of the system, the biosensors will be ready to be tested on real samples, monitoring the influence of the matrix effect, and will be incorporated in a bead-based immunoassay system developing a biosensor with the help of the really sensitive and spatio-temporal resolved ECLM.

REFERENCES

1. Panwar, N. *et al.* Nanocarbons for Biology and Medicine: Sensing, Imaging, and Drug Delivery. *Chem. Rev.* **119**, 9559–9656 (2019).
2. Abarrategi, A. *et al.* Multiwall carbon nanotube scaffolds for tissue engineering purposes. *Biomaterials* **29**, 94–102 (2008).
3. Ohno, Y., Maehashi, K. & Matsumoto, K. Label-Free Biosensors Based on Aptamer-Modified Graphene Field-Effect Transistors. *J. Am. Chem. Soc.* **132**, 18012–18013 (2010).
4. Cha, C., Shin, S. R., Annabi, N., Dokmeci, M. R. & Khademhosseini, A. Carbon-Based Nanomaterials: Multifunctional Materials for Biomedical Engineering. *ACS Nano* **7**, 2891–2897 (2013).
5. Jariwala, D., Sangwan, V. K., Lauhon, L. J., Marks, T. J. & Hersam, M. C. Carbon nanomaterials for electronics, optoelectronics, photovoltaics, and sensing. *Chem. Soc. Rev.* **42**, 2824–2860 (2013).
6. Baptista, F. R., Belhout, S. A., Giordani, S. & Quinn, S. J. Recent developments in carbon nanomaterial sensors. *Chem. Soc. Rev.* **44**, 4433–4453 (2015).
7. Shao, Y. *et al.* Graphene Based Electrochemical Sensors and Biosensors: A Review. *Electroanalysis* **22**, 1027–1036 (2010).
8. Castro, E. V. *et al.* Biased Bilayer Graphene: Semiconductor with a Gap Tunable by the Electric Field Effect. *Phys. Rev. Lett.* **99**, 216802 (2007).
9. Robinson, J. T., Perkins, F. K., Snow, E. S., Wei, Z. & Sheehan, P. E. Reduced Graphene Oxide Molecular Sensors. *Nano Lett.* **8**, 3137–3140 (2008).
10. Yang, W. *et al.* Carbon Nanomaterials in Biosensors: Should You Use Nanotubes or Graphene? *Angew. Chemie Int. Ed.* **49**, 2114–2138 (2010).
11. Geim, A. K. Graphene: Status and Prospects. *Science (80-.).* **324**, 1530–1534 (2009).
12. Jeon, I.-Y. *et al.* Large-Scale Production of Edge-Selectively Functionalized Graphene Nanoplatelets via Ball Milling and Their Use as Metal-Free Electrocatalysts for Oxygen Reduction Reaction. *J. Am. Chem. Soc.* **135**, 1386–1393 (2013).
13. Hernandez, Y. *et al.* High-yield production of graphene by liquid-phase exfoliation of graphite. *Nat. Nanotechnol.* **3**, 563–568 (2008).
14. Park, S. & Ruoff, R. S. Chemical methods for the production of graphenes. *Nat. Nanotechnol.* **4**, 217–224 (2009).
15. Li, X. *et al.* Large-Area Synthesis of High-Quality and Uniform Graphene Films on Copper Foils. *Science (80-.).* **324**, 1312–1314 (2009).
16. Hummers, W. S. & Offeman, R. E. Preparation of Graphitic Oxide. *J. Am. Chem. Soc.* **80**, 1339–1339 (1958).
17. Marcano, D. C. *et al.* Improved Synthesis of Graphene Oxide. *ACS Nano* **4**, 4806–4814 (2010).
18. Niyogi, S. *et al.* Solution Properties of Graphite and Graphene. *J. Am. Chem. Soc.* **128**, 7720–7721 (2006).
19. Liu, Z., Duan, X., Qian, G., Zhou, X. & Yuan, W. Eco-friendly one-pot synthesis of highly dispersible functionalized graphene nanosheets with free amino groups. *Nanotechnology* **24**, 045609 (2013).
20. Qian, X. *et al.* One-pot surface functionalization and reduction of graphene oxide with long-chain molecules: Preparation and its enhancement on the thermal and mechanical properties of polyurea. *Chem. Eng. J.* **236**, 233–241 (2014).
21. Loh, K. P., Bao, Q., Eda, G. & Chhowalla, M. Graphene oxide as a chemically tunable platform for optical applications. *Nat. Chem.* **2**, 1015–1024 (2010).
22. Zhang, S., Geryak, R., Geldmeier, J., Kim, S. & Tsukruk, V. V. Synthesis, Assembly, and

Applications of Hybrid Nanostructures for Biosensing. *Chem. Rev.* **117**, 12942–13038 (2017).
23. Iijima, S. Helical microtubules of graphitic carbon. *Nature* **354**, 56–58 (1991).
24. Dresselhaus, M. S., Dresselhaus, G., Saito, R. & Jorio, A. Raman spectroscopy of carbon nanotubes. *Phys. Rep.* **409**, 47–99 (2005).
25. Charlier, J.-C. Defects in Carbon Nanotubes. *Acc. Chem. Res.* **35**, 1063–1069 (2002).
26. Cao, J., Wang, Q. & Dai, H. Electromechanical Properties of Metallic, Quasimetallic, and Semiconducting Carbon Nanotubes under Stretching. *Phys. Rev. Lett.* **90**, 157601 (2003).
27. Bai, Y. *et al.* Super-durable ultralong carbon nanotubes. *Science (80-.).* **369**, 1104–1106 (2020).
28. Wu, Z. *et al.* Transparent, Conductive Carbon Nanotube Films. *Science (80-.).* **305**, 1273–1276 (2004).
29. Paradise, M. & Goswami, T. Carbon nanotubes – Production and industrial applications. *Mater. Des.* **28**, 1477–1489 (2007).
30. Chiang, M.-R. *et al.* Electron field emission properties of pulsed laser deposited carbon films containing carbon nanotubes. *J. Vac. Sci. Technol. B Microelectron. Nanom. Struct.* **19**, 1034 (2001).
31. Zhang, S. *et al.* Emerging Internet of Things driven carbon nanotubes-based devices. *Nano Res.* **15**, 4613–4637 (2022).
32. Fiorani, A. *et al.* Advanced carbon nanomaterials for electrochemiluminescent biosensor applications. *Curr. Opin. Electrochem.* **16**, 66–74 (2019).
33. Tasis, D., Tagmatarchis, N., Bianco, A. & Prato, M. Chemistry of Carbon Nanotubes. *Chem. Rev.* **106**, 1105–1136 (2006).
34. Fujigaya, T. & Nakashima, N. Non-covalent polymer wrapping of carbon nanotubes and the role of wrapped polymers as functional dispersants. *Sci. Technol. Adv. Mater.* **16**, 024802 (2015).
35. Zhou, Y., Fang, Y. & Ramasamy, R. Non-Covalent Functionalization of Carbon Nanotubes for Electrochemical Biosensor Development. *Sensors* **19**, 392 (2019).
36. Campo, J. *et al.* Optical Property Tuning of Single-Wall Carbon Nanotubes by Endohedral Encapsulation of a Wide Variety of Dielectric Molecules. *ACS Nano* **15**, 2301–2317 (2021).
37. Zhang, L. *et al.* Diels–Alder addition to fluorinated single walled carbon nanotubes. *Chem. Commun.* 3265 (2005). doi:10.1039/b500125k
38. Datsyuk, V. *et al.* Chemical oxidation of multiwalled carbon nanotubes. *Carbon N. Y.* **46**, 833–840 (2008).
39. Brunetti, F. G. *et al.* Microwave-Induced Multiple Functionalization of Carbon Nanotubes. *J. Am. Chem. Soc.* **130**, 8094–8100 (2008).
40. González-Domínguez, J. M. *et al.* Multipurpose Nature of Rapid Covalent Functionalization on Carbon Nanotubes. *Chem. - A Eur. J.* **21**, 18631–18641 (2015).
41. Hu, Y. *et al.* Growth of high-density horizontally aligned SWNT arrays using Trojan catalysts. *Nat. Commun.* **6**, 6099 (2015).
42. Ménard-Moyon, C., Fabbro, C., Prato, M. & Bianco, A. One-Pot Triple Functionalization of Carbon Nanotubes. *Chem. – A Eur. J.* **17**, 3222–3227 (2011).
43. Dresselhaus, M. S., Jorio, A. & Saito, R. Characterizing Graphene, Graphite, and Carbon Nanotubes by Raman Spectroscopy. *Annu. Rev. Condens. Matter Phys.* **1**, 89–108 (2010).
44. Corletto, A. & Shapter, J. G. Nanoscale Patterning of Carbon Nanotubes: Techniques, Applications, and Future. *Adv. Sci.* **8**, 2001778 (2021).
45. Zou, J. & Zhang, Q. Advances and Frontiers in Single-Walled Carbon Nanotube Electronics. *Adv. Sci.* **8**, 2102860 (2021).
46. Alegret, N. *et al.* Three-Dimensional Conductive Scaffolds as Neural Prostheses Based on

Carbon Nanotubes and Polypyrrole. *ACS Appl. Mater. Interfaces* **10**, 43904–43914 (2018).
47. Walcarius, A., Minteer, S. D., Wang, J., Lin, Y. & Merkoçi, A. Nanomaterials for bio-functionalized electrodes: recent trends. *J. Mater. Chem. B* **1**, 4878 (2013).
48. Cao, Q. & Rogers, J. A. Ultrathin Films of Single-Walled Carbon Nanotubes for Electronics and Sensors: A Review of Fundamental and Applied Aspects. *Adv. Mater.* **21**, 29–53 (2009).
49. Johnson, A. T. C. *et al.* DNA-decorated carbon nanotubes for chemical sensing. *Semicond. Sci. Technol.* **21**, S17–S21 (2006).
50. Heller, A. & Feldman, B. Electrochemical Glucose Sensors and Their Applications in Diabetes Management. *Chem. Rev.* **108**, 2482–2505 (2008).
51. Snow, E. S., Perkins, F. K., Houser, E. J., Badescu, S. C. & Reinecke, T. L. Chemical Detection with a Single-Walled Carbon Nanotube Capacitor. *Science (80-.).* **307**, 1942–1945 (2005).
52. Star, A. *et al.* Label-free detection of DNA hybridization using carbon nanotube network field-effect transistors. *Proc. Natl. Acad. Sci.* **103**, 921–926 (2006).
53. Tang, X. *et al.* Carbon Nanotube DNA Sensor and Sensing Mechanism. *Nano Lett.* **6**, 1632–1636 (2006).
54. Fu, Y. *et al.* Chemiresistive biosensors based on carbon nanotubes for label-free detection of DNA sequences derived from avian influenza virus H5N1. *Sensors Actuators B Chem.* **249**, 691–699 (2017).
55. Kybert, N. J., Lerner, M. B., Yodh, J. S., Preti, G. & Johnson, A. T. C. Differentiation of Complex Vapor Mixtures Using Versatile DNA–Carbon Nanotube Chemical Sensor Arrays. *ACS Nano* **7**, 2800–2807 (2013).
56. Heller, D. A. *et al.* Peptide secondary structure modulates single-walled carbon nanotube fluorescence as a chaperone sensor for nitroaromatics. *Proc. Natl. Acad. Sci.* **108**, 8544–8549 (2011).
57. Khamis, S. M. *et al.* DNA-decorated carbon nanotube-based FETs as ultrasensitive chemical sensors: Discrimination of homologues, structural isomers, and optical isomers. *AIP Adv.* **2**, 022110 (2012).
58. Sun, Q. *et al.* Chemiresistive sensor arrays based on noncovalently functionalized multi-walled carbon nanotubes for ozone detection. *Sensors Actuators B Chem.* **297**, 126689 (2019).
59. Luo, S.-X. L., Lin, C.-J., Ku, K. H., Yoshinaga, K. & Swager, T. M. Pentiptycene Polymer/Single-Walled Carbon Nanotube Complexes: Applications in Benzene, Toluene, and o -Xylene Detection. *ACS Nano* **14**, 7297–7307 (2020).
60. Doshi, S. M. & Thostenson, E. T. Thin and Flexible Carbon Nanotube-Based Pressure Sensors with Ultrawide Sensing Range. *ACS Sensors* **3**, 1276–1282 (2018).
61. Song, Y. *et al.* Carbon Nanotube-Modified Fabric for Wearable Smart Electronic-skin with Exclusive Normal-Tangential Force Sensing Ability. *Adv. Mater. Technol.* **4**, 1800680 (2019).
62. Hsiao, L.-Y. *et al.* Carbon nanotube-integrated conductive hydrogels as multifunctional robotic skin. *Carbon N. Y.* **161**, 784–793 (2020).
63. Liang, X. *et al.* Stable and Biocompatible Carbon Nanotube Ink Mediated by Silk Protein for Printed Electronics. *Adv. Mater.* **32**, 2000165 (2020).
64. Kim, H. *et al.* Highly Stretchable and Wearable Thermotherapy Pad with Micropatterned Thermochromic Display Based on Ag Nanowire–Single-Walled Carbon Nanotube Composite. *Adv. Funct. Mater.* **29**, 1901061 (2019).
65. Liao, J. *et al.* Nestable arched triboelectric nanogenerator for large deflection biomechanical sensing and energy harvesting. *Nano Energy* **69**, 104417 (2020).
66. Moon, J. H. *et al.* Self-Powered Inertial Sensor Based on Carbon Nanotube Yarn. *IEEE Trans. Ind. Electron.* **68**, 8904–8910 (2021).

67. Welsher, K., Sherlock, S. P. & Dai, H. Deep-tissue anatomical imaging of mice using carbon nanotube fluorophores in the second near-infrared window. *Proc. Natl. Acad. Sci.* **108**, 8943–8948 (2011).
68. Antaris, A. L. *et al.* Ultra-Low Doses of Chirality Sorted (6,5) Carbon Nanotubes for Simultaneous Tumor Imaging and Photothermal Therapy. *ACS Nano* **7**, 3644–3652 (2013).
69. Robinson, J. T. *et al.* In Vivo Fluorescence Imaging in the Second Near-Infrared Window with Long Circulating Carbon Nanotubes Capable of Ultrahigh Tumor Uptake. *J. Am. Chem. Soc.* **134**, 10664–10669 (2012).
70. Cui, K. *et al.* Tungsten–Carbon Nanotube Composite Photonic Crystals as Thermally Stable Spectral-Selective Absorbers and Emitters for Thermophotovoltaics. *Adv. Energy Mater.* **8**, 1801471 (2018).
71. Liang, S. *et al.* Microcavity-Integrated Carbon Nanotube Photodetectors. *ACS Nano* **10**, 6963–6971 (2016).
72. Mann, F. A., Lv, Z., Großhans, J., Opazo, F. & Kruss, S. Nanobody-Conjugated Nanotubes for Targeted Near-Infrared In Vivo Imaging and Sensing. *Angew. Chemie Int. Ed.* **58**, 11469–11473 (2019).
73. Wang, R., Wu, H., Chen, R. & Chi, Y. Strong Electrochemiluminescence Emission from Oxidized Multiwalled Carbon Nanotubes. *Small* **15**, 1901550 (2019).
74. Sardesai, N. P., Barron, J. C. & Rusling, J. F. Carbon Nanotube Microwell Array for Sensitive Electrochemiluminescent Detection of Cancer Biomarker Proteins. *Anal. Chem.* **83**, 6698–6703 (2011).
75. Zamolo, V. A. *et al.* Highly Sensitive Electrochemiluminescent Nanobiosensor for the Detection of Palytoxin. *ACS Nano* **6**, 7989–7997 (2012).
76. Juzgado, A. *et al.* Highly sensitive electrochemiluminescence detection of a prostate cancer biomarker. *J. Mater. Chem. B* **5**, 6681–6687 (2017).
77. Gao, X., Jiang, T. & Qin, W. Potentiometric aptasensing of Escherichia coli based on electrogenerated chemiluminescence as a highly sensitive readout. *Biosens. Bioelectron.* **200**, 113923 (2022).
78. Valenti, G. *et al.* Transparent Carbon Nanotube Network for Efficient Electrochemiluminescence Devices. *Chem. - A Eur. J.* **21**, 12640–12645 (2015).
79. Valenti, G. *et al.* Single Cell Electrochemiluminescence Imaging: From the Proof-of-Concept to Disposable Device-Based Analysis. *J. Am. Chem. Soc.* **139**, 16830–16837 (2017).
80. Kadimisetty, K. *et al.* 3D-printed supercapacitor-powered electrochemiluminescent protein immunoarray. *Biosens. Bioelectron.* **77**, 188–193 (2016).
81. Guo, Z., Sha, Y., Hu, Y. & Wang, S. In-electrode vs. on-electrode: ultrasensitive Faraday cage-type electrochemiluminescence immunoassay. *Chem. Commun.* **52**, 4621–4624 (2016).
82. Guo, Z. *et al.* Faraday cage-type electrochemiluminescence immunosensor for ultrasensitive detection of Vibrio vulnificus based on multi-functionalized graphene oxide. *Anal. Bioanal. Chem.* **408**, 7203–7211 (2016).
83. Lu, J., Wu, L., Hu, Y., Wang, S. & Guo, Z. Faraday Cage-Type Electrochemiluminescence Biosensor Based on Multi-Functionalized Graphene Oxide for Ultrasensitive Detection of MicroRNA-21. *J. Electrochem. Soc.* **164**, B421–B426 (2017).
84. Kannan, P., Chen, J., Su, F., Guo, Z. & Huang, Y. Faraday-Cage-Type Electrochemiluminescence Immunoassay: A Rise of Advanced Biosensing Strategy. *Anal. Chem.* **91**, 14792–14802 (2019).
85. Sentic, M. *et al.* Mapping electrogenerated chemiluminescence reactivity in space: mechanistic insight into model systems used in immunoassays. *Chem. Sci.* **5**, 2568–2572

(2014).
86. Rebeccani, S. *et al.* Electrochemiluminescent immunoassay enhancement driven by carbon nanotubes. *Chem. Commun.* **57**, 9672–9675 (2021).
87. Wang, H., Liao, L., Chai, Y. & Yuan, R. Sensitive immunosensor based on high effective resonance energy transfer of lucigenin to the cathodic electrochemiluminescence of tris(bipyridine) Ru(II) complex. *Biosens. Bioelectron.* **150**, 111915 (2020).
88. Liu, Y., Sun, Y. & Yang, M. A double-potential ratiometric electrochemiluminescence platform based on g-C 3 N 4 nanosheets (g-C 3 N 4 NSs) and graphene quantum dots for Cu 2+ detection. *Anal. Methods* **13**, 903–909 (2021).
89. Wang, X. *et al.* Enhancing electrochemiluminescence of FAPbBr3 nanocrystals by using carbon nanotubes and TiO2 nanoparticles as conductivity and co-reaction accelerator for dopamine determination. *Electrochim. Acta* **360**, 136992 (2020).
90. Song, C. *et al.* Quench-Type Electrochemiluminescence Immunosensor Based on Resonance Energy Transfer from Carbon Nanotubes and Au-Nanoparticles-Enhanced g -C 3 N 4 to CuO@Polydopamine for Procalcitonin Detection. *ACS Appl. Mater. Interfaces* **12**, 8006–8015 (2020).
91. Zanut, A. *et al.* Dye-Doped Silica Nanoparticles for Enhanced ECL-Based Immunoassay Analytical Performance. *Angew. Chemie Int. Ed.* **59**, 21858–21863 (2020).
92. Valenti, G., Fiorani, A., Li, H., Sojic, N. & Paolucci, F. Essential Role of Electrode Materials in Electrochemiluminescence Applications. *ChemElectroChem* **3**, 1990–1997 (2016).
93. Valenti, G. *et al.* Electrogenerated chemiluminescence from metal complexes-based nanoparticles for highly sensitive sensors applications. *Coord. Chem. Rev.* **367**, 65–81 (2018).
94. Voci, S., Al-Kutubi, H., Rassaei, L., Mathwig, K. & Sojic, N. Electrochemiluminescence reaction pathways in nanofluidic devices. *Anal. Bioanal. Chem.* **412**, 4067–4075 (2020).
95. Voci, S. *et al.* Surface-Confined Electrochemiluminescence Microscopy of Cell Membranes. *J. Am. Chem. Soc.* **140**, 14753–14760 (2018).
96. Fan, F.-R. F. & Bard, A. J. Observing Single Nanoparticle Collisions by Electrogenerated Chemiluminescence Amplification. *Nano Lett.* **8**, 1746–1749 (2008).
97. Chen, Z. & Zu, Y. Electrogenerated Chemiluminescence of the Tris(2,2′-bipyridine)ruthenium(II)/Tri- n -propylamine (TPrA) System: Crucial Role of the Long Lifetime of TPrA •+ Cation Radicals Suggested by Electrode Surface Effects. *J. Phys. Chem. C* **112**, 16663–16667 (2008).
98. Ma, C. *et al.* Catalytic route electrochemiluminescence microscopy of cell membranes with nitrogen-doped carbon dots as nano-coreactants. *Chem. Commun.* **57**, 2168–2171 (2021).
99. Zanut, A., Fiorani, A., Rebeccani, S., Kesarkar, S. & Valenti, G. Electrochemiluminescence as emerging microscopy techniques. *Anal. Bioanal. Chem.* **411**, 4375–4382 (2019).
100. Fiorani, A. *et al.* Spatially resolved electrochemiluminescence through a chemical lens. *Chem. Sci.* **11**, 10496–10500 (2020).
101. Guo, W., Zhou, P., Sun, L., Ding, H. & Su, B. Microtube Electrodes for Imaging the Electrochemiluminescence Layer and Deciphering the Reaction Mechanism. *Angew. Chemie Int. Ed.* **60**, 2089–2093 (2021).
102. Wang, N. *et al.* Dual Intramolecular Electron Transfer for In Situ Coreactant-Embedded Electrochemiluminescence Microimaging of Membrane Protein. *Angew. Chemie Int. Ed.* **60**, 197–201 (2021).
103. Zanut, A. *et al.* Insights into the mechanism of coreactant electrochemiluminescence facilitating enhanced bioanalytical performance. *Nat. Commun.* **11**, 2668 (2020).
104. Ma, C., Cao, Y., Gou, X. & Zhu, J.-J. Recent Progress in Electrochemiluminescence Sensing

and Imaging. *Anal. Chem.* **92**, 431–454 (2020).
105. Rebeccani, S., Zanut, A., Santo, C. I., Valenti, G. & Paolucci, F. A Guide Inside Electrochemiluminescent Microscopy Mechanisms for Analytical Performance Improvement. *Anal. Chem.* **94**, 336–348 (2022). https://pubs.acs.org/doi/full/10.1021/acs.analchem.1c05065
106. Bai, Y., Shu, T., Su, L. & Zhang, X. Functional nucleic acid-based fluorescence polarization/anisotropy biosensors for detection of biomarkers. *Anal. Bioanal. Chem.* **412**, 6655–6665 (2020).
107. Sharifi, M. *et al.* Cancer diagnosis using nanomaterials based electrochemical nanobiosensors. *Biosens. Bioelectron.* **126**, 773–784 (2019).
108. Xu, L., Li, D., Ramadan, S., Li, Y. & Klein, N. Facile biosensors for rapid detection of COVID-19. *Biosens. Bioelectron.* **170**, 112673 (2020).
109. Roche Diagnostic corporation. (2018). Available at: www.roche.com.
110. Wang, R., Wu, H., Chen, R. & Chi, Y. Strong Electrochemiluminescence Emission from Oxidized Multiwalled Carbon Nanotubes. *Small* **15**, 1901550 (2019).
111. Yang, L. *et al.* Atomic Precision Graphene Model Compound for Bright Electrochemiluminescence and Organic Light-Emitting Diodes. *ACS Appl. Mater. Interfaces* **12**, 51736–51743 (2020).
112. Kadimisetty, K. *et al.* Automated 3D-Printed Microfluidic Array for Rapid Nanomaterial-Enhanced Detection of Multiple Proteins. *Anal. Chem.* **90**, 7569–7577 (2018).
113. Miao, W., Choi, J.-P. & Bard, A. J. Electrogenerated Chemiluminescence 69: The Tris(2,2′-bipyridine)ruthenium(II), (Ru(bpy) 3 2+)/Tri- n -propylamine (TPrA) System RevisitedA New Route Involving TPrA •+ Cation Radicals. *J. Am. Chem. Soc.* **124**, 14478–14485 (2002).
114. Dutta, P. *et al.* Reactivity mapping of luminescence in space: Insights into heterogeneous electrochemiluminescence bioassays. *Biosens. Bioelectron.* **165**, 112372 (2020).
115. Marston, S. & Zamora, J. E. Troponin structure and function: a view of recent progress. *J. Muscle Res. Cell Motil.* **41**, 71–89 (2020).
116. Hammarsten, O., Mair, J., Möckel, M., Lindahl, B. & Jaffe, A. S. Possible mechanisms behind cardiac troponin elevations. *Biomarkers* **23**, 725–734 (2018).
117. Duque-Ossa, L. C., García-Ferrera, B. & Reyes-Retana, J. A. Troponin I as a Biomarker for Early Detection of Acute Myocardial Infarction. *Curr. Probl. Cardiol.* 101067 (2021). doi:10.1016/j.cpcardiol.2021.101067
118. He, S. *et al.* Integrating potential-resolved electrochemiluminescence with molecularly imprinting immunoassay for simultaneous detection of dual acute myocardial infarction markers. *Biosens. Bioelectron.* **201**, 113962 (2022).
119. Wang, J. *et al.* Ratiometric Fluorescent Lateral Flow Immunoassay for Point-of-Care Testing of Acute Myocardial Infarction. *Angew. Chemie Int. Ed.* **60**, 13042–13049 (2021).
120. Feng, S., Yan, M., Xue, Y., Huang, J. & Yang, X. Electrochemical Immunosensor for Cardiac Troponin I Detection Based on Covalent Organic Framework and Enzyme-Catalyzed Signal Amplification. *Anal. Chem.* **93**, 13572–13579 (2021).
121. T, R. *et al.* "On the Detection of cTnI - A Comparison of Surface-Plasmon Optical -, Electrochemical -, and Electronic Sensing Concepts". *Ann. Clin. Med. Case Reports* **06**, (2021).
122. Zhao, H. *et al.* Label-free electrochemical immunosensor based on PdCuPt/PPY/DCSC as a signal amplification platform for sensitive detection of cardiac troponin I. *Sensors Actuators B Chem.* **351**, 130970 (2022).
123. Wang, M. *et al.* Electrochemiluminescence detection of cardiac troponin I based on Au–Ag alloy nanourchins. *Analyst* **145**, 873–879 (2020).

124. Hong, C. *et al.* A dual-signal electrochemiluminescence immunosensor for high-sensitivity detection of acute myocardial infarction biomarker. *Biosens. Bioelectron.* **194**, 113591 (2021).
125. Yan, M. *et al.* Label-free immunosensor for cardiac troponin I detection based on aggregation-induced electrochemiluminescence of a distyrylarylene derivative. *Biosens. Bioelectron.* **192**, 113532 (2021).
126. Romiti, G. F. *et al.* Sex-Specific Cut-Offs for High-Sensitivity Cardiac Troponin: Is Less More? *Cardiovasc. Ther.* **2019**, 1–12 (2019).
127. Ahmadi, A. *et al.* Electrochemical immunosensor for determination of cardiac troponin I using two-dimensional metal-organic framework/Fe3O4–COOH nanosheet composites loaded with thionine and pCTAB/DES modified electrode. *Talanta* **237**, 122911 (2022).
128. Amodio, G., Antonelli, G., Varraso, L., Ruggieri, V. & Di Serio, F. Clinical impact of the troponin 99th percentile cut-off and clinical utility of myoglobin measurement in the early management of chest pain patients admitted to the Emergency Cardiology Department. *Coron. Artery Dis.* **18**, 181–186 (2007).
129. Greenslade, J. *et al.* Evaluating Rapid Rule-out of Acute Myocardial Infarction Using a High-Sensitivity Cardiac Troponin I Assay at Presentation. *Clin. Chem.* **64**, 820–829 (2018).
130. Cobas. Elecsys Troponin I STAT. **7**, 1–5 (2019).
131. Wang, Y. *et al.* One-Step Digital Immunoassay for Rapid and Sensitive Detection of Cardiac Troponin I. *ACS Sensors* **5**, 1126–1131 (2020).
132. Zhang, W. *et al.* In Situ Construction of Oriented Pt-PANI Needle-Like Nanoarrays-Based Label-Free Aptasensor for Ultrafast and Ultrasensitive Recognition of Cardiac Troponin I. *Adv. Mater. Interfaces* **8**, 2101543 (2021).
133. Wu, Z. *et al.* Electrochemiluminescence resonance energy transfer system fabricated by quantum state complexes for cardiac troponin I detection. *Sensors Actuators B Chem.* **336**, 129733 (2021).
134. Yan, H. *et al.* Sandwich-type electrochemical immunosensor for highly sensitive determination of cardiac troponin I using carboxyl-terminated ionic liquid and helical carbon nanotube composite as platform and ferrocenecarboxylic acid as signal label. *Sensors Actuators B Chem.* **277**, 234–240 (2018).
135. Rapino, S. *et al.* Microdrawing and highlighting a reactive surface. *J. Mater. Chem.* **20**, 7272 (2010).
136. Benck, J. D., Pinaud, B. A., Gorlin, Y. & Jaramillo, T. F. Substrate selection for fundamental studies of electrocatalysts and photoelectrodes: Inert potential windows in acidic, neutral, and basic electrolyte. *PLoS One* **9**, (2014).
137. Petrizza, L. *et al.* Electrochemical and Surface Characterization of Dense Monolayers Grafted on ITO and Si/SiO2 Surfaces via Tetra(tert-Butoxy)Tin Linker. *Electroanalysis* **28**, 2777–2784 (2016).
138. Hou, K. *et al.* Dye-anchored mesoporous antimony-doped tin oxide electrochemiluminescence cell. *Adv. Mater.* **21**, 2492–2496 (2009).
139. Frutiger, A. *et al.* Nonspecific Binding—Fundamental Concepts and Consequences for Biosensing Applications. *Chem. Rev.* **121**, 8095–8160 (2021).

CONCLUSIONS AND PERSPECTIVES

Electrochemiluminescence is a powerful analytical technique, very promising for ultrasensitive biomarker analysis, early disease diagnosis sensors, environmental investigations and monitoring of chemical and biological process.

Many different strategies were used for increasing ECL signal but a further increase in sensitivity is needed for biosensor applications. In this study, different strategies were proposed following a mechanistic study approach. Indeed, studies on ECL generation mechanism are scarce despite their importance.

New rational synthetic strategies prompted the development of nanomaterials with suitable features for increasing luminophores efficiency. Nano carbon dots (NCDs) doped with BODIPY organic compound (B-NCDs) showed a huge ECL efficiency with respect to other luminophores. The understanding of their structure influence on ECL signal and the mechanism emission generation were very useful for obtaining a very promising nanomaterial. The ECL efficiency of B-NCDs showed that it was mainly influenced by the surface-emitting states from the organic shell but also by the nano-environment of BODIPY in the core. The combination between ECL and nanomaterials was also successful for $[Ru(bpy)_3]^{2+}$-doped silica NPs. This union increased the ECL signal and allowed the application in bead-based immunoassay system and the analysis by ECL microscopy (ECLM). The synthetic procedure was fundamental for improving the number of dyes in a NP (ca 4800 complexes every NP) without enhancing the surface charge but allowing the diffusion of coreactant inside the NPs. An improved number of active complexes for ECL signal generation resulted in a 750% increase in signal intensity and a 30% improvement in signal stability with respect to the commercial immunoassay system.

The used combination between ECL, microscopy, and a beads-based immunoassay enhanced technique sensitivity with a new strategy. The investigation of the ECL mechanism and ECL emission efficiency spatial distribution showed a new mechanism at short distances (< 1 μm) from the electrode surface. The introduction of an additive (branched amine DPIBA) with a more stable carbocation successfully optimized coreactant oxidation, obtaining a 128% higher ECL signal. This increase was also obtained in commercially available Elecsys® assays performed with Cobas e 801 analyser.

Finally, those results were exploited for using CNTs nanomaterials in ECL-enhanced faraday cage type immunosensor and in the real application of an immunosensor. Specifically, the latter immunosensor targeted cardiac Troponin I which is a biomarker of acute myocardial infarction.

The creation of a conductive layer with CNTs improved the oxidation rate of TPrA, the spatial distribution of its radical and radical cation and the activation of a homogeneous mechanism never observed before in a beads-based system. Finally, the result was a 70% higher signal with respect to the commercial system.

The new strategies and mechanisms based on combination of ECL, microscopy and nanomaterials brought an enhancement in the sensitivity, efficiency, and temporal and spatial resolution of ECL technique, representing an important boost for development of clinical and diagnostic devices.

For example, CNTs was exploited in this project (chapter III) for developing an immunosensor for cardiac Troponin I (cTnI), biomarker for acute myocardial infarction (AMI) detection, reaching a LOD of 0.74 ng mL^{-1}. The sensor was under the critical point for AMI detection, but it is still not competitive with literature results. In the future, the LOD has to be lowered and the sensor has to be tested in real samples for monitoring the influence of the matrix effect. Then, it could be applied onto beads-based immunoassay system, increasing the biosensor performance.

Moreover, the discovered short distance mechanism can be combined to efficient nanomaterial-based luminophores for a further enhancement in the ECL sensitivity.

In conclusion, electrochemiluminescence has been successfully exploited for analytical application also through studies on the ECL mechanism generation. Mechanistic investigations singled out different strategies for increasing signal intensity and temporal and spatial resolution. The results were useful for developing biosensor for early disease diagnosis and clinical monitoring. The recent developments also gave an important boost towards a single-protein-molecule imaging and single-molecule detection with a super-resolved technique.

APPENDIX

1. Materials

For ECL measurements and beads/CNTs functionalization. Tri-n-propylamine (TPrA, MW=143.27 g/mol, ≥98% V/V), sodium phosphate monobasic dihydrate ($NaH_2PO_4 \cdot 2H_2O$, MW= 119.98 g/mol, ≥99%), sodium phosphate dibasic (Na_2HPO_4, MW=141.96 g/mol, ≥99%), phosphoric acid (H_3PO_4, MW=98,00 g/mol, ≥85%), dimethyl sulfoxide (DMSO, anhydrous, MW = 78.13 g/mol, ≥99.9%), MES sodium salt (MW = 217,22 g/mol, ≥99%), phosphate-buffered saline (PBS), tween®20, N-hydroxysuccinimide (NHS, MW = 115.09, ≥98%), N-(3-Dimethylaminopropyl)-N'-ethylcarbodiimide hydrochloride (EDC, MW = 191.70, ≥98%), and biotin (MW = 244.31, ≥99%) were purchased from Sigma-Aldrich.

4 μm beads coated with streptavidin were purchase by ThermoFisher scientific (Dynabeads beads); Roche Diagnostics Elecsys® beads originating from the SAP assay (bottle M), diameter 2.8 μm; MyOne beads (ThermoFisher scientific): Dynabeads MyOne Streptavidin T1, diameter 1 μm; Bio-Adembeads Streptavidin (Ademtech): Bio-MasterBeads Streptavidin, diameter 500nm and Bio-Adembeads Streptavidin, diameter 300nm.

Roche Diagnostics Free Conjugate (antibody labelled with biotin and $Ru(bpy)_3^{2+}$) originating from the SAP assay (bottle R2).

DPIBA was obtained from Roche Diagnostics (Penzberg, Germany).[1]

ITO from Kuramoto Seisakusho Co. Ltd., Tokyo, Japan.

Double-walled carbon nanotubes (DWCNT) were produced using the CVD method and purchased from Nanocyl S.A. (Sambreville, Belgium).

Graphene oxide powder (GO) were from Graphenea.

Multiwalled carbon nanotubes were produced by the CVD method and purchased from Nanostructured & Amorphous Material Inc. (Houston, Tx, USA).

Primary antibodies 19c7cc and secondary antibodies 560cc specific for cardiac Troponin I were purchased from HyTest.

Cardiac Troponin I TNNI3 from human heart, lyophilized powder was purchased from Sigma-Aldrich.

2. Specific instrumentation and methods

Photophysical investigations on B-NCDs by UniTs.[2] Absorption spectra of compounds were recorded on air-equilibrated solutions at room temperature with an Agilent Cary 5000 UV-Vis spectrophotometer, using quartz cells with path length of 1.0 cm. Emission spectra were recorded on an Agilent Cary Eclipse fluorescence spectrofluorometer.

Photophysical Measurements on $Ru(bpy)_3^{2+}$-doped silica NPs by UniBO, Prof. Prodi group.[3] UV−Vis absorption spectra were recorded at 25 °C using a PerkinElmer Lambda 45 spectrophotometer. The fluorescence spectra were recorded with a PerkinElmer Lambda LS55 fluorimeter and with a modular UV−Vis−NIR spectrofluorimeter Edinburgh Instruments FLS920 equipped with a photomultiplier HamamatsuR928P. The latter instrument connected to a PCS900 PC card was used for the time-correlated single-photon counting (TCSPC) experiments (excitation laser λ = 410 nm). NPs suspension was diluted with milli-Q water. Luminescence quantum yields (uncertainty ±15%) were recorded on air-equilibrated water solutions using $Ru(bpy)_3^{2+}$ as reference dye. The phosphorescence lifetime decays are fitted with a bi-exponential decay, the lifetimes values are reported as a weighted mean of two fitted components.

Transmission electron microscopy (TEM) and Dynamic Light Scattering (DLS) on $Ru(bpy)_3^{2+}$-doped silica NPs by UniBO, Prof. Prodi group.[3]

For TEM investigations, a Philip CM 100 transmission electron microscope was used operating at 60 KV and 3.05 mm copper grids (Formvar support film - 400 mesh). A histogram obtained by TEM images was fitted according to a Gaussian distribution obtaining the average diameter for the silica nanoparticles.

Silica nanoparticles size distributions were determined by dynamic light scattering (DLS) employing a Malvern Nano ZS instrument with a 633 nm laser diode. Samples were housed in disposable polystyrene cuvettes of 1 cm optical path length.

ζ-Potential Experiments on $Ru(bpy)_3^{2+}$-doped silica NPs by UniBO, Prof. Prodi group.[3] ζ-potential values were determined using a Malvern Nano ZS instrument. Samples were housed in disposable polycarbonate folded capillary cell (DTS1070, 750 μL, 4 mm optical path length). Electrophoretic determination of ζ-potential was made under Smoluchowski approximation in aqueous media at moderate electrolyte concentration.

Laser Scanning Confocal Fluorescence and Fluorescence Lifetime Imaging (FLIM) on $Ru(bpy)_3^{2+}$-doped silica NPs by UniBO, Prof. Prodi group.[3] The functionalized beads were characterized with an inverted Nikon A1R laser scanning confocal microscope. Images were collected using a Nikon PLAN APO 100x oil immersion objective, NA 1.45. Pinhole was set to 1 Airy Unit. In Laser Scanning Confocal Fluorescence Imaging a 401 nm CW laser was used as excitation, which was reflected onto a dichroic mirror (405 nm), while emission photons were collected through a 595/50 nm emission filter. In FLIM a time-correlated single photon counting (TCSPC) system of Picoquant GmbH Berlin was used with a 405 nm pulsed excitation laser at 25 kHz repetition frequency, the same dichroic mirror, a 560 nm longpass emission filter, a Hybrid PMA detector and a Picoquant TimeHarp correlation board.

Inductively coupled plasma mass spectrometry.[3,4] X Series II ICP-MS from Thermo Fisher was used to quantify the Ru conjugated to beads (beads@Triton and Ru@beads of different dimensions). Briefly, 500 µL of beads was dissolved in 358 µL of nitric acid (70%) and double-distilled water at a final volume of 5 mL and incubated overnight at 80°C. After dissolution, a clear solution was obtained. The total amount of Ru, as ppb concentration, was normalized to the total surface area of each bead size to obtain the density Ru μm^{-2} (see tables 2.2 and 2.4 in chapter II).

EPR spectra performed by Unipd[4] were obtained with a Bruker Elexsys spectrometer operating at X-band and equipped with an ER4103 TM cavity; a flat cell (0.5 mL) was used for the sample. Acquisition was conducted at room temperature, and spectrometer parameters were microwave attenuation 10 dB (~20 mW), sweep width 10 mT, 1024 points, time constant 10.24 ms, modulation amplitude 0.12 mT, conversion time 40.96 ms, 5 scan/spectrum. To improve S/N, 20 acquisitions were summed.

Mass spectrometry analysis[4] was performed by FFI (Fast Flow Injection) in a water/acetonitrile mixture (50/50 + 0.1% formic acid, 50 µl/min) on a Waters Xevo G2S QTof mass spectrometer (Milford, MA, USA) equipped with an electrospray (ESI) source. Capillary voltage was 1.5 kV in positive mode with a temperature of the source of 100 °C. Desolvation temperature was 350 °C while the gas flow was 10 L/h for the cone and 800 L/h for the desolvation.

Characterization of f-DWCNT.[5]

Transmission electron microscopy (TEM). TEM images were taken on a Philips EM 208 electronic microscope operating at 100 kV. Sample were prepared suspending the compound in DMF or water

and depositing some drops of the solution on copper grids covered by a carbon film of 3 mm. Solvent was dried overnight under vacuum.

Thermogravimetric analysis (TGA). TGA analysis were run on the instrument TGA Q500 from *TA Instruments* using N_2 gas flux (25 mL·min^{-1} flow rate) starting with an isotherm at 100 °C for 20 min and then heating at a rate of 10 °C·min^{-1} up to 1000 °C. Each sample was analysed at least 2 times and the average value of weight loss was reported.

Fluorescence spectroscopy. Emission spectra were collected on a Cary ECLIPSE spectrofluorimeter in 1 cm thick quartz cuvettes.

X-Ray photoelectron spectroscopy (XPS). The analyses were run with a SPECS Sage HR 100 spectrometer with a non-monochromatic X-ray source of Magnesium with a Kα line of 1253.6 eV energy and 250 W. An electron flood gun was used to compensate for charging during XPS data acquisition. The selected resolution was 30 and 15 eV of Pass. Measurements were made in an ultra-high vacuum (UHV) chamber at a pressure below 8·10^{-8} mbar. Fitting of the XPS data were done using CasaXPS 2.3.16 PR 1.6 software.

Characterization of beads 2.8 μm functionalized with CNT-Ru.[5]

Scanning electron microscopy (SEM). Scanning electron microscopy images were obtained using a Thermo Fisher Scientific Helios 450s electron microscope. The images were acquired using an acceleration voltage of 1 kV and a beam current of 6-13 pA, in high vacuum and in high-resolution mode.

Raman spectroscopy. Raman spectra were recorded with a Renishaw Invia Raman spectrometer equipped with a green laser (λ=532 nm) and plotted by means of the Wire 4.3 software.

Laser scanning confocal microscopy. Confocal microscopy images were acquired with a Zeiss LSM 510 Confocal Microscope equipped with a pulsed diode laser of 405 nm excitation wavelength. To allow proper comparison between different samples, the same microscope parameters (master gain, digital offset, pinhole dimension, laser power) were employed in all the experiments. For the images acquisition a 63x (1.40 N/A) oil objective with 575 nm LP filter was installed, and the pinhole was adjusted at 136 μm. Data analysis was performed using ImageJ 1.53c software (Wayne Rasband, National Institutes of Health).

ECL measurements.[2,3] ECL measurements were carried out with PGSTAT30 Ecochemie AUTOLAB instrument. The ECL signal generated by performing the potential step programs was measured with a photomultiplier (PMT) tube Acton PMT PD471 placed at a constant distance in front of the cell and inside a dark box. A voltage of 750 V was supplied to the PMT. The light/current/voltage curves were recorded by collecting the preamplified PMT output signal (by an ultralow-noise Acton research model 181) with the second input channel of the ADC module of the AUTOLAB instrument. Current is recorded by the picoamperometer Keithley 6485.

The ECL spectra of B-NCDs were performed by spectrometer/detector interface SpectraHub and by monochromator Acton Spectrapro 2300i, applying a constant potential of 1.6 V using PMT at 750 V of potential amplification, scanning from 400 to 800 nm with a step of 3 nm.

ECL measurements of B-NCDs and $Ru(bpy)_3^{2+}$-doped silica NPs were performed in three electrodes home-made transparent plexyglass cell using glassy carbon (GC) as working electrode, a Pt wire as counter electrode and Ag/AgCl, KCl (3 M) as reference electrode. GC was polished with 0.3 μm diamond paste (Struer) before each measurement.

ECL measurements of immunoassay specific for cTnI were performed in a three-electrode electrochemical cell (figure 4.1) with ITO modified as working electrode, Pt wire as counter electrode and Ag/AgCl, KCl (3 M) as reference electrode.

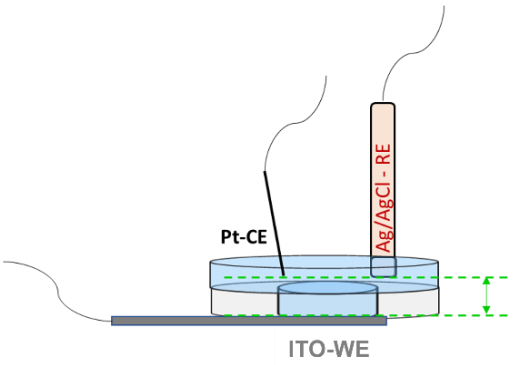

Figure 4.1. Setup of the three-electrode electrochemical cell used for immunoassay building and ECL measurements. ITO functionalized as working electrode (WE), Pt wire as counter electrode (CE), Ag/AgCl (KCl 3 M) as reference electrode (RE).

ECL imaging measurements.[3–5] For microscopic imaging, an epifluorescence microscope from Nikon (Chiyoda, Tokyo, Japan) equipped with an ultrasensitive EMCCD camera (EM-CCD 9100−13 from Hamamatsu, Hamamatsu Japan) was used with a resolution of 512 × 512 pixels and a size of 16 × 16 μm^2. The microscope was enclosed in a homemade dark box to avoid interferences from

external light. It was also equipped with a motorized microscope stage (Corvus, Märzhauser, Wetzlar, Germany) for sample positioning and with long-distance objectives from Nikon (100×/0.80 /DL4.5 mm, 40×/0.60 /DL3.6 mm and 20×/0.40 DL13 mm). The integrated system also included a potentiostat from AUTOLAB (PGSTAT 30).

The ECL/optical imaging of beads@Triton, Ru@beads, and beads@CNT-Ru, deposited on the working electrode and collected by a magnet, was performed using a solution of 0.2 M PB (pH 6.9), 180 mM TPrA and polidocanol surfactant in a PTFE homemade electrochemical cell comprising Pt working (0.16 cm^2), Pt counter, and Ag/AgCl (3 M KCl) reference electrodes.

The different solutions were inserted in the electrochemical cell with pressure-driven flow controller (OB1 Mk3, Elveflow) equipped with a flux sensor (Flow-04D working range from 0 to 1000 μL/min) and exchange when was necessary with a 10-way bidirectional valve (MUX distributor).

Images were recorded during the application of a constant potential of 1.4 V (vs. Ag/AgCl 3M KCl) for 4 s with an integration time of 8 s.

Surface generation–bead emission.[4] Ru@beads of different sizes (0.3, 0.5, 1, and 2.8 μm) were deposited on the working electrode and collected by a magnet. Finally, a glass cover slip was placed on top of the electrochemical cell, which was in contact with a solution of 0.2 M PB (pH 6.9) and 180 mM TPrA with or without DPIBA as an additive, as indicated. The ECL/optical imaging of surface generation–bead emission was performed using a PTFE homemade electrochemical cell comprising Pt working (0.16 cm^2), Pt counter, and Ag/AgCl (3 M KCl) reference electrodes.

Images were recorded while applying a constant potential of 1.4 V (vs. Ag/AgCl 3M KCl) for 4 s (0.5 s for TOF calculations) with an integration time of 8 s.

Tip generation–surface emission.[4] To study the effect of distance, we used a system comprising a transparent ITO electrode functionalized with $[Ru(bpy)_3]^{2+}$ as the emitting surface (**Ru@ITO**) and two different hemispherical Pt microelectrodes with diameters of 1.5 and 0.5 mm, respectively. The tip generation–surface emission experiments were performed using a PTFE homemade electrochemical cell comprising a Pt hemispherical microelectrode, Pt counter and Ag/AgCl (3 M KCl) reference electrodes in contact with a solution of 0.2 M PB (pH 6.9) and 180 mM TPrA. Modified surface was positioned under an inverted microscope (Nikon) equipped with an ultrasensitive EMCCD camera presented. A 4× objective was used in all experiments. This system was connected to a CH Instruments CHI910B apparatus that accurately controlled the position in the x-, y-, and z-coordinates using step motor elements. All measurements were recorded by moving the electrode

from a distance of 0.1 μm to 2.8 μm via the application of a potential from 0 to 1.4V (vs. Ag/AgCl 3M KCl) through cyclic voltammetry at a scan rate of 100 mV s^{-1} and recording both ECL signals and currents. For ECL images, the system was triggered to allow the acquisition of images in real-time during the application of potential. Images were obtained in a CCD mode sequence with an integration time of 200 ms at 4× magnification.

Elaboration of images. Software ImageJ was used to integrate the signals from ECL images with squares of 50×50px, 30×30px, 20×20px, and 20×20px for 2.8 μm and 4 μm, 1 μm, 0.5 μm, and 0.3 μm beads, respectively.

3. Elaboration procedures

Photoluminescence Quantum Yield of B-NCDs by UniTS.[2] The quantum yield (QY) measurements were performed using the relative determination, which is based on the comparison of the integral emission spectra of the sample and the standard (obtained under identical measurement conditions) for solution of known absorbances or absorption factor at the excitation wavelength.[6] We used Quinine Sulfate (QS, ϕ_f = 0.54 in 0.1 M aq. H_2SO_4) or Fluorescein (F, ϕ_f = 0.89 in 0.1 M aq. NaOH) as the standards (st) for the QY of the blue and the green emission, respectively.[6] We selected 300 nm and 466 nm as excitation wavelength for the QY of the blue and the green emission, respectively, according to published protocols and standards.[6] The fluorescence quantum yields were then calculated according to next equation:

$$\Phi_x = \Phi_{st} \cdot \frac{I_x}{I_{st}} \cdot \frac{\eta_x^2}{\eta_{st}^2}$$

I is the measured integrated fluorescence emission intensity, f is the absorption factor, η is the refractive index of the solvent and Φ is the quantum yield. Each value of the QY is an average of three independent measurements and calculations.

ECL relative efficiency of CDs.[2] The ECL relative efficiency (Φ_{ECL} in %) was measured by following a reported method, and $[Ru(bpy)_3]^{2+}$/TPrA were used as a reference.[7]

The relative ECL efficiency (Φ_{ECL}) was calculated using the relation below:

$$\Phi_x = 100 \times \frac{[\int ECL\ dt / \int i\ dt]_x}{[\int ECL\ dt / \int i\ dt]_{st}}$$

where x and st correspond to the tested CDs and the reference compound $[Ru(bpy)_3]^{2+}$ (see figure 4.2), respectively. Relative ECL efficiency (Φ_{ECL}) are reported in tables 1.3 and 1.4 in chapter I.

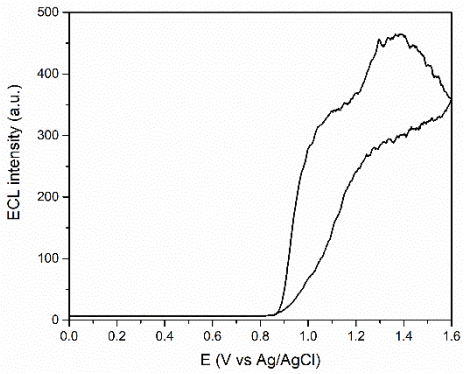

Figure 4.2. ECL potential curves of $Ru(bpy)_3^{2+}$. Experiments performed with TPrA 180 mM as co-reactant in PB 0.2 M as supporting electrolyte. Cyclic voltammetric analysis scanning from 0 V to 1.6 V, scan rate 0.1 V s^{-1}. GC electrode potential referred to Ag/AgCl at room temperature. Platinum wire as counter electrode.

Estimation of the average number of the complexes inside each NP by UniBO Prof Prodi group.[3] The final concentration of NPs has been calculated knowing the volume of water added to prepare the solution form isolated NPs. Specifically, volume of the NPs was obtained by TEM measurements and is useful for the calculation of each NPs' weight, considering 2.0 g mL^{-1} the density of the silica matrix. From this value, the number of NPs produced was estimated assuming that all the TEOS introduced were converted in silica NPs because a sufficient time is assigned before NPs isolation.

Turnover number (TON) and Turnover frequency (TOF).[4] TOF is the number of photons emitted in 1 s by a single luminophore. TON and TOF are defined as:

$$TON = \frac{\int_0^t ECL_{Ru@bead} - \int_0^t ECL_{bead}}{n° \; Ru@bead}$$

$$TOF = \frac{\int_0^t ECL_{Ru@bead} - \int_0^t ECL_{bead}}{n° \; Ru@bead \times t}$$

ECL emission ($ECL_{Ru@bead}$) was quantified by integration of ECL images (.tiff), as obtained with the CCD camera in the "surface generation-beads emission" for a time (t) of 0.5 s. Integrated ECL background (ECL_{bead}) was subtracted from the integrated ECL emission for each bead dimension. ECL_{bead} was measured with beads without Ru label.

In chapter 3[5]

$$TOF = \frac{\int_0^t ECL_{Ru@bead} - \int_0^t ECL_{bead}}{Fluorescence\ intensity\ x\ integration\ time}$$

ECL emission ($ECL_{bead@Ru}$) was quantified by integration of ECL images, as obtained with the CCD camera for a time (t) of 8 s. Integrated ECL noise (ECL_{bead}) was subtracted from the integrated ECL emission for each bead dimension. ECL_{bead} was measured without beads presence in images.

Integration time is the time when the potential 1.4 V is applied, and it is of 4 s.

Fluorescence intensity is the mean grey value of 126 beads images obtained using laser confocal microscopy technique.

4. Functionalization of materials

Beads functionalization.

Ru@beads. For each bead dimension, the total surface area was constant of 7×10^9 μm^2. Indeed, the volume of bead solution was 133.86 (0.3 μm), 134.48 (0.5 μm), 265.64 (1 μm) and 6000.00 (2.8 μm) μl, respectively.

Each beads solution was poured in a 20 mL vial, collected with a magnet for 2 minutes, and afterwards the supernatant was discharged. Then, washing with 10 mL bead buffer was repeated 2 times for 5 minutes each.

Beads were incubated with 18 mL of Roche Diagnostics Free Conjugate (2 h at 37°C) by using a tube rotator. Separation was carried out with a magnet for 2 minutes and the supernatant was discharged. This whole procedure was repeated 5 times. Finally, beads were stored in the bead buffers from Roche Diagnostics SAP assay bottle M (2.8-1 μm) or Ademtech buffer (0.5-0.3 μm) in a total volume of 800 μl.

For functionalization of **beads@Triton** Roche Diagnostics Free Conjugate was substituted by bio-Triton@RuNP solution (10 nM) in phosphate buffer (0.01 M). At the end of the fifth cycle, beads@Triton were washed five times in phosphate buffer (0.2 M) and polidodecanol surfactant to eliminate the unbounded nanoparticles and stored in bead buffer at 4°C.

Beads@CNT-Ru. Streptavidin-coated beads with a diameter of 2.8 μm were functionalized with biotinylated CNT labelled with the $[Ru(bpy)_3]^{2+}$ complex (CNT-Ru). The magnetic beads solution (diameter 2.8 μm; Dynabeads beads, ThermoFisher scientific, total surface area of 7×10^9 μm^2, 6 mL) was poured in a 20 mL vial, and the beads were collected using a magnet for 2 minutes. Afterwards, the supernatant was discharged and 18 mL of CNT-Ru solution (1.6 μM of Ru) in phosphate buffer saline (0.01 M) was added, followed by 3 hours incubation at 37 °C under rotation to form the biotin-streptavidin bond. The solution was separated with

a magnet and the supernatant discharged. **Beads@Ru** were obtained using the same procedure but using free conjugate (antibody labelled with biotin and $Ru(bpy)_3^{2+}$) instead of CNT-Ru solution. For **beads@fGO-Ru** a solution of fGO in PBS 0.01 M was used while for **4beads@CNT-Ru** and **4Beads@Ru** 665.1 µL, (total surface area of 7 $x10^9$ μm^2) of magnetic beads solution (diameter 4 µm; Dynabeads beads, ThermoFisher scientific) were used and 18 mL of respectively CNT-Ru solution (1.6 µM of Ru) in phosphate buffer saline (0.01 M). and Roche Diagnostics free conjugate.

Double functionalization of fGO-Ru.

A solution of TFA-monoprotected (1.2 mmol) and Boc-monoprotected (1.2 mmol) diamine in DMF (4 mL), were added one pot to a dispersion of pristine GO (50 mg) in DMF (10 mL) and finally TEA (1.2 mmol) were added. The mixture was stirred for 24h at 100 °C and then, after dilution with MilliQ water, was filtered on PTFE (0.45 µm pore size) and washed by redispersion/filtration with MilliQ water and MeOH. The black powder obtained was dried under vacuum overnight (figure 4.3).

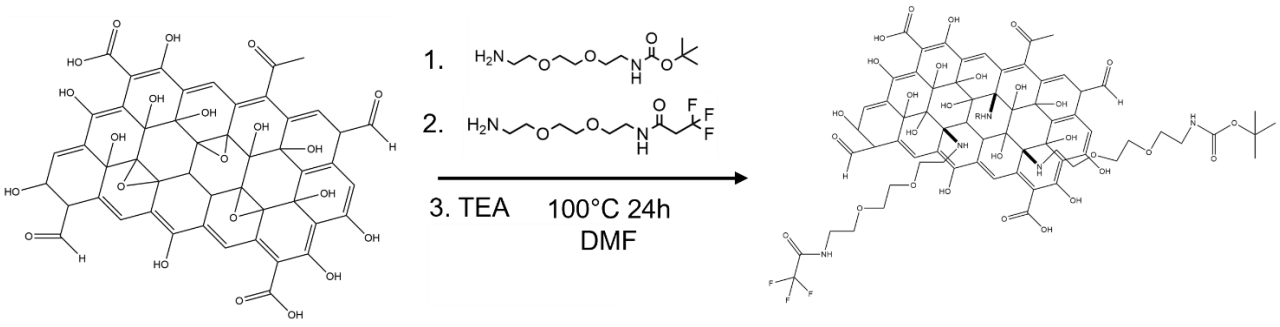

Figure 4.3. First step of GO double functionalization.

Then Boc protective groups was cleaved through HCl_{conc} in 1,4-dioxane, ultrasonication for 5 min. The suspension was stirred overnight, then filtered on PTFE (0.45 µm pore size) and washed by redispersion/filtration with MilliQ water and MeOH. $Ru(bpy)_3C_3H_6COOH$ was activated by EDC and NHS and then put into a dispersion of *fGO* (6.7 mg) in DMF (2 mL) and stirred overnight. The dispersion was filtered on PTFE (0.45 µm pore size) and washed by redispersion/filtration with MilliQ water and MeOH. NH_3 (concentrated aqueous solution) was added to a dispersion of *f*GO-Ru in MeOH, obtained by ultrasonication (5 min), and stirred overnight for removing TFA protective group. The dispersion was then filtered on PTFE (0.45 µm pore size) and washed by redispersion/filtration with MilliQ water and MeOH. Finally, biotin was dissolved in a MES buffer 0.1 M (pH = 6) and added for 20 minutes to a MES buffer solution containing EDC and NHS. 1 mg

of *f*GO-Ru was suspended in 100 μL of DMSO, sonicated for 20 minutes, and then added to the solution containing biotin, EDC, and NHS. The mixture was brought to 1 mL with MES buffer and maintained under rotation at 25 ^{0}C overnight. 200 μL of MES buffer solution containing biotin, EDC, and NHS was added to the mixture, which was then maintained under rotation for 72 hours (Figure S2). Afterwards, the solution was dialyzed for 24 hours at 25 ^{0}C in deionized water with 3–4 changes of water. Finally, the obtained solution of biotinylated fGO-Ru (figure 3.8 in chapter III) was diluted in 100 mL of PBS 0.01 M.

Double functionalization of CNT-Ru.

For the synthesis of CNT-Ru (figure 4.4), 100 mg of oxidized DWCNTs **(*ox*-DWCNT**) were sonicated for 1 hour in 100 mL of DMF to obtain a homogeneous dispersion. 150 mg of paraformaldehyde and 150 mg of the corresponding amino acid (1-(1,1-dimethylethyl) ester) were added 4 times (every 24 hours) to the suspension, which was stirred upon heating at 115 °C for 5 days. After being cooled to room temperature, the suspension was sonicated for 30 minutes and filtered on a Teflon membrane (Millipore, JHWP, 0.1 μm). The black solid was washed by redispersion/filtration in DMF, MeOH and Et_2O. The obtained product (97 mg) was dried under vacuum overnight. 60 mg of **DWCNT 1** were sonicated for 30 minutes in 40 ml of anhydrous DMF with a molar excess of DIEA (1,7 mL). Then, 100 equivalents of EDC were dispersed in 20 mL of anhydrous DMF and added to the mixture, that was stirred under Argon 1 hour at rt. After the addition of 100 equivalents of NHS, the solution was stirred under Argon overnight at rt. The solution was sonicated for 30 minutes and filtered on a Teflon membrane (Millipore, JHWP, 0.1 μm). The black solid was washed by redispersion/filtration in DMF, i-PrOH and Et_2O. The obtained product (57 mg) was dried under vacuum overnight. 10 mg of **DWCNT 1'** were sonicated for 50 minutes in 10 mL of anhydrous DMF with a molar excess of DIEA (100 μL). 2.5 mg of $Ru(bpy)_3^{2+}$ amine derivative were dissolved in 2.5 mL of anhydrous DMF and added to the reaction mixture, which was sonicated for 20 minutes and stirred under Argon for 24 hours at 45 °C. The mixture was sonicated and filtered on a Teflon membrane (Millipore, JHWP, 0.1 μm). The black solid was washed by redispersion/filtration in DMF, MeOH and Et_2O. The obtained product (8 mg) was dried under vacuum overnight. To remove Boc protecting group, **DWCNT 2** were treated with HCl:1,4-dioxane (1/2) overnight, affording free terminal amines which increase the solubility of the compound and are available for subsequent functionalization step with biotin, in this case.

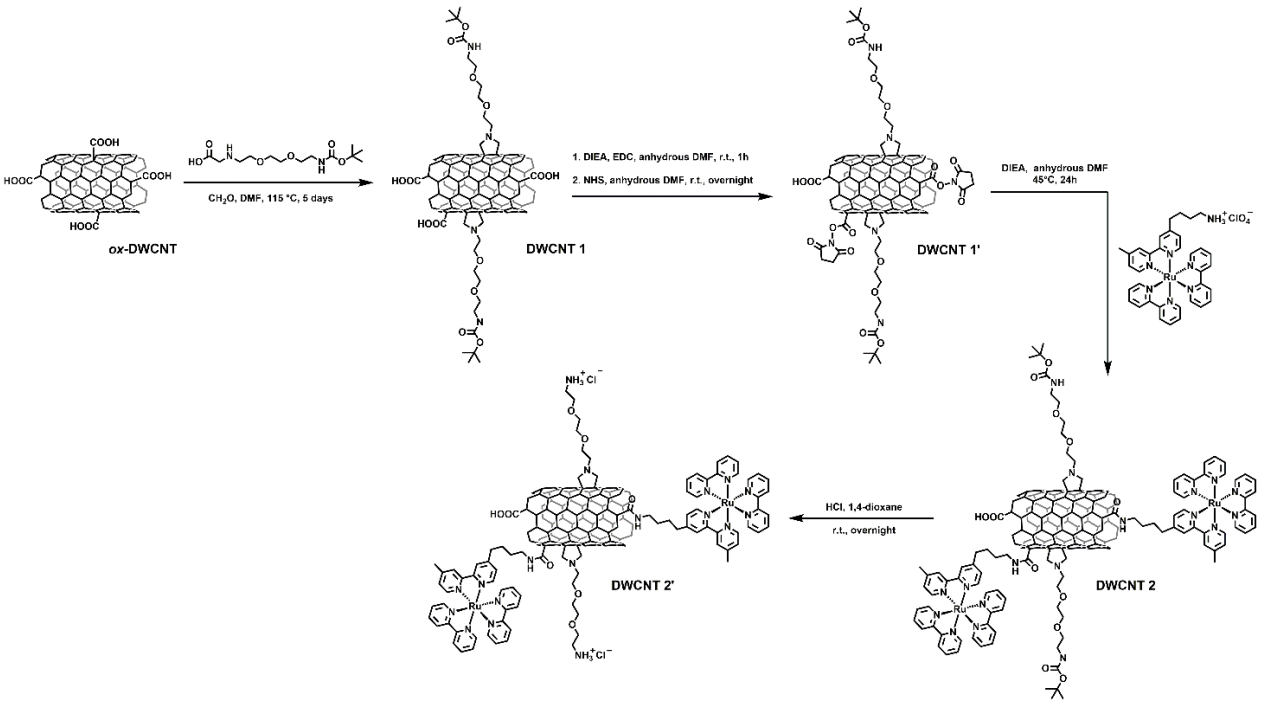

Figure 4.4. DWCNT 2′ synthetic path

Beyond the TGA analysis also XPS analysis were performed after each step for investigating the progress of the functionalization. In table 4.1 the elemental percentage composition was reported and in figure 4.5 is represented the XPS survey plot of the final compound DWCNT 2′. This analysis didn't show the presence of Ru complex for the low sensitivity of the technique. However, as reported in chapter III the ICP-MS analysis revealed a huge Ru concentration of 1.57 μg mg^{-1}.

	N %	C %	O %	Ru %
DWCNT ox	0.89	92.47	6.64	
DWCNT 1	3.47	74.53	22.00	
DWCNT 1'	3.70	68.38	27.10	0.82
DWCNT 2	3.83	62.71	32.96	0.49

Table 4.1. Elemental analysis of intermediates and final product DWCNT 2′

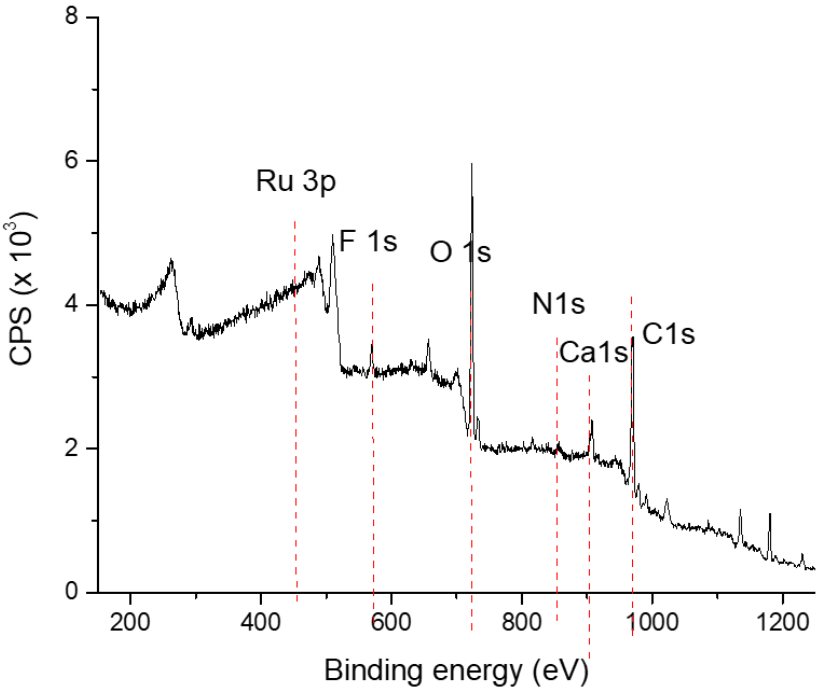

Figure 4.5. XPS survey plot of DWCNTs 2'

For functionalizing this DWCNTs with biotin, biotin was dissolved in a MES buffer 0.1 M solution (pH = 6) and added for 20 minutes to a MES buffer solution containing EDC and NHS. 0.4 mg of DWCNT 2' was suspended in 40 µL of DMSO, sonicated for 20 minutes, and then added to the solution containing biotin, EDC, and NHS. The mixture was brought to 1 mL with MES buffer and maintained under rotation at 25 ^{0}C overnight. 200 µL of MES buffer solution containing biotin, EDC, and NHS was added to the mixture, which was then maintained under rotation for 72 hours. Afterwards, the solution was dialyzed for 24 hours at 25 ^{0}C in deionized water with 3–4 changes of water. Finally, the obtained solution of biotinylated DWCNT 2' (CNT-Ru, figure 4.6) was diluted in 100 mL of PBS 0.01 M for subsequently labelled the micromagnetic beads.

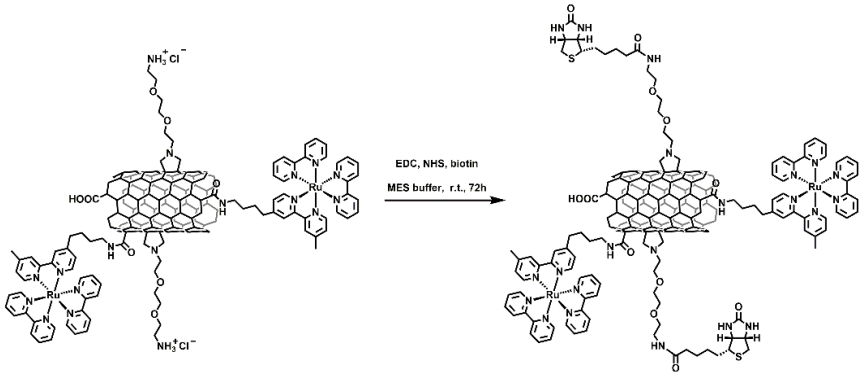

Figure 4.6. Biotinylation of DWCNT 2' for the attachment of the material to streptavidin magnetic beads.

5. **Synthesis of 1-(1,1-dimethylethyl) ester (Boc-monoprotected diamine) for functionalization of CNT-Ru**

Firstly, 0.05 mol of Di-ter-butyl decarbonate (Boc) in 75 mL of THF was added dropwise in 0.1 mol of (ethylenedioxy)bis(ethylamine) in 75 mL of THF along 2/3 hours at 0°C. After the addition, the mixture was stirred overnight at r.t. The solvent was removed under reduced pressure and then distilled water (100 mL) was added and the solution was filtered on celite. After extraction with hexane (3x150 mL) and then with AcOEt (3x150 mL), the organic layer (AcOEt) was dried under reduced pressure and with a vacuum pump. The extraction was monitored by TLC (eluent Cy:AcOEt = 1:9) flashed with ninhydrin. Tert-butyl[2-[2-(2aminoethoxy)ethoxyethyl]carbamate was obtained and analysed by ^{1}H-NMR. H^1 NMR (500MHz $CDCl_3$) δ: 5.17 (bs, 1H, NH); 3.59 (s, 4H, $2CH_2$); 3.51 (t, 2H, CH_2); 3.48 (t, 2H, CH_2); 3.28 (m, 2H, CH_2); 2.84 (t, 2H, CH_2); 1.59 (bs, 2H, NH_2); 1.40 (s, 9H, $C(CH_3)_3$).

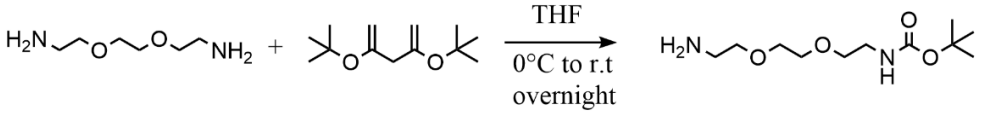

Figure 4.7. First step: synthesis of Tert-butyl[2-[2-(2aminoethoxy)ethoxyethyl]carbamate.

The product obtained was put in 150 mL of DCM and 2.7 mL of Et_3N and a solution of 100 mL of DCM and 2 mL of benzylbromoacetate was added dropwise overnight. The product 1-(1,1-dimethylethyl)13-phenylmethyl)ester was purified with flash chromatography (eluent AcOEt + MeOH 5%) and analysed by ^{1}H-NMR. H^1 NMR (500MHz $CDCl_3$) δ: 7.34 (m, 5H, Ph); 5.19 (bs, 1H, NH); 5.16 (s, 2H, $phCH_2$); 3.59 (m, 6H, $3CH_2O$); 3.50 (m, 4H); 3.28 (m, 2H, CH_2NH); 2.81 (t, 2H, CH_2); 2.19 (bs, 1H, NH); 1.42 (s, 9H, $C(CH_3)_3$);

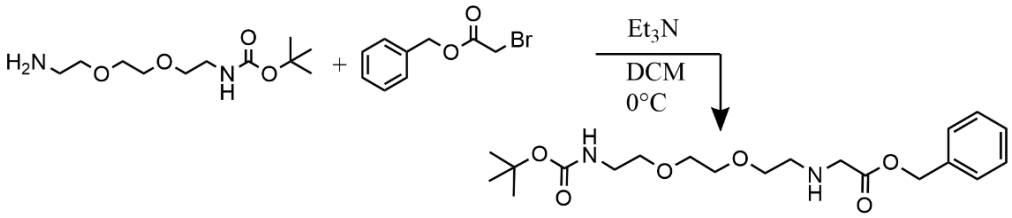

Figure 4.8. Second step: synthesis of 1-(1,1-dimethylethyl)13-phenylmethyl)ester.

The obtained product was added to 125 mL of MeOH, Ar bubbled, and Pd/C added until the solution turns black. After removing all the air present the solution was leaved under H_2 overnight. The product was precipitated under reduced pressure and through addition of Et_2O. The final product

1-(1,1-dimethylethyl) ester we are interested in was analysed by ^{1}H-NMR and used for CNTs functionalization.

H^{1} NMR (500MHz $CDCl_3$) δ: 3.9 (m, 3H, CH_2 and NH); 3.6 (m, 5H, CH_2 and NH); 3.5 (m, 2H, CH_2); 3.32 (m, 4H, CH_2); 1.45 (s, 9H, $C(CH_3)_3$);

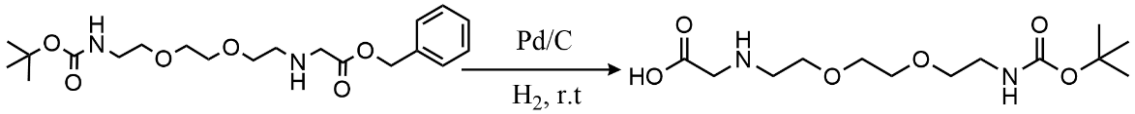

Figure 4.9. Final step of the synthesis of 1-(1,1-dimethylethyl) ester.

6. Biosensor assembly

The immunoassay specific for cTnI showed in chapter III and figure 3.27 was built following many steps. Between each of them we washed 5 times with a solution of phosphate buffer saline (PBS) 0.01 M and surfactant tween20 0.05% w/w and a solution of only PBS 0.01M (pH 7.4). The steps performed are the following:[8]

1) Incubation at 4°C overnight of polymerized ITO electrode with MWCNT-mAb1 0.5 mg mL^{-1} and a catalytic amount of EDC. MWCNTs-mAb1 are MWCNTs functionalized with capture antibody specific for cardiac Troponin I. For the functionalization 15 μL of EDC PBS 0.01M solution was deposited directly on ITO polymerized and then 35 μL of MWCNTs-mAb1 solution in PBS (pH 7.4) were added.
2) Blocking of antibody free sites with 40 μL of BSA 2% or MILK 5% in PBS 0.01 M + tween20 for 1.30 h at 37°C and change of solution after 1 h.
3) Incubation with 20 μL of cardiac Troponin solution for 1h at 37°C. This step was performed only with PBS 0.01 M pH=7.4, without troponin, for the blank sample. The Troponin solution was stored in freezer at -80°C with glycerol 85% 1:1 and diluted in PBS 0.01M obtaining the required concentration.
4) Incubation with 20 μL of MAb2-Ru 100 μg mL^{-1}, which is the detection antibody functionalized with luminophore $[Ru(bpy)_3]^{2+}$, for 1h at 37°C.

REFERENCES

1. Josel, H.-P., Andres, H., Windfuhr, M., Larbolette, O. & Quint, S. Branched-chain amines in electrochemiluminescence detection. (2017).

2. Arcudi, F. *et al.* Lighting up the Electrochemiluminescence of Carbon Dots through Pre- and Post-Synthetic Design. *Adv. Sci.* **8**, 2100125 (2021).

3. Zanut, A. *et al.* Dye-Doped Silica Nanoparticles for Enhanced ECL-Based Immunoassay Analytical Performance. *Angew. Chemie Int. Ed.* **59**, 21858–21863 (2020).

4. Zanut, A. *et al.* Insights into the mechanism of coreactant electrochemiluminescence facilitating enhanced bioanalytical performance. *Nat. Commun.* **11**, 2668 (2020).

5. Rebeccani, S. *et al.* Electrochemiluminescent immunoassay enhancement driven by carbon nanotubes. *Chem. Commun.* **57**, 9672–9675 (2021).

6. Würth, C., Grabolle, M., Pauli, J., Spieles, M. & Resch-Genger, U. Relative and absolute determination of fluorescence quantum yields of transparent samples. *Nat. Protoc.* **8**, 1535–1550 (2013).

7. Wallace, W. L. & Bard, A. J. Electrogenerated chemiluminescence. 35. Temperature dependence of the ECL efficiency of tris(2,2′-bipyridine)rubidium(2+) in acetonitrile and evidence for very high excited state yields from electron transfer reactions. *J. Phys. Chem.* **83**, 1350–1357 (1979).

8. Zamolo, V. A. *et al.* Highly sensitive electrochemiluminescent nanobiosensor for the detection of palytoxin. *ACS Nano* **6**, 7989–7997 (2012).